Switching and Phase Slippage in the Charge-Density-Wave
Transport of Niobium Triselenide

By

Richard Payton Hall

A.B. (Princeton University) 1980
M.A. (University of California) 1983

DISSERTATION

Submitted in partial satisfaction of the requirements for the degree of

DOCTOR OF PHILOSOPHY

in

PHYSICS

in the

GRADUATE DIVISION

of the

UNIVERSITY OF CALIFORNIA at BERKELEY

Approved:

. . . .
Chair   Date

****

Switching and Phase Slippage

in the

Charge-Density-Wave Transport

of Niobium Triselenide

Copyright   c   1988

Richard Payton Hall

Switching and Phase Slippage in the Charge-Density-Wave Transport of Niobium Triselenide
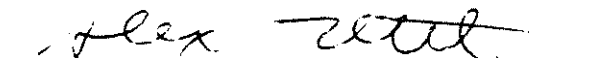
by

Richard Payton Hall

ABSTRACT

The phenomenon of switching has been studied in the lower charge-density-wave (CDW) state of $NbSe_3$. The dc current-voltage characteristics of selected crystals of nominally pure and iron-doped material display abrupt, hysteretic thresholds for nonlinear conduction. Narrowband current oscillations indicate that the thresholds represent the sudden onset of Fröhlich conduction by the CDW condensate.

Switching has been characterized by measurements of dc and ac electrical conductivity. Measurements of dc conductivity show that switching is distinguished from nonswitching transport by discontinuities in CDW current, large polarization before the onset of CDW motion, and an unusual temperature dependence of the electric fields necessary to initiate CDW motion. Switching is found to originate in the crystalline bulk of $NbSe_3$. Switching is not caused by surface defects or external electrical contacts, but is instead associated with strong, nonuniform pinning of a CDW. Measurements of ac conductivity show that switching CDWs are dynamically overdamped when pinned, but underdamped when sliding.

Switching has also been characterized by investigation of dynamical instabilities that occur under particular combinations of ac and dc drive. In crystals biased by a dc current, large and intermittent 1/f noise is observed in

regions of negative differential resistance. In crystals biased by combined dc and ac electric fields, period-doubling routes to chaos are observed during CDW mode-locking. The conditions necessary for the instabilities to occur are mapped out as a function of temperature, dc bias, ac frequency, and ac amplitude.

Analysis shows that switching can not be explained by standard models of CDW transport. Phase slippage and strong pinning are proposed as mechanisms of switching. A classical Hamiltonian is constructed to describe the dynamics of strongly pinned CDWs, and overdamped equations of motion are derived to model phase slippage in the CDW order-parameter. The equations qualitatively reproduce the experimental characteristics of switching CDWs. Thus, phase slippage provides a self-consistent explanation for the transport properties of switching CDWs.

Alex Zettl

Chairman, Dissertation Committee

To my wife, Elizabeth Miller-Hall,

and to our parents.

Acknowledgements

Table of Contents

(For page sequence only.)

CHAPTER 1: SURVEY OF THE THESIS

CHAPTER 1: SURVEY OF THE THESIS

This thesis studies the phenomenon of switching in charge-density-wave (CDW) transport.[1] The term *switching* refers to the threshold behavior of a CDW.[2] In nonswitching CDW transport, the velocity of a CDW increases gradually as an applied electric field exceeds the threshold field E_T for CDW depinning.[3-5] In switching transport, the CDW velocity increases abruptly and often hysteretically. The resulting difference between I-V curves for switching and nonswitching CDWs is quite striking. A nonswitching I-V curve departs smoothly from ohmicity at threshold, whereas a switching CDW displays one or several[6] steplike breaks.

The thesis research accomplished two results. First, switching was characterized in one type of CDW conductor, NbSe$_3$, through an extensive series of experiments.[7-15] Second, a theoretical model was constructed to explain the experimental results.[16,17] The main conclusion of the work is that switching represents a unique regime of transport in which the dynamics of the CDW amplitude is as important as the dynamics of the CDW phase. This conclusion is significant because amplitude dynamics is thought to be unimportant in nonswitching CDW transport. Therefore, the differences between switching and nonswitching transport are caused by qualitative, not just quantitative, differences in physics.

The purpose of this chapter is to provide an overview of the thesis research. The chapter is organized into four sections. The first section is an introduction that briefly reviews CDW transport. The second section is a survey of the experiments that were performed on switching CDWs. The third section

discusses the process of phase slippage in the CDW order-parameter, which is the physical mechanism proposed to explain switching. The fourth and concluding section is a guide to the rest of the thesis.

I. Charge-Density-Wave Transport

A *charge-density wave* (CDW) is a spatially periodic modulation of a metal's ionic lattice and electronic charge density. CDWs occur most readily in anisotropic metals whose Fermi surfaces share certain characteristics with the Fermi surfaces of idealized one-dimensional metals.[1] A charge-density wave is also called a *Peierls distortion* after R. E. Peierls, who noted that the electronic energy of a one-dimensional metal can be lowered by a spatial modulation of the metal's lattice.[18] In 1953, concurrently with Peierls' work, H. Frohlich proved that the total energy (the combined electronic and lattice energies) of a one-dimensional metal can also be lowered by a modulation of the metallic lattice.[19] In addition, Frohlich proved that a Peierls distortion can act as a superconductor of electrical current. In 1976, CDW conductivity was discovered in a real material, NbSe$_3$, by Monceau, Ong, and coworkers.[3] Charge-density waves in NbSe$_3$ do not act as superconductors, because of the defects, lattice anharmonicities, and other imperfections that are inevitably found in real materials. Since Frohlich's dynamical theory is exact only for perfect crystals, experimental and theoretical research since 1976 has focused on finding a theory which describes CDW conduction in nonideal crystals.

Even though Frohlich's theory is not exact for real CDW materials, it still serves as the starting point for more sophisticated models of CDW transport.

After a CDW material has undergone a Peierls distortion, the spatially-modulated electronic charge density of the material may be written as $n + \rho_{CDW}(x)$, where n is the average electronic density and $\rho_{CDW}(x)$ is the density modulation produced by the Peierls distortion. The spatial variation of the electronic charge-density wave is given by

$$\rho_{CDW}(x) = \rho\cos(Qx + \phi) , \qquad (1.1)$$

where ρ is the amplitude of the electronic density wave; $Q = 2k_F$ is the CDW wavevector, with k_F the electronic Fermi wavevector; and ϕ is the CDW phase with respect to the undistorted lattice. If the CDW wavelength $\Lambda = 2\pi/Q$ is incommensurable with the lattice constant a, then in an ideal crystal the energy of a CDW is independent of its phase.[19] Frohlich showed that electric fields couple directly to the phase of a CDW, and that the application of an electric field to an incommensurable CDW, even a vanishingly small electric field, causes the CDW phase to advance continuously, or to *slide*. Sliding CDWs carry an electrical current, because variations in ϕ correspond to displacements of electronic charge. The mechanism of current transport by CDW sliding is known as *Frohlich conductivity*.

In a real, non-ideal material such as NbSe$_3$, the energy of an incommensurable CDW is not independent of the CDW phase, because impurities and defects *pin* the CDW phase to preferred local values.[20-23] Therefore, infinitesimal electric fields do not cause the CDW to slide. If impurity and defect concentrations are small enough, however, finite electric fields can still *depin* the CDW, leading to a sliding CDW state with enhanced

conductivity. In conventional CDW depinning, the depinning process is smooth, with a well-defined *threshold field* E_T for the onset of CDW conduction and with no discontinuities in either chordal (V/I) or differential (dV/dI) resistance.[5] At very high electric fields the CDW dynamic conductance saturates as the CDW approaches a high-field, high-conductivity state.[3-5]

In contrast to conventional CDW depinning, the phenomenon of *switching* produces a sharp, often hysteretic discontinuity in the I-V characteristic of a CDW conductor. In many cases, the critical field E_C at which switching occurs corresponds to the onset of CDW motion, hence $E_C = E_T$. In other cases, switching is preceded by apparently conventional CDW depinning, so that $E_C > E_T$.[7] Multiple switches in a single I-V characteristic have also been reported.[6] Switching may be observed in real-time pulsed experiments, where application of a current pulse causes an abrupt transition to a high-conductivity state after a short delay.[2,24] Switching was first reported in the lower CDW state of $NbSe_3$. Since then, switching has been observed in selected crystals of TaS_3 (Ref. 25), $(NbSe_4)_{3.33}I$ (Ref. 26), $K_{0.3}MoO_3$ and $Rb_{0.3}MoO_3$ (Ref. 27). Furthermore, switching has been intentionally induced or enhanced by iron-doping $NbSe_3$ (ref. 6) or by irradiating the blue bronzes.[28] Therefore, switching has proven to be a general CDW phenomenon.

The magnitude of switching thresholds is characteristic of CDW depinning energies and suggests that the nonohmic current in switching crystals is carried by the CDW condensate, just as in nonswitching crystals. On the other hand, CDW transport is dramatically different in switching crystals than in nonswitching crystals. For example, this thesis will show that switching in

NbSe$_3$ is associated with negative differential resistance, bistability and large 1/f noise;[8] an inductive ac response;[9] and period-doubling routes to chaos.[10] In nonswitching NbSe$_3$ crystals, all of these effects are absent.

Most experimental and theoretical research has concentrated on smoothly depinning CDWs in nonswitching crystals. A number of models, both quantum[29] and classical,[30,31] have partially explained the dynamics of nonswitching CDWs. Despite a wide diversity of physical assumptions, these standard models commonly ascribe CDW motion to variations in the CDW phase and treat the CDW amplitude as constant and homogeneous throughout a crystal. The physical nature of CDW transport remains controversial, however, since it is unclear whether quantum tunneling or classical mechanics is the appropriate framework for describing CDW dynamics.

Because of the drastic differences between switching and nonswitching crystals, various *ad hoc* mechanisms have been introduced to explain switching: domain-coupling,[2,32] CDW self-blocking,[33] phase inertia,[10] and CDW current noise.[34] *Ad hoc* explanations for switching are rather unsatisfactory, because they obscure a fundamental issue. A theoretical model that correctly describes nonswitching transport should be a limiting case of a more general description that also encompasses switching. Thus it is important to understand switching at a fundamental level, because switching could provide a stringent test for any general theory of CDW transport, whether quantum or classical.

II. Experiments on Switching CDWs

This section summarizes the experimental results of the thesis research on

switching in NbSe$_3$. The primary goal of the research was to determine whether switching is an intrinsic aspect of CDW transport. The results of the research show that it indeed is. More precise goals of the research were to characterize the dynamics of switching CDWs; to relate these dynamics to the dynamics of nonswitching CDWs; and to compare the dynamics of switching CDWs to the predictions of existing models. The main result of the experiments is that switching corresponds to a qualitatively different type of CDW dynamics: CDW motion in the presence of strong, nonuniform pinning. Current discontinuities, phase slippage, and amplitude fluctuations are basic features of this type of CDW transport. As a result, switching cannot be adequately described by any purely phase-dynamical model of CDW sliding — a dynamical treatment of the CDW amplitude is also required. Although study was limited to a single CDW material, the thesis results are believed to be applicable to other CDW conductors as well.

Experiments on switching crystals of NbSe$_3$ may be grouped in one of two ways. A straightforward method is to classify experiments by the type of measurement probe that is applied to a crystal. In the following experiments, various combinations of dc and ac electric fields were applied to switching crystals. The combinations can be classified as 1) pure dc fields, 2) dc fields plus small ac fields, and 3) dc fields plus large ac fields, where "large" and "small" are measured relative to the threshold field of a crystal. This classification scheme is essentially how experiments are grouped in the main body of the thesis.

An alternate method of classifying experiments is to group them according to the type of response that is observed during an experiment. Although switching crystals display a wide variety of responses, most of which are very different from comparable responses in nonswitching crystals, the responses are now thought to be manifestations of just four general effects: CDW current discontinuities, phase polarization, avalanche depinning, and pseudo-inertia. Table 1 lists the four effects and the associated responses. (For completeness, the table lists some experiments that were not part of the thesis. Appropriate references are listed for these experiments.)

CDW current discontinuities are the most important category of effects associated with switching,[12] and for this reason they will be the focus of the present discussion. Current discontinuities are important first of all because they distinguish switching from nonswitching crystals. Current discontinuities are usually absent in nonswitching crystals, although they are sometimes present due to extrinsic factors such as gross crystal defects or temperature gradients. In contrast, current discontinuities are usually present in switching crystals, even in nearly ideal samples held at uniform temperatures.

CDW current discontinuities are also important because their presence requires fluctuations of the CDW amplitude. A discontinuity in CDW current actually represents a discontinuity in CDW phase velocity. A velocity discontinuity creates a compression of the CDW phase, because the phase accumulates on one side of the discontinuity. But CDW phase can not pile up indefinitely at a discontinuity, since there is an energy cost associated with

EFFECT	PROBE FIELDS	REFERENCE
CURRENT DISCONTINUITIES	dc	Chap. 3
CDW POLARIZATION		
Abrupt depinning	dc	Chap. 3
Hysteresis	dc	Chap. 3
Changes in low-field resistance	dc	Chap. 3
AVALANCHE DEPINNING		
Hysteresis-loop sublevels	dc	Chap. 3
Negative-differential resistance	dc	Chap. 5
Delayed response to pulsed fields	pulsed	Ref. 2
Breakup induced by temperature gradients	dc	Ref. 13
AC switching noise	dc + large ac	Ref. 15
PSEUDO-INERTIA		
AC Conductivity		
Overdamped pinned response	dc + small ac	Chap. 4
Underdamped sliding response	dc + small ac	Chap. 4
Dynamical Instabilities		
Period-doubling	dc + large ac	Chap. 5
Chaos	dc + large ac	Chap. 5
Noisy precursors	dc + large ac	Chap. 5

Table 1-1)   Experimental effects associated with switching.

compression of the phase. Eventually the energy cost of compressing the phase exceeds the energy cost of destroying the CDW state, and when this happens, the CDW disappears momentarily at the discontinuity.

The disappearance of the CDW is equivalent to the collapse of the CDW amplitude. When the amplitude collapses, the CDW phase becomes indeterminate and therefore may "slip" by factors of 2π. When the phase slips, some of the accumulated phase is released and it becomes energetically favorable for the CDW state to reform. The amplitude then regenerates, and this sets off a new cycle of phase compression and amplitude collapse as the phase begins to reaccumulate. Each time the CDW amplitude collapses, CDW current is converted into normal electronic current. The process of current conversion by periodic collapse of the CDW amplitude is known as *phase slippage*, and sites where the CDW amplitude fluctuates are called *phase-slip centers*.[12,35]

The other effects listed in Table 1 are straightforward consequences of phase slippage. For example, the category of CDW polarization refers to effects associated with compression and deformation of the CDW phase around phase-slip centers, and the category of avalanche depinning includes effects caused by phase slippage at one center triggering phase slippage at nearby centers. The last category of pseudo-inertia includes effects caused by the time-lag that it takes a 2π change of phase to diffuse from a phase-slip center into the bulk of a crystal. These effects are described in greater detail in Chapters 3-5.

III. Phase-Slip Dynamics

The discussion now turns to how phase slippage produces the abrupt depinning that is characteristic of switching transport. As mentioned earlier, amplitude fluctuations are a crucial feature of switching. Most models of nonswitching transport neglect the effect of amplitude fluctuations, because amplitude fluctuations are energetically expensive compared to phase excitations of the CDW order-parameter. In $NbSe_3$, for example, typical phase-pinning frequencies are 10^{10} Hz (Ref. 36), whereas amplitude fluctuation frequencies are 10^{12} Hz (Ref. 37). The observation of current discontinuities, and hence of amplitude fluctuations, indicates that CDWs are very strongly pinned in switching crystals, at least within localized regions near phase-slip centers.

The starting point for a phase-slip model of switching is a Hamiltonian H that includes the effects of both strong pinning and amplitude fluctuations. The form of the Hamiltonian is the same as for a phase-only model:

$$H = H_o + H_{pin} + H_{field} . \qquad (1.2)$$

Here H_o is an elastic energy that minimizes deformations of the CDW order-parameter; H_{pin} is a pinning term that binds the CDW to defects and impurities within a crystal; and H_{field} is an interaction term that couples the CDW to external electric fields. What is new in a phase-slip model is that H_{pin} includes the effect of strong pinning and that H_o includes the effect of amplitude fluctuations.

The physics of the phase-slip model is contained in the amplitude dependence of H_o. In a phase-only model,[21-23] the elastic energy is written as

$$H_o = f_o \int d^3\mathbf{x} \left(\frac{d\phi}{d\mathbf{x}} \right)^2 , \qquad (1.3)$$

where f_o represents the CDW condensation energy and lengths are measured in units of the amplitude coherence length. The important feature of Eq. 3 is that the elastic energy increases monotonically with gradients in the CDW phase. This occurs because the CDW amplitude is assumed to be constant and homogeneous throughout a crystal. In contrast, the CDW amplitude is treated as a dynamical variable in the phase-slip model,[17] and the elastic energy is written as

$$H_o = f_o \int d^3\mathbf{x} \left\{ \Delta^2 \left(\frac{d\phi}{d\mathbf{x}} \right)^2 + (\Delta - \Delta_o)^2 \right\}. \qquad (1.4)$$

Here Δ represents the normalized amplitude of the CDW and Δ_o represents its equilibrium value.

The phase-slip Hamiltonian, Eq. 4, can be derived from a Ginzburg-Landau expansion of the CDW free energy.[38] (Spatial derivatives of the amplitude should also be present in the Hamiltonian, but these terms have been neglected for simplicity.) Alternatively, Eq. 4 can be derived from the vibrational frequencies of the CDW normal modes. (This is the approach taken in Chap. 6.) The important feature of Eq. 4 is that the amplitude enters multiplicatively in the phase elasticity term. Because of this, large phase gradients reduce the size of the CDW amplitude, and conversely, reductions in the amplitude diminish

the elasticity of the CDW phase. If the amplitude collapses entirely, for example, then the elasticity vanishes completely. The second term of the Hamiltonian, proportional to $(\Delta - \Delta_o)^2$, adds a large energy penalty for amplitude collapse. Therefore, the CDW amplitude decreases only if large phase gradients are present. Note that if the CDW amplitude were always equal to its equilibrium value, then the phase-slip Hamiltonian of Eq. 4 would reduce to the simpler phase-only expression of Eq. 3.

The difference between a phase-slip and a phase-only Hamiltonian becomes important when strong pinning is considered. A strong pinning center can be defined as a site whose pinning energy is comparable to the CDW condensation energy, and the effect of such a center is to essentially fix the value of the CDW phase at that site.[17,23] As a result, when an electric field is applied to a strongly pinned CDW, the phase becomes extremely polarized, as indicated in Fig. 1a. In a phase-only model, that is all that happens. As larger electric fields are applied, the phase just becomes more polarized. Eventually the elastic energy of the phase exceeds the condensation energy of the CDW, and a 2π phase-slip must be put in by hand in order to relieve polarization. In contrast, large phase gradients in a Ginzburg-Landau model reduce the CDW amplitude, as shown in Fig. 1b. By the time the elastic energy of the phase has reached the condensation energy, the amplitude has collapsed completely. Therefore, phase slippage occurs spontaneously in a Ginzburg-Landau model.

During phase slippage, the elasticity of the CDW phase becomes unstable, and this has an important effect on how a CDW depins.[13] The elasticity of the CDW phase is effectively a function of its polarization, Figs. 3.16 and 6.1.

a PHASE - ONLY

E →

b PHASE - SLIP

E →

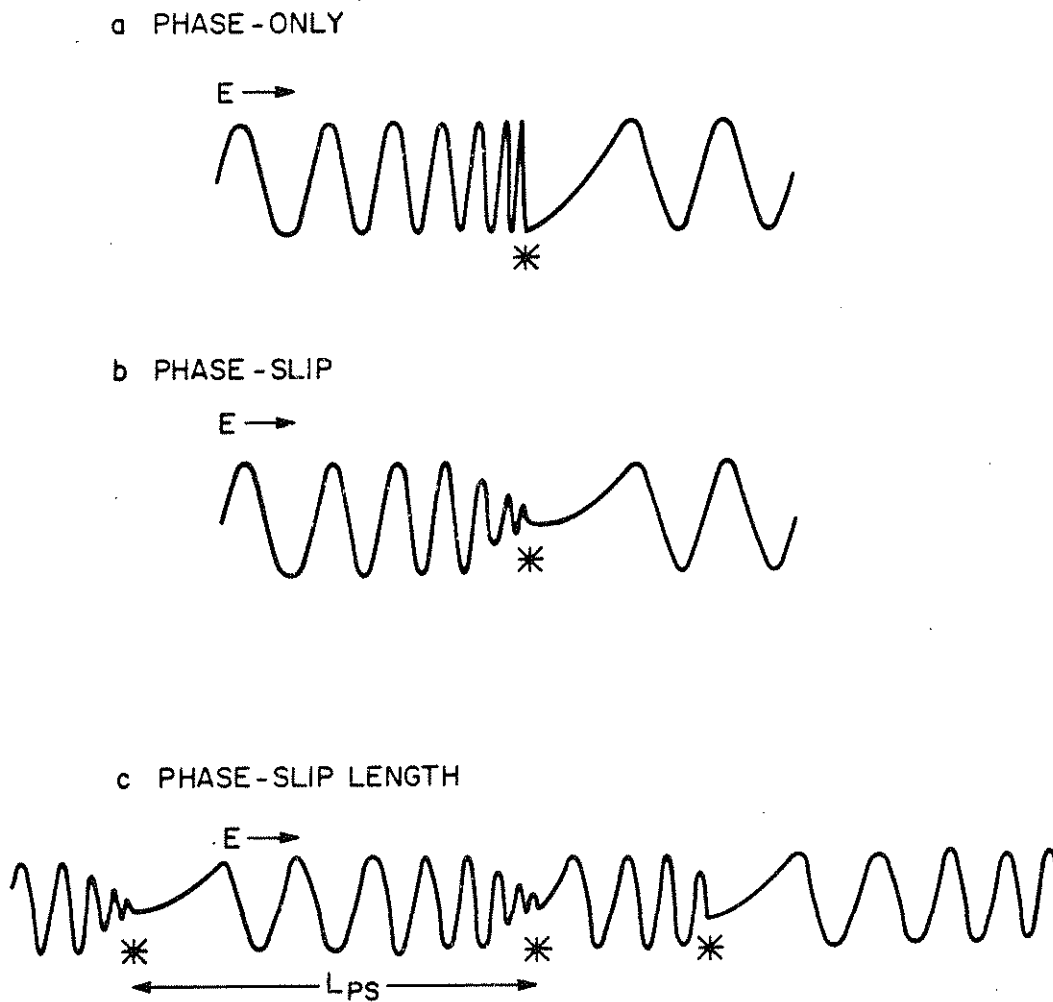c PHASE - SLIP LENGTH

.E →

L_{PS}

Fig. 1-1)   The effect of an electric field E on the order-parameter of a strongly
pinned CDW.   The asterisks denote strong pinning centers.
a) Phase polarization in a phase-only model, Eq. 1.3.   b) Phase-
polarization and amplitude collapse in a phase-slip model, Eq. 1.4.
c) The characteristic phase-slip length L_{PS} between phase-slip
centers.

When gradients in the phase are small, the phase acts like an ideal elastic field, with a restoring force that increases linearly with polarization. When larger gradients are present, however, the elasticity softens until the restoring force peaks at some critical gradient X_C. For gradients larger than X_C, the restoring force actually decreases with increasing polarization, making the phase unstable. In this unstable regime, phase polarization accelerates until the CDW amplitude collapses at some maximum gradient X_M. Just below the threshold electric field for CDW depinning, the phase gradients within a strongly pinned CDW are at the critical value X_C, and the elastic restoring force is at its maximum value. With a slight increase in the electric field, the phase gradients exceed X_C and the restoring force decreases. The electric field therefore becomes slightly uncompensated and the CDW begins to slide.

Whether CDW depinning is abrupt or smooth depends on the characteristic spacing L_{PS} between phase-slip centers, Fig. 1c. After a phase-slip occurs at a strong-pinning center, the phase gradient at the center is about $X_M - 2\pi/L_{PS}$. If this gradient is smaller than X_C, then at some point during the phase-slip cycle the elastic restoring force reattains its maximum value and the field energy is again almost compensated. Therefore, the average CDW velocity only slightly exceeds zero and the depinning process is smooth. On the other hand, if $X_M - 2\pi/L_{PS}$ exceeds X_C, then the restoring force energy never reapproaches its maximum value, and the electric field is always grossly uncompensated. In this case, the depinning process is abrupt.

Thus, the ratio of two length scales determines whether a strongly pinned CDW displays switching. The first length scale is just the spacing L_{PS} of the

strong-pinning centers. The second length scale is the critical value L_{SWITCH} defined by the phase gradients χ_C and χ_M:

$$L_{SWITCH} = \frac{2\pi}{\chi_M - \chi_C}. \qquad (1.5)$$

If $L_{PS} < L_{SWITCH}$, then smooth depinning occurs; whereas if $L_{PS} > L_{SWITCH}$, then switching occurs. This simple criterion for switching can become complicated in its application,[13] but the basic idea remains unchanged. Because of the elastic instability of the CDW order-parameter, the CDW phase can respond to the presence of a strong-pinning center only over a limited distance. Far away from a center, the phase is essentially unaffected by the center's presence once the CDW has become depinned. Therefore, when strong-pinning centers are spaced far apart in a crystal, the dynamics of the CDW phase become decoupled from the forces exerted by the centers. In this sense, switching is caused by strong pinning that is nonuniform on the length scale defined by the elastic coherence of the CDW phase.

IV. Guide to the Thesis

Sections II and III have stated the main points of the thesis: that phase slippage experimentally distinguishes switching from nonswitching CDW transport, and that phase slippage provides a natural theoretical explanation for switching. The rest of the thesis develops these points in greater detail. The thesis is organized into four parts. The first three parts sequentially cover CDW fundamentals (Chaps. 1-2), experiments on switching CDWs (Chaps. 3-5), and the phase-slip model of switching (Chap. 6). The last part of the thesis consists

of a conclusion (Chap. 7) and four appendices. With the exceptions of Chap. 2 and the conclusion, each chapter is divided into result and analysis sections, with a concluding section that summarizes the important points of the chapter.

Chapter 2 begins the main body of the text with a detailed and original introduction to theories of CDW formation and dynamics. The formation of charge-density waves is discussed in terms of single-electron wavefunctions and classical lattice dynamics, not the usual electron and phonon creation and annihilation operators. Most of the second-quantization results are rederived. Chapter 2 also collects together some useful results on the structure of $NbSe_3$, and discusses why a three-dimensional crystal can be treated as though it were a one-dimensional metal. The last part of Chap. 2 deals with CDW dynamics, which are introduced in terms of so-called sombrero surfaces. These surfaces provide a concrete way of thinking about the CDW amplitude and phase, about the difference between strong and weak pinning, and about the dynamics of the CDW order-parameter during phase slippage.

Chapter 3 is the first chapter that discusses the thesis research in detail, and it focuses on the response of switching CDWs to dc electric fields. Chapter 3 begins by discussing the growth of switching versus nonswitching crystals. Basically, very little is known about what causes one crystal to be switching and another one to be nonswitching. The thesis research did not attempt to address this question directly, because it was suspected that the problem might be one of chemistry rather than physics. The thesis results do touch upon the issue in a peripheral way, because an analysis of CDW velocity discontinuities leads to a conjecture about the role of lattice defects in switching crystals. The rest of

Chap. 3 is divided into experimental and analytical sections. The experimental section of Chap. 3 discusses a variety of effects, ranging from the temperature dependence of threshold fields to the bias-induced changes in low-field resistivity that are observed in switching crystals. The analytical section of Chap. 3 is divided into two parts. The first part deals with several phase-only models of switching, one of which was proposed by the author and co-workers. Phase-only models are shown to be inconsistent with the experimental results; therefore, the second part of the analytical section turns to a qualitative discussion of phase slippage. The discussion parallels Sec. III of the present chapter, but considers additional details such as velocity discontinuities, impurity and defect concentrations, and finite temperature effects.

Chapter 4 focuses on the response of switching CDWs to small ac electric fields. Small ac fields ideally act as nonperturbative probes of intrinsic CDW dynamics. The results of Chap. 4 reveal a dichotomy between the dynamics of pinned and sliding CDWs. When switching CDWs are pinned, they are dynamically equivalent to nonswitching CDWs (overdamped); but when switching CDWs are depinned, their dynamics is quite different (underdamped). Chapter 4 provides the first demonstration of an effective phase inertia induced by phase slippage.

Chapter 5 provides a second example of an effective phase inertia. When large ac fields are applied to a switching CDW in combination with a dc bias field, the CDW response displays a period-doubling route to chaos. Such a response is possible only if the CDW is effectively underdamped and, more importantly, only if the CDW dynamics has collapsed onto a single degree of

freedom. Period-doubling routes to chaos are an example of a dynamical instability in the CDW response. Chapter 5 also discusses a second type of dynamical instability, which is associated with negative differential resistance. This kind of instability depends on the couplings between phase-slip centers in a crystal.

Chapters 3-5 comprise the experimental work of the thesis. In the analysis sections of these chapters, the effect of phase slippage is explored in qualitative, model-independent terms. Chapter 6 represents the theoretical side of the thesis, and it introduces a specific model of phase slippage. Under certain conditions, the model reduces to a set of three coupled equations. The equations were analyzed in collaboration with M. Inui, who performed extensive numerical calculations of their dynamics. The equations exhibit switching, hysteresis, period-doubling routes to chaos, and an inductive, sliding ac conductivity. Thus, the equations qualitatively reproduce the dynamics of switching CDWs. Chapter 6 closes by scrutinizing the quantitative agreement between theory and experiment.

Chapter 7 concludes the main body of the text by briefly resummarizing the results of the thesis. The chapter includes a companion table to Table 1.1 that lists the physical origin of the effects associated with switching.

In addition to the main chapters, the thesis contains four appendices. Appendix A1 contains some derivational details of results cited in Chap. 2. Appendix A2 works through the calculation of a Peirls distortion in a model system, the Kronig-Penney model of one-dimensional metal. Appendix A3 describes a nonperturbative, four-probe sample holder used to map out current

domains within switching crystals. Appendix A4 is a list of publications written as a part of the thesis research.

CHAPTER 2: CDW FORMATION AND DYNAMICS

CHAPTER 2:   CDW FORMATION AND DYNAMICS

This chapter reviews previous research on CDW transport. The review is arranged as follows. Sec. I presents the theory of CDW formation in one-dimensional and quasi-one-dimensional crystals. The discussion emphasizes that CDW formation is due to classical properties of crystal lattices: electrons are described by single-particle wavefunctions and ions by Hamilton's equations of motion. Sec. II shows how the general theory of CDW formation applies to a real material like NbSe$_3$. The crystal and band structures of NbSe$_3$ are discussed, as well as the CDWs that are experimentally observed in NbSe$_3$. Sec. III describes the dynamics of sliding CDWs. Frohlich superconductivity and the amplitude and phase modes of CDWs are introduced in terms of the classical dynamics of Peierls distorted lattices. The effects of impurities on CDW dynamics are examined next, and the Fukuyama-Lee-Rice Hamiltonian is introduced. Some experiments on CDWs are reviewed, and the chapter closes with a survey of phenomenological models of CDW motion.

I. Microscopic Theory of Charge-Density Wave Formation

A. Peierls' zone-folding argument

R. E. Peierls proposed an elegant explanation of why a periodic lattice modulation lowers a crystal's electronic energy.[1] Consider a one-dimensional, linear array of atoms with an average spacing a. Fig. 1a shows the first electronic energy band for such a crystal in a nearly-free electron
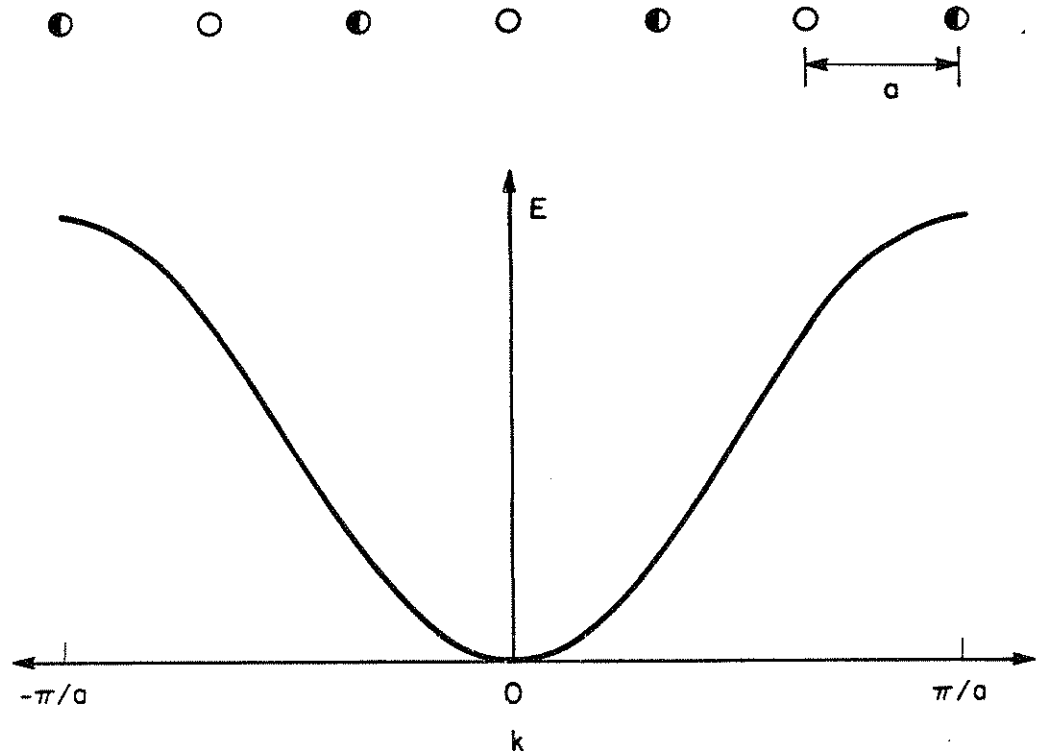
Fig. 2-1.a)   A   one-dimensional   crystal   in   the   nearly   free   electron
approximation.
Top: the crystal lattice. Circles represent ions. All ions are
identical; the shaded ions are only a guide to the eye. See the
next figure.
Bottom: the first conduction band. The Brillouin zone extends
from $-\pi/a$ to π/a.
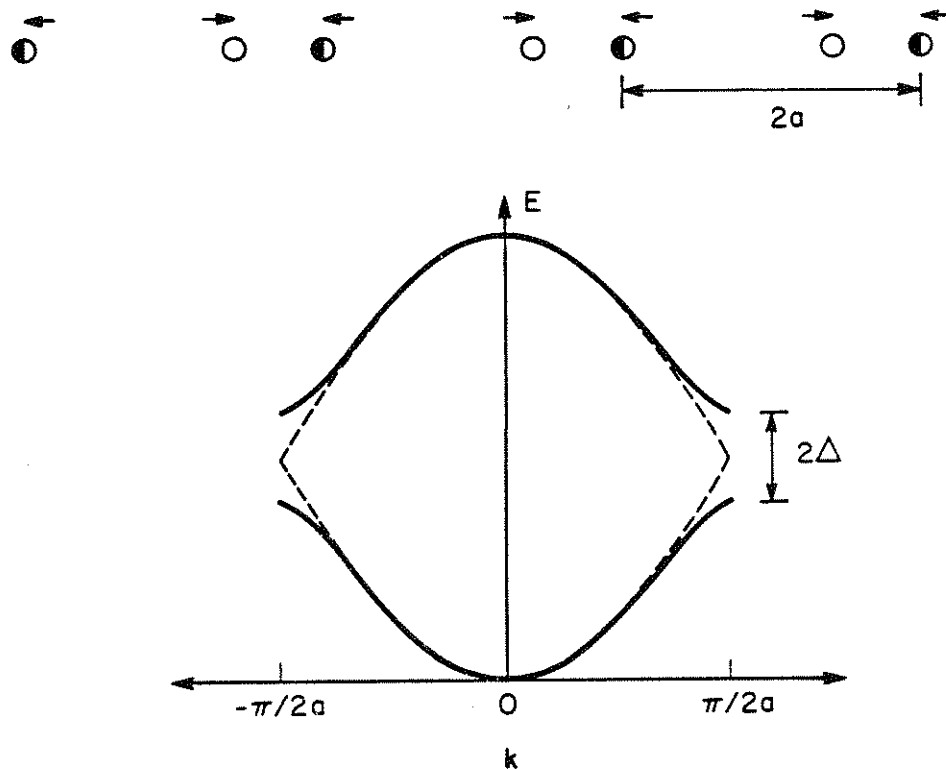
Fig. 2-1.b)   A one-dimensional crystal after a Peierls distortion.
Top: the distorted lattice. Arrows indicate shifts of the ions.
Bottom: the conduction band of the distorted crystal (solid line).
The Brillouin zone is half its original size, and the original
conduction band is folded back onto itself (dashed line). An
energy gap 2Δ opens up at the new Brillouin zone edge because
of Bragg reflection by electrons from the displaced ions. After
ref. 1.

approximation. If every r^{th} atom is displaced by a small amount, then the translational symmetry of the crystal is considerably reduced. The crystal's unit cell expands from 1 atom to r atoms, whereas the crystal's Brillouin zone shrinks from π/a to π/ra. Figure 1b shows the reduction in Brillouin zone for the case r = 2. If the crystal electrons did not interact with the displaced atoms, the electronic energy band would simply fold over onto itself, as shown by the dashed line in the figure. (Note that in Fig. 1b and succeeding figures, the distortion of the lattice is exaggerated for the sake of clarity. In real crystals, a Peierls distortion is small. In $NbSe_3$, the distortion amplitude is about $0.05\mathring{A}$, compared to a lattice constant of $3.5\mathring{A}$.)

Because electrons do interact with displaced atoms, the displaced atoms change the electronic potential $V_0(x)$ by an amount $V_1(x)$. The perturbing potential $V_1(x)$ is periodic with wavelength $\Lambda = ra$, so it can have Fourier components at wavevectors $\pm Q, \pm 2Q, \cdots \pm (r-1)Q$, where $Q = 2\pi/ra$. The perturbing potential $V_1(x)$ opens gaps in the electronic energy spectrum, as shown by the solid line in Fig. 2.1b. Essentially, the new gaps are caused by Bragg reflection of electrons from the distorted lattice, just as the original bandgaps at $\pm\pi/a$ are caused by Bragg reflection from the undistorted lattice. The magnitude $2\Delta_\ell$ of each new gap is

$$2\Delta_\ell = \mid \int dx \chi^*_{\ell Q/2}(x) V_1(x) \chi_{-\ell Q/2}(x) \mid \qquad (2.1)$$

where $\chi_k(x)$ is an electronic Bloch function of the undistorted lattice. If the electronic energy spectrum is viewed in an extended zone scheme, the gap index ℓ labels the wavevectors $\pm k_\ell = \pm\ell Q/2$ at which Peierls gaps open up.

· Each portion of an energy band below a Peierls gap is lowered in and energy, each portion just above is raised. If a gap occurs right at the Fermi surface, then at zero temperature filled electronic states are lowered in energy whereas empty states are raised. Peierls observed that the net *electronic* energy is therefore lowered by a periodic lattice distortion of wavelength $\Lambda = \pi/k_F$.

Peierls' zone-folding explanation can be applied rigorously only to crystals in which the Fermi wavevector is a rational fraction N'/M' of the Brillouin wavevector π/a. The integer M' is called a distortion's *order of commensurability*. As the integer M' increases, i.e. as the ratio $k_F/(\pi/a)$ tends toward an irrational number, the distorted Brillouin zone steadily shrinks. In the limit that $k_F/(\pi/a)$ is an irrational fraction, the unit cell of the distorted crystal becomes the entire crystal and its Brillouin zone a single point. Peierls' explanation breaks down, although perturbation theory shows that a periodic distortion of wavelength $\Lambda = \pi/k_F$ still opens gaps in the electronic spectrum of a crystal. A Peierls distortion is *commensurate* if the fraction $a/\Lambda = k_F/(\pi/a)$ is equal to the ratio of low-order integers, *incommensurate* otherwise. The distinction between commensurate and incommensurate Peierls distortions becomes important when vibrations of the distorted lattice are considered in Sec. III.

B. Frohlich's model

Not only does Peierls' zone folding explanation break down for incommensurate distortions, it also says nothing about the increase in lattice strain energy caused by Peierls distortions. In order for a Peierls' distortion to occur, the decrease in electronic energy must compensate the increase in lattice

occur, the decrease in electronic energy must compensate the increase in lattice strain energy. Using perturbation theory, Frohlich demonstrated that a Peierls distorted crystal has lower *total* energy than an undistorted crystal.[2]

Frohlich's Hamiltonian for a one-dimensional metal contains three terms: the unperturbed energies of electrons, the unperturbed energies of phonons, and a perturbing term due to the interaction of electrons and phonons. The Hamiltonian neglects any electron-electron interactions, and any effects of crystal dimensionality or temperature. In many-body notation, the Hamiltonian is

$$H = \sum_k \epsilon_k a_k^+ a_k + \sum_q \hbar\omega_q b_q^+ b_q + N^{-1/2} \sum_{k,q} g(k,q) a_{k+q}^+ a_k (b_{-q}^+ + b_q) . \qquad (2.2)$$

The ϵ_k are single-electron energies; the a_k^+ and a_k are electron creation and annihilation operators; the ω_q are phonon frequencies; and the b_q^+ and b_q are phonon operators. The integer N is the number of lattice sites in the crystal, and the energy $g(k,q)$ is the Frohlich electron-phonon coupling parameter, which is usually approximated by a constant g and taken outside the summations.

The Frohlich Hamiltonian is more sophisticated than is necessary for charge-density waves. First of all, electron operators in the Hamiltonian are constructed from creation and annihilation operators to ensure that solutions are properly antisymmetric in electron coordinates. But the Hamiltonian neglects Coulomb repulsion between electrons, so that all potentials in the Hamiltonian are functions of a single electron coordinate. Antisymmetrization has no effect on a single-coordinate potentials, and therefore the creation and

wavefunctions may be used in place of Slater determinants to describe electronic wavefunctions. Product wavefunctions, unlike Slater determinants, permit single-particle perturbation calculations of electronic energy shifts.

Similarly, the discrete nature of phonons never becomes important in Peierls distortions, even though a Peierls distortion is often called an "electron-phonon condensate". The number Q of condensed phonons is huge:

$$Q^2 = \frac{\nu}{\lambda} \frac{\Delta_o^2}{E_F \hbar \omega_{2k_F}} N \qquad (2.3)$$

Here ν is the degree of band-filling in a crystal, λ a dimensionless electron-phonon coupling constant, $2\Delta_o$ the magnitude of the gap in the electronic energy spectrum, E_F the Fermi energy, and ω_{2k_F} the frequency of the $2k_F$ normal mode. For NbSe$_3$, $\nu \sim \lambda \sim 0.25$, $\Delta_o = 35$ meV, $\hbar \omega_{2k_F} = 12$ meV, and $E_F \sim 1$ eV. These values give $Q \sim 0.1 N^{1/2}$. Since the number N of lattice sites is a very large number (for example, roughly 10^{13} for the crystal of Fig. 2.8), the quantum number Q is also large. By the Bohr correspondence principle, the distortion of a crystal's lattice may be calculated classically.

The approach of the following discussion, therefore, is to treat electrons as single particles moving within a classical, deformable lattice. Most of the usual second-quantized results will be rederived. For this thesis, the most important results are the following:

1)   The gap equation, Eq. 2.18, shows that a Peierls distortion always occurs in a one-dimensional crystal at zero temperature.

2) The distortion energy $E_{Peierls}$ shows a well-defined minimum at an optimal value of the lattice distortion, Fig. 2.2a.

3) The electronic gap Δ, the lattice distortion u, and the induced charge-density wave amplitude ρ are all equivalent order parameters for the Peierls instability, Eqs. 2.22 and 2.24 and Fig. 2.3.

Readers should feel free to glance at these equations and figures, and then skip ahead to the next section, unless of course they are interested in the derivations. Appendix A1 contains derivational details not shown in this section, and Appendix A2 shows how the results of this section apply to an idealized model of a one-dimensional crystal.

1. Mean-field approximation

In an undistorted crystal, the energy $E_0(k)$ of an electron of wave vector k is given by the Hamiltonian $H_0 = p^2/2m + V_0(x)$. The crystal potential $V_0(x)$ is the sum of ionic potentials $v(x-x_j)$ where x is the electron coordinate and x_j is the position of the jth ion. A *mean-field* calculation of a Peierls distortion assumes that each ion is periodically displaced. The position of the jth ion becomes $x_j + u_j$ where

$$u_j = u_{+Q} e^{iQx_j} + u_{-Q} e^{-iQx_j}. \tag{2.4}$$

Here Q is the wavevector of the distortion. Since u_j must be real, the Fourier components in (2.4) are given by $u_{\pm Q} = u\exp(\mp i\phi)$ where u is the *amplitude* of the distortion and ϕ is its *phase*. The phase ϕ will be set to zero for most of this discussion, but its physical significance is discussed further in Sec. III.

The ionic displacement given by (2.4) perturbs the original potential $V_0(x)$ by an amount $V_1(x)$. To first order in the distortions u_j, the potential $V_1(x)$ is given by

$$V_1(x) = -\sum_j u_j \frac{dv}{dx}. \tag{2.5}$$

A Bloch function of wavevector k is mixed by $V_1(x)$ with states of wavevector $k \pm Q$. For an electronic band less than half-filled, umklapp processes may be neglected and perturbation theory shows that the energy of an electron is given by

$$\begin{aligned}
E_1^\pm(k) = &\frac{1}{2}[E_o(k+Q)+E_o(k)] \\
&\pm \{[E_o(k+Q)-E_o(k)]^2 + 4|\Delta(k,+Q)|^2\}^{1/2}
\end{aligned} \tag{2.6}$$

The plus sign applies for $|k| > Q/2$ and the minus sign for $|k| < Q/2$. The matrix element $\Delta(k, +Q)$ is given by

$$\Delta(k, Q) = \int dx \chi_{k+Q}^*(x) \chi_k(x) V_1(x), \tag{2.7}$$

where k is assumed to be negative. (Energies for positive k are obtained by substituting $-Q$ for $+Q$.) When $|k| = Q/2$, Eq. (2.6) reduces to

$$E_1^\pm(Q/2) = E_o(Q/2) \pm |\Delta(-Q/2, Q)| \tag{2.8}$$

Just as Peierls noted, a gap opens up at the wavevector $Q/2$. If Q is chosen to be the twice the Fermi wavevector, then the net electronic energy is lowered by the distortion. Henceforth, Q will be taken to be $2k_F$.

Equation 6 is valid for both commensurate and incommensurate distortions. The only difference between commensurate and incommensurate distortions occurs when nonzero values of the phase ϕ are considered. For an

occurs when nonzero values of the phase ϕ are considered. For an incommensurate distortion, Eq. 6 remains valid when $\phi \neq 0$. For a commensurate distortion, nonzero values of ϕ raise electron energies on the average by $[|\Delta|^2/E_F][|\Delta|/W]^{M'-2}[\cos(M'\phi)-1]$ where W is the electronic bandwidth and M' is the distortion's order of commensurability.[3]

2. Electron-lattice interaction energy

Since $\Delta_{+Q} \equiv \Delta(-Q/2, Q)$ determines the size of the electronic gap, Δ_Q is called the *gap parameter*. Its modulus is denoted $\Delta = |\Delta_Q|$. The gap parameter is basically the Qth Fourier component of the perturbing potential $V_1(x)$. The gap parameter is proportional to the distortion amplitude u_Q because of the linearization (2.5):

$$\Delta_Q = G_Q u_Q , \tag{2.9}$$

where

$$G_{+Q} = -\int dx \tilde{\chi}^*_{+Q/2}(x)\tilde{\chi}_{-Q/2}(x)\frac{dv}{dx} . \tag{2.10}$$

Here tildes over Bloch functions indicate that the functions are normalized to unity over one unit cell. The modulus of G_Q is denoted G.

The perturbed energies $E_1(k)$ may be approximated by substituting Δ for $|\Delta(k,+Q)|$ in Eq. 6. The perturbed energies then may be summed to give the total electronic energy of the distorted crystal. The electronic energy consists of two components: E^0_{el}, the unperturbed electronic energy, and $E_{el-lattice}$, the *electron-lattice interaction energy*. The interaction energy $E_{el-lattice}$ is given by

This energy may be integrated to give a particularly simple form:

$$\underset{\sim}{E}_{el-lattice} \cong \underset{\sim}{\Delta}^2 \ln \underset{\sim}{\Delta} . \tag{2.12}$$

Single tilde subscripts indicate normalized variables: $\underset{\sim}{E}_{el-lattice} = E_{el-lattice}/[2n(0)E_B]$ and $\underset{\sim}{\Delta} = \Delta/[2E_B]$. Here E_B is an energy roughly equal to the bandwidth and $n(0)$ is the density of states at the Fermi level of the undistorted crystal. Figure 2a shows a graph of $E_{el-lattice}$, which is minimized when $\underset{\sim}{\Delta} = 1/\sqrt{e} = 0.6065$. Although not apparent from Fig. 2a, the behavior of $E_{el-lattice}$ is slightly subquadratic for small values of Δ. Fig. 2b shows this subquadratic behavior on a logarithmic plot. The dashed line in the figure has a slope of two, and the slope of $E_{el-lattice}$ is asymptotic to - but always slightly less than - two as Δ approaches zero. As will be discussed shortly, the subquadratic behavior of $E_{el-lattice}$ makes one-dimensional lattices absolutely unstable against Peierls distortions at zero temperature.

3. Peierls energy

A decrease in electronic energy due to $E_{el-lattice}$ must balance an increase in lattice energy due to strain. The lattice may be treated as a classical, linear array of ionic masses M that are tied together by springs of spring constant C. In the mean field approximation, the energy cost of the distortion is

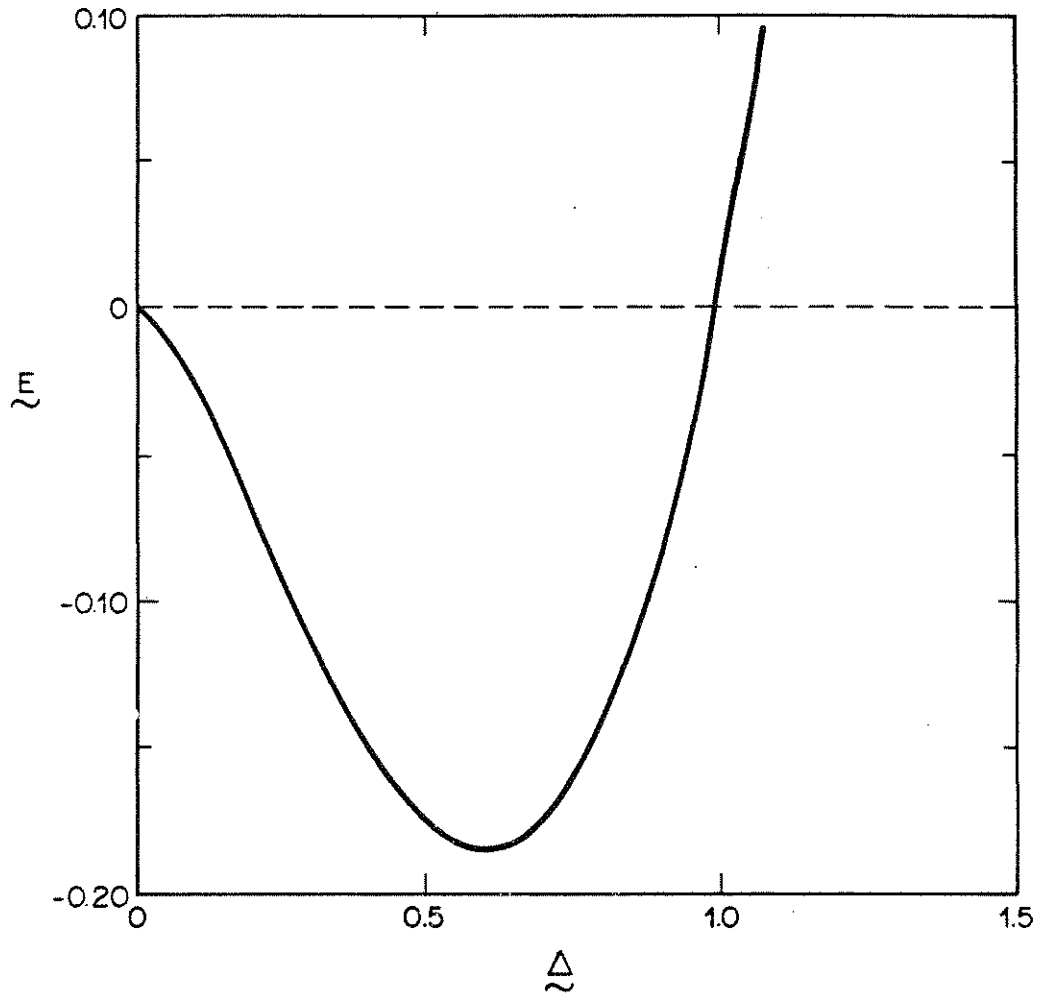$$E_{lattice} = NM\omega_{2k_F}^2 u^2 \tag{2.13}$$

Fig. 2-2.a) The normalized electron-lattice interaction energy versus the normalized gap parameter, shown on a linear plot. The interaction energy is minimized by a finite distortion of the lattice.
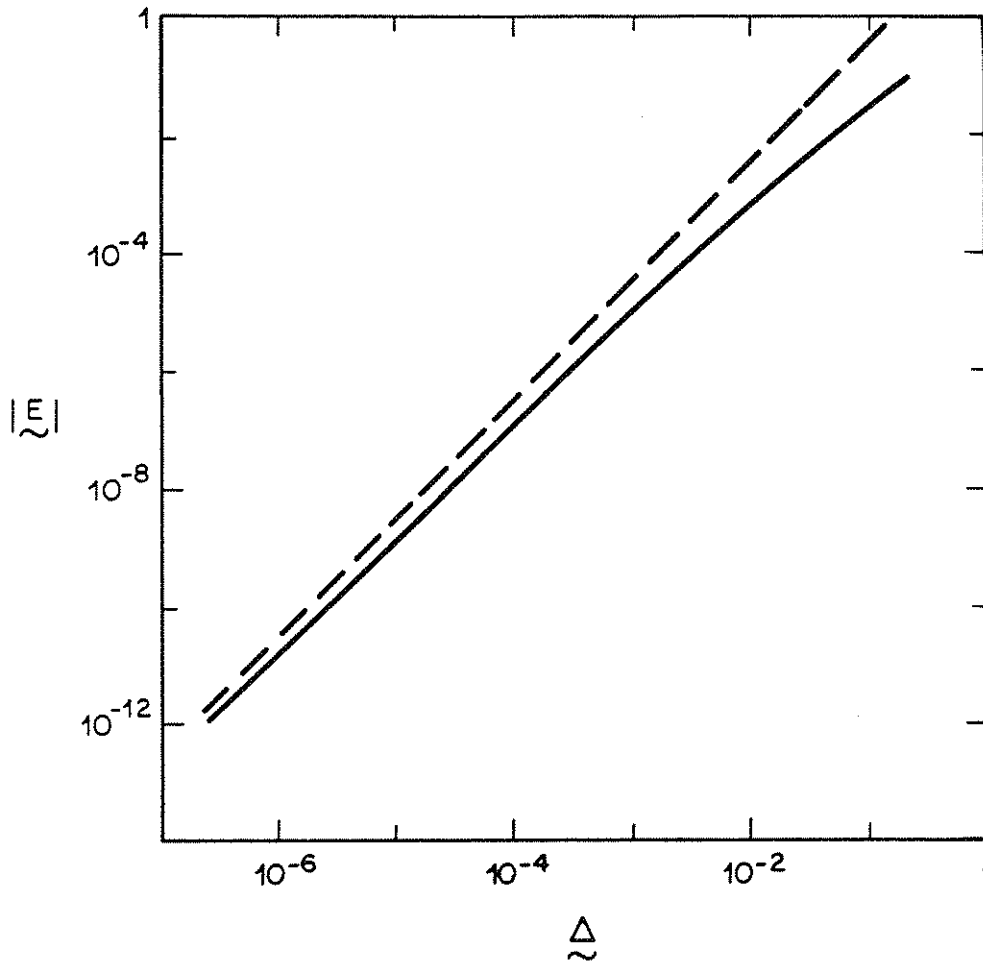
Fig. 2-2.b)   The electron-lattice interaction energy versus the gap parameter, shown on ʿa logarithmic plot. The dashed line displays a quadratic dependence on the gap parameter. The subquadratic dependence of the interaction energy makes one-dimensional crystals unstable against Peierls distortions.

where ω_{2k_F} is the frequency of the $2k_F$ normal lattice mode when electrons are absent.

The total crystal energy is given by

$$E = E_{el}^0 + E_{lattice} + E_{el-lattice} \cdot \tag{2.14}$$

This equation is the single-particle version of the many-body Frohlich Hamiltonian, Eq. 2. Only the lattice energy and the electron-lattice coupling energy are affected by the distortion, and it is convenient to lump these two terms together into a *Peierls distortion energy*, $E_{Peierls}$. The distortion energy $E_{Peierls}$ may be expressed in terms of a single distortion parameter, either Δ or u, since these two parameters are equivalent. Using the variable Δ, the Peierls energy may be integrated to give:

$$\underset{\sim}{E}_{Peierls} \cong \underset{\sim}{\Delta}^2 (\frac{1}{\lambda} + \ln \underset{\sim}{\Delta}) \tag{2.15}$$

where the dimensionless parameter $\lambda = n(0)G^2/2NM\omega_{2k_F}^2$. Because the electron-lattice interaction energy is slightly subquadratic in Δ, the magnitude of the electron-lattice energy is greater than the magnitude of the lattice energy for small values of Δ. Because the electron-lattice energy is negative for small values of Δ, the Peierls energy and the total crystal energy are reduced by small distortions of the lattice.

The parameter λ sets the scale of energy for $E_{Peierls}$, as may be seen by rewriting the Peierls energy in terms of scaled variables:

$$\underset{\approx}{E}_{Peierls} \cong \underset{\approx}{\Delta}^2 \ln \underset{\approx}{\Delta} \tag{2.16}$$

where $\underset{\approx}{E}_{Peierls} = \underset{\approx}{E}_{Peierls} \exp(2/\lambda)$ and and $\underset{\approx}{\Delta} = \underset{\approx}{\Delta}\exp(1/\lambda)$. The *scaled* Peierls energy has the same dependence upon the scaled gap parameter as the *unscaled* electron-lattice energy has upon the unscaled gap parameter.

The Peierls energy displays a minimum at an optimal value of Δ which is determined by:

$$0 = \frac{d}{d\Delta}\{E_{el-lattice} + E_{lattice}\} \tag{2.17}$$

Ignoring the unstable $\Delta = 0$ solution, this gives the equilibrium value of Δ as

$$\Delta_o = 2E_B e^{-1/\lambda} \tag{2.18}$$

Eq. 18 is the standard result obtained from the second-quantized Frohlich Hamiltonian. Usually λ is written in terms of the Frohlich constant g. The coupling constant G is related to g by

$$g = G(\hbar/2M\omega_{2k_F})^{1/2} \tag{2.19}$$

Substituting g for G gives the familiar form of the *electron-phonon coupling constant*:

$$\lambda = n(0)g^2/(N\hbar\omega_{2k_F}). \tag{2.20}$$

The Peierls gap equation, Eq. 18, has the same form as the BCS gap equation, with one important difference. The occurrence of the BCS groundstate depends on an attractive electron-electron interaction at the Fermi surface to produce Cooper pairing. In contrast, the Peierls distortion occurs regardless of the sign of the electron-lattice interaction, because of the g^2 dependence of λ. The sign of g determines only the *phase* of the induced

dependence of λ. The sign of g determines only the *phase* of the induced electronic density wave.

4. The charge-density wave induced by a Peierls distortion

The amplitude of the electronic density wave induced by a Peierls distortion is usually derived using the Lindhard response function, but it can be derived without using this formalism; see Appendix A1. By either method of calculation, the CDW amplitude ρ is proportional to the distortion amplitude $2u$ and the electronic gap 2Δ:

$$\rho = \frac{m\omega_{2k_F}^2}{aG}(2u) = \frac{M\omega_{2k_F}^2}{aG^2}(2\Delta). \qquad (2.21)$$

The CDW amplitude, the electronic gap, and the distortion amplitude are all equivalent order parameters for the Peierls instability. The equivalence of the parameters is a direct result of linearizing the perturbation energy $V_1(x)$ and the electronic density $\rho_{CDW}(x)$ to first order in the distortion amplitude u.

While Eq. 21 is sufficient to show that ρ, Δ, and u are equivalent order parameters, a real-space picture clarifies their relationships. The Fourier components of the lattice distortion, potential perturbation, and electronic density are given by

$$u_Q = u\exp(i\phi) \qquad (2.22a)$$

$$\Delta_Q = G_Q u_Q = Gu\exp(i\phi + i\xi_o) \qquad (2.22b)$$

$$\rho_Q = -\frac{1}{a}\frac{M\omega_{2k_F}^2}{G^2}\Delta_Q = \frac{M\omega_{2k_F}^2}{aG}u\exp(i\xi + i\xi_o + i\pi) \qquad (2.22c)$$

where the phase ξ_o is determined by G_Q:

The phase ξ_0 is $-\pi/2$ for repulsive ionic potentials $v(x)$ and $+\pi/2$ for attractive potentials; see Appendix A1. Eqs. 22 may be Fourier transformed back to real-space functions:

$$u_j = 2u\cos(Qx + \phi) \tag{2.24a}$$

$$v_1(x) = 2\Delta\cos(Qx + \phi + \xi_0) \tag{2.24b}$$

$$\rho_{CDW}(x) = \rho\cos(Qx + \phi + \xi_0 + 180°) \tag{2.24c}$$

The induced CDW is shifted by 180° from the Q modulation of the crystal potential. In turn, the potential modulation is either in-phase ($v > 0$), or 180° out-of-phase ($v < 0$) with the lattice *distortion* depending on the sign of the ionic potentials. Fig. 3 shows the spatial relationships of the several order parameters for both attractive and repulsive ionic potentials. Note that the lattice distortion in Fig. 3 is 90° out of phase with the displacement vectors u_j.

The spatial relationship of the potential perturbation $V_1(x)$ to the lattice distortion is easy to understand. Where the Peierls distortion crowds lattice ions together, the *magnitude* of $V_1(x)$ has a maximum. If the ionic potentials are repulsive, this maximum corresponds to a maximum of $V_1(x)$; if they are attractive, to a minimum of $V_1(x)$. This quantity is the potential energy of the CDW, so the electrostatic potential that one would measure with a voltmeter (or a scanning tunneling microscope) is $V_1(x)/(-e)$. The electron density is 180° out-of-phase with $V_1(x)$ because electrons move toward regions of lower potential and away from regions of higher potential.
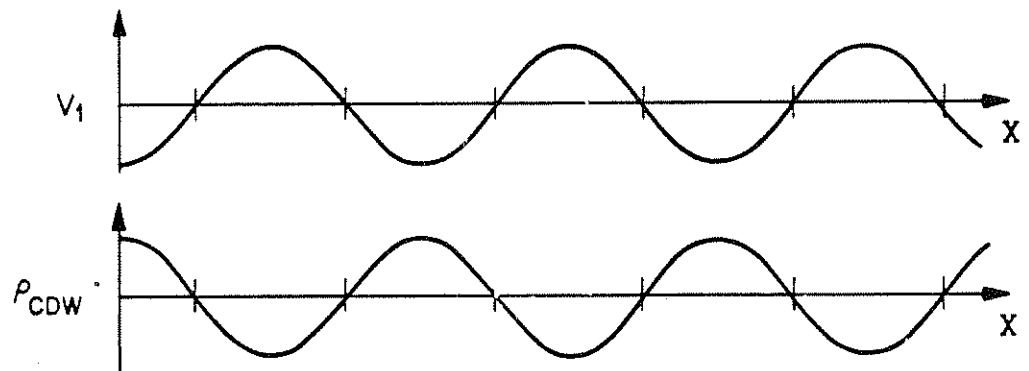
a.
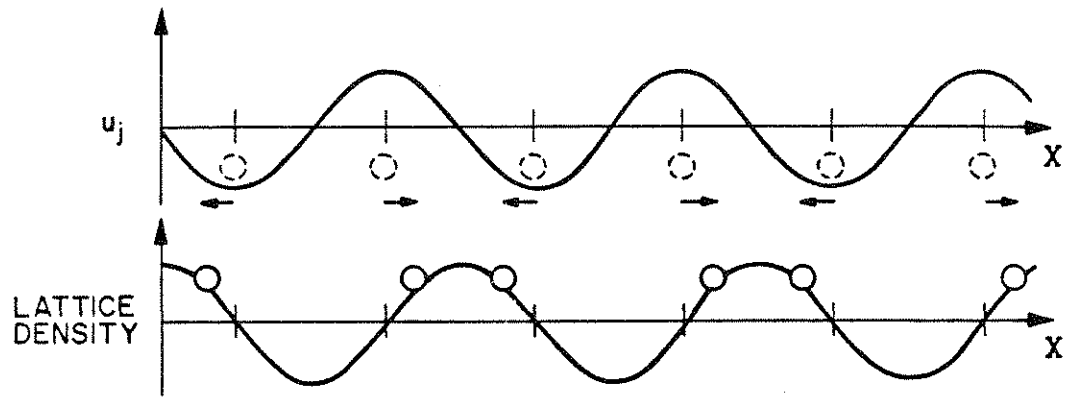
b. REPULSIVE IONS
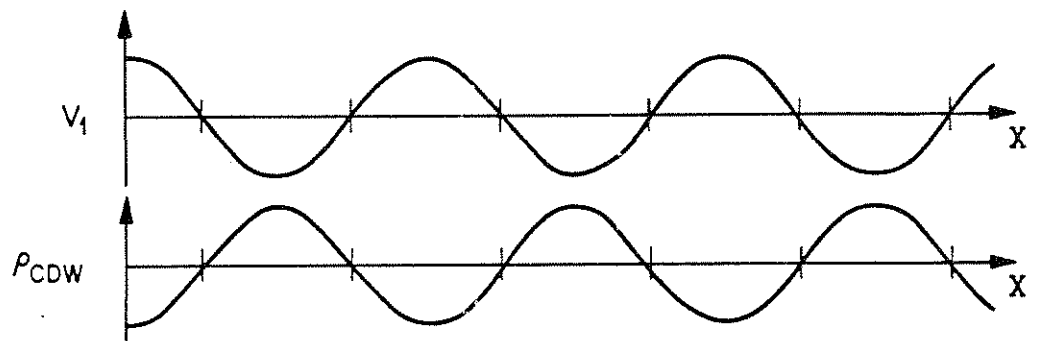
c. ATTRACTIVE IONS

Fig. 2-3)   The spatial relationship of various CDW order parameters. (a) The lattice displacement vectors u_j versus the resulting lattice distortion. (b) The ionic perturbation potential V_1 versus the electronic density modulation ρ_{CDW}, for the case of an attractive electron-ion interaction. (c) The same plot for the case of an attractive electron-ion interaction.

C. *Effects of temperature, dimensionality, and electron-electron interactions*

The discussion so far has neglected the effects of finite temperature, lattice dimensionality, and electron-electron interactions. These factors play a critical role in the formation of CDWs in real crystals. At nonzero temperatures, for instance, electrons in a Peierls distorted crystal are thermally excited above the Peierls gap. Electronic states below the Peierls gap have reduced energy because of the distortion, but states above have increased energy. Nonzero temperatures reduce the occupancy of the sub-gap states and raise the occupancy of the super-gap states. Past a critical temperature T_P, a Peierls distorted crystal has higher energy than an undistorted crystal, and the crystal undergoes a phase transition from the distorted to the undistorted state. This section shows how the *Peierls temperature T_P* may be calculated from the *Lindhard response function.*[4] (Appendix A1 relates the Lindhard function to the mean-field theory of the previous section.) Similarly, the discussion so far has been limited to CDW formation in strictly one-dimensional crystals, one atomic diameter in width. Real crystals, of course, have a width much larger than a single atomic diameter. This section shows why charge-density waves occur in three-dimensional crystals, again by using the Lindhard response function.[5] Finally, the Frohlich model contains no term to represent coulombic repulsion between electrons. Coulombic repulsion acts to smooth out variations in electron density, and thus suppress CDWs (Ref. 6). This section concludes by summarizing very briefly the effect of electron-electron interactions on Peierls distortions.

1. Lindhard response function

The Lindhard response function is given by[7]

$$\chi(q, T; u) = \sum_k \frac{f^o(k) - f^o(k+q)}{E(k+q) - E(k)} , \qquad (2.25)$$

where f^o is the Fermi-Dirac distribution function and $E(k) = E(k; u)$ is the electronic energy of a state of wavevector k in the presence of a Peierls distortion of magnitude u. Above the Peierls temperature $u = 0$ and $E(k) = E_o(\mathrm{k})$; below the Peierls temperature, $u \neq 0$ and $E(k) = E_1(k)$. The response function χ determines the normal mode vibrational frequencies of a crystal. Above the Peierls temperature, the frequency of a normal mode q is given by

$$\Omega_q^2 = \omega_q^2 - \frac{G^2 \chi}{NM} \qquad (2.26)$$

where ω_q is the frequency of the qth normal mode in the absence of electrons.[4]

The response function $\chi(q, T; u)$ may be calculated for several limiting cases.[4] If no distortion is present, the electronic Bloch functions may be approximated by plane waves. At zero temperature, the response function for a one-dimensional crystal is

$$\chi(q, T = 0; u = 0) = \frac{n(0)}{(q/k_F)} \ln \left| \frac{1 + (q/2k_F)}{1 - (q/2k_F)} \right| . \qquad (2.27)$$

The one-dimensional response function diverges logarithmically at $q = 2k_F$. At temperatures above zero, the response at $q = 2k_F$ is given by:

$$\chi(q = 2k_F, T; u = 0) \cong \frac{1}{2} n(0) \ln(1.14 E_B / k_B T) \qquad (2.28)$$

decreasing temperature, it steadily increases.

2. Effect of temperature

Combining Eqs. 26 and 28 implies that a Peierls transition always occurs at a nonzero temperature regardless of the stiffness of a one-dimensional lattice (at least in the mean-field approximation). The onset of the transition occurs when the frequency of the $2k_F$ normal mode reaches zero. This mean-field temperature is given by[4]

$$k_B T_P^{MF} = 1.14 \ E_B e^{-1/\lambda} \tag{2.29}$$

Below the Peierls temperature, the frequency of the $2k_F$ normal mode must remain zero. This places a consistency condition on $X(2k_F,\text{T}; u_o)$ which reduces to:

$$\frac{1}{\lambda} = \int_0^{E_B} \frac{d\epsilon}{E} \tanh(E/2k_B T) \tag{2.30}$$

In the integrand of Eq. 30, $E = (\epsilon^2 + \Delta_o^2)^{1/2}$. Equation 30 is an implicit equation for Δ_o, identical in form to the BCS gap equation. Combining Eqs. 18 and 29 gives a relationship familiar from the BCS theory:

$$2\Delta_o(T=0) = 3.5 \ k_B T_P^{MF} \tag{2.31}$$

This mean-field transition temperature is only an estimate of the true transition temperature, as discussed in the next section.

3. Effect of dimensionality

As the transverse dimensions of a hypothetical crystal increase from one atomic diameter to thousands or millions, they eventually exceed the transverse

3. Effect of dimensionality

As the transverse dimensions of a hypothetical crystal increase from one atomic diameter to thousands or millions, they eventually exceed the transverse mean free path of the crystal's electrons. When this happens, the Brillouin zone becomes three-dimensional and an electron's energy may become dependent on the transverse components of its wavevector k. The degree to which energy depends on transverse components of k is reflected in the topology of the crystal's Fermi surface. For a band in the first Brillouin zone, a near isotropic dependence of electron energy on wavevector produces a three-dimensional Fermi surface that is topologically equivalent to a sphere; dependence on one but not both transverse components of k produces a two-dimensional, cylindrical Fermi surface; and a minimal dependence on either transverse component produces a one-dimensional, planar Fermi surface.

The last section showed that divergence of $X(q=2k_F,\text{T};\ u=0)$ is sufficient to cause a Peierls transition. Divergence of X produces a softening of the lattice's $2k_F$ normal mode and a $2k_F$ modulation of the lattice at the Peierls temperature. The divergence of X is determined by the shape of the Fermi surface. A one-dimensional surface causes X to diverge at $q=2k_F$, but two- and three-dimensional surfaces result in a finite X at all wavevectors.

A divergence of the electronic response at *any* wavevector $\mathbf{q}$, not necessarily $|\mathbf{q}| = 2k_F$, will cause a softening of a lattice's normal mode and a corresponding q modulation of the lattice at sufficiently low temperatures. If there exist large portions of the Fermi surface for which $E(\mathbf{k}\dot{+}\mathbf{q})=E(\mathbf{k})$, then

Fermi surface need not be perfectly planar. NbSe$_3$ is an example of a real crystal whose Fermi surface is nested but not planar, Fig. 2.7.

It is fortuitous that strict one-dimensionality is not necessary for a Peierls transition, because a phase transition due to short-range forces can *not* occur in one dimension above zero temperature.[8] This statement contradicts the results of the last section, which showed that a mean-field phase transition occurred at nonzero temperature. The mean-field results are in fact incorrect, because Eq. 2.14 for the total crystal energy neglects the energy of all lattice modes beside the $2k_F$ mode. The short-range, screened electron-ion and ion-ion forces of the Frohlich Hamiltonian are effectively turned into long-range forces of wavevector $2k_F$ by omitting the other modes. Inclusion of all lattice modes suppresses the Peierls transition. However, a pseudo-transition may still occur for a weakly three-dimensional crystal. Lee *et al*[9] estimate that the true transition temperature is about one-fourth the mean-field value, $T_P = T_P^{MF}/4$.

4. Effects of electron-electron interactions

The Frohlich Hamiltonian neglects all electron-electron interactions. This approximation simplifies treatment of the Peierls phase-transition, but it also precludes the occurrence of other types of phase-transitions. The Frohlich Hamiltonian is justified only to the degree that a Peierls distortion dominates the low-temperature groundstates of certain materials, such as NbSe$_3$. In other materials, or in some CDW materials under applied stresses, the Peierls transition may be suppressed and other broken-symmetry groundstates may dominate. For example, applying pressure to NbSe$_3$ increases the energy cost of lattice distortions and causes NbSe$_3$ to enter a superconducting phase.

the low-temperature groundstates of certain materials, such as $NbSe_3$. In other materials, or in some CDW materials under applied stresses, the Peierls transition may be suppressed and other broken-symmetry groundstates may dominate. For example, applying pressure to $NbSe_3$ increases the energy cost of lattice distortions and causes $NbSe_3$ to enter a superconducting phase. Considerable research has gone into studying the competition between the various groundstates of low-dimensional conductors.[6] Besides CDWs and Cooper pairs, these groundstates include spin-density waves. The Frohlich Hamiltonian appears adequate for $NbSe_3$, however, and other groundstates will not be discussed further.

II. *Charge-Density Wave Formation in NbSe₃*

A. *Crystal structure of NbSe₃*

Crystals of $NbSe_3$ are long and skinny. A section of an $NbSe_3$ crystal is shown in Fig. 4a. The crystal is 2.5 mm long, but only 2.7 μm $\times$ 1.0 μm in cross-section; a thousand-fold physical anisotropy is typical for $NbSe_3$ crystals. The cross-section of an $NbSe_3$ crystal tends to be uniform over the entire length of the crystal; crystals do not taper off near their ends. Changes in cross-section, when they do occur, usually occur abruptly.

$NbSe_3$ crystals may be cut cleanly with an ordinary surgical scalpel. Fig. 4b shows a cut end of the crystal from Fig. 4a. Under close examination, the end appears layered. The layering is caused by the anisotropic tensile strength of $NbSe_3$. An $NbSe_3$ crystal can withstand large longitudinal stresses, but may be peeled apart easily by transverse stress.

Dimensional and tensile anisotropies are reflections of the crystalline structure of $NbSe_3$. Fig. 5a shows the structure of $NbSe_3$ over several unit cells, one of which is outlined in the figure.[11] Fig. 5b depicts a more three-dimensional view of the of Nb and Se atoms. The building block of the unit cell is a trigonal prismatic cage, six Se atoms at the cage corners and an Nb atom at the center. Trigonal edges of neighboring cages are shared to create long chains which run the length of a crystal. Six chains make up each unit cell with neighboring chains staggered by half a cage length.

The axes of a unit cell are shown in Fig. 5. The *b* axis is parallel to the chain

(For page sequence only.)

Fig. 2-4) Scanning electron micrographs of an NbSe$_3$ crystal. (a) A typical crystal section. *Left:* magnification of 1,570 times. *Right:* detail of boxed region on left, magnification by an additional factor of 10. Scale bar of 6.37 μm refers to left-hand photo. (Same photograph as Fig. 3.4.) (b) A cut end of the crystal, magnification of 20,300 times. The scale bar represents 0.493 μm.

a)

17KU   1.57KX 6.__H 3827

b)

17KU   20 3KX   493n 3842
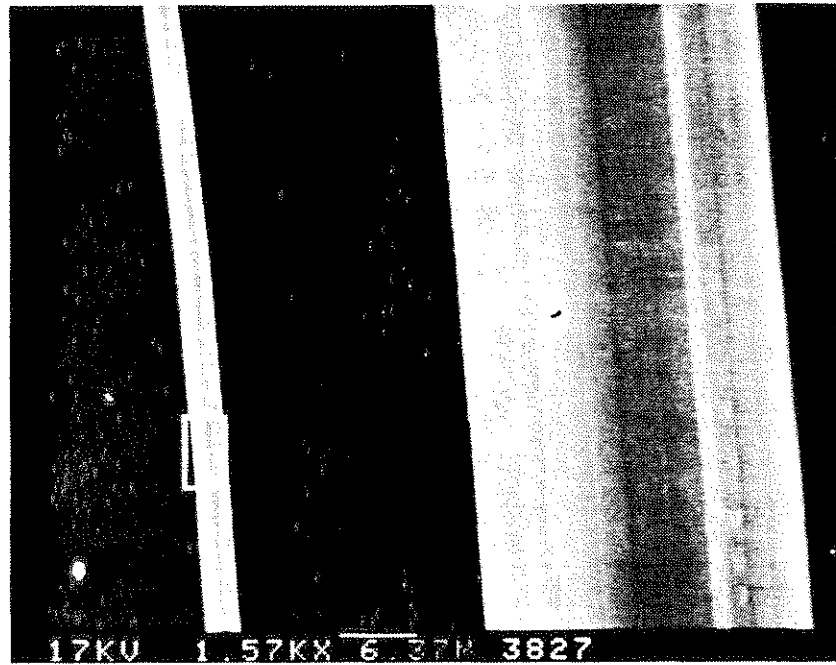
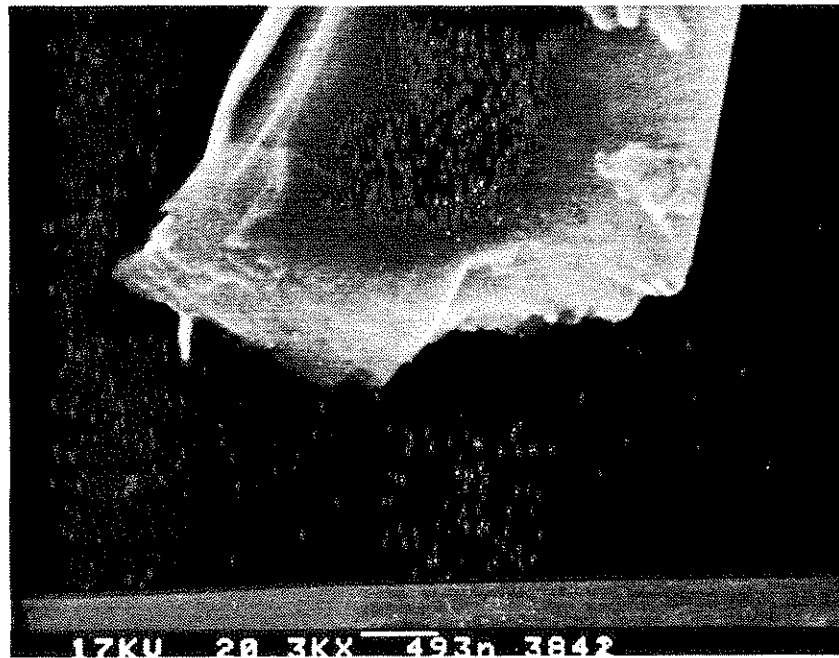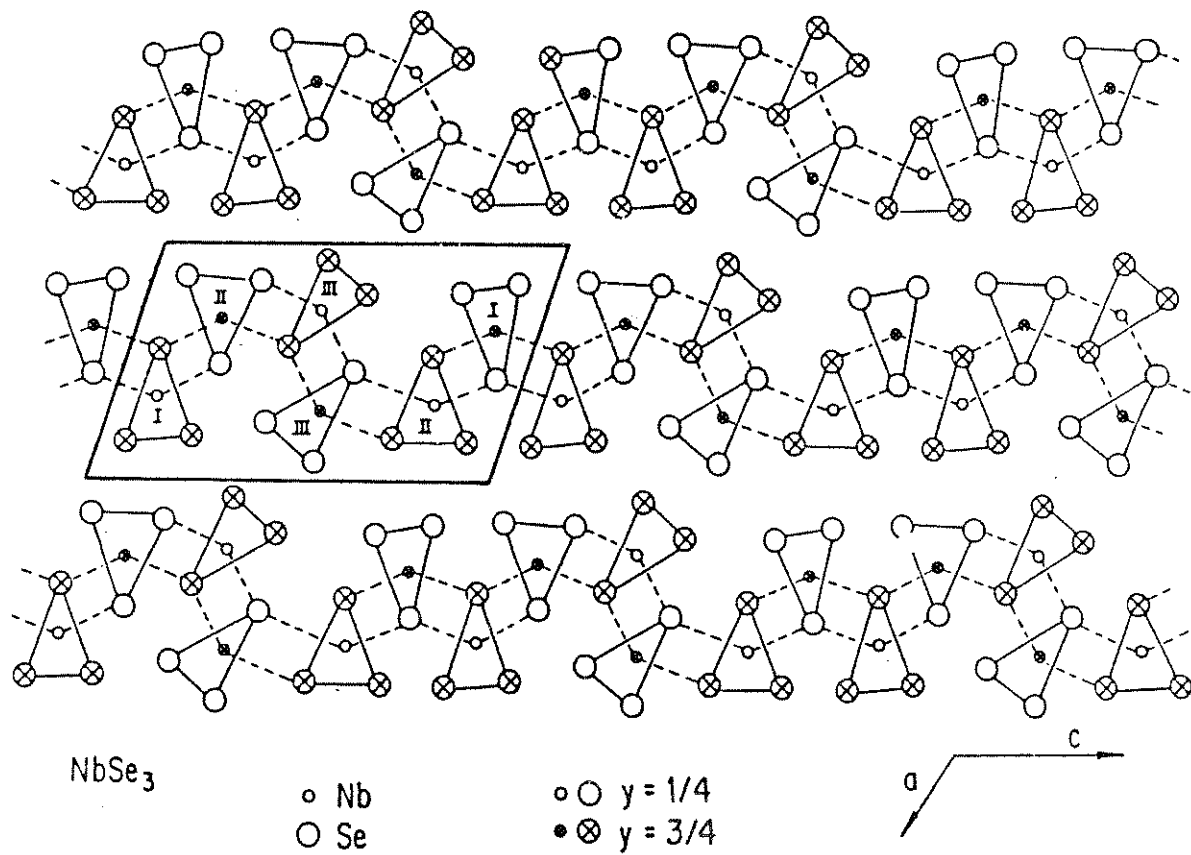Fig. 2-4

Fig. 2-5.a) The crystal structure of NbSe₃. The parallelogram outlines a single unit cell. The Nb and Se ions form trigonal chains in the b direction, which points out of the page. In each unit cell, there are three types of chains, denoted I, II, and III. Each chain type is represent twice. From ref. 21, after ref. 11.

$NbSe_3$

b

∠1/4

∠-1/4
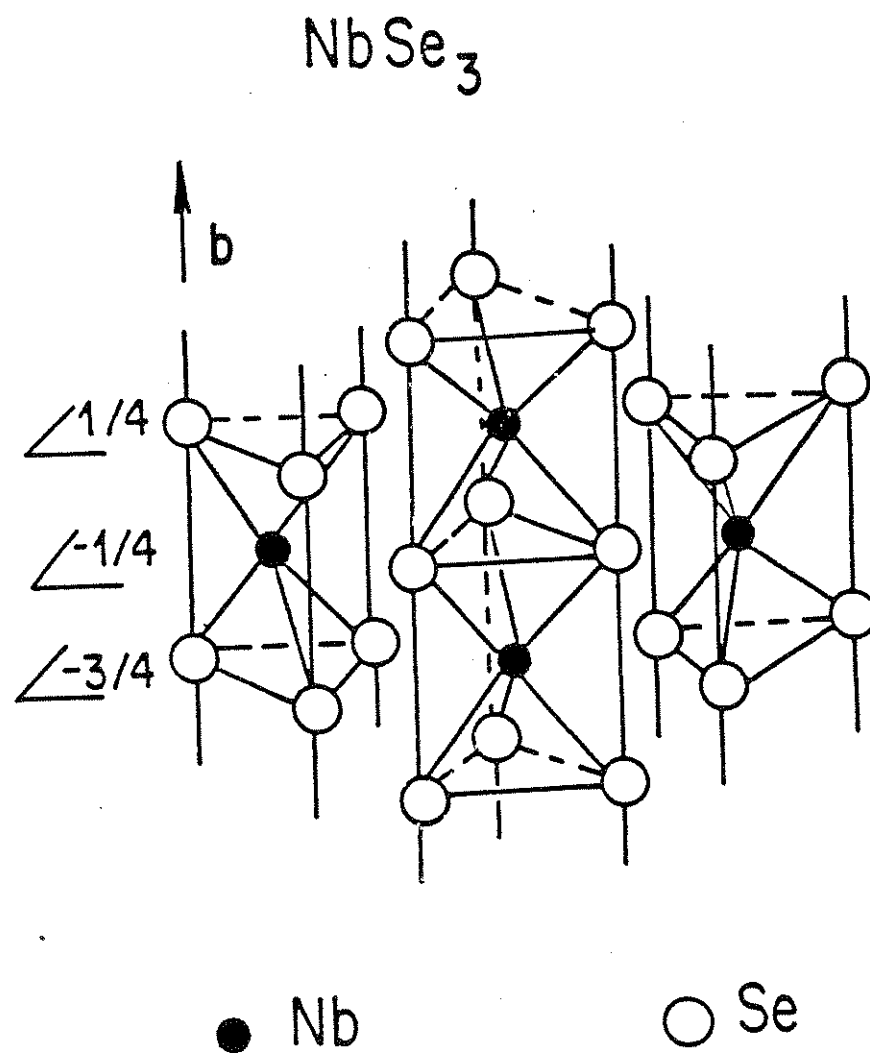
∠-3/4

● Nb   ○ Se

Fig. 2-5.b)   A three-dimensional view of the Nb-Se chains. From ref. 21, after ref. 13.

direction. The a and c axes are perpendicular to the b axis, but at a monoclinic angle of 109 ° with respect to one another. As shown in Fig. 5a, Nb-Se bonds tie neighboring chains together to form layers which lie parallel to the b-c plane. Van der Waals forces hold neighboring planes together. The relative weakness of the van der Waals forces produces the layering of Fig. 4b.

Intra-chain Se-Se spacings vary among the six chains of a unit cell. A cross-section of an $NbSe_3$ chain is an isosceles triangle, and the length of the Se-Se bond along the short edge may be used to classify the chains into three types. In descending order, *type I* chains have strong Se-Se bonds (Se-Se distance of 2.37 Å), *type II* chains have intermediate strength Se-Se bonds (Se-Se distance of 2.49 Å), and *type III* chains have weak Se-Se bonds (Se-Se distance of 2.91 Å). Two chains of each type exist within each unit cell. Fig. 5a shows the chain locations. The symmetry of a unit cell is $P2_1/m$: the unit cell has a screw axis parallel to the b axis, a mirror plane parallel to the a-c plane, and a space inversion point. The unit cell of $NbSe_3$ measures $10.1 \times 15.9 \times 3.5 \text{Å}^3$.

B. Electronic band structure of NbSe₃

The three types of Se-Se bonds play a critical role in the band structure of $NbSe_3$. Shima and Kamimura[12] performed a band structure calculation for $NbSe_3$, based on a linear combination of atomic orbitals, by constructing electronic bands from the s and p orbitals of Se $(4s^2 4p^4)$ and the d and s orbitals of Nb $(4d^4 5s)$. For each chain, the three Se atoms contribute three s-type bands and nine p-type bands, and each Nb atom contributes a d-type band. In type I and II chains, however, one of the p-type bands is constructed from an antibonding σ^* orbital and lies above the d-type band contributed by

from an antibonding σ^* orbital and lies above the d-type band contributed by Nb. In ascending order, therefore, the lowest energy bands of $NbSe_3$ are 18 (6×3) s-type bands, 48 (6×8) p-type bands, 2 (2×1) σ antibonding p-type bands, and 6 (6×1) d-type bands. The total number of electrons per unit cell is 138. Each band takes 2 electrons per unit cell, so the Fermi level lies in the middle of the d-bands.

Fig. 6a shows the Brillouin zone of $NbSe_3$, and Fig. 6b shows the band structure caclulated by Shima and Kamimura. The Fermi level cuts bands 69 - 73, the first through fifth of the d-type bands contributed by Nb. These bands have mainly a d_{z^2}-type symmetry because of the hexagonal ligand field. Consequently, the conduction bands of $NbSe_3$ tend to be aligned along the b axis with little transverse spread. This quasi-one-dimensionality is evident in the energy band diagram of Fig. 6b. Conduction bands 69 - 73 are fairly flat along the transverse directions of the Brillouin zone, e.g. in the planes G-B-A-Y-G and Z-D-E-C-Z. Along longitudinal directions, e.g. the G-Z line, the bands display considerable dispersion.

Five Fermi surfaces are associated with the five conduction bands. By calculating partial densities of states, Shima and Kamimura assigned conduction bands 69, 72, and 73 to type I and II chains, and bands 70 and 71 to type III chains. As shown in Fig. 7, Fermi surfaces 69 and 72 form a nesting pair, as do surfaces 70 and 71. Fermi surface 73 is warped and partially closed; it does not appreciably nest.
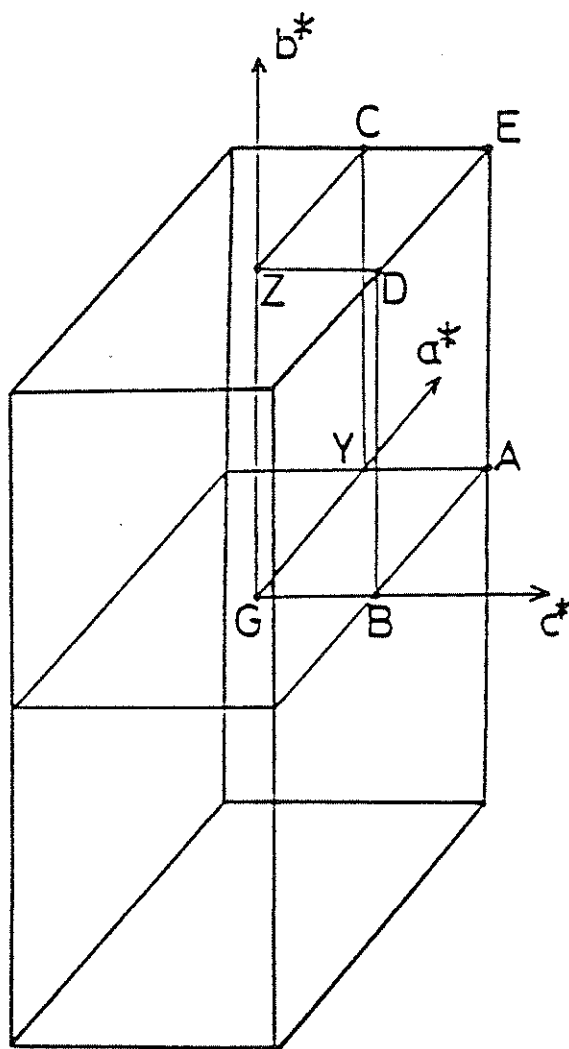
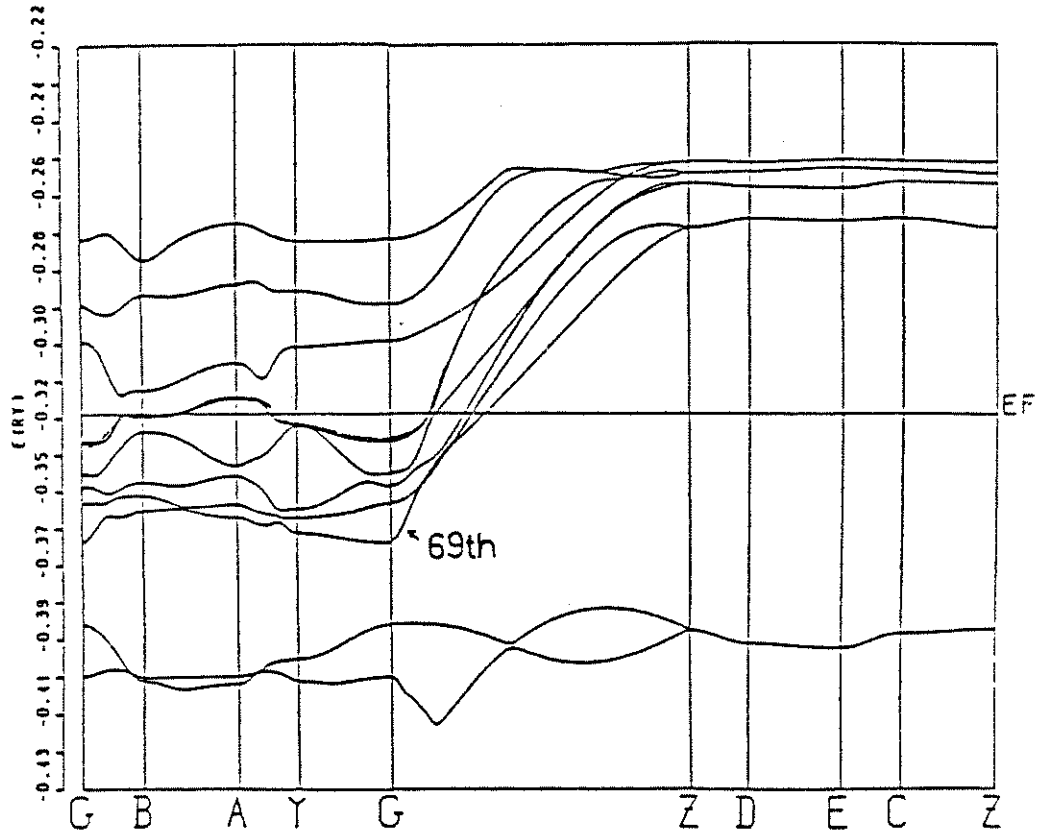Fig. 2-6.a)   The Brillouin zone of NbSe$_3$. From ref. 12.

Fig. 2-6.b)   The band structure of NbSe$_3$. The Fermi energy intersects 5 bands, 69-73, that are formed mainly from Nb d-type orbitals. From ref. 12.
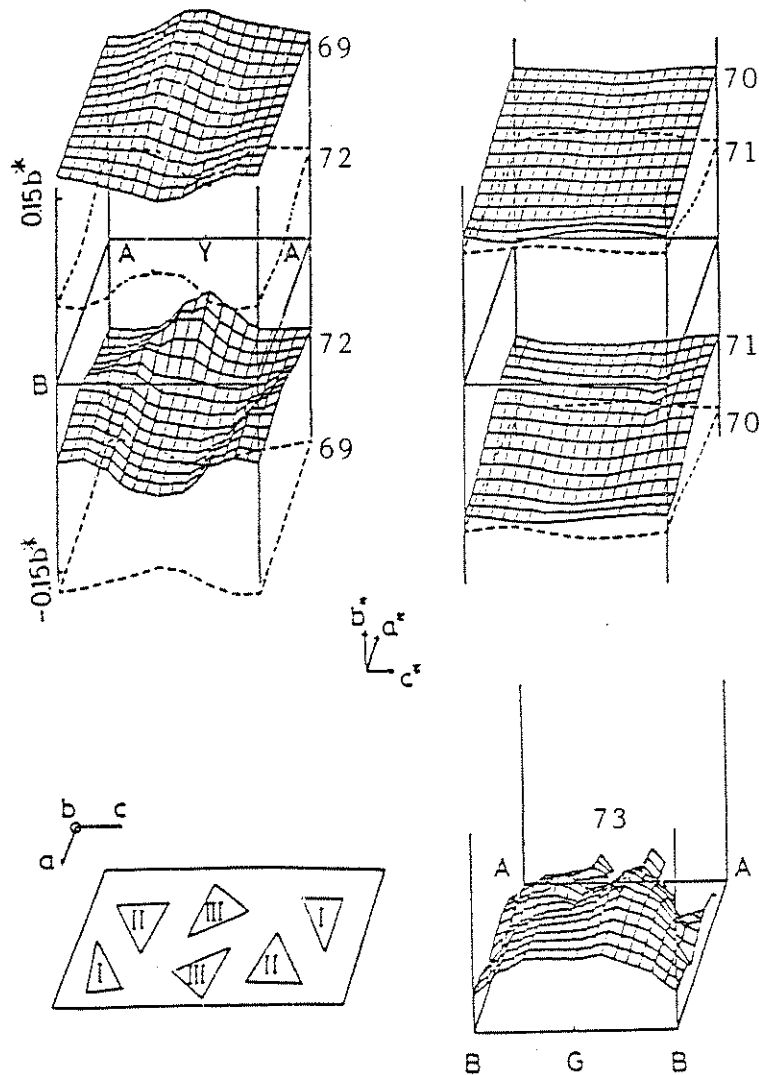
Fig. 2-7)   The five Fermi surfaces of NbSe$_3$. Fermi surfaces 69 and 72 form a nesting pair that is assigned to type I and II chains; the nesting is associated with the lower CDW state ($T_2 = 58$K). Fermi surfaces 70 and 71 form a second nesting pair that is assigned to type III chains; the nesting is associated with the upper CDW state ($T_1 = 142$ K). Fermi surface 73 is associated with type I and II chains and does not nest. From ref. 12.

C. Charge-density waves in $NbSe_3$

Measurements of dc electrical conductivity are the easiest tests for charge-density wave formation. Formation of a CDW creates a gap at the Fermi surface, thereby destroying conduction states. In the presence of pinning, small electric fields do no accelerate a CDW, so CDW conductivity cannot compensate for the decrease in normal electronic conductivity. Therefore, CDW formation is usually marked by an increased dc resistivity in *low-field* measurements.

Fig. 8 shows the low-field resistivity of $NbSe_3$ as a function of temperature.[13] Starting at room temperature, decreasing temperature causes a decrease in the metallic resistivity of $NbSe_3$. A large resistive anomaly occurs at $T_1 = 142$ K and peaks at 125 K. Below 125 K, resistivity again decreases down to $T_2 = 58$ K, where a second resistive anomaly occurs. The second anomaly peaks at 49 K, and resistivity again decreases down to very low temperatures, where it saturates at an impurity-limited value. The resistive anomalies at T_1 and T_2 mark the formation of two independent CDWs. From the changes in conductivity, Ong and Monceau[13] estimate that 20% of $NbSe_3$'s Fermi surface is destroyed at T_1 and 60% of the remaining surface is destroyed at T_2.

Lattice diffraction experiments are conclusive tests of charge-density wave formation. A Peierls distortion causes a modulation of the crystal lattice which produces satellite peaks around the main Bragg peaks in a diffraction experiment. The position of a satellite peak depends on the wavevector of the Peierls distortion, whereas the intensity of a satellite peak depends on the amplitude of the distortion. In $NbSe_3$, two sets of satellite peaks are observed:
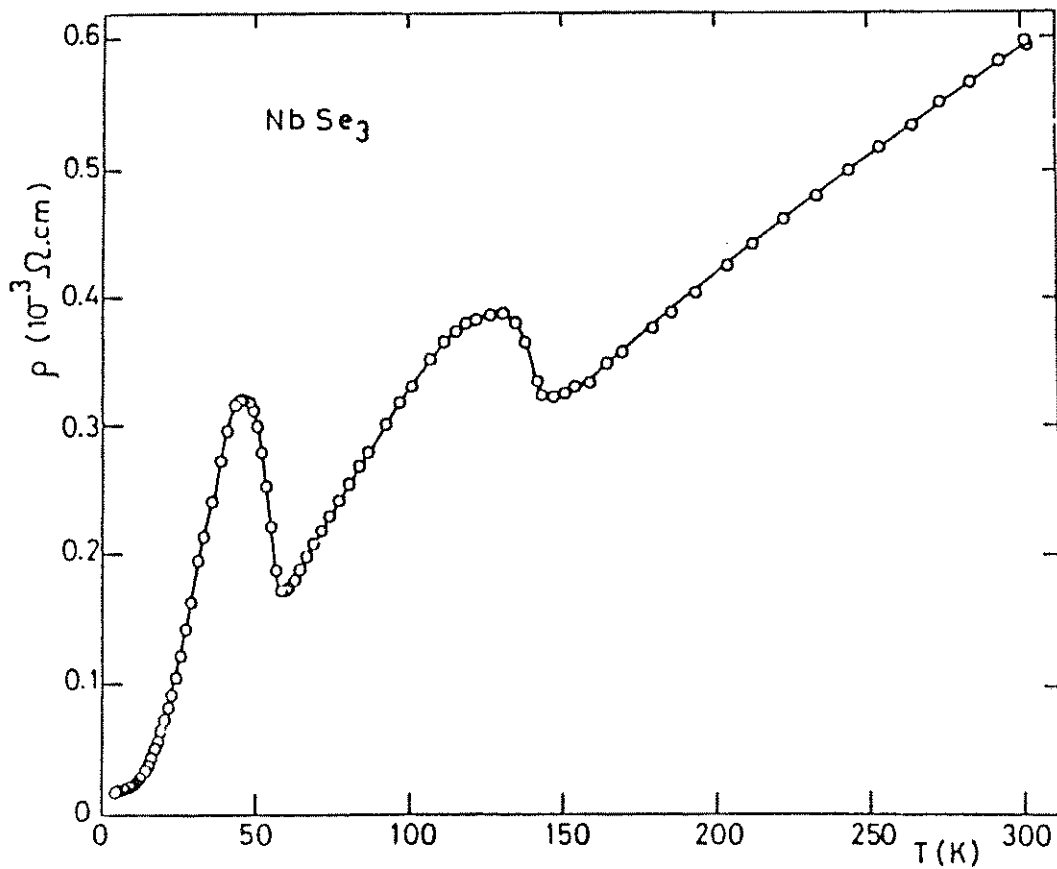
Fig. 2-8)   The low-field resistivity of NbSe₃ as a function of temperature.
Resistivity anomalies at $T_1 = 142$ K and $T_2 = 58$ K signal the
formation of two independent CDW states. From ref. 13.

one set for the CDW which forms at T_1 (Ref. 11) and a second set for the CDW which forms at T_2 (Ref. 14). The wavevector of the upper CDW is $\mathbf{q}_1 = (0, .243 b^*, 0)$, and the wavevector of the lower CDW is $\mathbf{q}_2 = (.5 a^*, .263 b^*, .5 c^*)$. NMR measurements[15] suggest that the upper CDW forms on type III chains, whereas the lower CDW forms on type I chains. Low-temperature tunneling experiments[16] indicate an electronic gap of $2 \Delta_o = 70$ meV due to the lower CDW.

The band structure and Fermi surfaces calculated by Shima agree reasonably well with the experimental data. The Fermi surfaces of bands 70 and 71 are the flattest surfaces and therefore the most suscpectible to a Peierls distortion. The upper CDW is assigned to this nesting pair, in agreement with the NMR measurements. The calculated nesting vector is $\mathbf{q}_1 = (0, .23 b^*, 0)$, in good agreement with the experimental value. The lower CDW is assigned to Fermi surfaces 69 and 72. This assignment places the lower CDW on chains I *and* III, in slight disagreement with the NMR result. The calculated lower nesting vector is $\mathbf{q}_2 = (0, .22 b^*, 0)$, in poor agreement with the experimental value. Agreement between the calculated and observed nesting vector $\mathbf{q}_2$ is improved if one assumes that adjacent $\mathbf{q}_2$ CDWs are spatially ordered. If adjacent CDWs are out of phase by 180°, then their Coulomb energy is minimized. Such ordering changes the calculated nesting vector to $\mathbf{q}_2 = (.5 a^*, .22 b^*, .5 c^*)$, in better agreement with the observed value.

The warped and partially closed seventy-third Fermi surface explains the metallic conductivity of $NbSe_3$ below the second CDW transition. The density

based on low-temperature specific heat and Knight shift data. The shape of the Fermi surface, however, is in poor agreement with Shubnikov-de Haas measurements.[17]

D. Mean-field parameters for NbSe$_3$

Table 2.1 summarizes the measured mean-field parameters of NbSe$_3$. These values may be used to check the mean-field theory for self-consistency. For example, the gap parameter and mean-field transition temperature should be related by $2\Delta_o = 3.5\,k_B T_P^{MF}$. If dimensionality effects are important, the mean-field temperature is reduced by about 4 (Ref. 9), so that $2\Delta_o = 14\,k_B T_P$. In the lower CDW state of NbSe$_3$, the experimental value of $(2\Delta_o/k_B T_P)$ is 13.8.

The values in Table 2.1 may also be used to estimate the mean-field parameters λ and G_o. The gap equation is $\Delta_o = 2E_B\exp(-1/\lambda)$. If $2E_B$ is assumed equal to NbSe$_3$'s bandwidth (see Appendix A2), then $\lambda = 0.33$ for the lower CDW state of NbSe$_3$. As a check on this value, λ may also be estimated from the Frohlich mass:

$$(m^*/m_e) \cong 4\Delta_o^2/\lambda(\hbar\omega_{2k_F})^2 \ .$$

(See Sec. III.) Sridhar et al.[18] estimate that $(m^*/m_e) \cong 100$, which combined with the listed values of Δ_o and ω_{2k_F} gives $\lambda = 0.34$. This excellent agreement may be coincidental because of the uncertainty in $2E_B$.

The Frohlich parameter G is given by $G^2 = \lambda 2NM\omega_{2k_F}^2/n(0)$. Estimating that $n(0)/N = 1$ state/eV (Ref. 12) and that $M = 93$ amu gives $G = 1.5$ eV/Å

Parameter	Value	Measurement	Ref.
Δ_o	35 meV	Tunneling	16
$\omega_{2k_F}/2\pi$	2.75 THz	Neutron scattering	19
$n(0)$, 300K	1.3 states/(Nb-eV) 1.6 states/(Nb-eV)	Band calculation NMR	12 15
$n(0)$, 0 K	.41 states/(Nb-eV) .35 states/(Nb-eV) .28 states/(Nb-eV)	Band calculation Specific heat NMR	12 20 15
Bandwidth	1.4 eV 1.2 eV 2.8 eV	Band calculation Susceptibility Thermopower	12 21 21

Table 2-1) Mean-field parameters for NbSe$_3$.

for the lower CDW state. Combined with the gap parameter Δ_o, this implies that the amplitude of the lower Peierls distortion is $2u_o = 0.05$Å. The lattice constant of NbSe$_3$ is 3.5 Å, so the Peierls distortion is a 1% effect.

III. Sliding Charge-Density Waves

A. Dynamics of charge-density waves in perfect crystals

This section discusses the translation and vibration modes of Peierls distortions in perfect crystals. A Peierls distortion has two independent degrees of freedom, its amplitude u and its phase ϕ. The dependence of the Peierls distortion energy on u has been discussed in some detail already. This section begins with a discussion of the dependence of $E_{Peierls}$ on ϕ.

Eq. 2.24 and Fig. 2.3 show that ϕ determines the orientation of a Peierls distortion with respect to the undistorted crystal lattice. For a commensurable CDW of order 2, there are two energetically optimal orientations: $\phi = 0$ ° and $\phi = 180$ ° with u given by (2.18). An order M' commensurate CDW has M' optimal orientations with respect to its host lattice: $\phi = 2\pi/M'$, $2(2\pi/M')$, ..., $(M'-1)(2\pi/M')$. At each equivalent orientation, the Peierls energy has the same dependence on u as at $\phi = 0$ °. A convenient way of displaying this equivalence is to combine the amplitude u and phase ϕ into a single polar coordinate, $\psi = u e^{i\phi}$.

If all values of ϕ are considered, $E_{Peierls}$ forms an energy surface over the ψ polar plane. At each optimal value of ϕ, the energy surface has a "pocket" of minimum energy: 2 pockets for an order 2 commensurable CDW, 4 pockets for

an order 4, M' pockets for an order M'. As ϕ moves away from one of its optimal values, the distortion energy increases. Fig. 9 depicts energy surfaces for commensurable CDWs of increasing order. As the order of commensurability increases, the "walls" between the pockets in the energy surface become smaller because the effect of commensurability goes as $[\Delta_o^2/E_F][\Delta_o/W]^{M'-2}$ (Ref. 3). As M' increases, the distinction between a high-order commensurable CDW and a truly incommensurable CDW becomes academic, and the energy surface $E_{Peierls}$ assumes the sombrero shape shown in Fig. 9d.

The sombrero energy surface of Fig. 9d is fundamental to widely disparate branches of physics, as P. W. Anderson points out.[22] The shape is characteristic of a *broken continuous symmetry*. Sombrero curves appear in physics ranging from Goldstone bosons in particle physics to cosmic strings in astrophysics. The translational invariance of an undistorted lattice is the broken symmetry of incommensurable CDWs. Associated with broken continuous symmetries is a phenomenon which Anderson calls *generalized rigidity*. For CDWs, generalized rigidity results from the rotational invariance of $E_{Peierls}$. As Eq. 2.39b will show, the energy of a CDW in a perfect crystal is minimized if ϕ is uniform throughout. If one "grabs" ϕ at an end of a crystal and starts cranking it through revolutions of 2π, the phase ϕ in the rest of the crystal will follow the rotations rigidly.

Rotational invariance of $E_{Peierls}$ occurs because the energy of an incommensurable CDW does not depend on ϕ. In the language of Hamiltonian
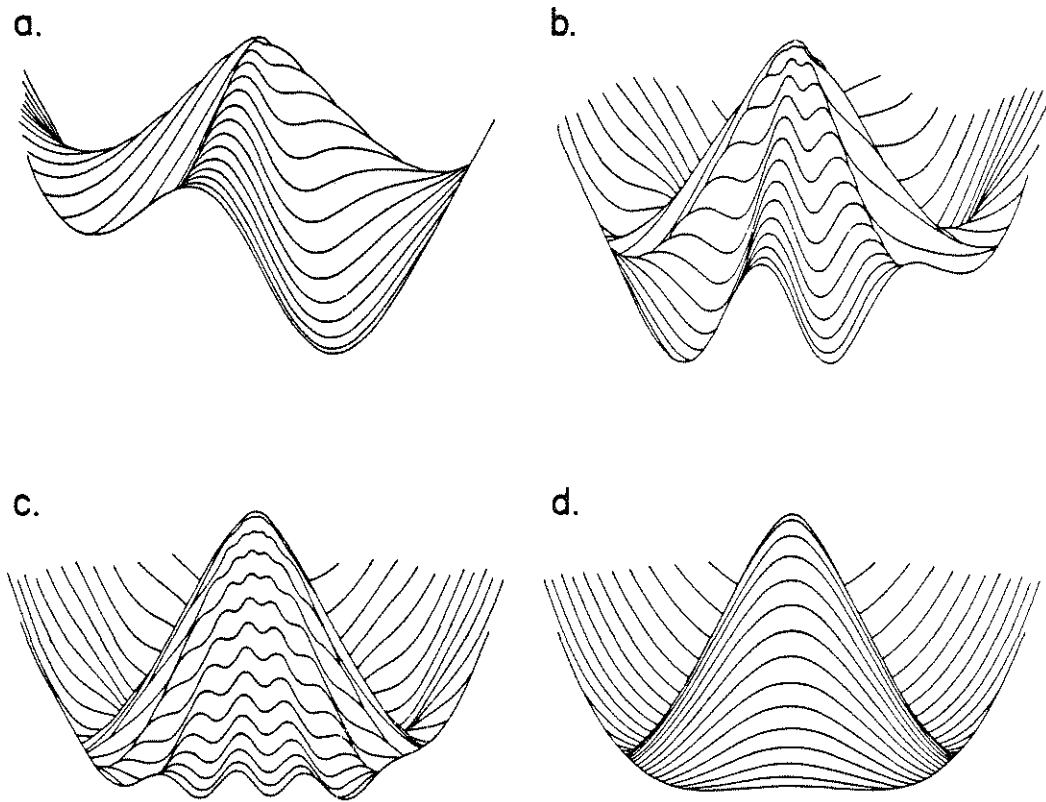
Fig. 2-9)   Energy   surfaces   for   CDWs   with   increasing   orders   of
commensurability: (a) order   4,   (b) order   8,   (c) order   16,   and
(d) incommensurable. Because of its shape, the energy surface of an
incommensurable CDW is referred to as a sombrero surface.

mechanics, ϕ is a cyclical coordinate and therefore a conserved, generalized momentum is associated with $\dot{\phi}$. Frohlich[2] noted that a constant angular frequency $\dot{\phi}$ corresponds to the periodic oscillation of lattice ions but to the time-independent *sliding* of conduction electrons. The combination of ionic oscillation and electronic sliding is the generalized momentum associated with $\dot{\phi}$.

The basic idea of Frohlich conductivity is shown in Fig. 10. As time advances through one period $T = 2\pi/\dot{\phi}$, an ion in the lattice oscillates one cycle about its equilibrium position. In contrast, the electronic density wave advances by one wavelength along the crystal. The sliding CDW carries a current $J_{CDW} = ne\rho_c\dot{\phi}/2k_F$ where n is the spatial density of electrons in the undistorted (as well as distorted) lattice. The fractional charge density ρ_c is related to the CDW amplitude ρ and is normalized to 1 at zero temperature. Because the generalized momentum associated with $\dot{\phi}$ is conserved, CDW current flows without dissipation once it has been set into motion. Therefore in a perfect crystal, an incommensurable CDW is a superconductor of electrical current.

Although only the electrons in a CDW slide along a crystal, the lattice ions also contribute to the kinetic energy of a CDW. In order for the CDW electrons to slide with a velocity v, the lattice ions must oscillate with an angular frequency $\dot{\phi} = 2\pi v/\Lambda$. The kinetic energy of a sliding CDW is therefore much larger than the kinetic energy of its electrons. Frohlich adopted a convention of lumping the ionic kinetic energy into the electronic kinetic energy by means of an effective electronic mass. The difference between the kinetic energy of a sliding CDW and the unrenormalized kinetic energy of the electrons is ascribed
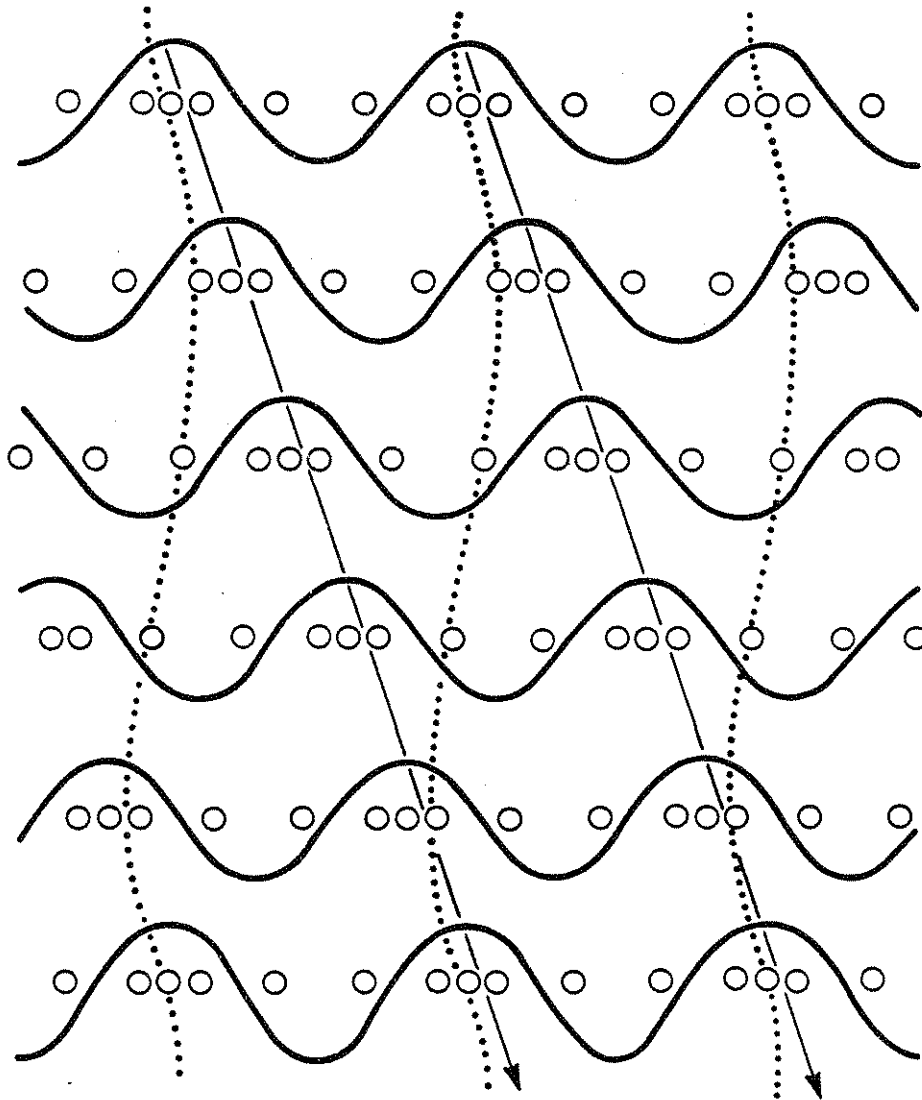
Fig. 2-10)   The motion of electronic and ionic charge during Frohlich conductivity. Solid lines represent electronic charge and circles represent lattice ions. As time advances from the top to the bottom of the figure, the CDW completes one period of its motion. The electronic density wave advances by one wavelength, while the ionic lattice oscillates through one cycle.

to an increased electronic mass.

An elegant calculation of the electronic effective mass is due to M. J. Rice.[23] The effective mass m^* at zero temperature is defined by

$$n(\frac{1}{2}m^*v^2)= n(\frac{1}{2}mv^2)+ \frac{1}{a}(\frac{1}{2}M<\dot{u}_j^2>) . \qquad (2.33)$$

The first term on the right is the electronic kinetic energy; the second term is the ionic kinetic energy. The rms ionic velocity is

$$<\dot{u}_j^2> = <[2u_o\dot{\phi}\sin\phi]^2> \qquad (2.34)$$
$$= 2u_o^2\dot{\phi}^2 .$$

Therefore the effective electronic mass is

$$m^* = m(1+\frac{2Mu_o^2\dot{\phi}^2}{a\rho_c nv^2 m}) . \qquad (2.35)$$

The second term may be rewritten in terms of the electron-phonon coupling constant, the $2k_F$ phonon frequency, and the zero temperature gap parameter:

$$m^* = m(1+4\Delta_o^2/\lambda(\hbar\omega_{2k_F})^2) . \qquad (2.36)$$

In contrast to uniform perturbations of the CDW phase, a uniform perturbation of the CDW amplitude raises the CDW energy. The increase in energy may be calculated by expanding $E_{Peierls}$ about the equilibrium value of u_o. If the CDW amplitude changes by an amount δu, the change in CDW energy is

$$\delta E = \frac{1}{2}(\delta u)^2 \frac{d^2 E}{du^2} \tag{2.37}$$

$$= \frac{1}{2}(\delta u)^2 n(0) G^2 .$$

In Fig. 9d, $n(0)G^2$ is the curvature of E_{Peiels} in the brim of the sombrero.

In a distorted lattice, a uniform perturbation of either amplitude or phase has a wavevector of $2k_F$. By analogy with Eq. 13, the change in energy due to a $2k_F$ amplitude distortion may be expressed in terms of an effective $2k_F$ normal mode frequency:

$$\delta E = NM\lambda\omega_{2k_F}^2 (\delta u)^2 . \tag{2.38}$$

For comparison, note that the energy of a CDW is not changed by a $2k_F$ phase distortion, so the $2k_F$ normal frequency is zero; i.e. the charge density wave slides uniformly. For wavevectors different from $2k_F$, Lee, Rice, and Anderson[3] calculate the amplitude and phase frequencies to be

$$\Omega_+^2 = \lambda\omega_{2k_F}^2 + \frac{1}{3}\frac{m}{m^*} v_F^2 \mid q - 2k_F \mid^2 , \tag{2.39a}$$

and

$$\Omega_-^2 = \frac{m}{m^*} v_F^2 \mid q - 2k_F \mid^2 , \tag{2.39b}$$

where Ω_+ is the frequency of the amplitude mode and Ω_- is the frequency of the phase mode. Eisenreigler[24] and Walker[25] both note that the CDW phase and amplitude modes are the *classical* normal modes of an incommensurable lattice.

B. Pinning of charge-density waves in nonideal crystals

Real crystals are not perfect but contain impurities, defects, grain boundaries, and surfaces. In a real crystal, the energy of even an incommensurable CDW depends on its orientation (i.e. phase) with respect to the imperfections of its host lattice. This loss of translation invariance is known as *pinning*. A CDW is pinned to a particular orientation because in that orientation its interaction energy with the crystal is minimized. Pinning is reflected in the energy surface of a CDW. As a first approximation, the distortion energy $E_{Peierls}$ loses its rotational invariance and becomes a tilted sombrero, Fig. 11a. (The figure is only a first approximation to the true pinning potential of a CDW. A real pinning potential is more "ragged" than the smooth sinusoidal potential illustrated.)

The effect of pinning is actually more complicated than shown in Fig. 11a. Besides the loss of translational invariance, phase uniformity is also lost. The CDW phase retains uniformity only over short regions called *domains*,[26] as shown schematically in Fig. 11b. The length of a domain is determined by balancing the elastic energy of a CDW against the pinning energy of imperfections within a crystal.

To calculate CDW elasticity, a useful approximation is due to Fukuyama,[27] who noted that CDW dynamics often can be simplified. Equation 39 shows that the phase mode of a CDW requires much less energy to excite than the amplitude mode. It is usually valid to treat the CDW amplitude as rigid and to consider only phase excitations of a CDW. With this approximation, Fukuyama
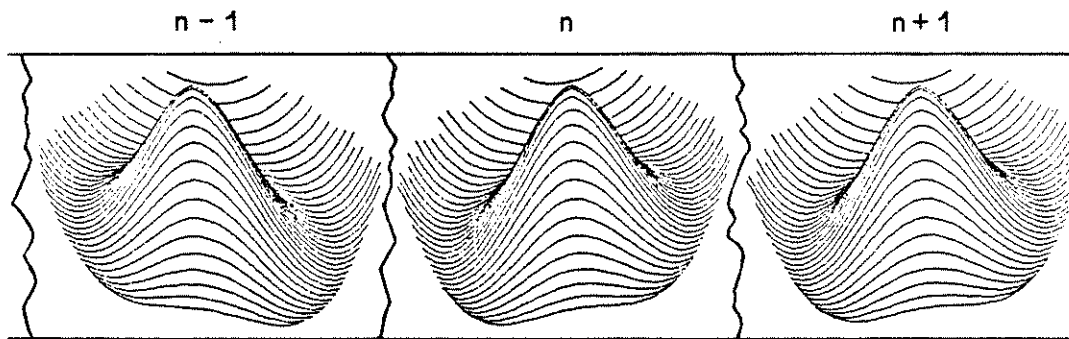
a. PINNING
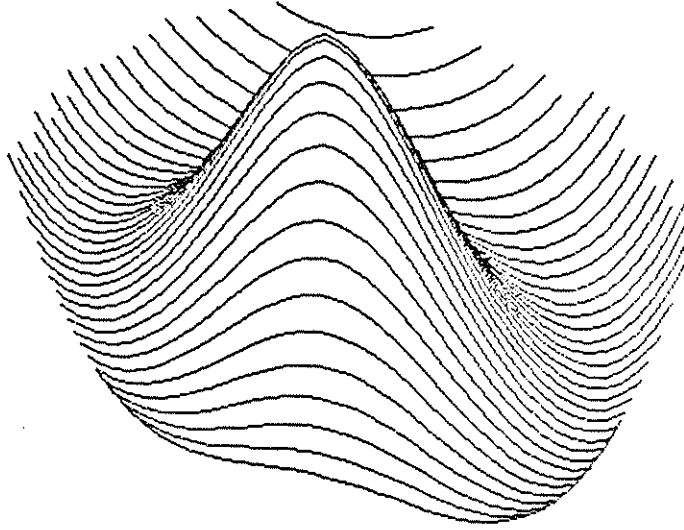
b. DOMAINS

Fig. 2-11) The energy surface of a pinned incommensurable CDW. (a) The
energy surface within a pinning domain. (b) The formation of
pinning domains within a crystal.

derived a Hamiltonian for CDW phase dynamics. At zero temperature, the kinetic energy of a CDW is $\frac{1}{2} n m^*(\Lambda \dot\phi/2\pi)^2$ and the elastic energy of the CDW increases quadratically with $(d\phi/dx)$. In other words, the CDW phase behaves like an elastic continuum. An appropriate Hamiltonian for the CDW phase is

$$H_o = \int dx \left\{ \frac{nm^*}{2} (\Lambda \dot\phi/2\pi)^2 + \frac{K}{2} \left(\frac{d\phi}{dx}\right)^2 \right\} , \tag{2.40}$$

where $K = nmv_F^2/(2k_F)^2$ is the stiffness of the CDW phase.

Impurities are the most common type of crystal imperfection. The interaction energy of a CDW with impurities (of a single type) is

$$H_{pin} = \sum_j \int dx \, \rho_{CDW}(x) \, v \, (x - x_j) , \tag{2.41}$$

where summation is over all impurities, which are randomly distributed within a crystal at positions x_j. Because the CDW amplitude mode is rigid, the Hamiltonian (2.41) is valid only over long length-scales. Also, the interaction of an impurity with a CDW is screened, so the impurity potential is relatively short-ranged. Therefore, Fukuyama approximates the impurity potential by a delta function:

$$H_{pin} = \sum_j V_I \, \rho_o \, \cos \, (2k_F \, x_j + \phi_j) . \tag{2.42}$$

Here ϕ_j is the CDW phase at the jth impurity site. The Fukuyama phase Hamiltonian is $H = H_o + H_{pin}$.

The elastic energy of a CDW is $\frac{1}{2} K \int dx (\nabla \phi)^2$ and is minimized when ϕ is uniform throughout a crystal. On the other hand, the impurity interaction

energy is minimized when the CDW phase adjusts so that $\phi_j = \pi - 2k_F x_j$ at each impurity site. The energy gained from a nonuniform phase is $V_I \rho_o$ per impurity, whereas the elastic energy cost per impurity is approximately $\frac{1}{2} K (n_i)^2 / n_i$, where n_i is the (one-dimensional) impurity concentration. Fukuyama and Lee[26] define a dimensionless parameter which is the ratio of impurity to elastic energies:

$$\epsilon = \frac{2 V_I \rho_o}{K n_i} \qquad (2.43)$$

Strong pinning corresponds to $\epsilon \gg 1$: a CDW minimizes its energy by adjusting its phase at each impurity. Strong pinning occurs for large impurity potentials or small impurity concentrations. *Weak pinning* corresponds to $\epsilon \ll 1$: a CDW minimizes its energy by keeping its phase as uniform as possible.

With strong pinning, a CDW is "stuck" at each impurity site. On the average, the CDW phase changes by π between each impurity site, so the average length L_o of a domain is $L_o = 1/n$ for the case of strong pinning. A reasonable (three-dimensional) impurity concentration is 10 ppm, so a typical domain length is $L_o = (3.5\text{Å})(10^5)^{1/3} = 140\text{Å}$.

With weak pinning, a CDW is not pinned by any one impurity. Instead, the CDW phase adjusts to minimize the CDW energy at many impurity sites simultaneously. Within a domain, the impurity potential energy is

$$V(L_o) = V_I \rho_o \text{Re}\left\{ \sum_j{}' e^{i(2k_F x_j + \bar{\phi})} \right\} . \qquad (2.44)$$

The sum is restricted to impurities within a length L_o, where $\bar{\phi}$ is the average

phase within that length. Eq. 44 may be viewed as a random-walk problem, and on average the sum gives

$$V(L_o) = V_I \rho_o (n_i L_o)^{1/2} \cos(\phi_o + \overline{\phi}) , \tag{2.45}$$

where ϕ_o is some random angle that depends on the exact spatial distribution of impurities within a domain. If the average phase adjusts to be $(\pi - \phi_o)$, then the impurity pinning energy is minimized:

$$V_{\min}(L_o) = - V_I \rho_o (n_i L_o)^{1/2} . \tag{2.46}$$

Neighboring domains have different optimal phases, so the CDW phase must interpolate smoothly from one domain to the next in order minimize pinning energy within each domain. The elastic energy cost of this variation is

$$E_{elastic}(L_o) = \frac{1}{2} K \int_0^{L_o} dx < (\frac{d\phi}{dx})^2 >_{average} \tag{2.47}$$

$$= \frac{1}{2} K (\alpha L_o)^{-1} ,$$

where α is a numerical factor of order 1 that depends on details of averaging and phase interpolation. Minimizing the combined energy of Eqs. 45 and 47 gives

$$L_o = \{(\alpha \pi \epsilon)^{2/3} n_i\}^{-1} \tag{2.48}$$

For weak pinning, $L_o \sim n_i^{-1/3}$. Thus for equal concentrations, domain lengths are larger for weak impurities than for strong impurities. In NbSe$_3$, x-ray diffraction measurements have demonstrated the presence of (presumably weak) domains longer than 0.5 μm (Ref. 14).

The Fukuyama Hamiltonian may be used to calculate the strength of an electric field sufficient to depin a CDW. Independent of the assumptions behind the Fukuyama Hamiltonian, a quasi-static electric field couples only to the phase of a CDW, since the Frohlich current depends on $\dot{\phi}$, not $\dot{\rho}$. An electric field is quasi-static if its frequency ω is much smaller than the minimum frequency of the amplitude mode $\lambda^{1/2}\omega_{2k_F}$. For NbSe$_3$, the amplitude frequency is about 1600 GHz (50 cm^{-1}), so frequencies less than infrared are quasistatic.

An electric field term may be added to the Fukuyama Hamiltonian which, in the absence of pinning, accelerates a CDW to reproduce the Frohlich current:

$$H_{field} = \int dx \frac{\rho_{eff} e n E_x \phi}{(2k_F)} \ . \tag{2.49}$$

The field E_x is the longitudinal component of the electric field and the normalized density ρ_{eff} is related to the density ρ_c. Near zero temperature (where ρ_c approaches 1) and near the Peierls temperature (where ρ_c vanishes as Δ_o), the densities are equal, but in between these extremes, ρ_{eff} may differ from ρ_c. The *Fukuyama-Lee-Rice*[28] *Hamiltonian* is $H = H_o + H_{pin} + H_{field}$, where the different terms come from Eqs. 2.40, 2.42 and 2.49, respectively.

Using a Ginzburg-Landau expansion for the free energy of a CDW, Lee and Rice[28] estimate the *threshold field* E_T necessary to depin a CDW. For weak pinning,

$$E_T = \epsilon^4 (\xi_\perp^2 \ \xi_\| n_i)^2 \ (\Delta_o^2/E_F)/(e\Lambda) \ , \tag{2.50}$$

where $\xi_\perp$ and $\xi_\|$ are the transverse and longitudinal amplitude coherence

coherence length is given by $\xi_{\parallel} = \hbar v_F / \pi \Delta_o$. For NbSe$_3$, this length is about 20Å. The transverse coherence length is reduced by the ratio of bandwidth anisotropy ratio, which in the case of NbSe$_3$ is about a factor of 10. The important feature of Eq. 50 is that E_T is proportional to the square of the weak impurity concentration. In contrast, for strong impurities at low temperature, the threshold field is proportional to the first power of the strong impurity concentration:

$$E_T = n_i \Delta_o / e\Lambda . \qquad (2.51)$$

In addition, because of the factor of $\epsilon^4 (\xi_\perp^2 \xi_{\parallel})^2$, the threshold field for weak impurities is much less than the threshold field for comparable concentrations of strong impurities. For concentrations of one part in 10^5, Lee and Rice estimate $E_T = 10$ meV/cm for weak impurities and $E_T = 1000$ meV/cm for strong impurities.

C. Experimental characteristics of sliding charge-density waves

Currently no microscopic theory exists that describes CDW motion when impurities are present. The models that do exist are phenomenological and based on experimentally observed characteristics of sliding CDWs. As a prelude to a discussion of these models, this section reviews some experiments on CDW dynamics.

1. Field and frequency dependent conductivity

Sliding CDW transport was discovered by Monceau, Ong and coworkers[29] when they observed that the resistivity of NbSe$_3$ depends on the electric field

applied across the material. Fig. 12a displays the field-dependent conductivity associated with the first resistivity anomaly of $NbSe_3$. An inset shows the low-field resistivity of $NbSe_3$ for reference. As the strength of an applied electric field increases, the resistivity of $NbSe_3$ decreases as the current density through the material increases. Fig. 12b shows that the lower resistivity anomaly of $NbSe_3$ is also field dependent. At high electric fields, the resistivity of $NbSe_3$ saturates at a value which is field-independent. This limiting value of resistivity is indicated by the solid lines in the figures; its reciprocal value is known as the *high-field conductivity* of $NbSe_3$.

The field-dependent resistivity of $NbSe_3$ is associated with the CDWs that cause the anomalies at T_1 and T_2. At temperatures above $T_1 = 144K$, for example, $NbSe_3$'s resistivity is independent of electric field. X-ray diffraction studies show that the field-dependent resistivity is not caused by a destruction of the CDW state.[14] Since the discovery of nonlinear conductivity by Ong *et al.*, transport studies have provided both direct and indirect evidence that the field-dependent resistivity of $NbSe_3$ is due to CDW sliding.[30,31]

CDWs do not slide in $NbSe_3$ until sufficiently large electric fields are applied.[32] Fig. 13 displays an I-V curve of $NbSe_3$ in the lower CDW state. At low electric fields, the I-V curve is linear, indicating normal ohmic conductivity. At larger fields, the I-V curve bends upward as the lower CDW begins to slide and $NbSe_3$ begins to carry an *excess current*. Excess current may be sensitively monitored by measuring the dynamic resistance of a crystal, dV/dI. At low fields, Fig. 13 shows that the dynamic resistance of $NbSe_3$ is constant, but past
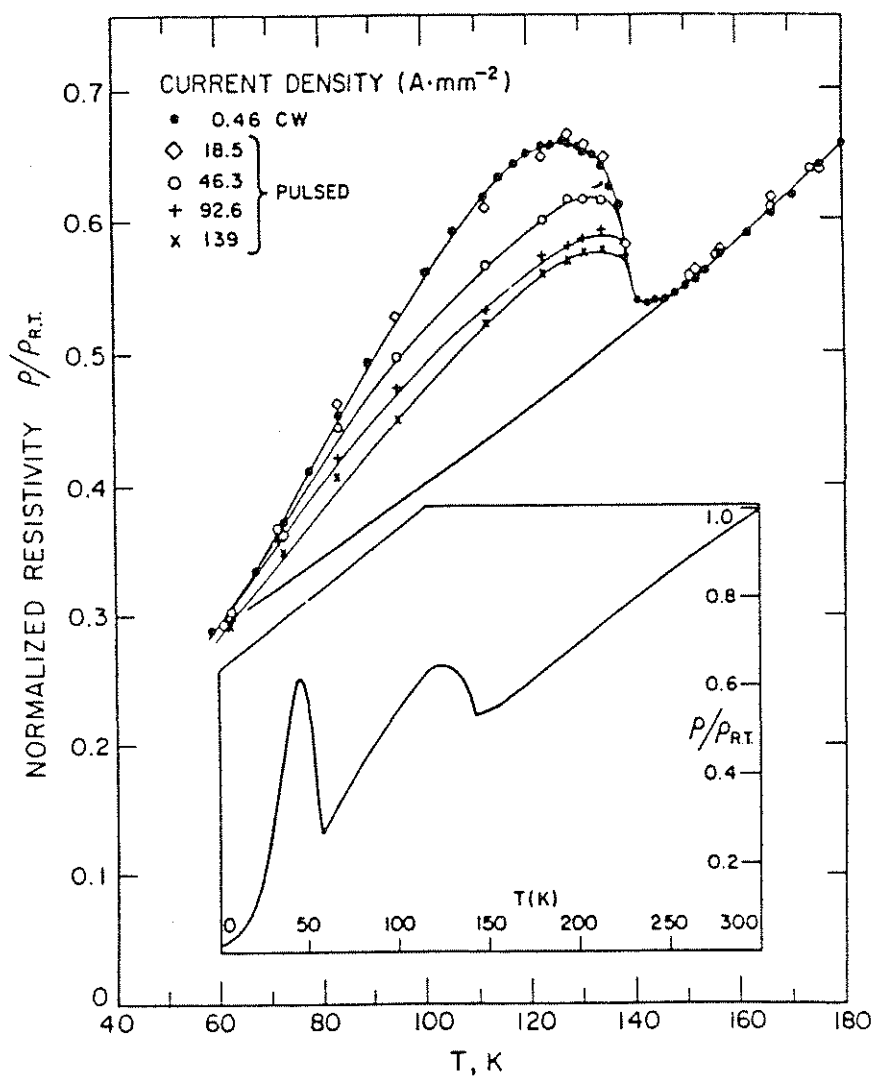
Fig. 2-12.a)   The field-dependent conductivity associated with the first resistivity anomaly of NbSe$_3$ (T_1 = 142K). The inset shows the low-field resistivity of NbSe$_3$. From ref. 29.
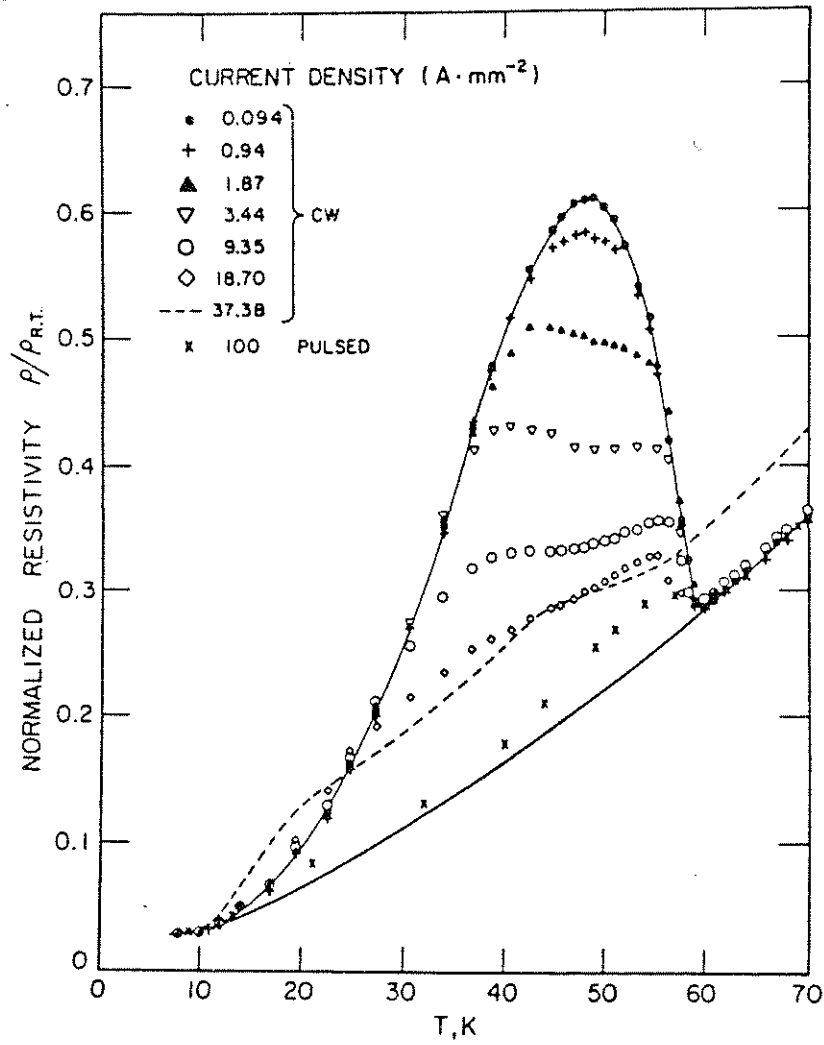
Fig. 2-12.b)   The field-dependent conductivity associated with the second resistivity anomaly of $NbSe_3$ ($T_2 = 58K$). From ref. 29.
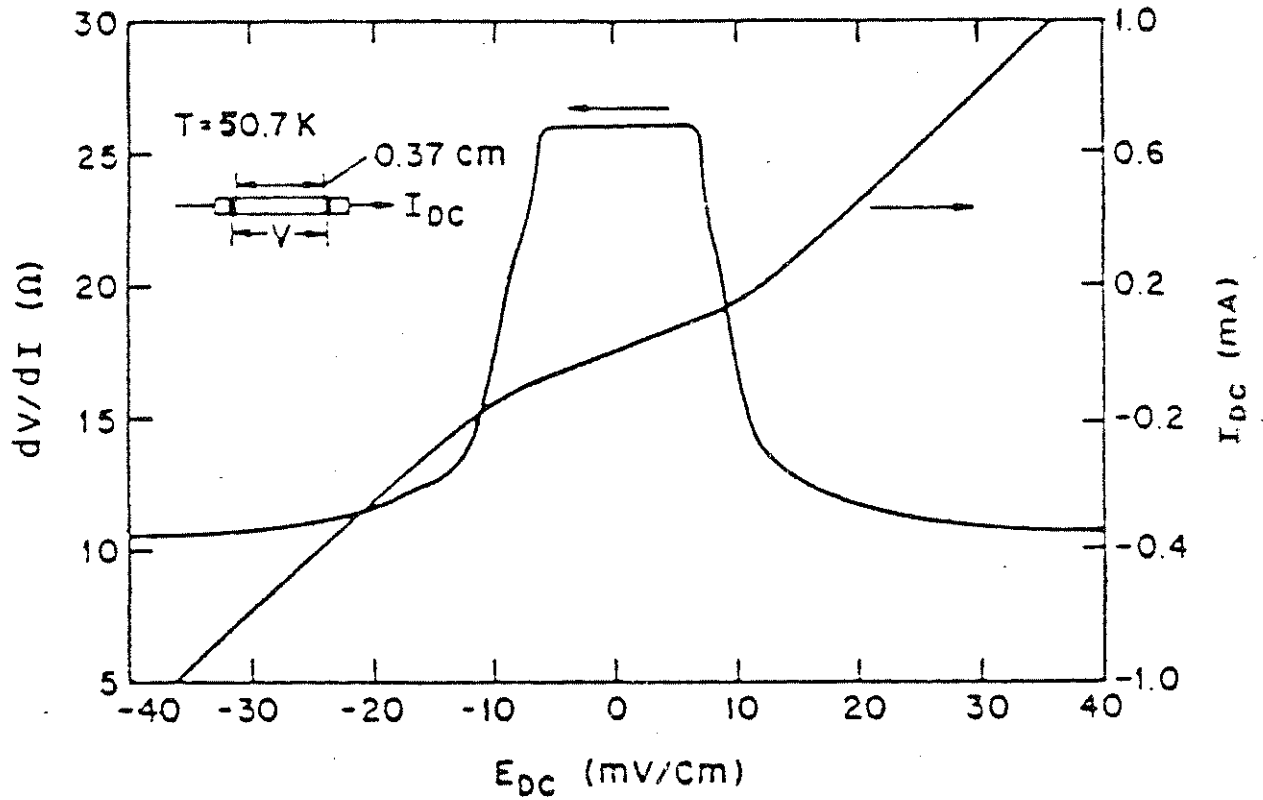
Fig. 2-13) I-V and dV/dI characteristics of NbSe₃ in the lower CDW state. The inset shows the four-probe measurement configuration. From ref. 32.

a sharp threshold field, the dynamic resistance drops as the lower CDW begins to slide.

The nonlinear conductivity of NbSe$_3$ usually may be described by an empirical formula suggested by Fleming:[33]

$$\sigma(E) = \sigma_a + \sigma_b \exp[-E_o/(E-E_T)] . \tag{2.52}$$

The prefactor σ_a is the low-field, ohmic conductivity of NbSe$_3$ and the sum $(\sigma_a + \sigma_b)$ is the high-field conductivity. In the exponent, E is the applied electric field, E_T is the threshold field, and E_o is an adjustable parameter.

Eq. 52 is usually interpreted in terms of a *two-fluid model*. Electrons in a Peierls-distorted metal are either *normal electrons* or belong to the *CDW condensate*. Normal electrons are electrons that are thermally excited above the Peierls gap or that belong to a portion of the Fermi surface which is unaffected by nesting. The CDW condensate are electrons that have energies below the Peierls gap and that belong to the nested portion of the Fermi surface. (In a material such as NbSe$_3$, which has two independent CDWs, electrons are further distinguished as belonging to either the first or second CDW condensate.)

A two-fluid model assumes that normal and CDW electrons act as independent carriers of electrical current; i.e. that in an electric field the drift velocities of the two types of electrons are independent. Assuming that a two-fluid model is appropriate, the first term in Eq. 2.52 is due to normal electrons and the second term is due to the CDW condensate. In other words, a two-fluid model assigns excess current above E_T entirely to the current I_{CDW} carried by

the CDW condensate. Equation 2.52 predicts a smooth increase in CDW velocity as the threshold field for CDW conduction is exceeded.

Threshold fields in NbSe$_3$ are both temperature and sample dependent.[33] The temperature dependence is displayed in Fig. 14, where a dashed line shows the low-field resistance of NbSe$_3$ for reference. In each CDW temperature regime, the minimum threshold field coincides with the peak of the resistivity anomaly. Thresholds fields in the lower CDW regime are much lower than threshold fields in the upper regime, so the threshold field below T_2 may be assigned unambiguously to depinning of the lower CDW.

The sample dependence of threshold fields is due to variations in impurity concentration. In high quality NbSe$_3$ crystals, the most common impurity is Ta, which generally occurs at levels of 200 ppm. Since Ta is isoelectronic with Nb, it should act as a weak impurity. Deliberate doping of NbSe$_3$ with Ta, however, shows that $E_T \sim (n_i)^\alpha$ where n_i is the Ta concentration and α is an exponent between 1 and 2 (Ref. 34). This exponent indicates that Ta's strength as impurity is intermediate between the strong and weak behavior predicted by Lee and Rice.

Conductivity in NbSe$_3$ is not only field dependent, but also frequency dependent. At 9.3 GHz, for example, the resistivity anomalies of NbSe$_3$ are suppressed to the same limiting value reached with high (dc) fields.[13] Frequencies both above and below 9.3 GHz are not as effective in suppressing the resistivity anomalies.[18,35] The frequency dependence of conductivity in NbSe$_3$ provides important information about CDW dynamics. Using a two-fluid
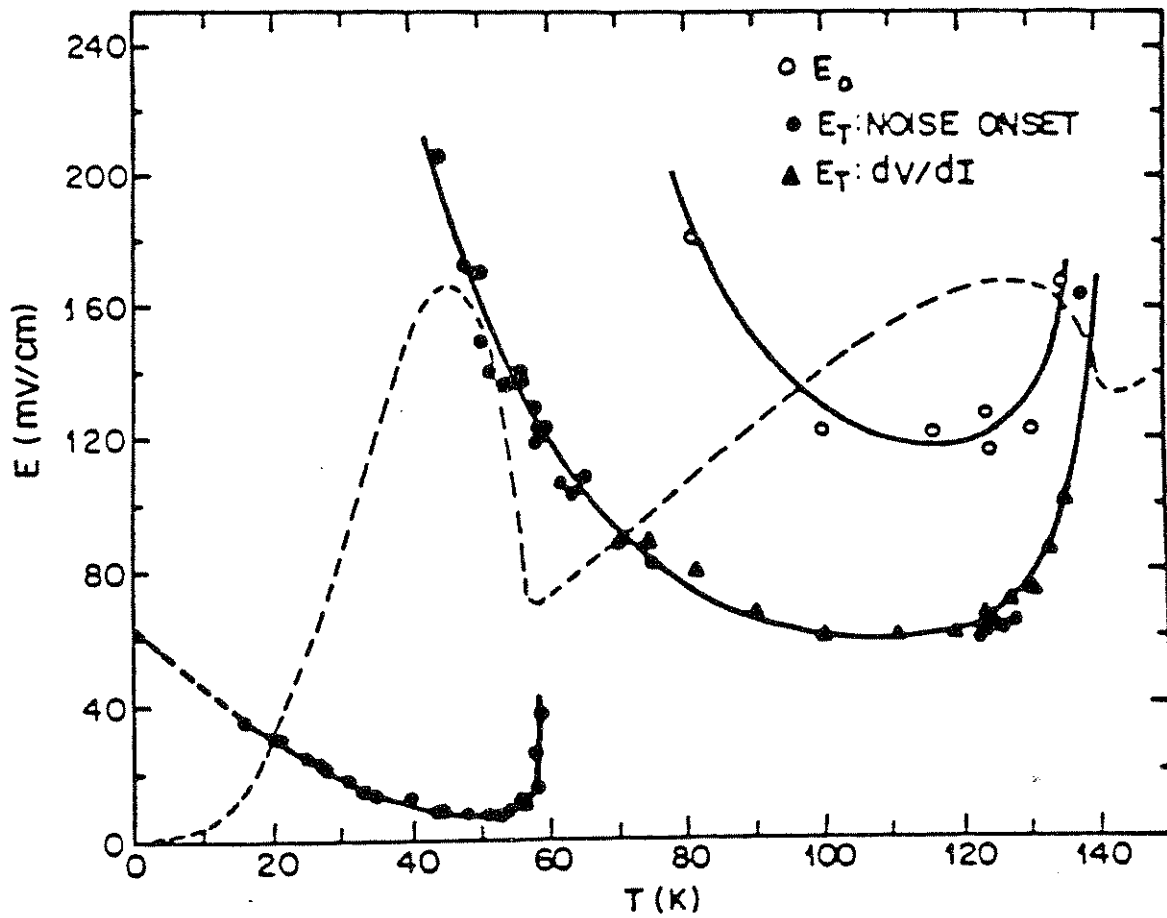
Fig. 2-14)   The temperature dependence of E_T and E_o (see Eq. 2.52). The dashed line shows the low-field resistivity of NbSe$_3$ for reference. From ref. 33.

model, the contribution of the lower CDW to ac conductivity may be found by subtracting the contribution due to normal electronic conduction. The result, σ_{CDW}, may be described by the response of an *overdamped oscillator*:

$$\text{Re } \sigma_{CDW}(\omega) = \frac{ne^2\tau}{m^*}\{1+(\omega_o^2\tau/\omega)^2\}^{-1} \tag{2.53a}$$

$$\text{Im } \sigma_{CDW}(\omega) = \frac{ne^2\tau}{m^*}\{\frac{\omega_o^2\tau}{\omega}\}\{1+(\omega_o^2\tau/\omega)^2\}^{-1} \tag{2.53b}$$

Here Re σ_{CDW} represents the in-phase component of dc conductivity and Im σ_{CDW} the out-of-phase component. The time-constant τ describes CDW dissipation and the frequency ω_o reflects the strength of CDW pinning; the product $\omega_o^2\tau/2\pi$ is typically 100 MHz in NbSe$_3$ (Ref. 35). Both parameters will be discussed in the section on phenomenological models. The important feature of Eqs. 53a and 53b is that CDW inertia is negligible compared to the viscous damping experienced by a CDW. Recently, the conductivity of NbSe$_3$ was measured at extremely high frequencies in the mm-wave range. These measurements permit estimates of the CDW inertia. For the lower CDW, Sridhar et al.[18] estimate that

$$95 \lesssim \frac{m^*}{m_e} \lesssim 117, \tag{2.54}$$

while for the mass of the upper CDW they measure $m^* = 270\, m_e$.

2. Conduction noise and interference effects

When a CDW slides, its velocity is not constant, even if the applied electric field is kept constant. Instead, the CDW velocity consists of a time-independent dc component and a small, oscillating ac component. The

oscillating component is called *narrow-band noise.*[32] Narrow-band noise may be viewed directly on an oscilloscope or may be decomposed into Fourier components using a spectrum analyzer. In high quality NbSe$_3$ crystals, narrow-band noise consists of a single, sharp Fourier fundamental and higher harmonics of the fundamental. The fundamental frequency of narrow-band noise depends on the electric field applied across a sample. Monceau *et al.*[36] found that the frequency of a narrow-band noise fundamental is proportional to the excess current I_{CDW} carried by a CDW. In most samples, the frequency of the narrow-band noise fundamental begins at zero and increases linearly as I_{CDW} increases.

A second type of conduction noise associated with CDW sliding is *broad-band noise.*[32] As its name implies, broad-band noise possesses a wide distribution of Fourier components. A power spectrum of broad-band noise shows that its frequency components fall off as $\omega^{-0.8}$ (Ref. 37). At frequencies above 1 MHz, broad-band noise is at least 10 times smaller than narrow-band noise in a typical sample.

If an ac electric field is applied to NbSe$_3$ in addition to a dc field, interference may occur between the extrinsic ac signal and the intrinsic narrow-band noise. The effects of such interference are observed in a variety of measurements.[35] Fig. 15 shows the ac conductivity of NbSe$_3$ when a dc field larger than threshold is simultaneously applied. In this kind of experiment, the ac electric field E_{ac} is small compared to both the dc electric field E_{dc} and the threshold field E_T. The biased ac conductivity is generally similar in shape to
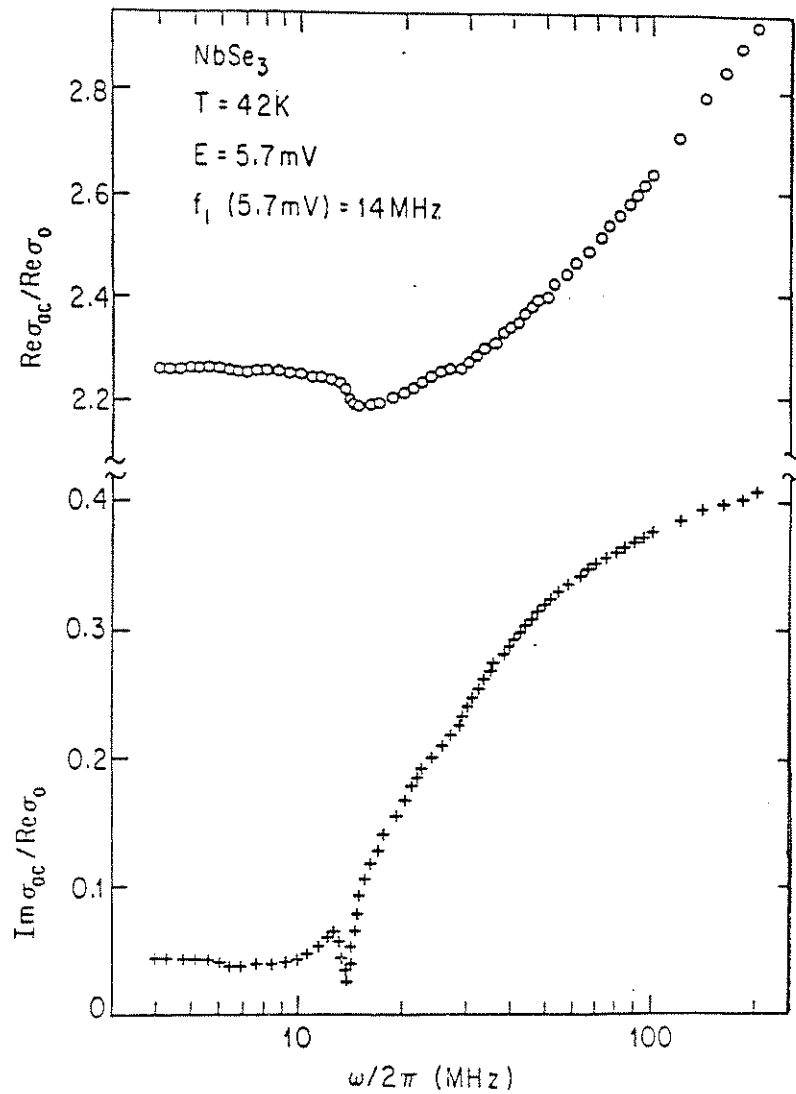
Fig. 2-15)   The ac conductivity of NbSe$_3$ when the lower CDW is depinned. The conductivity has been normalized to the low-field conductivity σ_o. Resonances occur at 14 and 28 MHz, when the applied ac frequency matches the first or second harmonic, respectively, of the narrowband noise frequency f_1. From ref. 35.

the unbiased conductivity. One rather trivial difference between the conductivities is that Re $\sigma(\omega)$ is offset from zero for the biased measurement, which is due to the reduced dc dynamic resistance of a CDW past threshold. A more important difference between the biased and unbiased conductivities is the presence of sharp, inductive dips in the both the real and imaginary components of the biased ac conductivity curves. In Fig. 15, prominent dips occur at 14, 28 and 42 MHz, frequencies which exactly match the narrow-band noise fundamental and its higher harmonics. Inductive dips in ac conductivity measurements are one example of *ac-dc interference.*

A second type of ac-dc interference may be observed in dc I-V curves, Fig. 16a. In this type of measurement, the frequency of the ac signal is fixed and the dc bias is varied. The amplitude of the ac signal is no longer small, but is now comparable to the dc and threshold fields. The curves in Fig. 16a are parametrized by the amplitude of the applied ac signal, whose frequency is 100 MHz. When the applied ac signal is zero, as in the top trace, a normal I-V curve is measured. (To compare this I-V curve with Fig. 13, note that the horizontal and vertical axes are interchanged between the figures. In Fig. 16a, the sample was current-biased and its voltage response was measured.) When the amplitude of the applied ac signal is nonzero, a regular series of steps appear in the IV traces. These steps are called *Shapiro steps,* in analogy with a similar phenomenon in superconductivity. Steps are numbered $n = 1, 2, 3, ...$ according to the figure. The height of a Shapiro step, shown schematically in the inset, depends on both the frequency and magnitude of the ac signal.
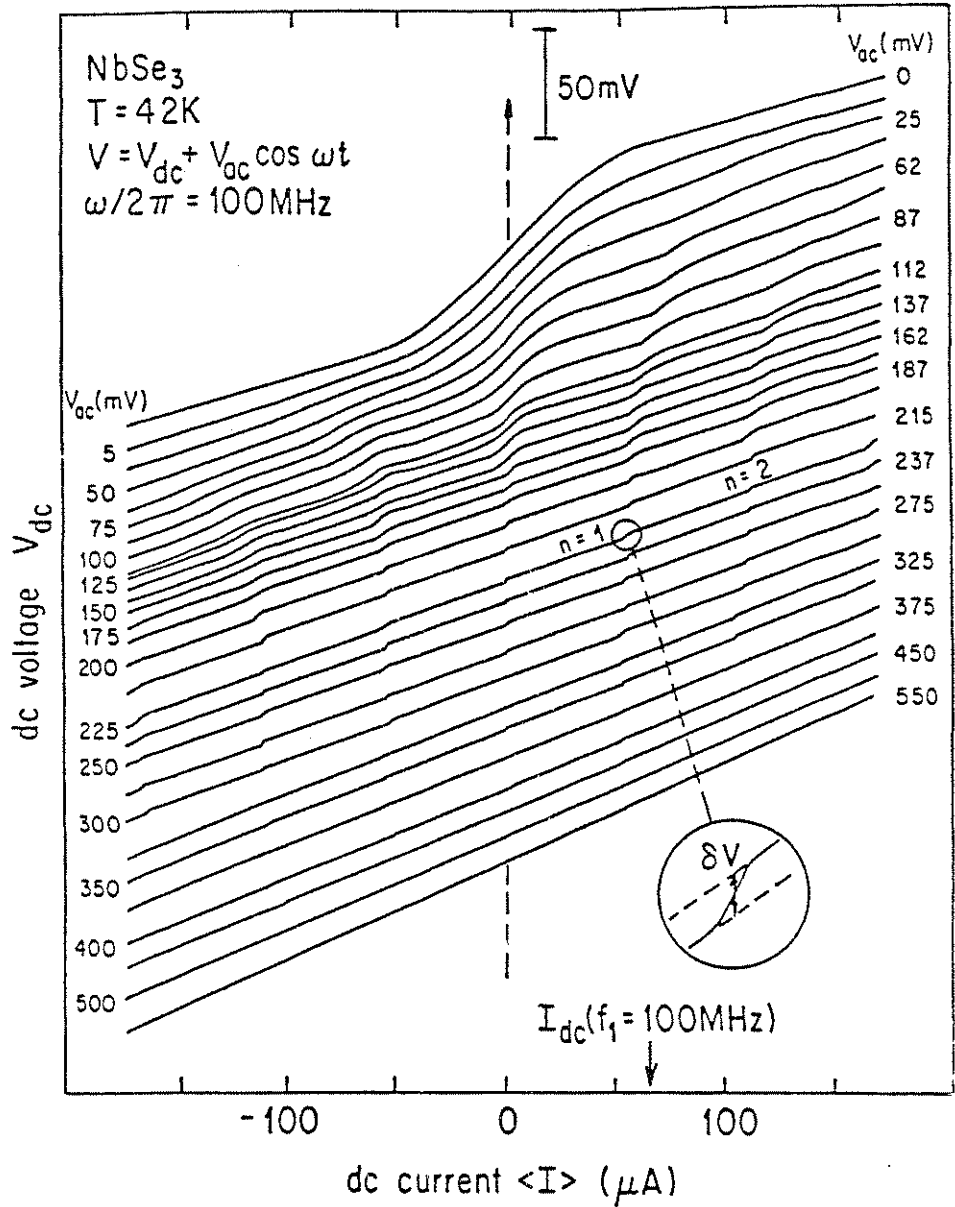
Fig. 2-16.a)   I-V characteristics of NbSe$_3$ in the presence of a 100 MHz ac signal. The curves are parametrized by the amplitude V_1 of the ac signal. As V_1 increases, Shapiro steps are observed when the narrowband noise frequency matches the first ($n = 1$) or second ($n = 2$) harmonic of the ac frequency. From ref. 35.
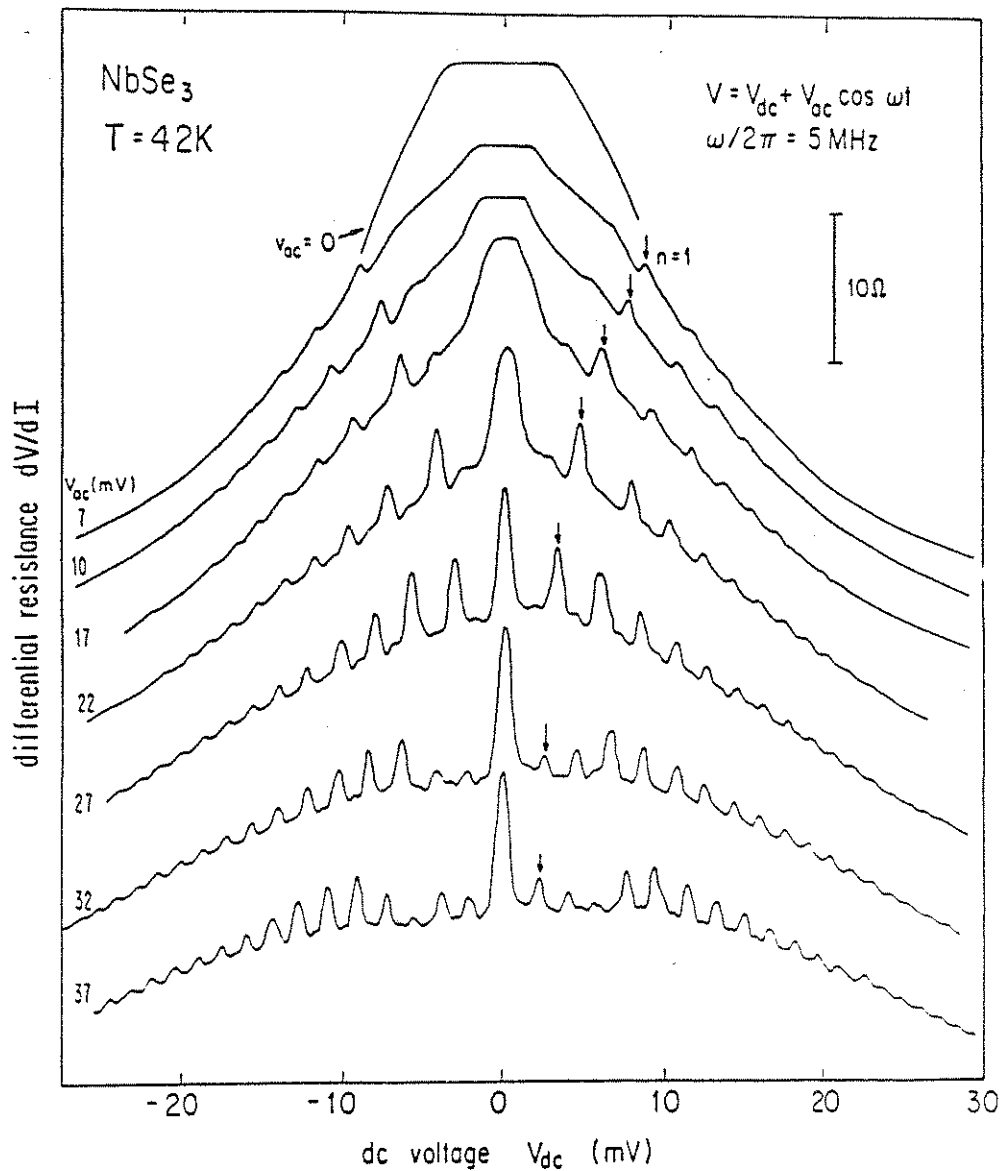
Fig. 2-16.b)   dV/dI characteristics of NbSe₃ in the presence of a 5 MHz ac signal. Peaks in the dV/dI curves correspond to Shapiro steps in I-V curves. Because of the sensitivity of the dV/dI technique, both subharmonic ($n = \frac{1}{2}, \frac{3}{2}, \frac{5}{2}, ...$) and high-order harmonic ($n > 10$) steps are evident in the data. From ref. 35.

For low ac frequencies, Shapiro steps are small and difficult to resolve directly on an I-V curve. A dV/dI measurement allows more sensitive detection of the steps. Fig. 16b shows a series of dV/dI curves when the ac frequency is 5 MHz. On a dV/dI curve, a Shapiro step appears as a peak; when current-driven, the area underneath a peak equals the height of the corresponding step. In addition to the peaks due the main harmonic steps, close examination of the dV/dI curves reveals small, smeared peaks which occur midway between the main peaks. These *subharmonic* peaks are labelled $n = 1/2, 3/2, 5/2, ...$ in later plots.

3. Switching and hysteresis

In some $NbSe_3$ crystals, the velocity of the lower CDW does *not* increase smoothly as a crystal's threshold field is exceeded. In these anomalous crystals, the excess current carried by a CDW jumps abruptly from zero to a large value. This phenomenon is known as *switching*.[38] Switching may be observed directly in I-V curves, Fig. 17. In this figure, the (current-driven) I-V curve becomes smoothly nonlinear in the usual way at 42 K. As the sample's temperature is lowered to 37.5K, a region of *negative differential resistance* develops at threshold. This region sharpens into an abrupt switch at 34K. At lower temperatures, the CDW no longer repins at the same bias at which it depins. This *hysteresis* is quite prominent by 26.5K.

At threshold, the switch from the ohmic to the nonohmic state is not instantaneous, but occurs after a short delay.[38] The time-dependent response of a crystal during a switch is shown in Fig. 18a. At time $t = 0$, a 200 μsec pulse of
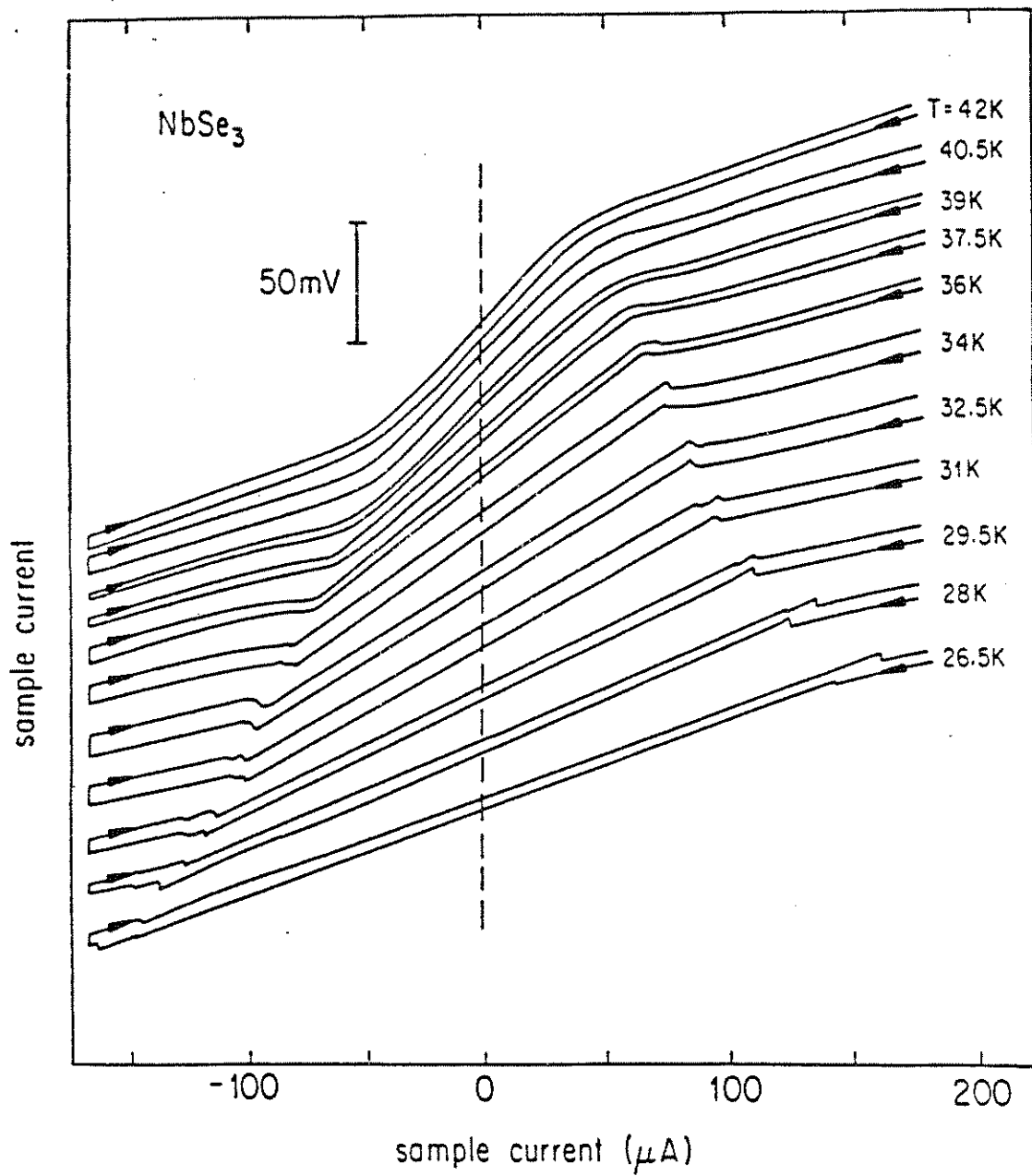
Fig. 2-17)   I-V characteristics of a switching NbSe₃ crystal. Arrows indicate the direction of the bias sweep. From ref. 21.
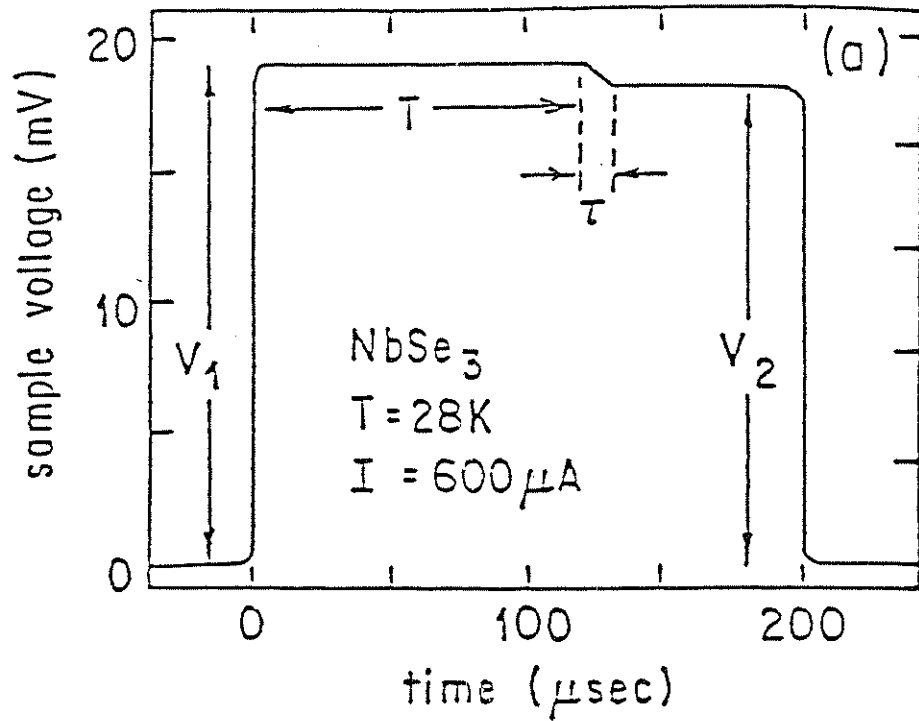
Fig. 2-18.a)   The response of a switching crystal to an applied current pulse. For current pulses above threshold, the voltage response switches from V_1 to V_2 after a delay time T. The response requires a transition time τ for completion. From ref. 38.
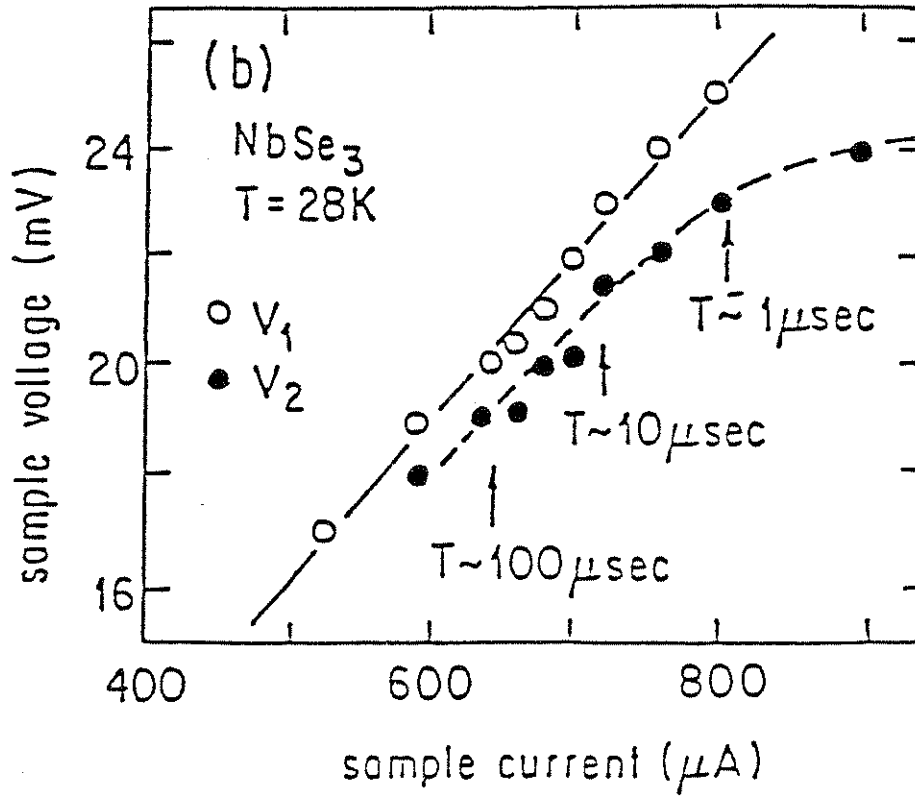
Fig. 2-18.b)   The ohmic (V_1) and switching (V_2) responses of Fig. 18a as a function of pulse amplitude I. The threshold for the onset of switching is $I_T \cong 600\ \mu A$. Also shown is the time T that switching lags the application of a pulse. From ref. 38.

current is applied to the crystal. If the pulse height is less than the crystal's threshold current, then the voltage response of the crystal is rectangular. If the current pulse height is larger than I_T, however, then the voltage response of the crystal jumps downward from an ohmic voltage V_1 to a non-ohmic voltage V_2. The switch from V_1 to V_2 occurs after a time delay T and requires a transition time τ for completion. The delay time T depends on how much the bias pulse exceeds threshold. Fig. 18b schematically displays the average delay time T as a function of $(I - I_T)$. When $(I - I_T)$ is small, the ohmic and non-ohmic states dissipate about the same amount of power, so the energy difference between the states is small and the switch between the states is delayed a relatively long time, $T = 100\,\mu\text{sec}$. When $(I - I_T)$ is large, the energy difference between the states is large and the switch is delayed a short time, $T = 1\,\mu\text{sec}$. The delay times displayed in Fig. 18b represent average values. For any given value of the pulse height I, there is considerable scatter about the mean. As I increases above I_T, not only does the average delay time decrease, but also the scatter in delay times decreases. Data are fit reasonably well by Lorentzian line shapes.

D. Phenomenological models of sliding charge-density waves

There is a myriad of phenomenological models that attempt to describe CDW dynamics. Each model correctly describes at least one aspect of CDW sliding, but no model has successfully described all aspects. This section will discuss some of the dynamical models that apply directly to the thesis results. These models fall into three groups. The first group consists of classical, phase-only models that neglect the dynamics of the CDW amplitude and treat the

amplitude models that treat the CDW amplitude, as well as the phase, as a dynamical variable. The last group consists of CDW switching models. Only models in the first two groups will be described here, because CDW switching models are discussed at length in Chap. 3.

1. Classical models of phase dynamics

As mentioned earlier, pinning destroys the translational invariance of the CDW phase. If pinning is not severe, however, then the CDW amplitude is not affected, even when an electric field is applied to the CDW. This is shown in the energy surface of Fig. 11a, where pinning destroys the azimuthal symmetry of $E_{Peierls}$, but does not change its radial dependence. When an electric field is applied to such a CDW, the amplitude of its order-parameter remains constant while its phase revolves around the brim of the tilted energy surface. This is the starting point for phase-only models of CDW dynamics, in which the amplitude is kept fixed and only the phase is allowed to vary.

The condition on CDW pinning can be made more quantitative by requiring that any change δu in the CDW amplitude be much smaller than the CDW amplitude u itself. From Eq. 37, the energy δE required to change the amplitude by δu is given by $\delta E = \frac{1}{2} n(0) G^2 (\delta u)^2$. Setting this energy equal to the pinning energy $\rho_0 V_I$ in Eq. 42, the condition on pinning becomes $\rho_0 V_I \ll \frac{1}{2} n(0) \Delta_0^2$; i.e., the pinning energy must be much smaller than the CDW condensation energy. In terms of Fig. 11a, the requirement is that the
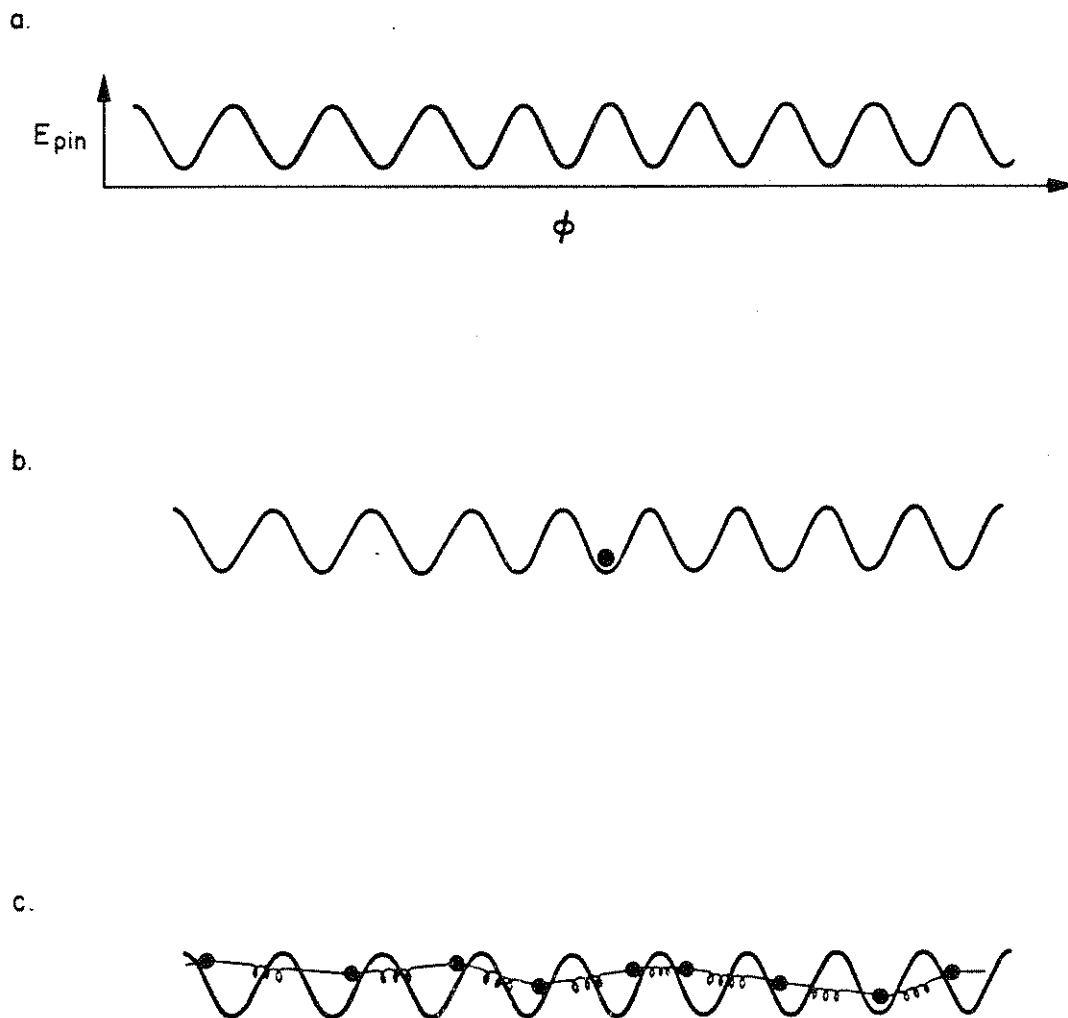
a.

b.

c.

Fig. 2-19)   Phase-only models of CDW dynamics. (a) Pinning energy versus
CDW phase. (b) The rigid-phase approximation, in which the
CDW phase is treated as a single domain. (c) The deformable-
phase approximation, in which the phase is treated as a collection
of domains.

azimuthal curvature be much smaller than the radial curvature in the brim of the energy surface. When this condition is met, the potential energy of a Fukuyama-Lee-Rice domain is (to first approximation) a sinusoidal function of just its phase ϕ, as shown in Fig. 19a.

Classical, phase-only models of CDW dynamics are built directly on the ideas introduced so far. From Eq. 40, the kinetic energy of the phase is written as $\frac{1}{2} m^* \dot{\phi}^2$; from Eq. 49, the coupling to an applied electric field is written as $E\phi$; and from the above discussion, the interaction with pinning centers is written as a term periodic in ϕ. In order to reproduce the conductivity limits observed in CDW transport, a phenomenological dissipation term is introduced in which CDW damping is proportional to $\dot{\phi}$. Finally, the elasticity of the phase itself must be described. There are two ways to do this. As shown schematically in Fig. 11, the CDW phase is fairly rigid within a Fukuyama-Lee-Rice domain. Therefore one approach is to treat the phase within an entire crystal as though it formed a single, rigid domain (Fig. 19b). The second approach is to treat the phase as though it comprised a deformable array of domains, with each domain in the crystal elastically connected to its neighbors (Fig. 19c). Because of its relative simplicity, the rigid model is considered first.

a. Rigid classical model

In the rigid classical model of Grüner, Zawadowski and Chaikin,[39] the equation of motion for a CDW is

$$\frac{d^2\phi}{dt^2} + \frac{1}{\tau}\frac{d\phi}{dt} + \omega_o^2 \sin\phi = \frac{e}{m^*}EQ \ , \qquad (2.55)$$

where τ is a time-constant describing dissipation, ω_o is a pinning frequency representing the strength of the impurity potential, m^* is the Frolich mass of the CDW electrons and E is the applied electric field. Another useful form of Eq. 55 is

$$\beta \frac{d^2\phi}{dt^2} + \frac{d\phi}{dt} + \sin\phi = e' , \qquad (2.56)$$

where $\beta = (\omega_o \tau)^2$ and $e' = E/E_T$ with $E_T = m^*\omega_o^2/eQ$. (Henceforth, the prime will be dropped from the normalized electric field.) The constants β and E_T are respectively known as the *inertial parameter* and the *threshold field* of the rigid classical equation. In Eq. 56, time is measured in units of $(\omega_0^2)^{-1}$, where the product $\omega_o^2\tau$ is known as the *cross-over frequency*.

Eqs. 55 and 56 have a very intuitive interpretation, Fig. 19b. In the rigid classical model, a CDW is dynamically equivalent to a point particle moving over a sinusoidal potential, such as a marble rolling on a laundry washboard. Applying an electric field to the CDW is like tilting the washboard underneath the marble. When the washboard is tilted a small amount, the washboard corrugation prevents the marble from rolling, but when the washboard is tilted a lot, the marble starts to roll in a bumpy manner over the washboard's peaks and valleys. Similarly, small electric fields (less than E_T) do not depin a CDW, but large electric fields (greater than E_T) do. Just like the rolling marble, a sliding CDW also moves in a bumpy manner. The bumpy motion leads to a CDW current composed of two components: a time-independent dc current and an oscillatory ac current, where the frequency of the ac current is exactly proportional to the dc current. Thus the rigid classical equation not only

predicts the existence of a threshold field E_T for the onset of CDW sliding, it also predicts the presence of narrowband noise in the current carried by a sliding CDW.

Besides narrowband noise and threshold fields, the rigid classical equation qualitatively models a variety of other CDW phenomena. For example:

1) CDW conductivity in the classical model is bounded by well-defined limits for electric fields of large amplitude or high frequency. These high-field and high-frequency limits are equal, just as they are in real CDW materials.

2) The ac conductivity of the classical equation is easily calculated, for pinned CDWs, and leads to overdamped behavior, as in Eqs. 2.53, in the limit that $\omega_o \tau \ll 1$. For this reason, the inertial terms are usually dropped from Eqs. 55 and 56, and the rigid classical equation simplifies to:

$$\dot{\phi} = e - \sin\phi . \qquad (2.57)$$

3) The rigid classical equation also predicts the occurrence of Shapiro steps when large ac as well as dc fields are applied to a CDW. The height δI of the nth (voltage-driven) Shapiro step is given by

$$\delta I = 2 \, | J_n(e_{ac}/\Omega) | , \qquad (2.58)$$

where Ω is the normalized ac frequency, e_{ac} is the normalized ac amplitude, and $J_n(x)$ is the Bessel function of order n. With one modification, the Shapiro steps that are observed in NbSe$_3$ display

modification, the Shapiro steps that are observed in $NbSe_3$ display an oscillatory dependence on ac frequency and amplitude which is well described by Eq. 58. The modification is that the maximum height of a (current-driven) Shapiro step is reduced by an empirical factor α_s:

$$\delta V = 2 \ \alpha_s \ |J_n(i_{ac}/\Omega)| \ . \tag{2.59}$$

Here i_{ac} is the normalized ac bias current, I_{ac}/I_T.

Despite these successes, the rigid classical model does not accurately reproduce all aspects of CDW motion. One failure of the model is its prediction for sliding ac conductivity, as will be discussed in Chap. 4. A second, closely related failure is its prediction for CDW velocity near threshold. The rigid classical model predicts the CDW velocity to scale as $(E-E_T)^{\frac{1}{2}}$, whereas experiments show that the velocity scales as $(E-E_T)^{\nu}$ with $\nu > 1$. Both of the failures can be traced to the assumption of a rigid CDW phase. The next section discusses deformable-phase models that avoid this assumption.

b. Deformable-phase models

In the sliding regime, the phase elasticity of a CDW plays an important role in its dynamics. Phase elasticity may be included in CDW dynamics by using the Fukuyama-Lee-Rice Hamiltonian.[40-42] Since CDW dynamics are overdamped, the kinetic energy of a CDW may be neglected. The energy density becomes:

(In Eq. 60, the sign of the impurity pinning energy is trivially redefined so that Eq. 64 resembles the rigid classical model.) Motion of the CDW phase is described by relaxational dynamics:

$$\frac{d\phi(x)}{dt} = -\frac{2k_F\tau}{m^*}\left\{\frac{\delta H}{\delta\phi}\right\} \qquad (2.61)$$

$$= \frac{2k_F\tau}{m^*}\left\{-K\left(\frac{d^2\phi}{dx^2}\right) - \frac{\rho_{eff}neE}{(2k_F)} + \rho_o V_I \sum_j \delta(x-x_j)\sin(2k_F x + \phi)\right\}$$

Equation 61 is an extremely nonlinear partial-differential equation. To obtain numerical solutions, a discretized equation may be obtained by ignoring phase variations on length-scales shorter than the average impurity spacing. This approximation allows the damping term, $d\phi/dt$, to be evaluated only at impurity pinning sites. The rest of Eq. (2.61) may be integrated exactly between impurity sites. The result is

$$\frac{d\phi_j}{dt} = -\frac{2k_F\tau}{m^*}\sum_j\left\{K\left[\frac{(\phi_{j+1}-\phi_j)}{x_{j+1}-x_j} - \frac{(\phi_j-\phi_{j-1})}{x_j-x_{j-1}}\right]\right.$$
$$\left. -\frac{1}{2}\frac{\rho_{eff}neE}{2K_F}[x_{jH}-x_{j-1}] + \rho_o V_I \sin(\beta_j+\phi_j)\right\} , \qquad (2.62)$$

where $\phi_j = \phi(x_j)$ and $\beta_j = 2k_F x_j$. The distances $(x_{j+1}-x_j)$ and (x_j-x_{j-1}) are randomly distributed, but numerical simulations show that an adequate approximation is to set these distances equal to their mean value $(n_i)^{-1}$, where n_i is the impurity concentration. The phases β_j, however, are usually kept random. Just as with the rigid classical model, a characteristic time may be defined from the impurity interaction and the damping coefficient τ. A threshold field cannot be analytically determined, but a characteristic field strength is defined by the impurity strength and concentration. A natural scale

threshold field cannot be analytically determined, but a characteristic field strength is defined by the impurity strength and concentration. A natural scale of parameters is the following:

$$
\begin{aligned}
\text{length:} \quad & x_o = (n_i)^{-1} \\
\text{energy:} \quad & V_I \rho_o \\
\text{time:} \quad & t_o = m^* / 2 k_F V_I \rho_o \tau \\
\text{electric field:} \quad & E_o = 2 k_F n_i V_I \rho_o / \rho_{eff} n e
\end{aligned}
$$

$$(2.63)$$

In these units, the CDW phase electricity is $\alpha = K n_i / V_I \rho_o$. Note that $\alpha = 2/\epsilon$, where ϵ is the Fukuyama-Lee pinning parameter from Eq. 43. The final normalized version of Eq. 62 has a particularly simple form:

$$
\dot{\phi}_j = e - \sin(\beta_j + \phi_j) - \alpha(2\phi_j - \phi_{j+1} - \phi_{j-1}). \tag{2.64}
$$

Here $e = E / E_o$.

Eq. 64 is an almost infinite set of coupled, first-order differential equations, one equation for each impurity site x_j in a crystal. Although nontrivial to solve, Eq. 64 also has a simple interpretation, Fig. 19c. Instead of a single particle on a washboard, as in the rigid classical model, Eq. 64 describes many coupled particles on a washboard. Each particle represents the CDW's phase at a particular impurity site, and the particles are coupled together by springs of force constant α. Because of the random phases β_j, all the particles do not sit simultaneously in their respective washboard minima.

is about 20, and the phase elasticity dominates impurity pinning. However, by coarse-grain averaging the effect of many impurities, Eq. 64 may be scaled in order to study CDW dynamics on length-scales comparable to the Fukuyama-Lee-Rice length. In the scaled equation, $\alpha \sim 0.2$ and each scaled phase ϕ_j corresponds to the average phase within a Fukuyama-Lee-Rice domain. The scaled phases β_j represent the optimal domain phases $\pi - \phi_0$ calculated in Eq. 45. In some cases, Eq. 64 may be simplified further by assuming that the phases β_j are not random, but are merely incommensurate with the impurity washboard potential. (If the periodicity of the β_j is commensurate, Eq. 64 is essentially equivalent to the rigid classical equation.) L. Sneddon[42] uses this *incommensurate chain* approximation to calculate ac conductivity above threshold. Sneddon's result is discussed further in Chap. 4.

2. Models that include amplitude dynamics

Phase models may be adequate to describe CDW sliding in the bulk of a crystal, but they are inadequate to describe CDW motion near the ends of a crystal, where a moving CDW collides with a stationary CDW. This is shown in Fig. 20, which sketches the electronic and ionic components of a sliding CDW at the end of a one-dimensional crystal. The interface region (hatched symbols) between the sliding and pinned segments of the CDW represents a discontinuity in the CDW phase velocity, and hence the CDW amplitude must periodically
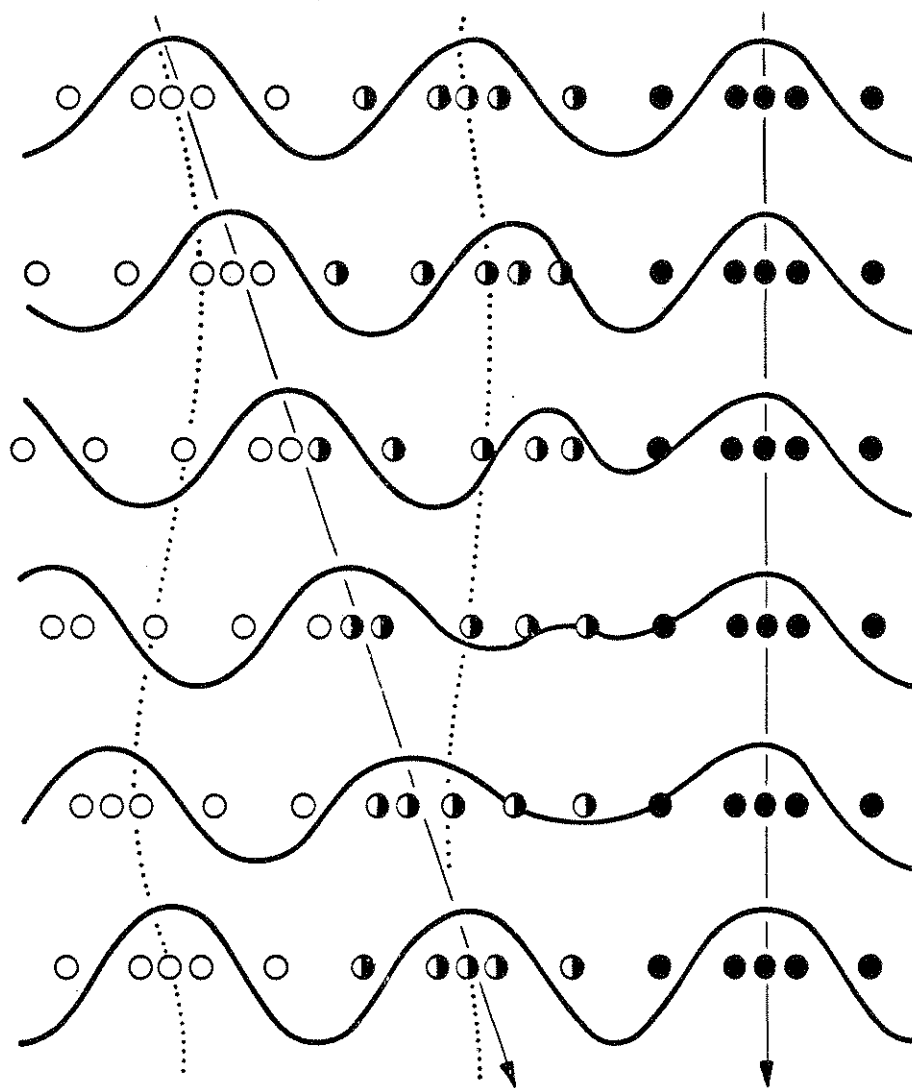
Fig. 2-20) The motion of electronic and ionic charge density phase slippage.
Solid lines represent electronic charge and circles represent lattice
ions. As time advances from the top to the bottom of the figure, a
moving CDW (open symbols) collides with a pinned CDW (filled
symbols). The CDW phase slips by 2π in the interface region
(half-filled symbols).

collapse there (see Chap. 1). For this reason, any model of CDW dynamics must treat both the CDW amplitude and phase as dynamical variables at the end of a crystal. Two models have been proposed. The first model, by Ong and Maki,[43] is a qualitative description appropriate to three-dimensional crystals; whereas the second model, by Gorkov,[44] is a quantitative theory appropriate to one-dimensional crystals. The model of Ong and Maki is considered first.

a. Phase vortices

Ong and Maki point out that in a three-dimensional crystal, the CDW amplitude should collapse at a velocity discontinuity via the generation of *phase vortices*. A phase vortex is a topological singularity in the CDW order-parameter which consists of an inner core and an outer whorl. In the core of the vortex, the CDW amplitude is zero and the CDW phase is indeterminate. The core is essentially a one-dimensional filament that extends across the width of a crystal with a diameter equal to the coherence length ξ of the CDW amplitude. In the whorl of the vortex, the amplitude is nonzero and the phase is described by

$$\phi(x,y) = \arctan(y/x) , \qquad (2.65)$$

where the z-axis is chosen parallel to the vortex core.

The function (2.65) resembles an Escher staircase, Fig. 21. Starting at any point in vortex whorl, the CDW phase increases as the vortex core is circumnavigated. After a complete circuit around the core, the phase has increased by 2π from its starting value. But because 2π changes of phase are not significant in this context, the phase has actually returned to its starting

(For page sequence only.)

Fig. 2-21)   Detail of the lithograph *Ascending and Descending* by M. C.
             Escher (1960). The staircase in the figure is a way of visualizing
             the phase of a CDW at a phase vortex, Eq. 2.65. From ref. 45.
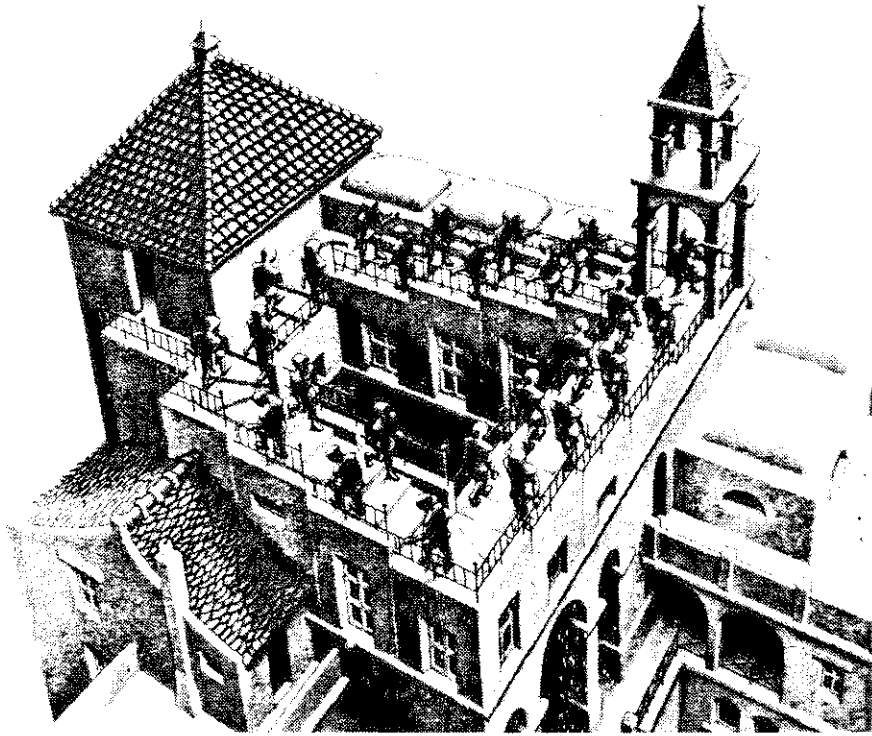
Fig. 2-21

value. The only point where the phase is ever discontinuous is at the vortex core itself.

The essential feature of a vortex is that it can act as an "eraser" of CDW phase. Figure 22a shows the geometry considered by Ong and Maki. In region I of a crystal ($x > 0$), an electric field forces a CDW to slide toward a current-extraction contact. In region II of the crystal underneath the contact ($x < 0$), the electric field is zero and the CDW is stationary. Vortices form as the electric field pushes phase fronts toward the sliding-stationary interface ($x = 0$), and they act as the terminating edges of the fronts, Fig. 22b. The arrival of a phase front produces a 2π phase difference across the interface, but the passage of a vortex removes the difference. In the geometry of Fig. 22, vortices move parallel to the interface, in the y direction, toward the current contact. Each vortex vanishes when it reaches the contact, eliminating 2π of the accumulated phase.

Phase vortices occur in three-dimensional crystals because they are the most efficient means of removing excess phase. In a three-dimensional crystal, the interface between the sliding and stationary segments of a CDW is a two-dimensional sheet. If the CDW amplitude were to collapse across the entire sheet, the energy cost would be $\frac{1}{2}n(0)\Delta_0^2 L_z L_y \xi_\parallel$, where L_z and L_y are the transverse dimensions of the crystal. But when vortices occur, the amplitude collapses only along the cores, with an energy cost of $\frac{1}{2}n(0)\Delta_0^2 L_z \xi_\perp \xi_\parallel$. An additional energy penalty is the energy cost of stretching the CDW phase around a vortex core. This cost is given by
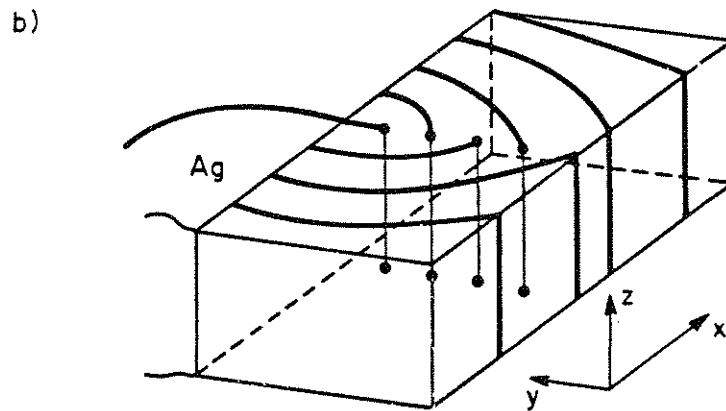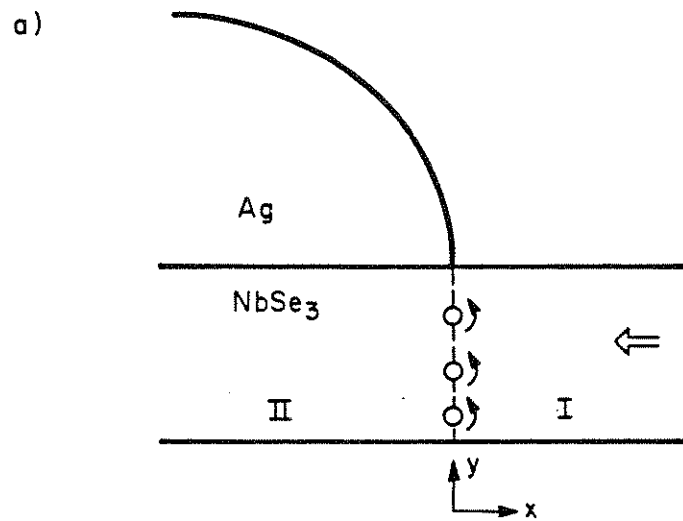
Fig. 2-22) A cross-section (a) and a three-dimensional view (b) of a silver paint contact on NbSe$_3$. Volumes I and II represent bulk and shunted regions of the NbSe$_3$ crystal, respectively. Circles (a) and thin lines (b) represent phase vortices. From ref. 43.

$$\frac{K}{2}\int dxdy(\nabla\phi)^2 = \pi n(0)\Delta_o^2\xi_{\parallel}\xi_{\perp}\ln(L_o/\xi_{\parallel}) ,$$

so that the total energy cost of vortex formation is

$$E_{Vortex} = \frac{1}{2}n(0)\Delta_0^2 L_z\xi_{\parallel}\xi_{\perp}(1 + 2\pi\ln(L_o/\xi_{\parallel})) . \qquad (2.66)$$

Compared to the cost of complete amplitude collapse, the cost of vortex formation is smaller by a factor of $(\xi_{\perp}/L_y)(1 + 2\pi\ln(L_o/\xi_{\parallel}))$. Typical numbers are $\xi_{\parallel} \sim 10^{-9}$m and $L_o \sim 10^{-6} - 10^{-4}$m, so vortex formation is favored to occur in crystals forty to seventy times wider than $\xi_{\perp}$. Since $\xi_{\perp}$ is about 10^{-10}m, whereas typical crystal diameters are 10^4 times larger, this means that vortex formation should occur in practically all crystals. Thus, CDW dynamics are quite complex in a three-dimensional crystal, because the ends of the crystal generate a turbulent interaction of the CDW phase and amplitude.

b. Ginzburg-Landau equation

The model of Ong and Maki is extremely important as a conceptual description of CDW motion, but it does not provide a dynamical description of the CDW phase and amplitude. Independently of Ong and Maki, Gorkov proposed a complementary description of CDW motion, in which he derived a set of Ginzburg-Landau equations for the phase and amplitude, and then studied the dynamics of the equations in one dimension. Gorkov's normalized equations for the phase and amplitude are

$$\dot{\Delta} = [1-(d\phi/dx)^2 - \Delta^2]\Delta + d^2\Delta/dx^2 \qquad (2.67a)$$

$$\Delta^2\dot{\phi} = - E\Delta^2 + \frac{d}{dx}\left[\Delta^2\frac{d\phi}{dx}\right] \qquad (2.67b)$$

$$\dot{\Delta} = [1-(d\phi/dx)^2 - \Delta^2]\Delta + d^2\Delta/dx^2 \qquad (2.67\text{a})$$

$$\Delta^2\dot{\phi} = -E\Delta^2 + \frac{d}{dx}\left[\Delta^2\frac{d\phi}{dx}\right] \qquad (2.67\text{b})$$

Alternatively, when the amplitude and phase are combined into a single complex order parameter $\psi = \Delta e^{i\phi}$, the equations reduce to

$$\dot{\psi} = \psi - |\psi|^2\psi + \frac{d^2}{dx^2}\psi - iE\psi \qquad (2.68).$$

In these equations, the normalized CDW current is given by $j = -\Delta^2\dot{\phi}$. The dynamics of the phase and amplitude are not determined until appropriate boundary conditions are specified. Gorkov's choice was to fix both the phase and amplitude at the ends of a crystal, $\phi = 0$ and $\Delta = 1$.

The dynamics of Gorkov's equations are generally consistent with the description of phase-slippage presented in Chap. 1. In the absence of an electric field, the CDW phase and amplitude are uniform throughout a crystal. When an electric field is applied to the crystal, the phase becomes distorted. The largest phase distortion occurs at the center of the crystal, but the largest phase gradients occur a few coherence lengthes away from the ends of the crystal. The largest distortions of the amplitude also occur at the crystal ends, because of the $(d\phi/dx)^2$ term in Eq. 67b. When a sufficiently large field E_T is applied, the amplitude is suppressed completely at these points. For fields larger than E_T, the CDW begins to slide and the amplitude begins to oscillate. The CDW motion is periodic, and during most of a CDW cycle, the amplitude remains close to its undistorted value. Amplitude collapse and subsequent regeneration occur very quickly, on a time-scale that is fast compared to the CDW period.

at threshold. However, the nonswitching behavior is probably the result of Gorkov's boundary conditions, which preclude bistability in the CDW amplitude. With another choice of boundary conditions, for example $d\Delta/dx = 0$, the CDW amplitude could be suppressed by strong phase polarization, and therefore Eqs. 67 and 68 should display switching and hysteresis.

Despite the possibility of switching and hysteresis in Gorkov's equations, the equations are not a useful starting point for understanding the results of this thesis. The equations have two disadvantages. First, the equations do not include the effect of pinning on CDW dynamics, and the results of this thesis show that strong pinning plays an important role in switching crystals. Second, the equations do not reproduce the dispersion relations of Lee, Rice, and Anderson, which serve as the basis of nonswitching models of CDW dynamics. Therefore the equations cannot be used to compare the dynamics of switching and nonswitching CDWs. For these reasons, another set of equations is derived in Chap. 6 to describe the coupled dynamics of the CDW amplitude and phase.

CHAPTER 3: DC CHARACTERISTICS

CHAPTER 3: DC CHARACTERISTICS

This chapter discusses the response of switching crystals of pure and iron-doped $NbSe_3$ to applied dc fields. Experimental methods include measurement of I-V and dV/dI characteristics, narrowband noise spectra, and the spatial distribution of CDW currents. The chapter and results are organized as follows. Section I, on materials and methods, discusses factors that influence the occurrence of switching in $NbSe_3$ crystals. Section II reports measurements of dc CDW conductivity. The measurements fall into three groups: characterization of dc properties, study of their temperature dependence, and examination of their spatial uniformity within single switching crystals. Section III discusses the implications of the experimental results and then analyzes the results in terms of several models. Section IV, the conclusion, summarizes the results of the chapter.

I. Materials and Methods

Samples used in the experiments consisted of single crystals of nominally pure and iron-doped $NbSe_3$, prepared by conventional vapor-transport methods.[1] The amount of iron incorporated into the Fe_xNbSe_3 crystals ($x = 0.03$ by starting materials) was much less than the nominal doping, below the approximately 1% sensitivity of a microprobe analysis. Precisely where in the $NbSe_3$ matrix the iron was incorporated (substitutionally or between chains) was not determined. Typical crystal dimensions for both the Fe_xNbSe_3 and $NbSe_3$ crystals were 2mm $\times$ 3 μm $\times$ 2 μm.

Crystals of nominally pure $NbSe_3$ were obtained from several different

preparation lots, each produced by identical procedures. Switching was observed only in the lower CDW state, but was not extensively searched for in the upper CDW state. The ratio of switching to nonswitching samples varied widely among $NbSe_3$ batches. In some lots, no samples displayed switching, whereas in others over 50% showed switching. The incidence of switching was found to depend on the age of a batch. In particular, crystals over 6 months old did not display switching. Nearly the original incidence of switching could be restored, however, by etching the batch in hot, concentrated H_2SO_4. A similar aging effect was observed in Fe_xNbSe_3, but etches of H_2SO_4 were less effective in restoring switching in this material. The incidence of switching was consistently higher in Fe_xNbSe_3 than in $NbSe_3$.

The incidence of switching was studied as a function of sample dimension and quality. Sample quality was monitored either by the number of surface defects, measured by scanning electron microscopy, or by crystal purity, measured by either the threshold field at 48 K or by the residual resistivity ratio. No dependence was observed on either sample dimension or quality. Preliminary results had shown switching to be more prevalent in thinner samples,[2] but simply reducing a given sample's cross-section did not consistently induce switching. For example, reducing the cross-section of a well-aged crystal had no effect on its I-V characteristic. A correlation of switching with cross-sectional area does exist, but it is related to the issue of transverse CDW coherence, as is discussed later in this chapter.

Current leads were applied to crystals using silver paint and fine gold wires. Both two-probe and four-probe conductivity measurements were made. For the

four-probe measurements, a special sample holder was constructed that enabled voltages to be measured anywhere along a sample's length;[3] this probe is described in Sec. II and in greater detail in App. A3.

II. Results

A. I-V characteristics and threshold fields

Switching I-V characteristics of pure and iron-doped $NbSe_3$ crystals were found to be nearly identical.[4] Fig. 1a shows current-driven I-V characteristics that are typical for switching crystals of $NbSe_3$, at selected temperatures in the lower CDW state. Fig. 1b shows similar I-V characteristics for Fe_xNbSe_3. Switching occurs only over a limited temperature range, from about 15 to 35 K in $NbSe_3$ and from about 40 to 50 K in Fe_xNbSe_3. These temperature ranges are somewhat sample-dependent. In $NbSe_3$, for example, switching may occur at temperatures as high as 42 K, or it may not begin until below 30 K. In both $NbSe_3$ and Fe_xNbSe_3, at temperatures above the switching regime, the chordal resistance V/I is a smooth function of the applied current bias, and the differential resistance dV/dI remains positive along the I-V curve. As the switching regime is entered, a region of negative differential resistance appears and develops into an abrupt switch with decreasing temperature. Well into the switching regime, switching becomes hysteretic, and departure from the switching regime occurs at still lower temperatures, as the switch height decreases and hysteresis increases. Multiple as well as single switches are observed in Fe_xNbSe_3 and $NbSe_3$, and switching occurs in either voltage or
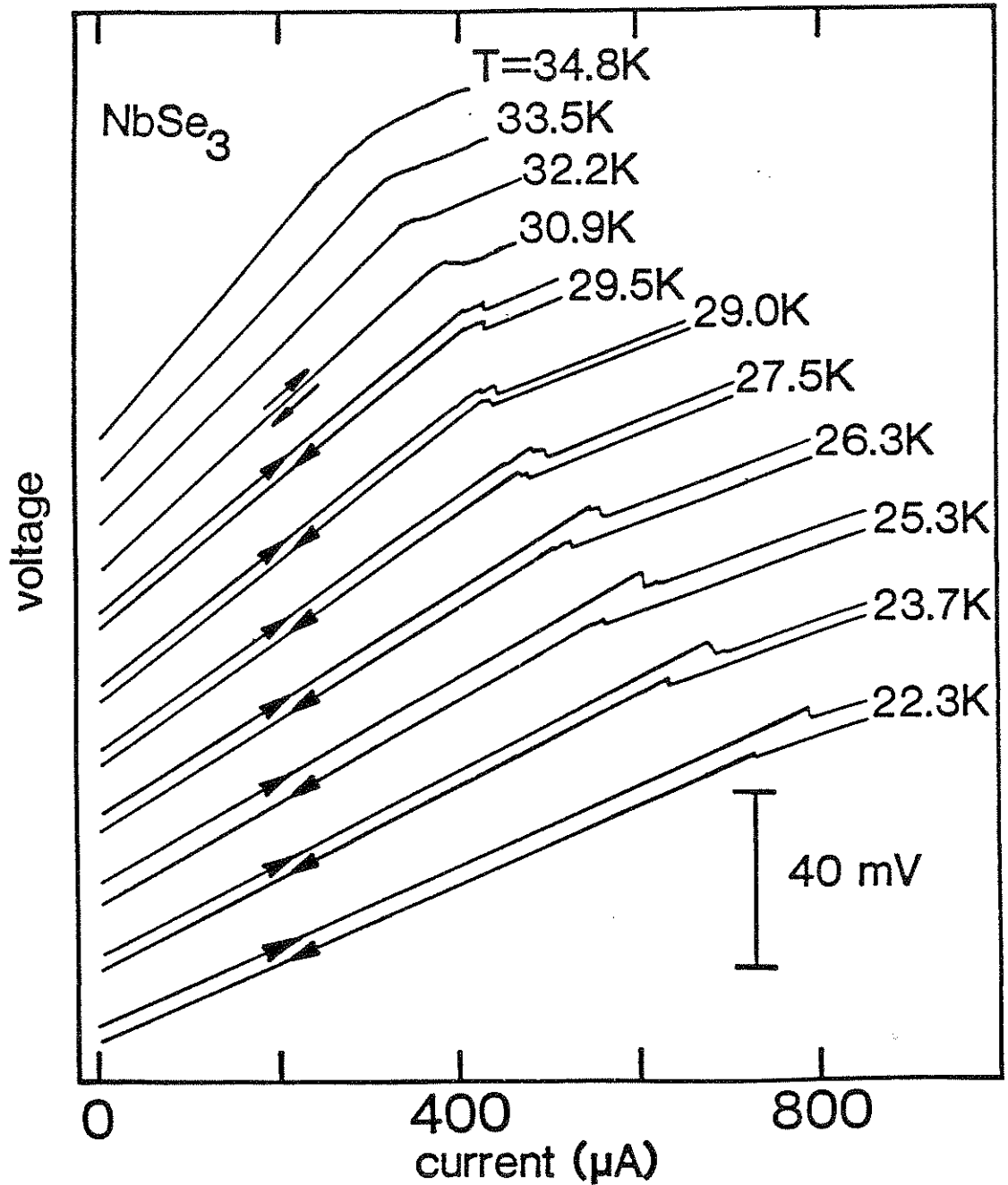
Fig. 3-1.a)   Current-driven dc I-V curves for a switching crystal of $NbSe_3$. Arrows indicate the direction of bias sweep. For temperatures below 30 K, the traces for forward and reverse bias sweep have been vertically offset for clarity.

Fig. 3-1.b) Current-driven dc I-V curves for a switching crystal of Fe_xNbSe_3. Arrows indicate the direction of bias sweep. For temperatures below 48 K, the traces for forward and reverse bias sweep have been vertically offset for clarity.
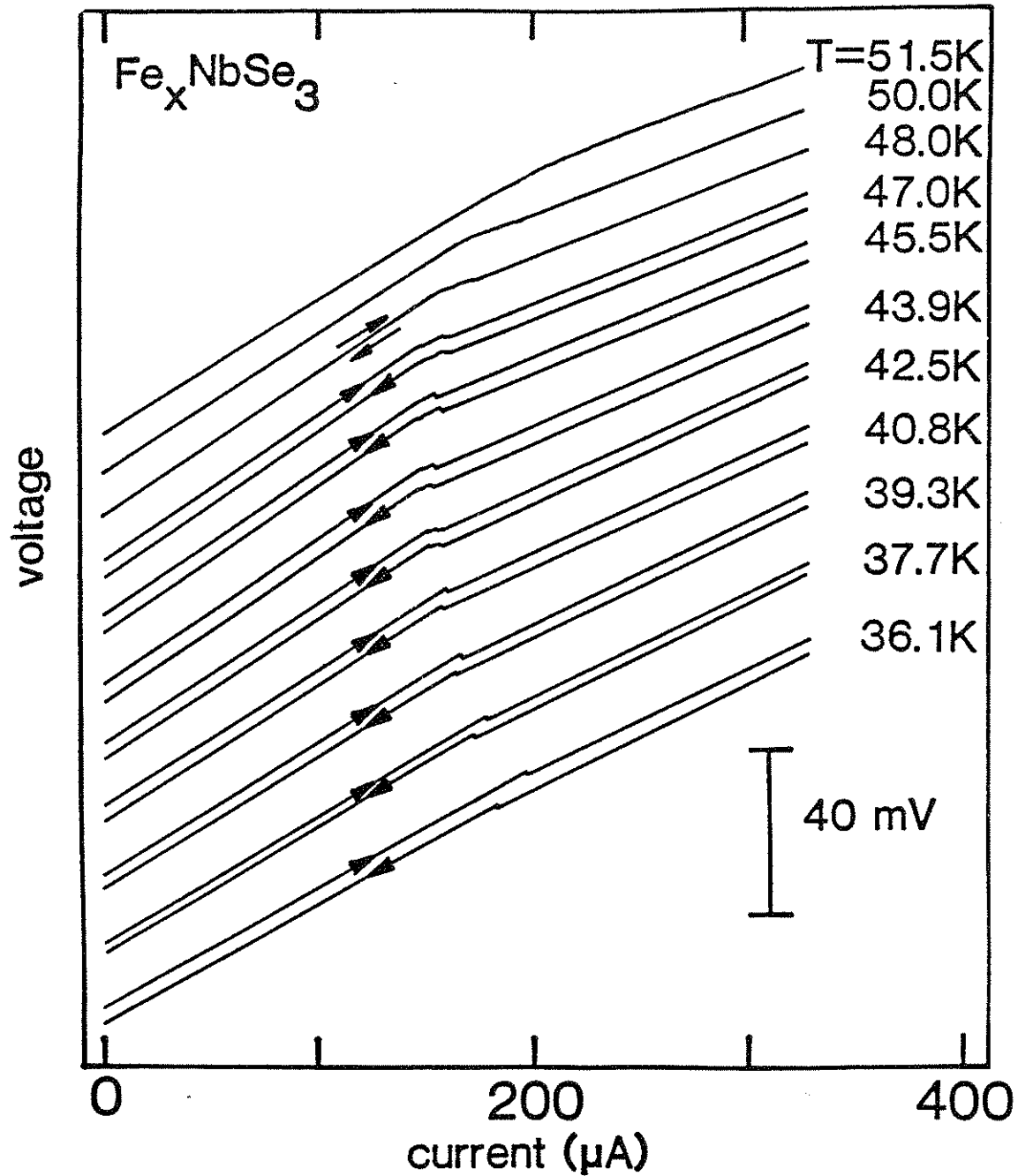
current-driven experiments. (As an example, Fig. 6b shows a voltage-driven I-V characteristic of an NbSe$_3$ crystal with nine switches.) The size of switching is sample-dependent. The largest switching, i.e. the largest relative discontinuity in an I-V characteristic, was observed in undoped NbSe$_3$ crystals.

A feature common to both NbSe$_3$ and Fe$_x$NbSe$_3$ is that dynamic conductance is roughly constant past the switching threshold.[2] This may be seen in the I-V curves of Fig. 1, where the switching curves have nearly uniform slope in the nonlinear region. In *non*switching crystals, the inverse differential conductance dV/dI attains constant values only when the applied field is about 4 to 5 times the threshold field.[5] Switching crystals reach the high-field conductivity state immediately past threshold, which suggests that CDW pinning effectively collapses at threshold.

The critical threshold field E_C in switching crystals is nearly independent of temperature. The temperature independence of switching thresholds in NbSe$_3$ crystals is quite striking.[2] Fig. 2a shows threshold fields of switching and nonswitching NbSe$_3$ crystals, normalized to their extrapolated $T = 0$ values. (Normalization is necessary because of the wide spread in threshold fields; see below.) For reference, the figure also displays Fleming's curve for threshold fields in nonswitching NbSe$_3$ crystals.[5] Threshold fields E_T have the same general temperature dependence for all nonswitching samples; e.g. they begin to rise gradually as the temperature is cooled below 50 K and change by about 100% between 35 and 20 K. In contrast, E_T in switching samples rises quite abruptly just before the switching regime is entered, and then is roughly

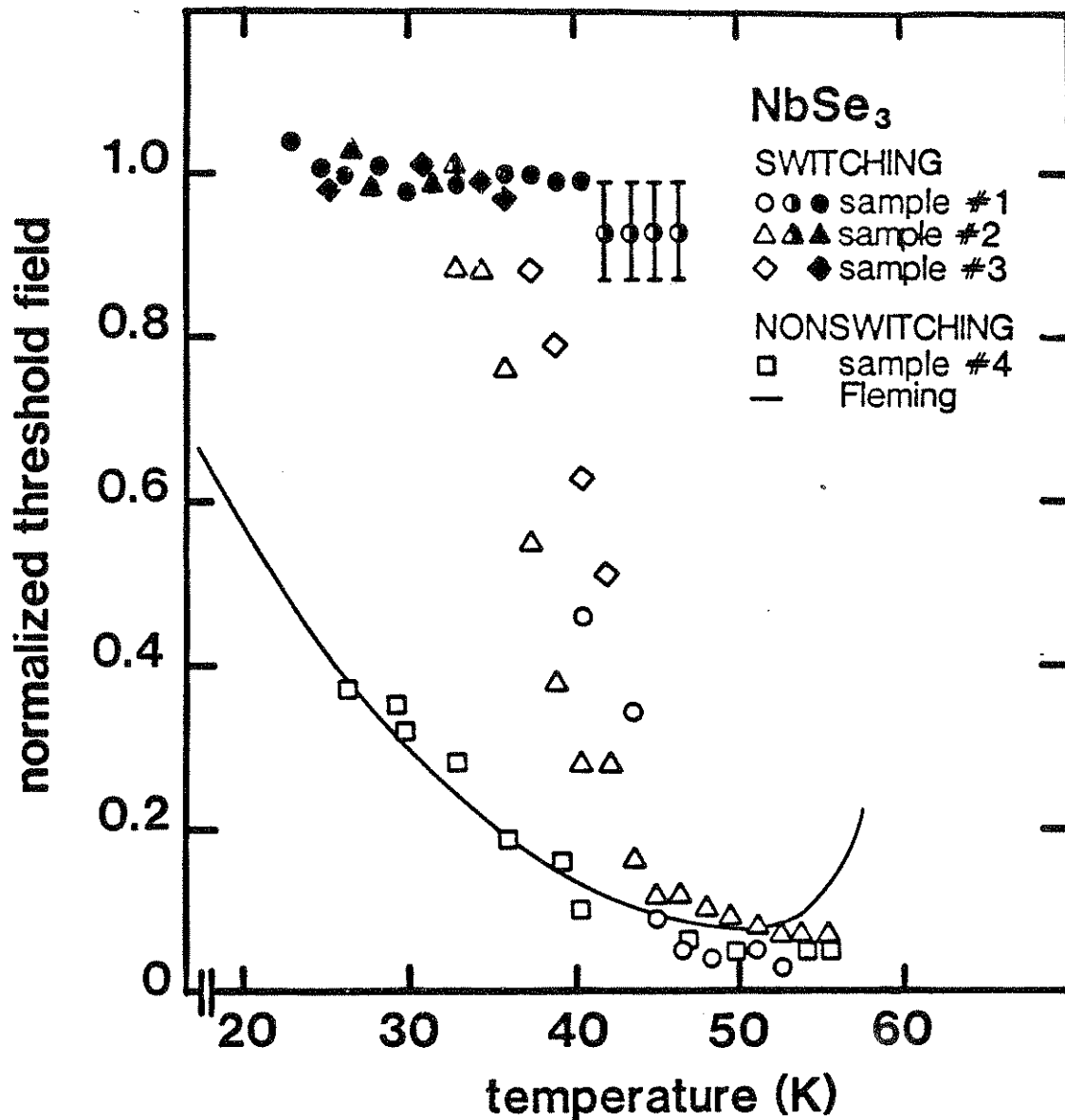Fig. 3-2.a) Normalized threshold fields for CDW depinning in switching and nonswitching crystals of $NbSe_3$. The open symbols represent thresholds E_T for smooth depinning, the solid symbols represent thresholds $E_C = E_T$ for switching, and the half-filled symbols represent switching thresholds E_C when a crystal depins smoothly at a lower bias E_T. Fleming's curve for nonswitching thresholds is adapted from ref. 5.
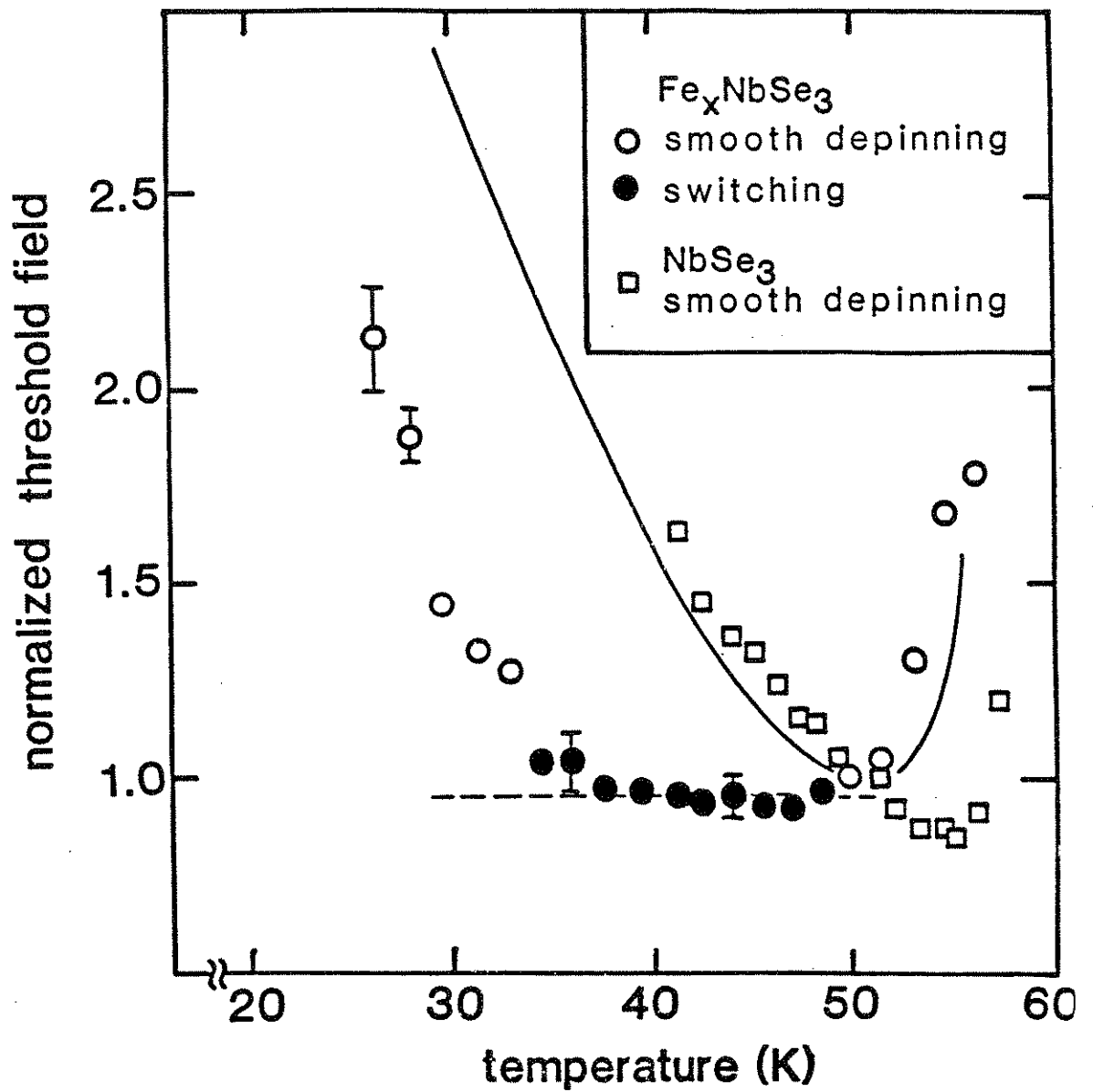
Fig. 3-2.b)   Normalized threshold fields for a switching Fe_xNbSe_3 crystal and a nonswitching $NbSe_3$ crystal. Fleming's curve for nonswitching $NbSe_3$ is adapted from ref. 5.

constant, to within 10%, inside the switching regime where $E_T = E_C$. In the temperature range 41 K to 46 K, half-filled symbols indicate switching thresholds E_C that are preceded by conventional depinning, with $E_T < E_C$.

The temperature independence of switching thresholds in Fe_xNbSe_3 is somewhat less dramatic, because nonswitching thresholds are less temperature dependent between 40 to 50 K. Fig. 2b shows threshold fields of a switching Fe_xNbSe_3 crystal and a nonswitching $NbSe_3$ crystal. The threshold fields have been arbitrarily normalized to their 51 K values, and again for reference the figure displays Fleming's curve for nonswitching $NbSe_3$ threshold fields. Switching in this Fe_xNbSe_3 crystal occurred mainly between 40 and 48 K. In this temperature range, the crystal's threshold field $E_T = E_C$ is nearly constant (solid circles). In contrast, threshold fields of nonswitching crystals change by 50% between these temperatures. Outside of the switching regime, the threshold field E_T of the Fe_xNbSe_3 crystal is strongly temperature dependent (open circles). The atypical temperature dependence of switching thresholds - in $NbSe_3$ and Fe_xNbSe_3 - suggests that a different physical mechanism is responsible for CDW depinning in switching crystals than the usual phase-depinning that occurs in nonswitching crystals.[2]

Switching threshold fields E_C are generally large, and in the switching regime the onset of nonlinear conduction typically occurs at $E_T = E_C$. In $NbSe_3$, switching thresholds are between 300 and 1500 mV/cm, and in Fe_xNbSe_3, switching thresholds are between 100 and 500 mV/cm. These fields are 10 to 100 times larger than nonswitching thresholds observed at comparable
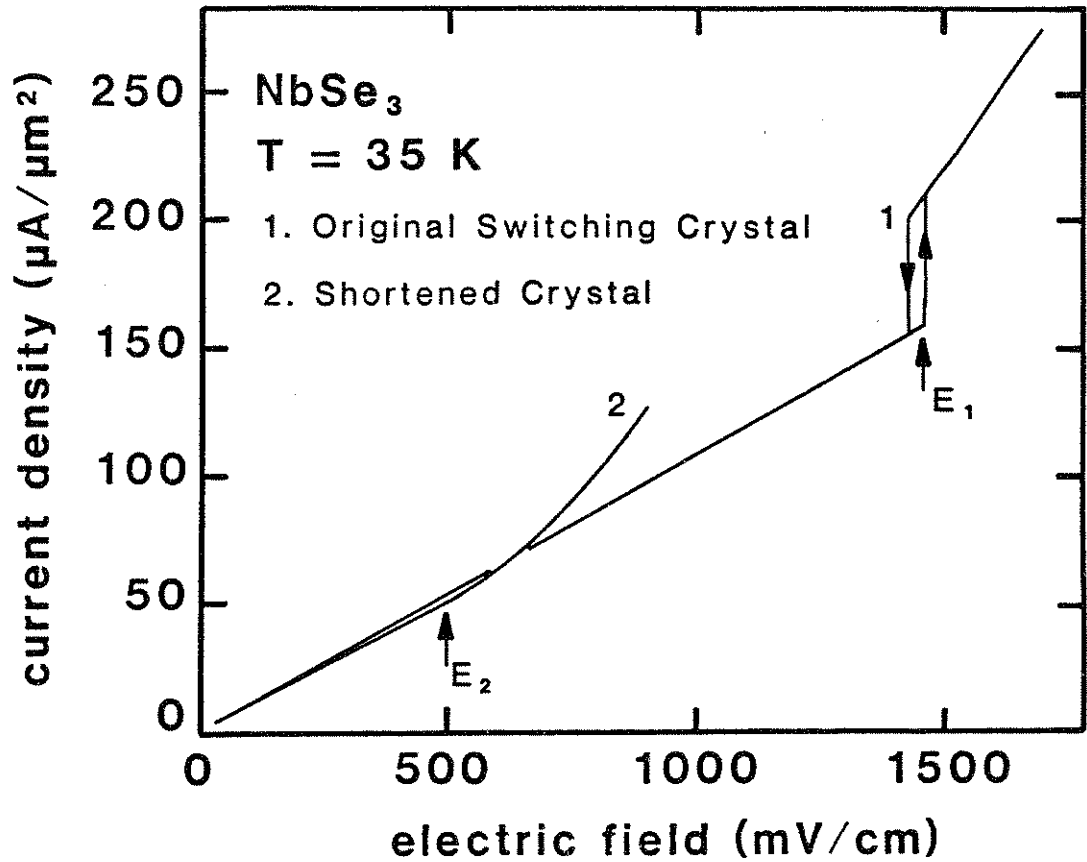
Fig. 3-3)   Voltage-driven, switching I-V curve for an uncut crystal of $NbSe_3$, and nonswitching I-V curve for the same crystal after it has been shortened from 2.8 to 2.5 mm.

temperatures in the highest quality NbSe$_3$ crystals.[5,6] Although switching fields are always large, nonswitching thresholds can be equally large, and comparisons of threshold fields in randomly selected crystals reveal no critical value of threshold field above which switching always occurs.

A more fruitful comparison is of E_C for switching and E_T for nonswitching behavior in the *same* crystal. Other researchers have performed this kind of comparison by irradiating nonswitching crystals.[7] They find that irradiation produces switching, and that the onset of switching is accompanied by an increase in threshold field E_T. We have performed the inverse experiment: we have induced nonswitching behavior in switching crystals. By physically cutting and thereby shortening a switching crystal, switching can be eventually eliminated. Fig. 3 shows $J = I/A$ ($A =$ sample cross-sectional area) versus E curves for an NbSe$_3$ crystal at 35 K. The uncut crystal was 2.8 mm long and displayed a large hysteretic switch at a threshold field of $E_1 = 1450$ mV/cm. The cut crystal was 300 μm shorter, and depinned smoothly at $E_2 = 480$ mV/cm. (No additional nonlinearity was observed at 1450 mV/cm.) Other crystals displayed the same general dependence of switching on length, although not as dramatically; some crystals were shortened to 100 μm before they stopped switching.

B. Nonuniform pinning and current discontinuities

Reducing the length of a *non*switching crystal does not induce switching, but reducing the cross-sectional area sometimes does. NbSe$_3$ crystals may be easily cleaved by splitting them parallel to the b-c or b-a planes of the unit cell. Fig. 4

(For page sequence only.)

Fig. 3-4)   SEM micrograph of a switching NbSe$_3$ crystal. No surface defects
are apparent. Left: typical crystal section. Right: detail of boxed
region on the left, magnification by an additional factor of ten.
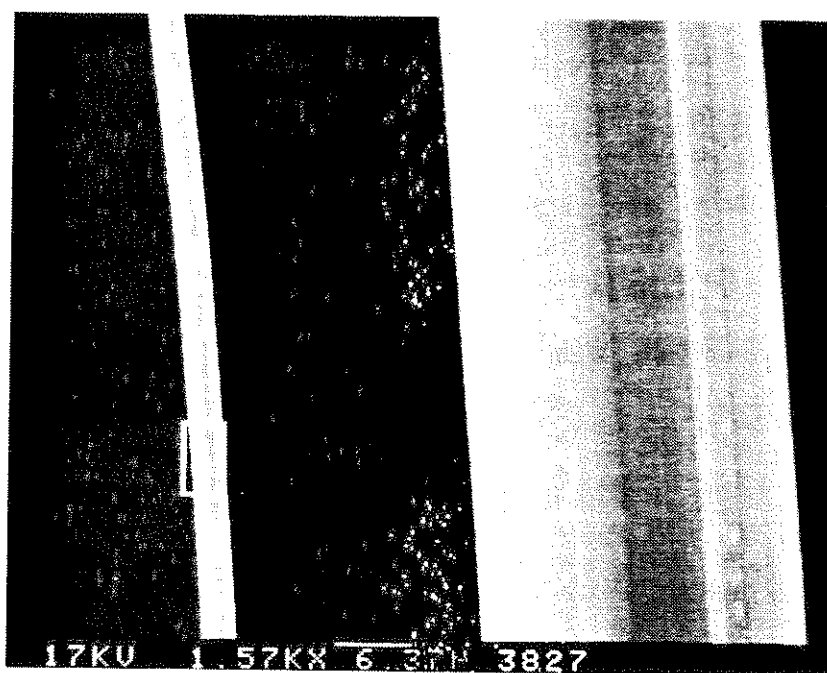Scale bar of 6.7 μm refers to the left-hand photo.

Fig. 3-4

shows a micrograph of a crystal that was split from a larger crystal. The length of both split and unsplit crystals was 2.5 mm. The cross-sectional area of the unsplit crystal was 28 μm^2, whereas the cross-sectional area of the split crystal was 2.7 μm^2. The split crystal appears uniform, with no damage visible anywhere along the crystal surface, indicating that splitting is an effective way of reducing a crystal's cross-sectional area in a nondestructive way.

Figs. 5a and 5b show J-E curves at 29 K for the parent crystal and for the split crystal of Fig. 4, respectively. The parent crystal depins smoothly at $E_T = 48$ mV/cm, but the split crystal switches at $E_C = E_T = 675$ mV/cm. Threshold fields at 48 K, a standard measure of crystal quality, also changed. The threshold field of the starting crystal was 16 mV/cm, but the threshold field of the split crystal was 70 mV/cm. The higher threshold fields of the split crystal - both at 48 and 29 K - indicates that the CDW is pinned more effectively in the split (switching) than in the unsplit (nonswitching) crystal.

Similar changes in switching and threshold field were observed in a number of other split crystals. The effect of splitting suggests the presence of localized, strongly pinning regions, sparsely distributed within NbSe$_3$ and Fe$_x$NbSe$_3$ crystals. Elimination of these strongly pinning regions (as occurs by physically cutting them from the crystal) causes a switching crystal to become nonswitching. Conversely, reducing the cross-sectional area of a crystal by splitting may induce switching in a previously nonswitching crystal. If the width of a crystal is large compared to the CDW phase coherence length, then CDW current can flow around localized regions that are strongly pinned,
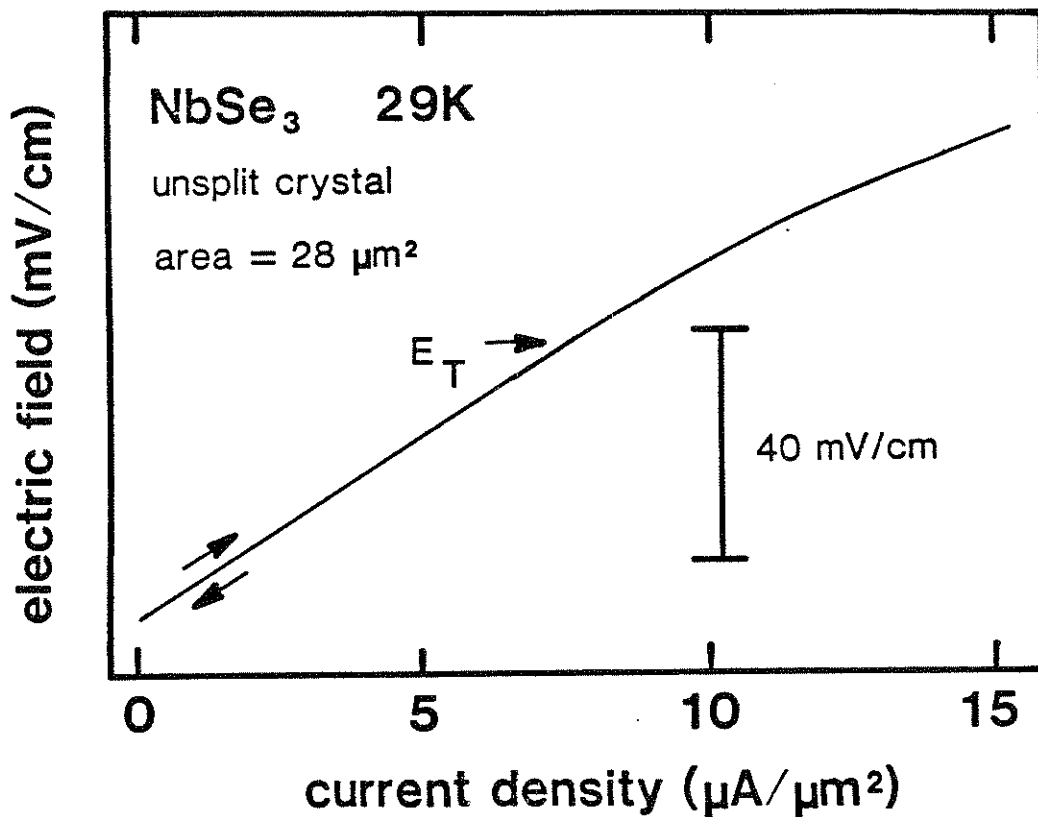
Fig. 3-5.a)   Current-driven I-V characteristics of an NbSe$_3$ crystal at $T = 29\ K$. The traces for forward and reverse bias sweeps have been offset vertically for clarity. The threshold field E_T is indicated by an arrow for the lower trace.
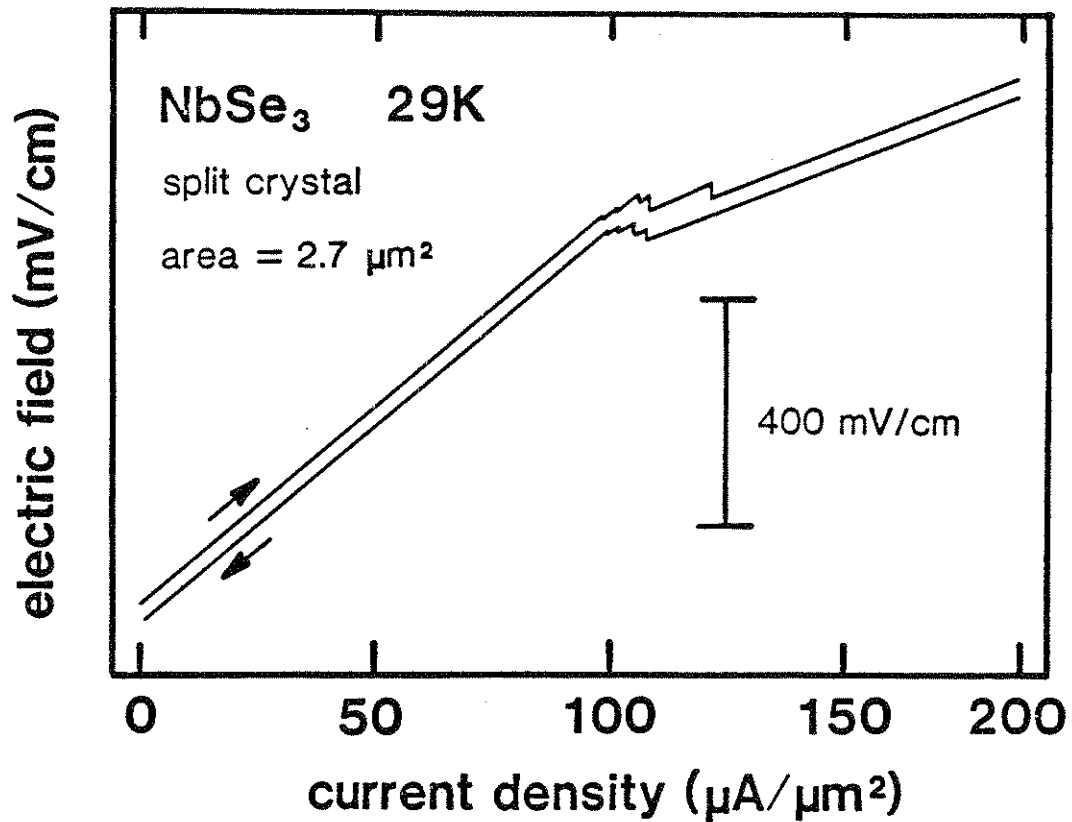
Fig. 3-5.b)   Current-driven I-V characteristics for an NbSe$_3$ crystal at $T = 29\ K$. The crystal was obtained by "splitting" the parent crystal of (a). Multiple switching is clearly observed. The traces for forward and reverse bias sweeps have been vertically offset for clarity.

leading to uniform depinning with no switching. On the other hand, if the crystal width is comparable to the transverse coherence length, then localized regions of strong pinning can initially obstruct CDW current and ultimately result in switching. Transverse phase coherence lengthes in $NbSe_3$ are roughly $0.4 - 0.8$ μm for threshold fields of 16 to 70 mV/cm.[8] Therefore the diameter of the split crystal in Fig. 4 is comparable to the transverse CDW coherence length. In contrast, the diameter of the unsplit crystal is much larger, which is consistent with the much smaller pinning in that crystal.

The discussion now turns to another series of experiments, where current domains were directly observed by nonperturbative measurements of local dc conductivities.[3] Fig. 6a schematically illustrates the four-terminal probe used to make such measurements. Current leads, terminals 1 and 4, were attached to the ends of a crystal using silver paint. Two additional voltage-sensing leads, terminals 2 and 3, were formed by pressing fine metal wires against the crystal surface. The pressures as well as locations of probes 2 and 3 could be adjusted independently during an experiment. Adjusting the pressure of the probes changed their contact resistance to the crystal. When the probes were lightly applied, their contact resistances were large and the probes did not perturb the current distributions within a crystal. The probes could be placed anywhere along a crystal with an accuracy of ± 5 μm.

Fig. 6b displays a voltage-driven I-V characteristic of an $NbSe_3$ crystal with nine switches, measured across terminals 1 and 4. The switches were unaffected by either contact 2 or 3, whether the contacts were lifted or applied. Fig. 6c
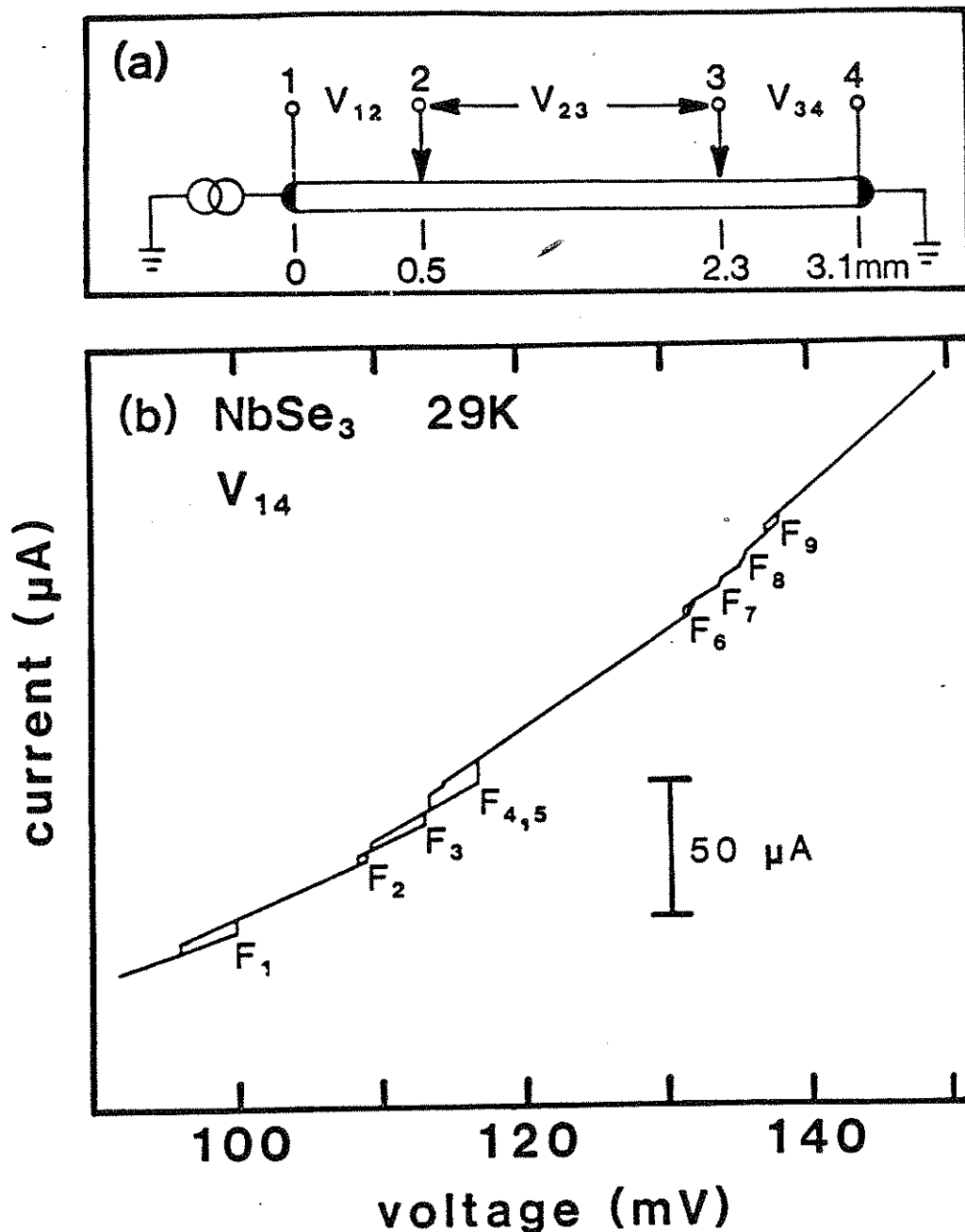
Fig. 3-6.a) 4-terminal measurement configuration. Terminals 2 and 3 are movable and non-perturbative. The indicated distances refer to terminal positions used in b) and c).

b) Voltage-driven I-V characteristics of an $NbSe_3$ crystal at $T = 29\ K$, measured between terminals 1 and 4 (2 probe) as indicated in a). The traces for forward and reverse bias sweeps have been offset vertically for clarity. The switches are identified with a number, which also identifies a particular peak in the narrow band noise spectrum (see Fig. 3-7).

Fig. 3-6.c)   Current-driven I-V characteristics for the same NbSe$_3$ crystal as used in b). The three traces refer to the local I-V characteristic of three different segments of the crystal (see a).

shows current-driven I-V characteristics across successive segments of the same crystal, when probes 2 and 3 were lightly applied to the crystal. (Segment lengthes are shown in the inset.) Fig. 6c shows that when a switch occurs in a complete I-V characteristic, a corresponding switch occurs in at least one, but not all, of the partial I-V characteristics. Therefore each sw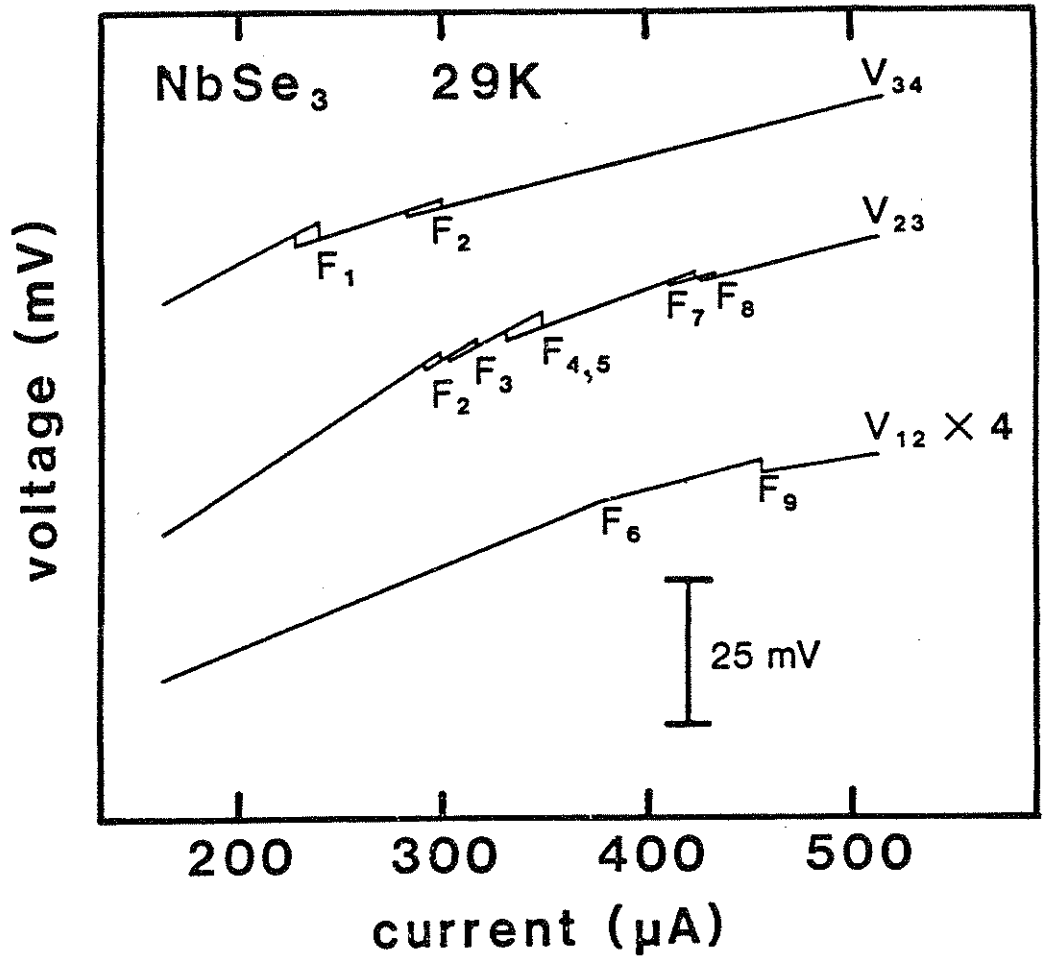itch signals local depinning of the CDW. Threshold fields vary by 50% in Fig. 6c, so the CDW is nonuniformly pinned within the crystal.

In general, switching in $NbSe_3$ and $Fe_x NbSe_3$ is characterized by nonuniform pinning and formation of current domains. Narrow-band noise measurements show that the CDW drift velocity within a current domain is independent of its drift-velocity within other domains.[3] For example, each successive switch in Fig. 6b corresponds to a new fundamental noise frequency entering the total noise spectrum. Fig. 7 shows traces of frequency versus total CDW current for the first six narrow-band noise fundamentals. Unlike nonswitching crystals, the frequency of a fundamental is not proportional to the *total* excess CDW current. Each switch produces a jump in the total CDW current and thus a break in the traces of Fig. 7. After each switch, the slope of each frequency trace is lower, as would be expected if CDW current were to flow in spatially separated domains.

The size of a current carrying domain may be estimated from $J'_{CDW} = ne\Lambda f'$, where J'_{CDW} is the excess current density carried by that particular domain, n is the density of carriers condensed in the CDW state, Λ is the CDW wavelength, and f' is the frequency generated by that domain. For example, assuming that
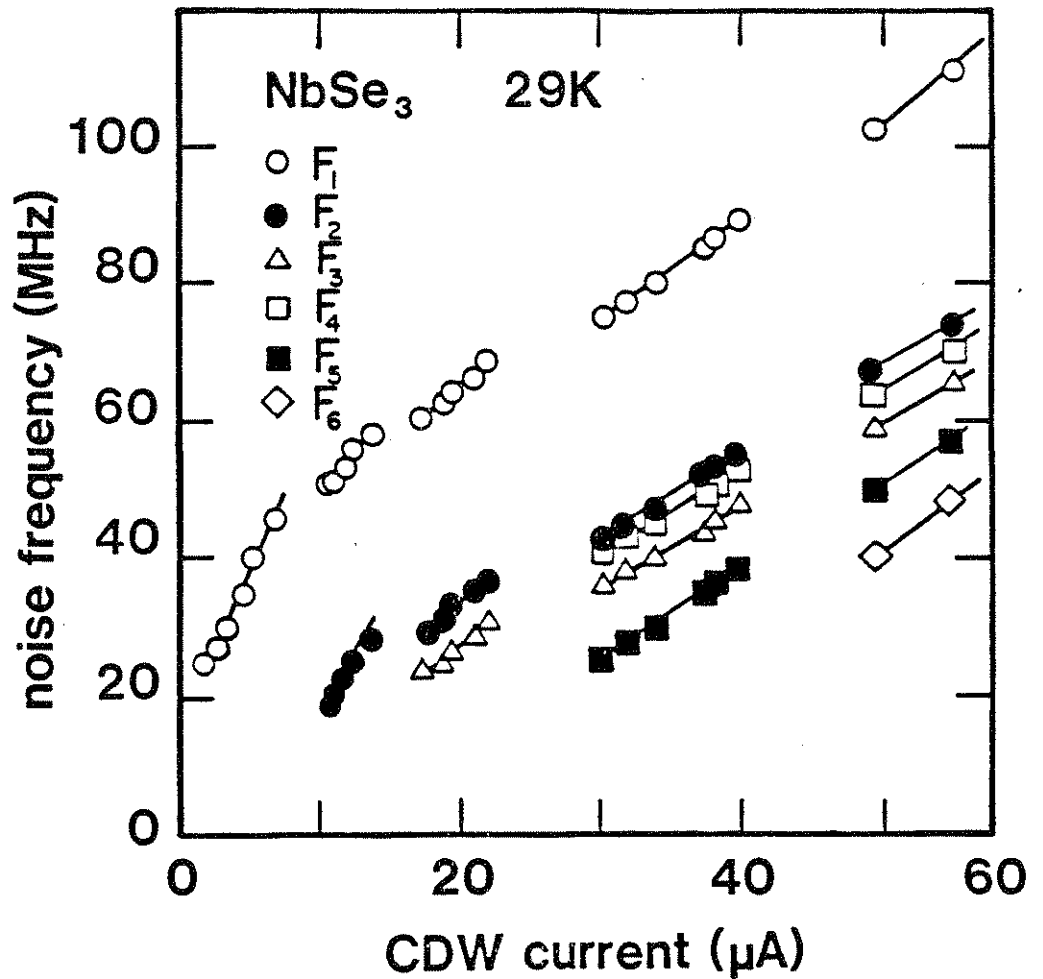
Fig. 3-7)   Narrow-band noise frequency versus *total* CDW current for the same NbSe3 crystal as used in Figs. 3-6b) and c). The measurement is performed between terminals 1 and 4 (2 probe). The different symbols refer to noise peaks which first appear at a particular switch, and are associated with a specific current domain. The data become linear and extrapolate to (0,0) only if the excess current axis is that appropriate to the specific current-carrying domain.

$n = 10^{21}\ cm^{-3}$ and $\Lambda = 14$ Å, the first switch in Fig. 6a corresponds to a volume of 2100 μm^3, which agrees with the crystal dimensions and the probe spacing. This volume indicates a serial arrangement of domains, i.e. domains stacked end-to-end along the crystal rather than side-by-side across the crystal. The slope of frequency versus current in Fig. 7 also indicates a serial arrangement of domains within the crystal.

The volume and arrangement of current domains may be determined directly by moving probes 2 and 3 independently along a crystal and measuring I-V characteristics in different sample segments.[3] Such measurements were performed in a number of NbSe$_3$ and Fe$_x$NbSe$_3$ crystals. Fig. 8a shows the probe arrangement and Fig. 8b shows the I-V characteristics for a single Fe$_x$NbSe$_3$ crystal. The full I-V curve (between terminals 1 and 4) indicates two distinct switches. By independently moving probes 2 and 3 and remeasuring the I-V characteristics, it was determined that the first switch at I_{S1} corresponds to the depinning of a region "A", whereas the second switch at I_{S2} corresponds to the depinning of a second region "B". The two regions are identified at the top of the figure. The interface between regions A and B is ·very sharp. Fig. 9 shows the magnitude of the switch at I_{S1} and the magnitude of the switch at I_{S2}, measured as functions of the positions of probes 2 and 3, respectively. The intersection of the lines through the data points indicates that the interface between regions A and B is well defined, and located 776 μm from terminal 1. Figs. 8a and 8b are characteristic of switching samples of NbSe$_3$ and Fe$_x$NbSe$_3$. It is consistently found that current domains are
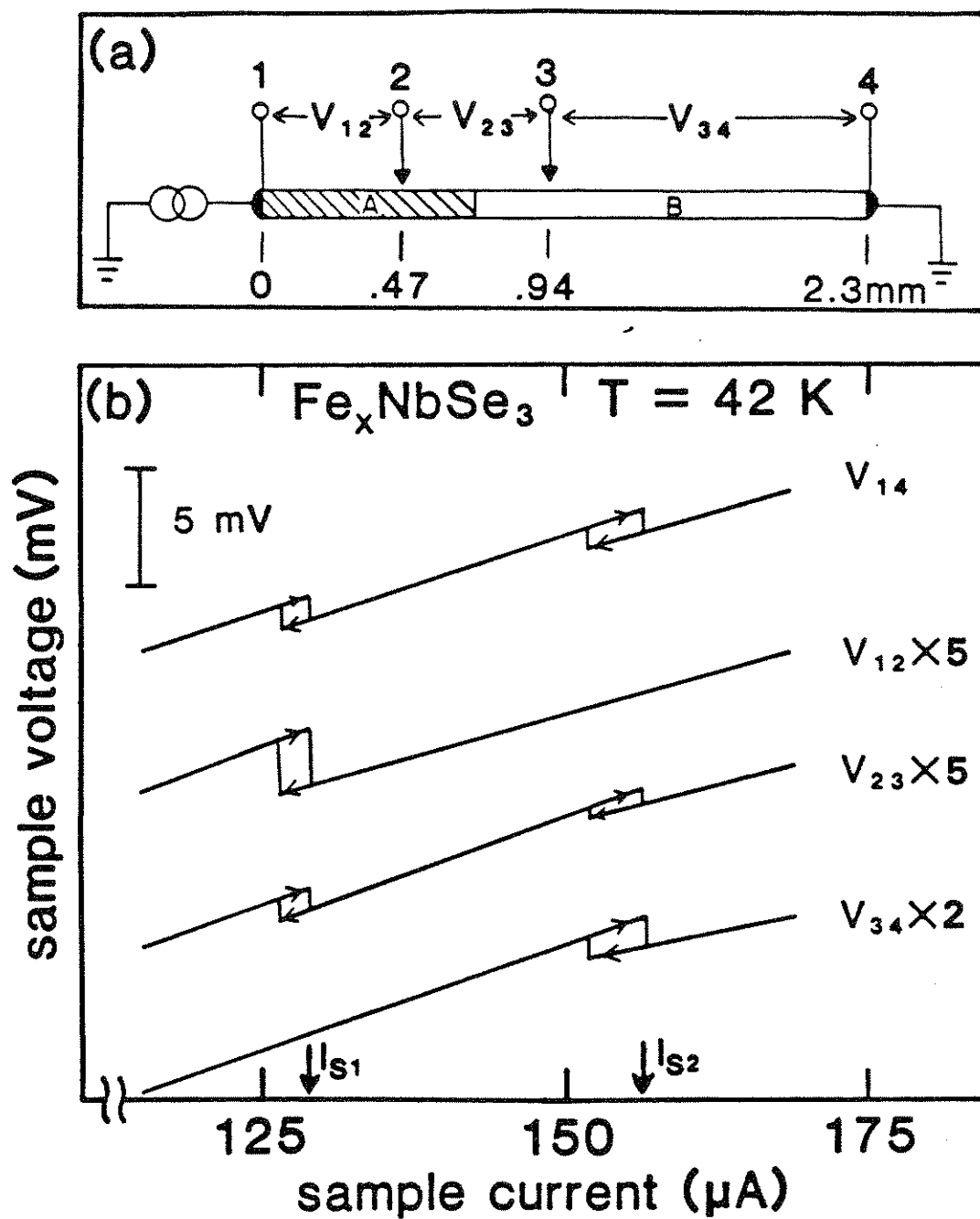
Fig. 3-8.a)   Voltage probe configuration for I-V traces shown in (b).

      b)   Simultaneously recorded current driven I-V traces for different segments of a single $Fe_x NbSe_3$ crystal at $T = 42\ K$. I_{S1} and I_{S2} identify the two critical currents for switching.
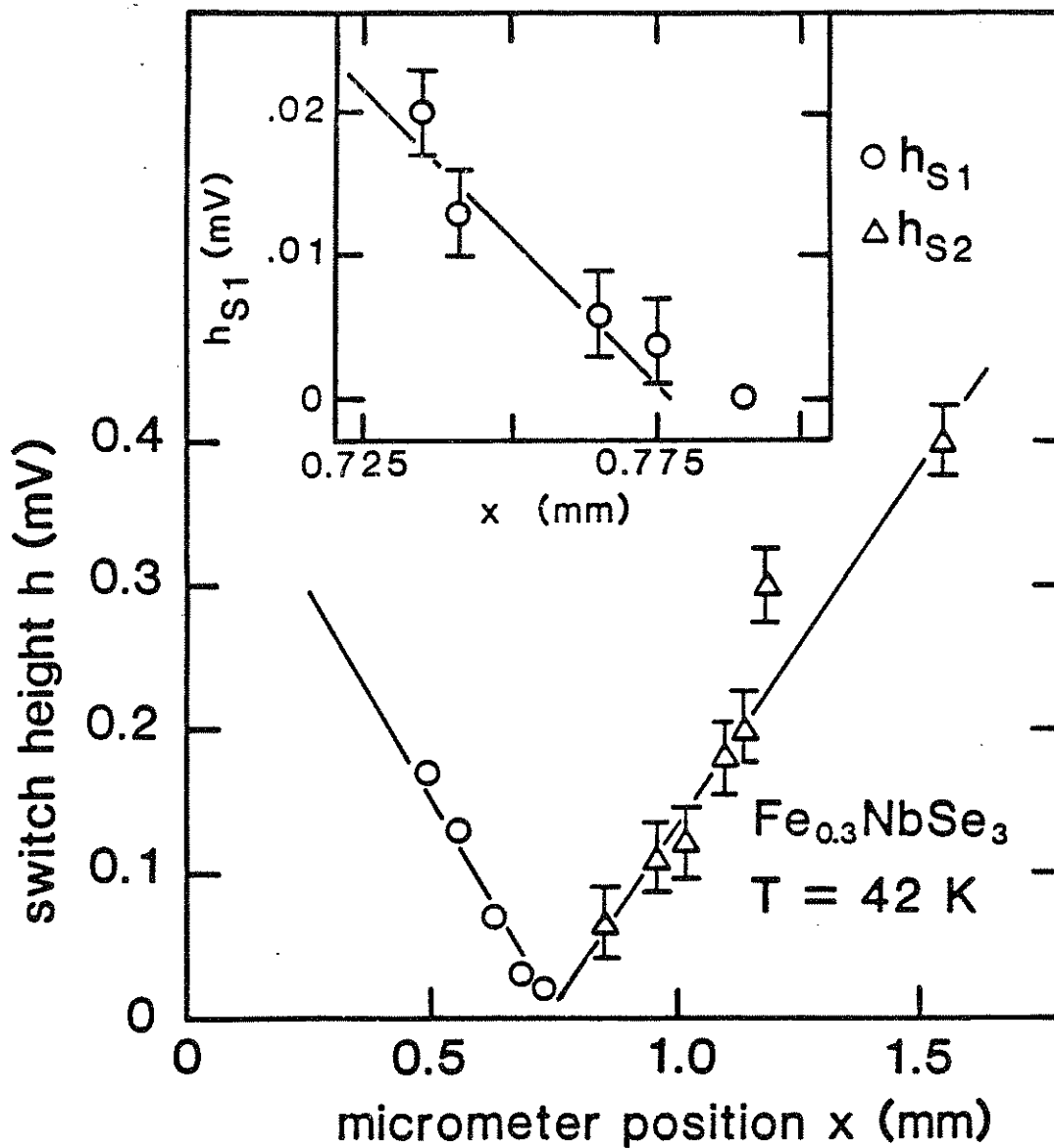
Fig. 3-9)   Switching height h (as measured directly from I-V traces, such as shown in Fig. 3-8b), versus probe position for an Fe_xNbSe_3 crystal at $T = 42\ K$. The circles refer to switch 1, the triangles refer to switch 2. The vertex of the two straight lines identifies the location of the phase slip interface in this crystal. The inset shows h_{S1} near the phase-slip region in greater detail.

arranged serially and that interfaces between domains are abrupt to within the experimental resolution (several microns). In these interface regions, CDW current is discontinuous. Condensed electrons are converted into normal carriers, and vice versa. Just as in superconductors[9] and superfluids,[10] current conversion takes place by periodic collapse of the CDW amplitude, at a rate set by the difference in CDW phase velocity between adjacent regions. These interface regions are therefore referred to as phase-slip centers.[3,11]

No distinguishing surface defects are associated with phase-slip centers. Figure 10 shows a micrograph of the phase-slip region in the Fe_xNbSe_3 crystal of Figs. 8a and 8b. Although some minor surface defects are evident, no major surface features are found in the phase-slip region. Conversely, some switching crystals, such as in Fig. 4, have virtually perfect surfaces. Thus switching can not be ascribed to surface contamination or to surface defects.

C. Avalanche depinning

The previous section demonstrates that pinning is nonuniform within switching crystals: switching crystals consist of a number of macroscopic current domains with independent threshold fields. A related issue is whether pinning is uniform inside one of these domains. This section describes a series of experiments which show that current domains are susceptible to breakup into smaller domains, and that pinning therefore can be non-uniform within a single domain.[4,12]

Fig. 11 shows a series of voltage-driven I-V curves for $NbSe_3$ at selected

Fig. 3-10)   Composite SEM micrograph of the phase-slip region in the
              $Fe_x NbSe_3$ crystal of Figs. 3-8 and 9. The phase-slip center lays
              within ± 20 μm of the micrograph center. (The uncertainty is due
              to possible error in alignment between the photo and Fig. 3-9.)
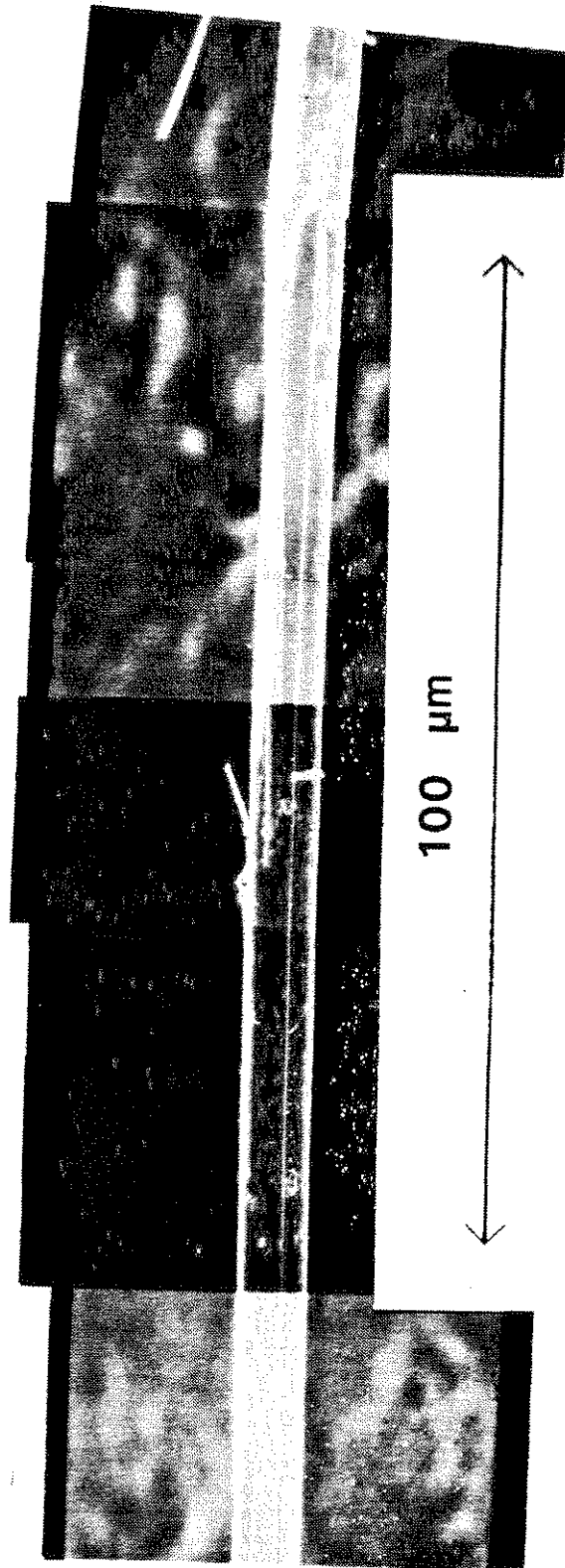
Fig. 3-10

(For page sequence only.)

temperatures in the lower CDW state, obtained by first monotonically increasing, and then monotonically decreasing, the bias voltage.[12] At 40 K, switching at the threshold E_C for CDW conductivity is clearly observed. At 35 K, switching is again observed at E_C, but a well-defined hysteresis loop has developed for the single switching event into or out of the sliding CDW state. With decreasing temperature below 35 K, the hysteresis becomes more pronounced.

An important feature of the hysteretic response in Fig. 11 is the appearance of additional switching structure for temperaures below 30 K. For example, at 28.3 K the transition back to the pinned CDW state for decreasing bias is comprised of a series of two small switches, rather than a single large switch as occurs at 30 K. At temperatures below 28 K, additional switching structure is observed during increasing bias as well, and in general, additional switching structure appears with decreasing temperature. At 23 K, for example, the transition to the "fully conducting" CDW state (where the hysteresis loop has closed and increases in dc bias result in no further switches) occurs by a series of at least four switches; the transition back to the fully pinned state occurs via two switches.

The additional switching structure which develops in the hysteretic regime reflects transitions between well-defined current-carrying states.[12] Fig. 12a shows the detailed I-V characteristics within the hysteresis loop at 23.5 K for the same NbSe$_3$ sample as was used for Fig. 11. The solid lines represent the overall hysteretic I-V structure, consistent with that displayed previously in
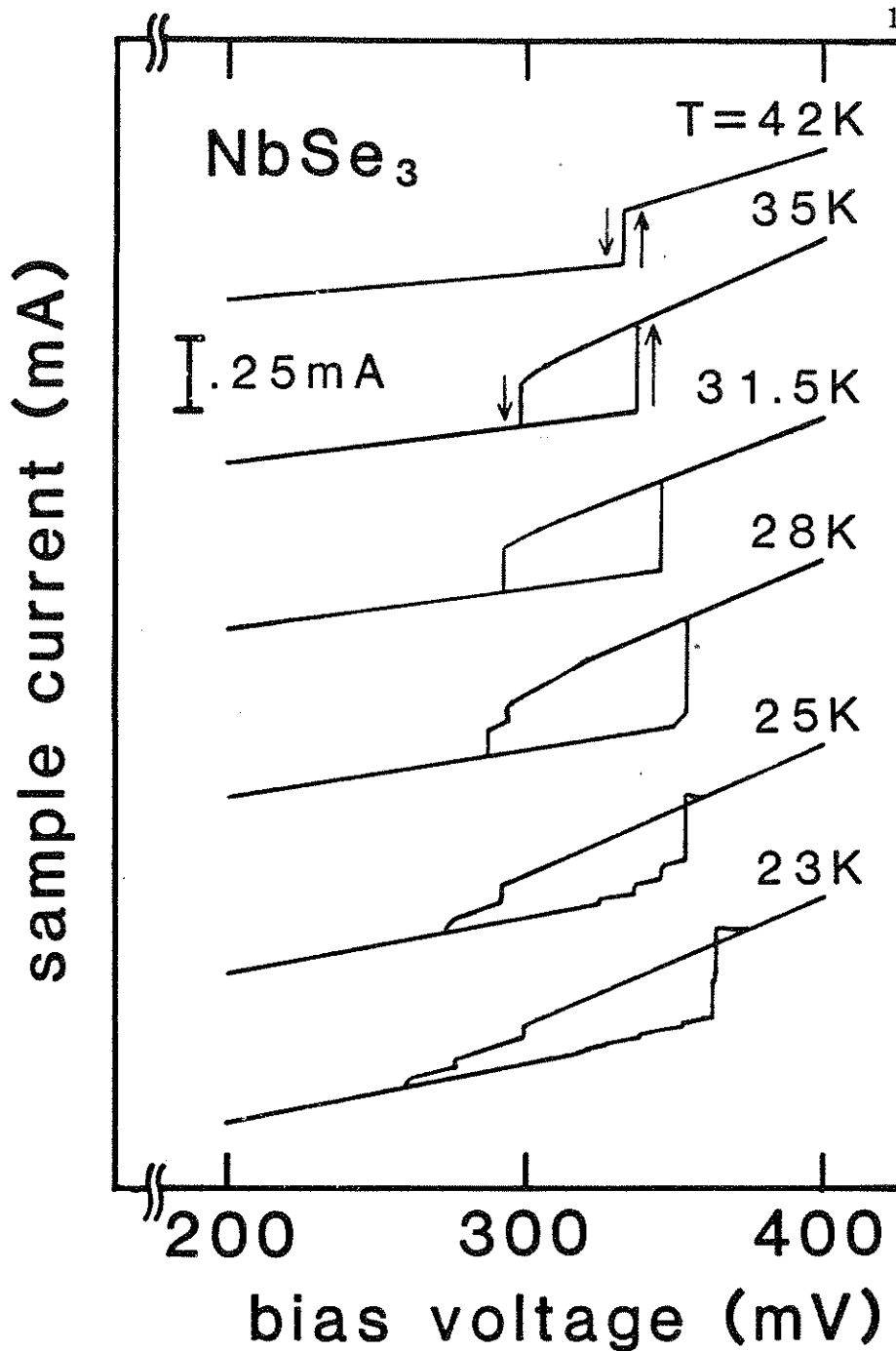
Fig. 3-11) Voltage-controlled I-V characteristics of NbSe$_3$ at selected temperatures in the switching regime. Additional switching structure is observed on the hysteresis loop at lower temperature.

Fig. 11. The striking features of Fig. 12a are the dashed lines, which represent distinct, repeatable, and quasi-stable current-carrying states. The direct mapping of the first of these states (labeled 1 in the figure) was achieved by slowly advancing the dc bias from zero into the hysteretic regime, until a small switch occured, and then immediately reversing the direction of bias sweep. The I-V characteristic of this sublevel state was then traced out by slowly varying the dc bias and recording the resulting current. A vertical transition from sublevel 1 to a second sublevel, labeled 2, is indicated by a vertical arrow in Fig. 12a. This second sublevel, and subsequent sublevels, were traced out in a fashion similar to that described for level 1. Since sublevels 1, 2 and 3 were achieved by first starting the dc bias voltage from zero, these structures are classified as *lower sublevel states*. As shown in Fig. 12a, distinct sublevel structure is also observed if the dc bias is started from a high level exceeding threshold. Sublevels thus achieved are labeled 4, 5, 6 and 7 in the figure. These structures are classified as *upper threshold* states, since they are arrived at by first decreasing the dc bias voltage from above threshold.

The substructure indicated in Fig. 12a was found to be entirely reproducible. However, upon tracing out the various sublevels, transitions between sublevels did not always occur at the same dc bias value. The vertical arrows represent repeatable transition points. Since these transitions are determined solely by the bias magnitude, they are identified as electric field-induced. As indicated in Fig. 12a, both upward and downward electric field-induced transitions are observed. Other non-repeatable transition points, not indicated on Fig. 12a,
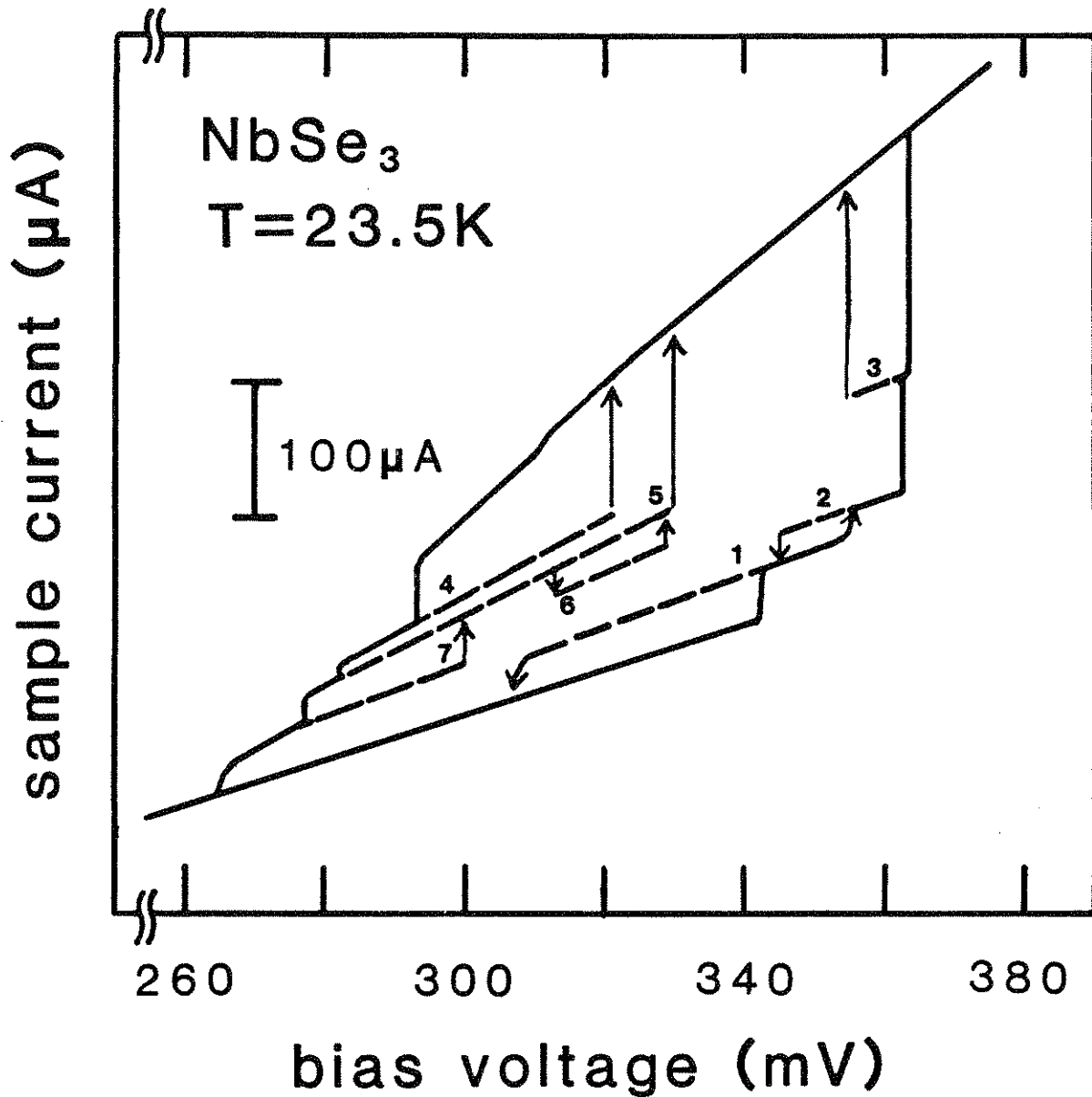
Fig. 3-12.a) Detail of I-V structure of NbSe₃ at 23.4 K. The numbered dashed lines represent distinct sublevel states; the vertical arrows correspond to electric field-induced transitions between the states (see text).
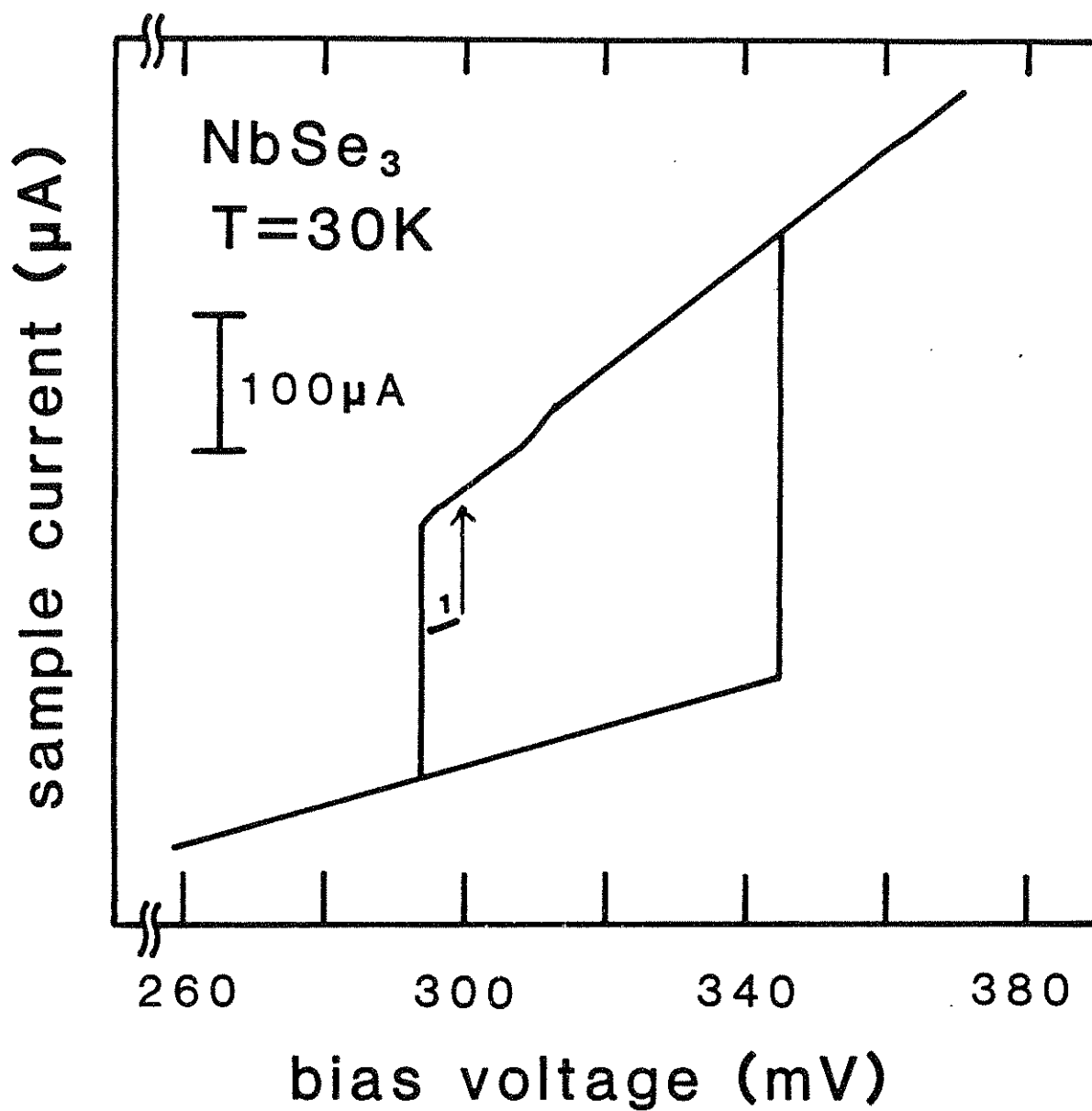
Fig. 3-12.b)   Detail of I-V structure at 30 K. Only one *stable* sublevel state is
observed within the hysteresis loop.

were also obtained. These transitions occured if the system was left unperturbed for a sufficiently long time on a particular sublevel, with a (fixed) dc bias voltage relatively close to the indicated vertical arrows. The time scale for waiting for such transitions to occur was often on the order of seconds to minutes, and these transitions are identified as induced by thermal fluctuations. Because of this sensitivity to thermal fluctuations the substrates in Fig. 12a are classified as quasi-stable.

The importance in distinguishing between "lower" and "upper" sublevel states in Fig. 12a lies in that *no* transitions were found to occur between a state in the lower group to a state in the upper group, or vice versa. It is thus possible that the two groups of sublevel states do not coexist. The lower sublevel states might be established only as the dc bias voltage V_{dc} is increased past the lower threshold field of the hysteresis loop, while the upper sublevel state would seem to be established only as V_{dc} is decreased past the upper threshold field. Increasing V_{dc} past the upper threshold field, or decreasing V_{dc} past the lower threshold field, would then effectively eradicate the lower and upper sublevel states, respectively.

The strong temperature dependence of the overall hysteresis loop shown in Fig. 11 is reflected in the sublevel structure. Fig. 12b shows the complete sublevel structure observed at 30 K. Only one sublevel state is clearly resolved, in contrast to the six defined at 23.5 K. Above 30 K, no sublevel structure was observed within the overall hysteresis loop. Clearly, the formation of stable sublevel structure is a highly temperature-dependent process.

The results are consistent with a macroscopic domain structure, where the sublevel structure, corresponding to distinct current-carrying states, results from a particular (relatively stable) configuration of pinned and current-carrying CDW domains. The same basic model has been used to account for negative differential resistance (NDR) in $NbSe_3$, where chaotic instabilities are attributed to rapid hopping between distinct current-carrying states.[15] In fact, the only significant difference between the states assumed in that analysis, and those directly observed here (at lower temperatures), is the relative energy spacing between the sublevels. In the NDR region, the energy spacing is significantly less, allowing for an increased transition rate (assuming a temperature independent attempt frequency), and hence chaotic response in the kHz and MHz frequency range.[15]

As an independent test of whether the sublevels in Fig. 12 correspond to different configurations of pinned and depinned domains within the crystal, the narrowband noise spectrum of the crystal was measured using a spectrum analyzer. The results support a domain interpretation. For example, on sublevel 3 in Fig. 12a, the noise spectrum indicates three depinned domains, while on sublevel 2, the spectrum indicates only two depinned domains. The successive disappearance of the stable sublevel structure in $NbSe_3$ with increasing temperature above 23 K suggests that the strength of the phase-slip centers (i.e. the ability of the phase-slip centers to break the CDW velocity locally) is strongly temperature dependent. As the temperature is increased, weak phase-slip centers are annealed out, effectively phase-linking domains together and reducing the number of switches in the I-V characteristic. At

relatively high temperatures (still in the switching regime), only the strongest phase slip center remains active, permitting at most two distinct switches. Should one domain have a substantially greater depinning voltage than the other (as might occur, for example, if one domain is relatively small), then only one distinct switch into and out of the "fully conducting" region will occur, as demonstrated in Fig. 12b.

The results of Figs. 12a and 12b show that large current domains are susceptible to breakup into smaller domains, and that large current domains contain latent phase-slip centers. The presence of latent phase-slip centers can be demonstrated directly by temperature-gradient experiments.[4] Temperature-gradient experiments show that latent phase-slip centers are present in small as well as large current domains, and at low as well as high temperatures. The ubiquitous presence of latent phase-slip centers strongly suggests that depinning within a current domain occurs by an avalanche-type process. Depinning at one center triggers depinning at the next center, which causes a *depinning wave* to travel down the length of current domain.[14] A current domain appears to depin simultaneously along its length only when probed by isothermal dc measurements. Avalanche processes within a current domain become apparent when switching is probed by temperature-gradient experiments or by experiments sensitive to the time-development of switching (e.g. pulsed current measurements,[13] and experiments on negative differential resistance[15] and ac switching noise[16]).

D. CDW polarization

Non-uniform pinning should produce local variations in the threshold field for CDW depinning. In turn, local variations in threshold field should produce macroscopic polarization of the CDW in a switching crystal.[17] When an electric field exceeds the local threshold field, the CDW attempts to slide. If an adjacent region is not depinned, the elasticity of the CDW prevents CDW current from flowing until a phase-slip center forms or until the adjacent region depins. Phase-slip centers are energetically costly (see below), so the CDW phase can develop appreciable gradients across distances comparable to the Fukuyama-Lee-Rice length. Phase polarization is thought to be observed by localized resistivity changes in switching TaS_3 crystals.[18]

Large, subthreshold resistivity changes have been observed in a switching $NbSe_3$ crystal by employing spatially resolved 3-terminal dV/dI measurements. Fig. 13a shows the contact arrangement. (The crystal regions "A" and "B" are meaningful only in the low temperature, switching regime.) Fig. 13b shows dV/dI traces at 48 K corresponding to the crystal segments between probes 1 and 4; probes 1 and 2; and probes 2 and 4. At 48 K, the three regions depin simultaneously and display identical dV/dI characteristics. No hysteresis is present in the low-field resistance. This is not the case at lower temperatures that are within the switching regime.

Fig. 13c shows localized dV/dI measurements of the same $NbSe_3$ crystal at 27 K. At this temperature the crystal consists of two well-defined regions, "A" and "B", which depin independently. These regions were mapped out in a
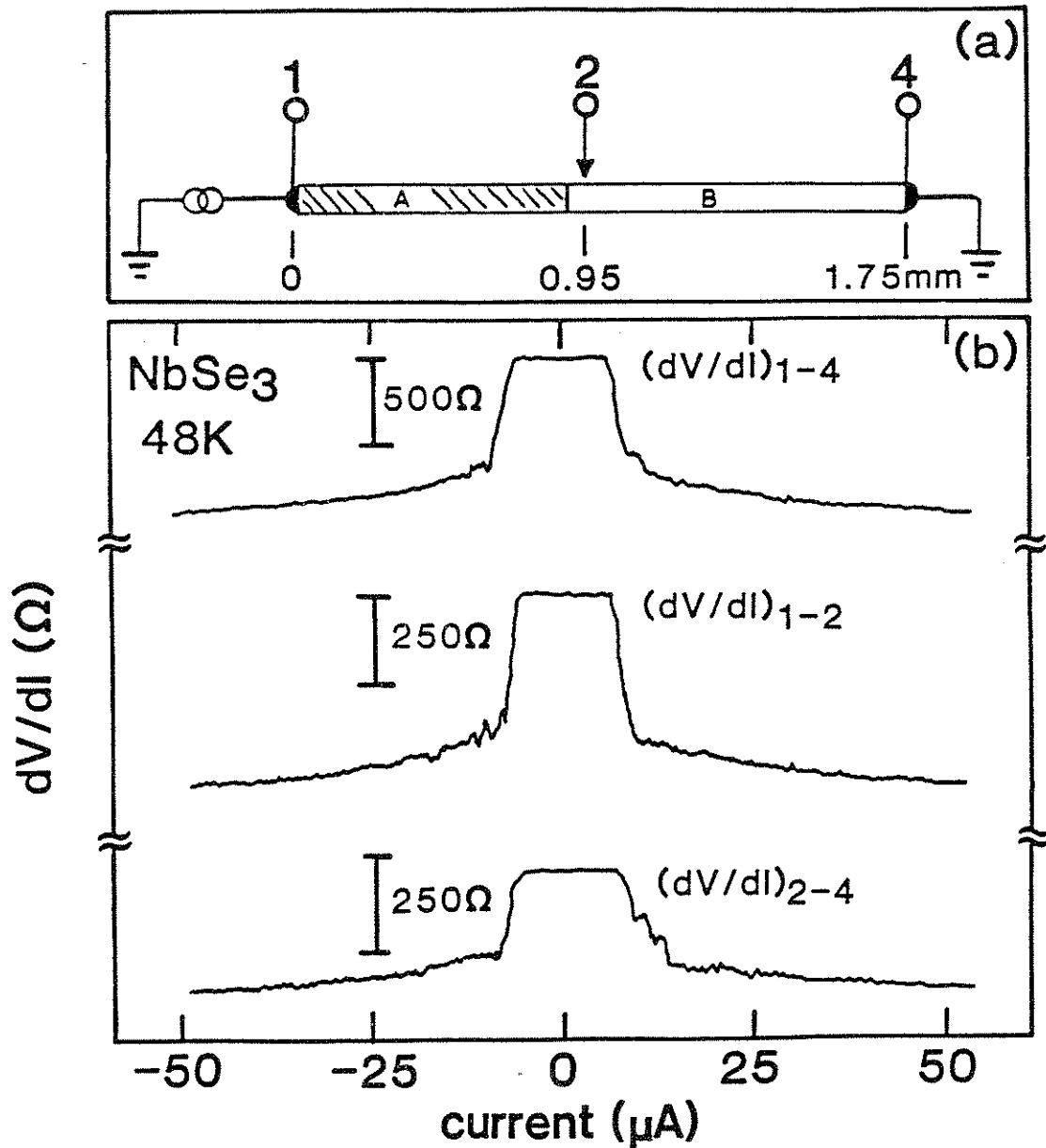
Fig. 3-13.a) Three-terminal probe configuration for dV/dI measurements of Figs. 3-13 b) and c), and Fig. 3-14. The regions "A" and "B" in the crystal become meaningful only at low temperatures, in the switching regime.

b) dV/dI traces for entire NbSe$_3$ crystal (terminal 1 and 4), and left and right hand segments (see a), all measured at $T = 48\ K$. The CDW depins uniformly throughout the crystal at E_T at this temperature.
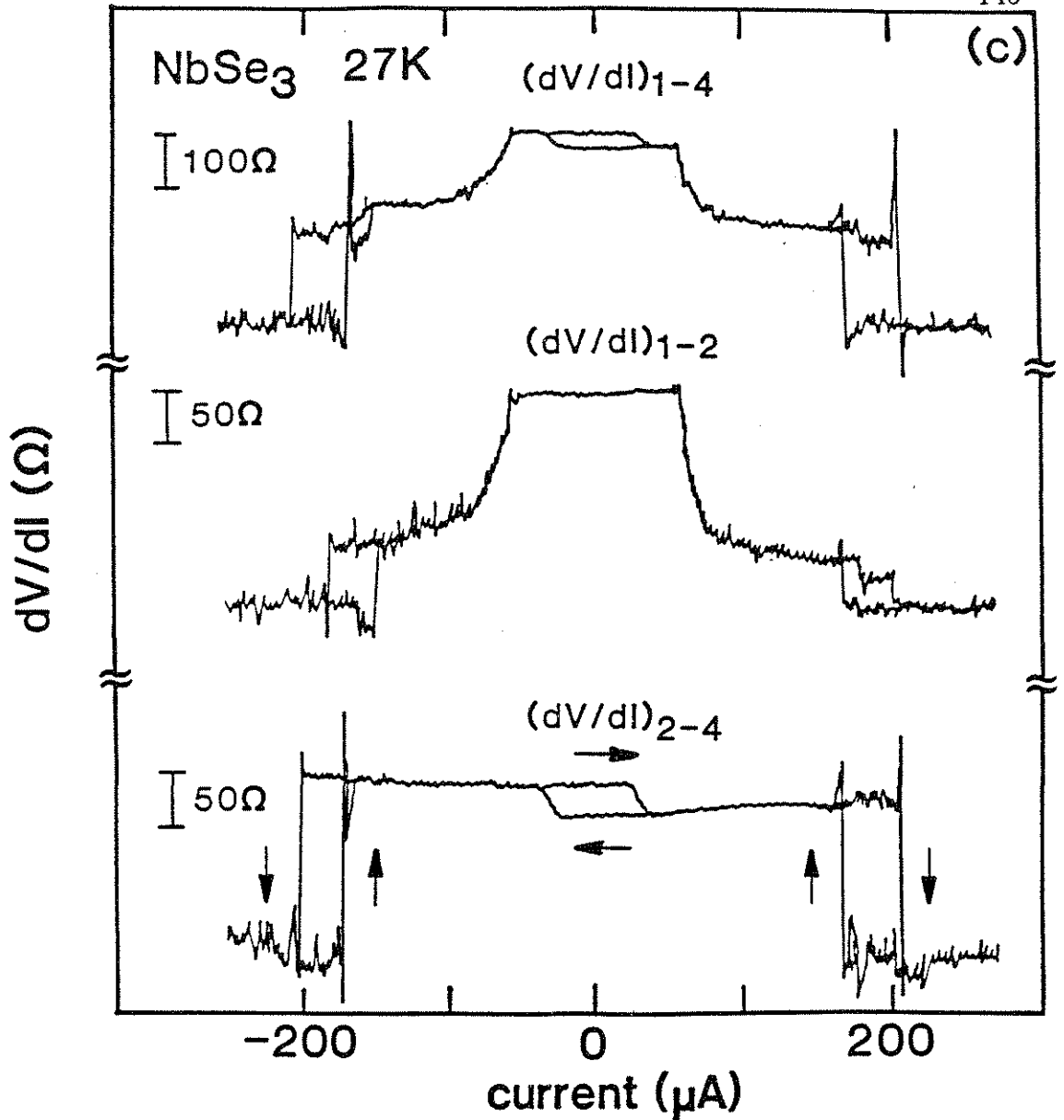
Fig. 3-13.c)   Same as b), but for sample temperature $T = 27$ K. Depinning is not uniform throughout the crystal. The top trace shows the dV/dI characteristics for the entire crystal. Strong low-field hysteresis is observed below E_T, and switching occurs at high bias current. The middle trace shows the dV/dI characteristics primarily for region A (see Fig. 3-13a). No low-field hysteresis is observed in this "normally depinning" region. The bottom trace shows the dV/dI characteristics for region B (see Fig. 3-13b). This region is associated with strong low-field hysteresis and switching.

series of I-V experiments similar to those described for Fig. 8. Region A depins normally at a current bias of 57 μA, whereas region B switches at a current bias roughly 3.5 times larger. The dV/dI plots of Fig. 13c were made with probe 3 raised and probe 2 placed inside region B. The top trace is the dV/dI response of the entire crystal, and the second and third traces correspond approximately to the regions A and B. The second trace, measured across mainly region A, has a concave-upward shape characteristic of nonswitching CDWs, except for a small contribution from region B. The third trace, measured across most of region B, has an entirely different shape. Excluding the region near zero bias, the trace resembles a hysteretic step function. The dynamic resistance of the switching region changes abruptly from the pinned, zero-field value to the saturated, high-field limit. The top trace, the response of the entire crystal, is a linear superposition of regions A and B.

Near zero bias, region B displays two repeatable and distinct resistivity states. The lower resistivity state is reached by increasing the current bias past $I_P = 33$ μA and then reducing the bias to zero. The upper resistivity state is reached by sweeping the bias below $- I_P = 33$ μA and then back to zero. The low-field resistivity of region B displays a "memory" of the polarity of the preceding bias sweep, provided that the bias exceeds either of the critical values $\pm I_P$. This polarization effect is large, approximately 15% of the low-field resistance of region B. The strong polarization effect is closely connected with switching since it occurs in the switching region of the crystal.

Fig. 13c shows that the critical bias I_P, the polarization threshold for switching region B, is comparable to the threshold bias of nonswitching region

A. This suggests that polarization in region B is caused by the CDW depinning from impurities in some parts of the region, but remaining pinned in others. CDW current in region B is prevented from flowing by the CDW elasticity, until region B switches (and completely depins) at a much higher bias. The temperature dependence of the polarization effect is consistent with this interpretation. Fig. 14 shows dV/dI measurements across region B from 48 to 28 K. Between 48 and 40 K, the dV/dI curve loses its concave-upward shape past threshold, and low-field hysteresis sets in at the same time. A change of scale at 40 K and then at 35 K clarifies what is happening to the CDW in region B. As temperature is reduced, the CDW only partially depins at the higher temperature threshold I_T. Further depinning takes place past I_T, and by 37 K, a second threshold is clearly evident as a pronounced downward bend in the dV/dI curve. At lower temperatures, this bend sharpens into the switch that is observed at 28 K. The polarization field I_P is a remanent of the nonswitching threshold I_T at higher temperatures. Evidently, a large polarization and accompanying elastic strain is necessary to produce depinning at the switching threshold.

Near zero bias, the upper and lower resistivity states of region B appear to be just two of an infinite number of stable polarization configurations of the CDW. Fig. 15 shows the low-field resistivity of region B in closer detail at 38 K. If current is monotonically swept from below $- I_P = - 10 \mu A$ to above $+ I_P$ and then back again, only the upper and lower resistivity states of region B are mapped out. If the current sweep is reversed as the transition is made from one state to the other, however, then a series of sublevels are attained inside the
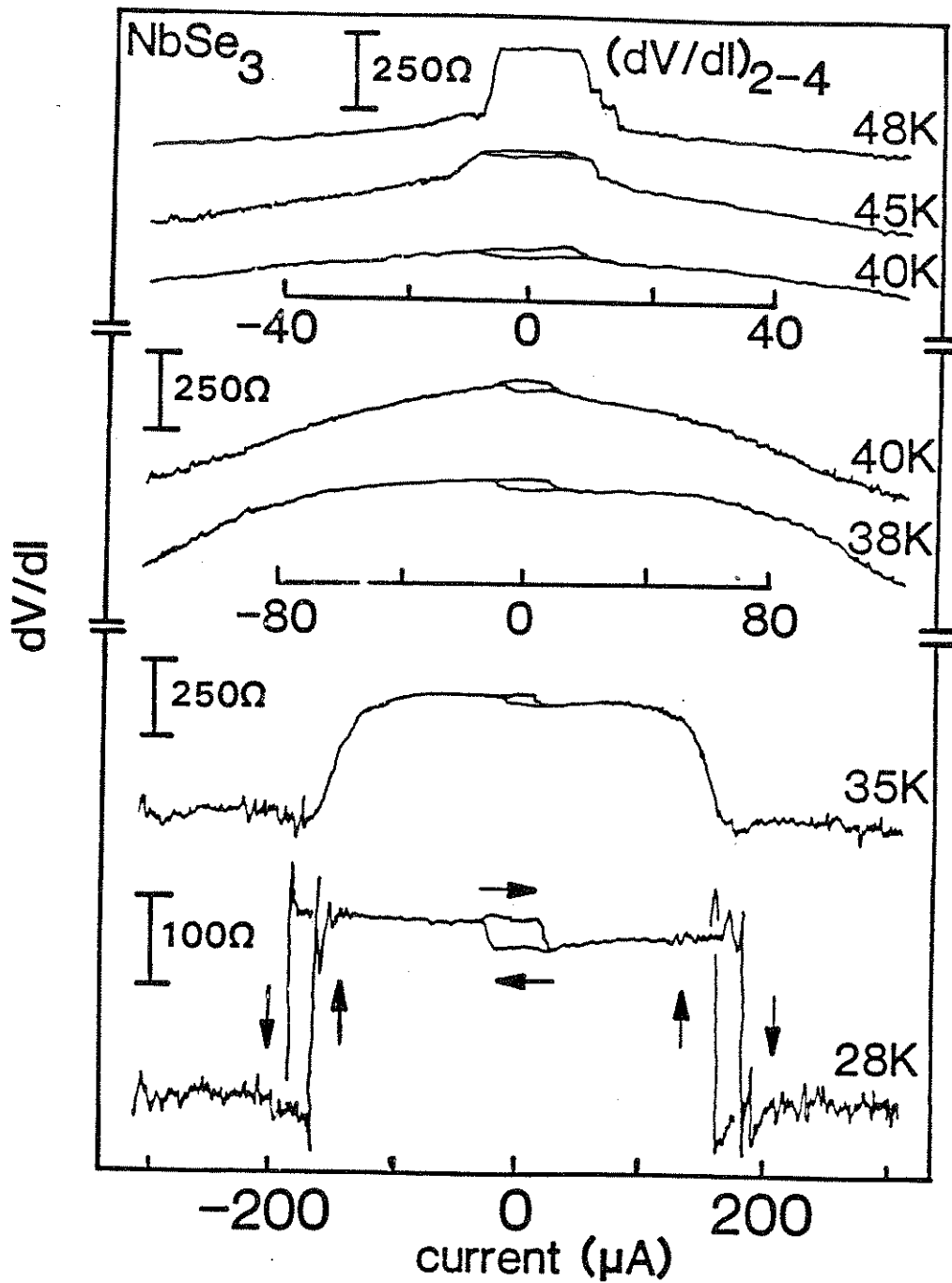
Fig. 3-14) dV/dI versus I at selected temperatures for the switching region (region B) of the NbSe₃ crystal of Fig. 3-13.
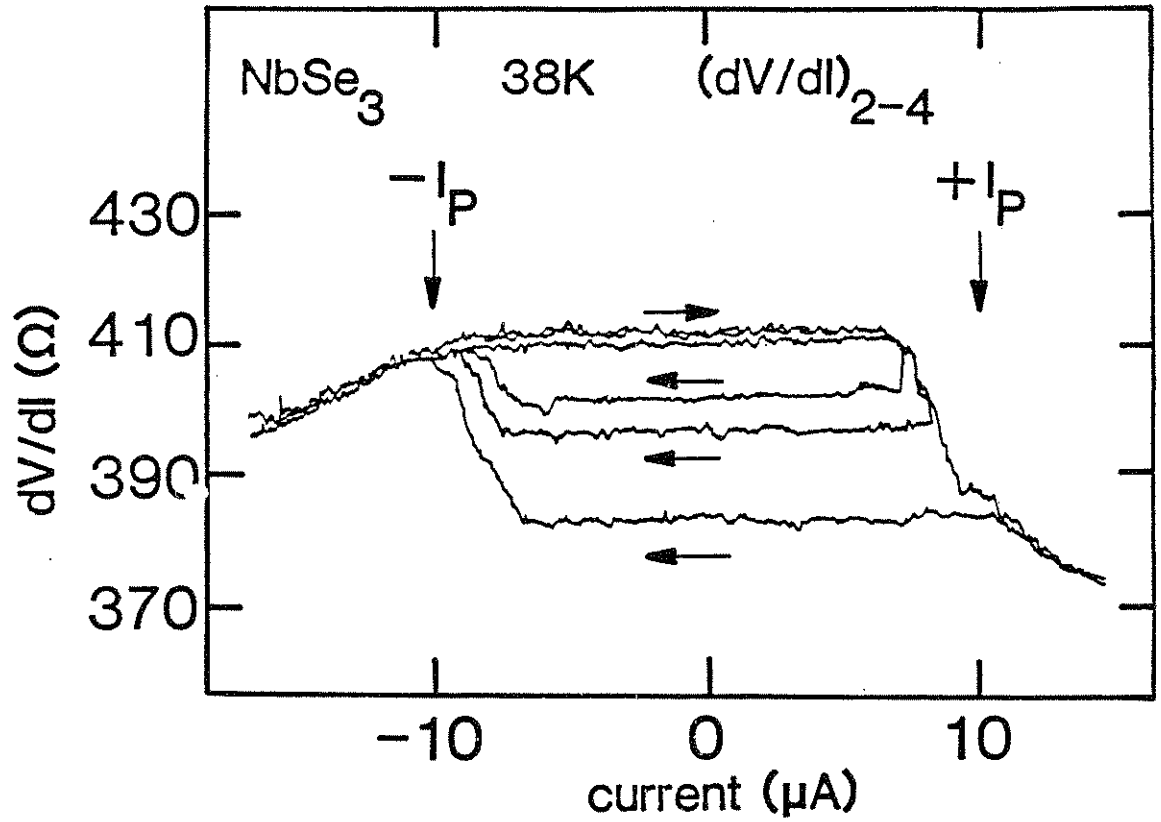
Fig. 3-15) Detail of low-field polarization states of the NbSe$_3$ crystal of Figs. 13 and 14. The arrows indicate bias sweep direction.

hysteresis loop. Two such sublevels are indicated in the figure.

Similar polarization and memory effects have been previously observed in NbSe$_3$ by Ong *et al.*, although they were not recognized as being associated with switching.[19] In general, polarization experiments have been performed using only a 2-contact configuration, which can obscure inhomogeneous polarization and current distributions. Mihaly and Tessema[20] have also reported related polarization effects in $K_{0.3}MoO_3$, where switching-like behavior is observed. The large magnitude of the effect that is observed here in switching NbSe$_3$ is due to the coexistence of switching and nonswitching regions within the same crystal. In switching crystals that contain no nonswitching regions, smaller polarization effects have been observed.

III. Analysis

1. Experimental implications

Switching in pure and iron-doped NbSe$_3$ is apparently caused by the same mechanism, although switching occurs at higher temperatures in Fe_xNbSe_3 than in NbSe$_3$. In both materials, measurements of differential resistance suggest that switching corresponds to an effective collapse of CDW pinning past threshold. Consequently, CDWs in switching crystals make an abrupt transition from a pinned, zero-velocity state to an effectively high-field state. This process of depinning is very different from the usual process of phase-depinning that occurs in nonswitching crystals, as is underscored by the atypical temperature independence of switching critical fields E_C. Threshold fields are generally large in switching crystals, so that pinning forces must be large, but large threshold

fields alone do not cause switching. Other attempts to distinguish switching from nonswitching crystals - by crystal quality and by crystal dimensions - have also been unsuccessful. Surface inspection of switching crystals show that switching crystals are not physically damaged or otherwise different from nonswitching crystals. By elimination, strong impurities or internal lattice defects remain as likely causes of switching.

Other experiments point directly to a random, internal distribution of strong pinning centers - strong as strong impurities or lattice defects - as the probable cause of switching. As demonstrated by examination of hysteresis loops or by measurement of local conductivity within a single crystal, a characteristic feature of switching crystals is the tendency to break into spatially distinct domains of uniform CDW current. These domains are separated by phase-slip centers which convert excess CDW current into normal electronic current via periodic collapse of the CDW amplitude. Narrow-band noise measurements, hysteresis loop sublevels, and temperature-gradient experiments show that strong pinning centers and amplitude fluctuations can exist even inside current domains. Nonuniform pinning produces a large amount of CDW phase polarization, with a threshold for the onset of polarization effects that is clearly a remanent of the usual phase-depinning process.

In the analysis that follows, the discussion shall first consider previously proposed models of switching. These models prove to be inconsistent with experiment. The analysis therefore proposes another mechanism for switching: phase slippage and CDW amplitude fluctuations.

2. Phase dynamical models of switching

In NbSe$_3$ and Fe$_x$NbSe$_3$, switching is associated with hysteresis,[13] bistability,[15] negative differential resistance,[15] and chaos.[21] Similar phenomena have been observed in other systems, e.g. semiconductors under large electric fields. There the effects are attributed to single particle processes such as thermal runaway, impact ionization, or avalanche breakdown. None of these single-particle processes appears appropriate to NbSe$_3$ or Fe$_x$NbSe$_3$. Impact ionization and avalanche breakdown require fields of at least 1000 V/cm, whereas in NbSe$_3$ switching results from fields between 0.1 and 1 V/cm. Thermal runaway is ruled out because it requires a material's resistivity to decrease with increasing temperature; in pure and iron-doped NbSe$_3$, switching occurs only when $d\rho/dT > 0$.

A number of CDW-based models have been proposed to account for various aspects of switching. Joos and Murray[14] have proposed a domain coupling model; Janossy and Kriza[17] have suggested a CDW self-blocking mechanism; Hall et al.[21] have considered a single degree of freedom model with inertia; and Wonneberger[22] has proposed a single degree of freedom model with current noise. A common feature of these models is that they ascribe switching CDW phase dynamics, and neglect or assign an insignificant role to amplitude fluctuations. The models often reproduce certain experimental results, but they cannot describe all the phenomena of CDW switching discussed in this chapter.

In the domain coupling model of Joos and Murray, a switching crystal is divided into an arrangement of otherwise unspecified domains. When an electric field exceeds the threshold for CDW depinning, each domain is assigned

a certain probability for depinning, and once depinned, a domain can trigger neighboring domains to also depin, so that a depinning wave propagates along a crystal. This model reproduces the delay times observed in pulsed switching experiments,[13] but the physics behind domains and their intercouplings is unclear, as is why they should behave differently in switching versus nonswitching crystals. From a mathematical point of view, the description is a kinetic Ising model.

The simplified nature of the Joos-Murray model results in problematic I-V characteristics. A more serious difficulty is that the model requires no CDW current to flow in a switching crystal until the CDW has depinned in all portions of the crystal; this is inconsistent with numerous experiments that demonstrate that current domains may depin independently within a given crystal. The usefulness of the Joos-Murray model is that it involves a domain-configuration (as observed experimentally) with tractable statistics in the time domain (an issue not discussed here). It is a many-degree-of-freedom model.

The CDW self-blocking model of Janossy and Kriza is also a many-degree-of-freedom model. It proposes that macroscopic polarization of a CDW interferes with depinning and delays CDW conduction until the CDW can relax from a polarized state. As discussed earlier, and illustrated in Figs. 13 and 14, large polarization effects are indeed associated with switching CDWs. In the self-blocking model, the origin of the unusual polarization (as opposed to polarization in non-switching crystals) remains unspecified. An interesting implication of the model is that if dc bias is swept slowly enough, then switching should not be observed in the I-V characteristics of a crystal. In

experiments, however, no unusual time dependence (at long time scales) is observed in the switching characteristics of NbSe$_3$ or Fe$_x$NbSe$_3$. Finally, just as with the Joos-Murray model, the self-blocking model requires that no CDW current flows in a crystal until the CDW depins along the entire crystal length (which is inconsistent with experiment, as stated previously).

Both the CDW inertial model of Hall *et al.*, and the CDW current model of Wonneberger *et al.* are based on the single-particle classical equation of motion proposed by Gruner, Zawadowski, and Chaikin,[23]

$$\frac{d^2\phi}{dt^2} + \frac{1}{r}\frac{d\phi}{dt} + \omega_0^2 \sin\phi = \frac{e}{m^*}EQ, \qquad (3.1)$$

where ϕ is the CDW phase, t is a time variable, r is a time-constant describing dissipation, ω_0 is a pinning frequency representing the strength of the impurity potential, m^* is the Frolich mass of the CDW electrons and E is the applied electric field. Usually, the inertial term (first term on the left) is neglected because the phase relaxation rate (order 10^{-11} sec) is much faster than either ω_0 or the frequency of the applied electric field. In the inertial model of switching, the first term in Eq. (1) is retained, which is equivalent to specifying that $\omega_0 \gtrsim 1/r$. Thus the inertial model requires either large pinning or small damping. In the current-noise model, the inertial term is neglected, but an additional noise term is added to the right-hand side of Eq. (2). The magnitude of the noise term is a function of the CDW velocity, so Eq. (2) must be solved self-consistently. For switching to occur, current-noise must increase sharply as the CDW velocity approaches zero. The physical origin of this noise remains unspecified.

The inertial model of switching is equivalent to the resistively-shunted-junction (RSJ) model with capacitance, which is commonly discussed in the Josephson junction literature.[24] It predicts switching hysteresis, bistability, and chaos, all of which are observed in switching crystals of $NbSe_3$. However, the parameters of the model are not self-consistent when applied to CDW dynamics. The model required either very large pinning (large values of ω_0) or very small damping (small values of $1/r$) for switching to occur, but neither assumption is justified by experiment. Typically, ω_0 in nonswitching crystals is much smaller than $1/r$, $\omega_0 r \sim 3 \times 10^{-2}$. The phase relaxation rate $1/r$ does not appear to change in switching crystals, because the high-field conductivity limit is the same for switching as for nonswitching crystals.[2] Large pinning is observed in switching crystals, but it is not so large as to indicate underdamped motion. Since threshold fields[23] scale as ω_0^2, underdamped motion in $NbSe_3$ would imply threshold fields in switching crystals that are roughly a thousand times larger than those in nonswitching crystals. In $NbSe_3$ crystals, the ratio between switching and nonswitching threshold fields is between a factor of three and ten. This discrepancy can be overcome by invoking velocity-dependent pinning or damping, but such extensions appear inconsistent with ac conductivity measurements.[25,26] Lastly, a serious limitation of the single-degree-of-freedom inertial model is that it is unable to provide a plausible explanation for the existence of current domains.

The current-noise model of Wonneberger suffers from the same problems with current domains. The most objectionable feature of this model, however, is the functional form of the conduction noise necessary to induce switching and

hysteresis.[22] During measurements of current noise using a voltage-driven configuration, no large increases in noise have been observed near the critical switching field E_C. This lack of noise is inconsistent with the basic mechanism of Wonneberger's model.

3. A phase-slip mechanism for switching

A common limitation of all the models discussed above is a neglect of CDW amplitude fluctuations. Experiments suggest that switching is intimately tied to the amplitude fluctuations that are associated with velocity discontinuities in switching crystals. The unusual phase polarization which precedes switching also suggests that a primary role is played by CDW pinning and pinning centers. The next section, therefore, turns to a discussion of how amplitude fluctuations can affect both the phase elasticity of a CDW and the effective pinning of a CDW at sites of especially strong pinning.

1. CDW elasticity and amplitude fluctuations

CDW dynamics can be drastically altered by amplitude fluctuations, because the CDW phase and amplitude are not exact normal coordinates of CDW motion.[27] Often this distinction is of little importance. If only weak impurities are present, then the CDW amplitude is uniform in the bulk of a crystal. Therefore the parameters which determine phase motion may be treated as constants. However, if CDW dynamics are dominated by phase slippage (as occurs in regions of CDW velocity discontinuity), rather than by the usual process of phase depinning, then amplitude fluctuations can result in an unstable CDW phase elasticity.

The elasticity of the CDW phase plays a critical role in CDW dynamics. In the Fukayama-Lee-Rice (FLR) Hamiltonian,[28-30] the CDW phase responds as an elastic continuum to the net force resulting from impurity pinning and applied electric fields. The equilibrium phase $\phi(x)$ minimizes an energy given by

$$H = \int d^3x \left\{ \frac{1}{2} \sum_i K_i \left(\frac{d\phi}{dx_i}\right)^2 - \sum_j \rho V_j \delta(\mathbf{x} - \mathbf{x}_j) \cos[\mathbf{Q} \cdot \mathbf{x} + \phi(\mathbf{x})] \right. \tag{3.2}$$

$$\left. - e\rho_{eff} nE\phi(\mathbf{x})/Q \right\}$$

where the first term represents the elastic energy of the CDW, the second term the pinning energy, and the third term the electric field energy. Here the K_i are elastic constants of the CDW phase, V_j is the strength of the jth impurity, and ρ_{eff} is the effective coupling of the CDW to the electric field E. The CDW elasticity is anisotropic. In directions transverse to the CDW wavevector $\mathbf{Q}$, the elastic constant is given by[30]

$$K_{\perp} = \eta^2 K \tag{3.3}$$

where K is the longitudinal elastic constant and $\eta \sim 0.1$ is the bandwidth anisotropy of NbSe$_3$. Following Lee and Rice,[30] anisotropy may be formally eliminated by scaling the transverse spatial dimensions:

$$H_{elastic} = \frac{1}{2} \int dx dy' dz' K'(\nabla'\phi)^2 \tag{3.4}$$

where $dy' = dy/\eta$, $dz' = dz/\eta$, and $K' = \eta^2 K$.

The FLR Hamiltonian is inappropriate for describing large amounts of phase polarization, because it purposely neglects any fluctuations of the CDW amplitude. Since the CDW amplitude is determined by balancing the lattice energy cost of a Peierls distortion against the energy gained from enhanced

electron-phonon interactions in a deformed lattice, large CDW phase gradients reduce the CDW amplitude for two reasons. First, deformations of the CDW phase require an amount of energy proportional to $(\nabla \phi)^2$, so the energy cost of a Peierls distortion is increased. Second, gradients of the CDW phase effectively change the CDW wavevector, so that the energy gained from electron-phonon interactions is reduced. For sufficiently large phase gradients, the CDW amplitude must collapse.

Large phase gradients also reduce the CDW phase elasticity. The general dependence of the restoring force $\delta H_{elastic}/\delta \phi$ on $|\nabla \phi|$ is shown in Fig. 16. For small phase gradients, $\delta H_{elastic}/\delta \phi$ is linear in $|\nabla \phi|$, as discussed by Fukuyama. For large phase gradients, the CDW amplitude collapses; the CDW phase becomes indeterminate; and therefore the restoring force $\delta H_{elastic}/\delta \phi$ must vanish. The effective restoring force attains a maximum value at some critical phase gradient X_c. For phase gradients larger than X_c, the phase elasticity begins to decrease and the restoring force enters an unstable regime. In this regime, amplitude collapse occurs because of positive feedback between increasing polarization and decreasing elasticity.

When amplitude collapse is complete, the CDW phase slips by π (or a multiple, depending on boundary conditions); the gradient $|\nabla \phi|$ decreases; and the amplitude reforms. If polarization has build up over a long distance L, then the reduced gradient after collapse is $(X_m - 2\pi/L)$, where X_m is the gradient at which the CDW amplitude vanishes. When $2\pi/L < (X_m - X_c)$, the CDW elasticity remains unstable after the amplitude reforms, and collapse reoccurs until the forces which produce polarization are reduced. In essence, the
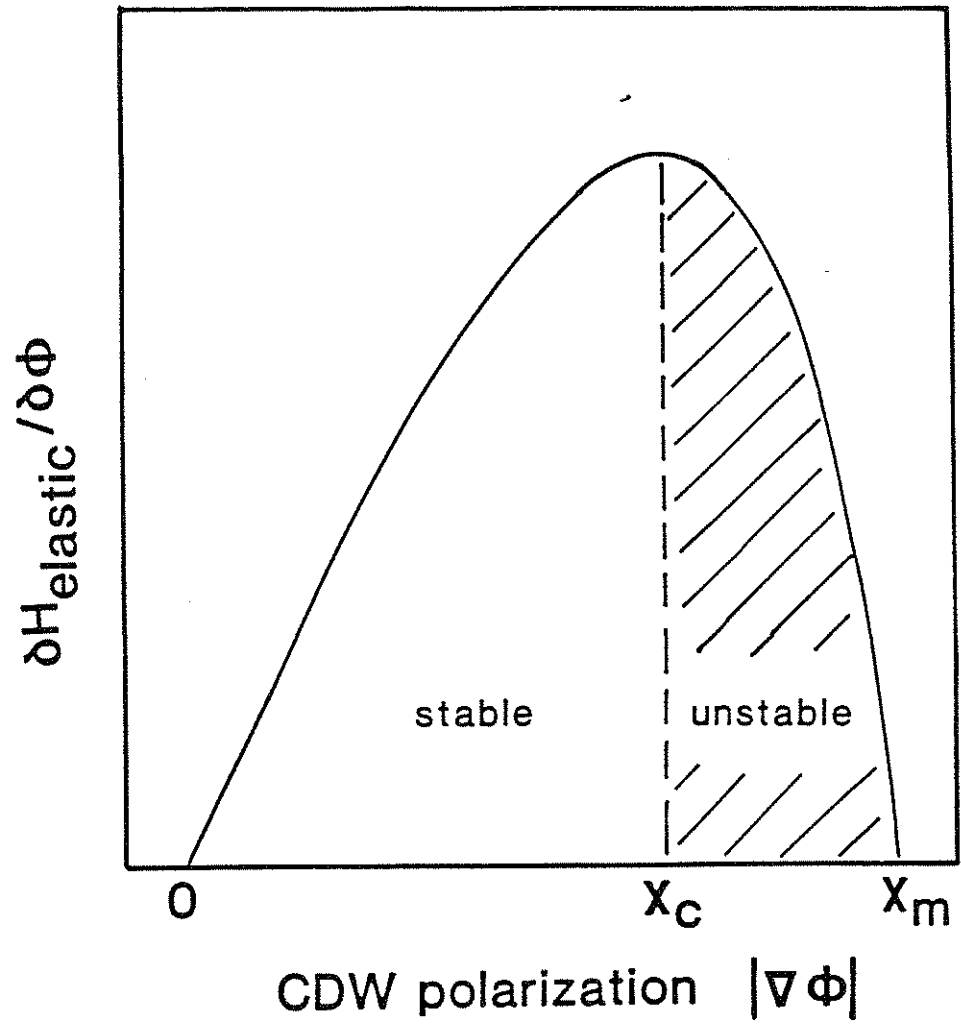
Fig. 3-16)   CDW phase elasticity as a function of CDW phase polarization (see text).

polarization $(X_m - X_c)$ defines a length scale for the stability of the phase mode. Polarization of a CDW over distances longer than $2\pi/(X_m - X_c)$ can lead to an extremely nonlinear response, e.g. abrupt depinning. The critical length for nonlinear effects may be estimated as follows. The energy density $\frac{1}{2}KX_m^2$ is at least as large as the CDW condensation energy $n(0)\Delta_o^2$, where $n(0)$ is the Fermi level density of states and Δ_o is the equilibrium value of the CDW gap. If X is defined to be the fractional polarization $(X_m - X_c)/X_m$, then the *critical polarization length scale* is

$$L_c \gtrsim \xi(\frac{2\pi}{X})\sqrt{K/2n(0)\Delta_o^2\xi^2} \tag{6}$$

where ξ is the CDW amplitude coherence length and $K/2n(0)\Delta_o^2\xi^2 = \pi^2/8$. The fraction X is about 0.4 in Ginzburg-Landau theories, so the length L_C is about 15ξ. In NbSe$_3$, this length is a few hundred angstroms.

2. Switching and velocity discontinuities

This thesis proposes that switching results from the combined effect of elastic instability and phase-slip at strong pinning centers; i.e. at crystal defects that strongly pin the CDW phase. Later, the nature of the strong pinning centers implied by experiments will be considered in detail, but for now a strong pinning center is simply defined as a defect whose pinning strength exceeds the condensation energy of the CDW state.[29,30] Depinning from a strong pinning center therefore occurs only when the CDW amplitude collapses.

In order to make a connection with the results of Fig. 16, consider a highly simplified case in which a CDW is pinned by a concentration n_s of isolated

strong pinning centers in an otherwise perfect crystal at zero temperature. When an electric field is applied, segments of the CDW that lay between pinning centers are restrained from sliding only by the elasticity of the CDW phase. As the strength of the electric field increases, these segments become increasingly polarized. Eventually, the increasing polarization shifts the CDW elasticity from the stable to the unstable region of Fig. 16. Phase slippage then occurs at the strong pinning centers and the CDW begins to slide. If the spacing $L = (\eta^2 n_s)^{-1/3}$ of pinning sites is large enough, then the CDW polarization is not significantly relieved by the phase-slip process. Consequently, the CDW elasticity remains in the unstable regime of Fig. (15) and the CDW velocity is determined only by the applied electric field. The J-E curve is therefore linear past threshold and the CDW jumps immediately into the high-field conductivity state. This produces a sharp switch at threshold and a flat dV/dI curve past threshold. The J-E curve is also hysteretic, because the electric field must be reduced below a smaller threshold $E'_T = E_T(L_c/L)^2$ in order for the CDW elasticity to become stable again. Thus the instability of the CDW phase under large amounts of polarization provides a natural mechanism for abrupt depinning and hysteresis.

Besides abrupt depinning and hysteresis, phase slippage can also produce velocity discontinuities under certain conditions. It is known experimentally that not all strong pinning centers produce velocity discontinuities, since temperature gradient experiments demonstrate the existence of phase-slip centers within current domains. It is also expected theoretically that not all phase-slip centers, e.g. isolated strong impurities, will be strong enough to break

the velocity coherence of a CDW. The problem of velocity discontinuities has been considered in some detail by Gorkov, and independently by Ong and Maki.[34] For a crystal of sufficient width, the most efficient means of creating a CDW velocity discontinuity is via phase vortices.[34] Around a phase vortex, the CDW phase is described by $\phi = \arctan(y/\eta x)$, where the z-axis is chosen to be parallel to the vortex core. The energy density ϵ_{BREAK} necessary to create a phase vortex is quite large compared to the energy density sufficient to depin a CDW. For strong impurities, this ratio is

$$\epsilon_{BREAK}/\epsilon_{DEPIN} \sim (L_o/\xi)\{1 + \alpha \ln(L_o/\xi)\} \tag{3.6}$$

where the first term within the brackets is due to the vortex core and the second term to the elastic energy of the CDW phase. The constant $\alpha = K/n(0)\Delta_o^2\xi^2$ is of order unity, and for strong impurities the FLR length L_o is just the mean distance between impurities. For threshold fields less than 1 V/cm, the ratio L_o/ξ is greater than 8 (assuming $\Delta_o = 35$ meV and $\xi = 20\text{Å}$[40]). Therefore the energy required to create a vortex is an order of magnitude larger than the energy required to depin a CDW. This implies that a random distribution of strong impurities will not lead to the velocity discontinuities that are associated with switching in NbSe$_3$. A similar conclusion holds for weak impurities.

A plausible suggestion is that the strong-pinning and phase-slip centers associated with velocity discontinuities arise from "ultrastrong" pinning sites. Essentially, ultrastrong pinning centers are large-scale versions of single impurities. Ultrastrong pinning centers, for example, might arise from abnormally high local concentrations of strong impurities, or other crystal

defects such as dislocation lines or phase inclusions (in the case of $Fe_x NbSe_3$).
Because of their larger size, however, ultrastrong pinning centers tend to form
vortices and hence velocity discontinuities.

The pinning effect of an ultrastrong pinning site depends on its size and, to
a more limited degree, on its shape. When a center's cross-section is one-
dimensional, amplitude collapse occurs over the entire center. The pinning
energy of the center is

$$E(\varsigma) \sim \eta \, n(0)\Delta_o^2\xi^2\varsigma \qquad (3.7)$$

where ς is the effective center diameter. In contrast, if a center's cross-section is
two-dimensional, then amplitude collapse over the entire center is energetically
unfavorable. Instead, phase-slippage occurs by vortex rings that form around
an effective circumference of the center. The pinning energy of the center
would be roughly

$$E(\varsigma) \sim \eta \, n(0)\Delta_o^2\xi^2\varsigma\{1 + \alpha \ln(\varsigma/\eta\xi)\} \qquad (3.8)$$

where ς now represents the effective circumference. For any shape center, the
local energy density necessary for phase-slippage is about

$$\epsilon(\varsigma) \sim \eta \, E(\varsigma)/\varsigma^3 \; . \qquad (3.9)$$

Whenever the characteristic size of an ultrastrong pinning center becomes
comparable to the transverse dimensions of a crystal, the center is likely to
cause a discontinuity in CDW current.

Large phase polarization, and thus switching, would be produced by a
distribution of ultrastrong pinning centers whose concentration is sparse on the

length scale of $[K/2\epsilon(\varsigma)]^{1/2}$ where ς is the effective center size. When a crystal contains centers with a variety of sizes, the spatial arrangement of the centers as well as their sizes is important. With an absolutely uniform distribution of centers, two additional length scales are set by those centers whose combined size ς_M and density $n(\varsigma_M)$ have the largest pinning effect on the CDW:

$$n(\varsigma_M)E(\varsigma_M) = \max_{\varsigma} n(\varsigma)E(\varsigma) . \tag{3.10}$$

The *phase-slip length scale* L_{PS} is the mean distance between defects of size ς_M. The *switching length scale* L_{SW} is the critical pinning center spacing that determines whether depinning causes the CDW phase elasticity to enter the unstable regime of Fig. (15):

$$L_{SW} \gtrsim \sqrt{K/2\epsilon(\varsigma_M)} . \tag{3.11}$$

In the absence of additional impurities, a CDW depins when the electric field energy density exceeds $n(\varsigma_M)E(\varsigma_M)$. Switching occurs if the phase-slip length scale is longer than the switching length scale.

Real switching crystals have pinning inhomogeneities that presumably correspond to a random distribution of centers, not a uniform distribution. Randomness complicates the definition of phase-slip and switching length scales. For a given electric field, whether phase-slippage occurs at centers of a particular size ς depends not only on the product $n(\varsigma)E(\varsigma)$, but also on the size and density of neighboring centers. The dominant defect size ς_M can be lowered by avalanche effects. If ς_M is the dominant size in a uniform distribution, then in a random distribution some centers of size ς_M will occur in portions of a crystal that have less pinning than the average. The CDW at those centers will

depin at field energies less than $n(\varsigma_M)E(\varsigma_M)$. The premature depinning will increase the strain on neighboring sections that have not yet depinned, and the additional strain can trigger a depinning wave within the crystal. Avalanche events of this nature can explain the sublevels within hysteresis loops,[12] the breakup of switches under temperature gradients, and the delay times observed in pulsed experiments.[13] Avalanche events also provide an important connection with the concept of a depinning wave in the Joos-Murray model.

3. Regimes of switching

For clarity, our discussion has thus far neglected the complications caused by finite temperature effects and the presence of weak impurities. In this section, we consider these effects, which play an important role in determining whether switching is observed in real crystals.

a. Impurity concentrations

When only weak impurities are present within a CDW conductor, their concentration determines a FLR phase-coherence length L_W.[3-5] When both weak and strong pinning centers are present, the ratio of the weak impurity FLR length L_W to the phase-slip length L_{PS} determines the qualitative nature of CDW dynamics. For $L_{PS} \gg L_W$, CDW sliding is dominated by phase-depinning, but for $L_{PS} \ll L_W$, CDW dynamics are governed by phase-slip. For $L_{SW} \ll L_{PS} \ll L_W$, switching can occur. The existence of these regimes has at least two experimental implications. First, doping a crystal with strong impurities will cause switching only if the weak impurity concentration is sufficiently low. If the weak impurity concentration is too large, then L_W is

comparable to L_{SW} and consequently the condition for switching can not be satisfied. Second, the current contacts to a crystal, even though they may strongly pin a CDW, in general will not cause switching. In a crystal with only weak impurities, the phase-slip length is simply the distance between contacts. Since typical crystal lengths are much longer than the FLR length, contacts cannot cause switching. Even if a sample's length were reduced below the FLR length, switching still might not occur, unless the weak impurity concentration were sufficiently low so that $L_{SW} \ll L_W$. This might explain why simply reducing the length of nonswitching samples has not been observed to induce switching.

b. Finite temperature effects

Nonzero temperatures cause the phase-slip and switching lengths to change from their $T = 0$ values. In superfluids[32] and superconductors,[33] phase-slippage is thermally activated. Gill[34] has recently proposed that phase slippage at the contacts of CDW conductors is also thermally activated. The activation energy in Gill's work would correspond to the defect energy $E(\varsigma)$ described in this paper. The result of thermal activation would be to reduce the pinning effect of small centers compared to the effect of large centers. For uniform distributions, this would make both the dominant center size ς_M and the switching threshold field strong functions of temperature.

The fact that switching thresholds are independent of temperature is evidence that strong pinning centers are distributed nonuniformly. If depinning occurs by phase-slip cascades, then switching critical fields should be strongly temperature dependent only until the dominant centers are "frozen in"; after

that, threshold fields should be determined by the spatial arrangement of the dominant centers. In NbSe₃, thermal activation is consistent with the rapid increase in threshold field that is associated with the onset of switching. Fig. 17 shows the threshold field as a function of temperature for a switching NbSe₃ crystal. Switching occurs below 40 K, where the threshold field is relatively independent of temperature. Above 40 K, the threshold field has been fit to

$$E_T(T) = E_o \exp\{E(\varsigma)/k_B T\} \tag{3.12}$$

where $E_o = 7.0 \, \mu V/cm$, $E(\varsigma) = 41$ meV, and k_B is Boltzman's constant. The value of $E(\varsigma)$ is relatively insensitive to the form assumed for $E_T(T)$; a fit to $E_T(T) = (k_B T/L') \exp\{E(\varsigma)/k_B T\}$ yields $E(\varsigma) = 50$ meV. Assuming that Eq. (7) applies, 40 meV corresponds to $\varsigma = 0.1 \, \mu m$. Below 40 K, the sharp change in slope indicates that thermal activation is no longer important.

Thermal activation during the onset of switching also agrees qualitatively with the consistent decrease in switching onset temperatures that coincides with increasing crystal quality. In general, one would expect that smaller ultrastrong pinning centers would be necessary to induce switching in higher quality crystals, since the effect of weak impurities is smaller in these crystals. Therefore, higher quality crystals should have lower switching onset temperatures. This correlation is indeed observed in our experiments and in the experiments of other groups. Switching-like behavior occurs at very low temperatures in extremely high quality NbSe₃ crystals. Coleman[6] has reported striking zero-differential resistance anomalies at 1.1 K in NbSe₃ crystals that have threshold fields of ~1 mV/cm at 48 K. Switching occurs at the next lowest temperatures (~30 K) in the moderate quality NbSe₃ used in the present
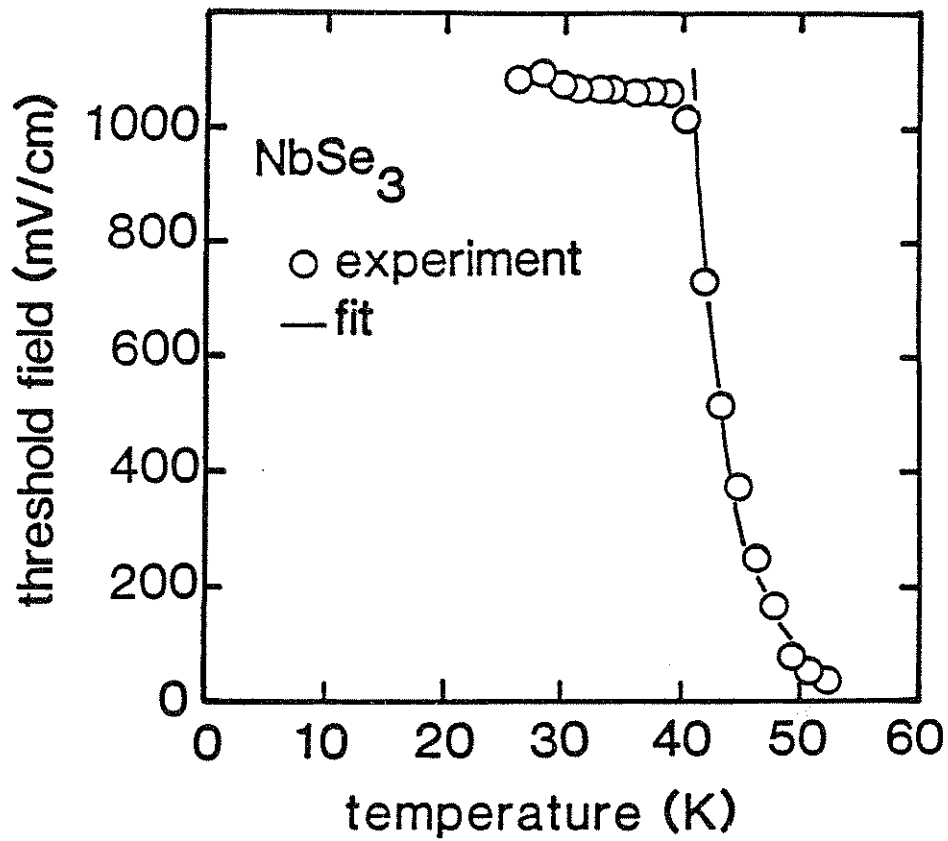
Fig. 3-17) Fit of the onset of switching in NbSe$_3$ to an activated temperature behavior. The solid line is Eq. 3.12, with parameters given in the text.

experiments ($E_T \sim 30 \, \text{mV/cm}$ at 48 K). Switching occurs at the highest temperatures (~ 50 K) in $Fe_x NbSe_3$, which even in nonswitching crystals has threshold fields of at least 100 mV/cm at 48 K.

c. Lattice defects

The occurrence of switching in nominally pure $NbSe_3$, as well as $Fe_x NbSe_3$, suggests that strong pinning centers may result not only from strong impurities, but also lattice defects. Gross lattice defects — such as grain boundaries or twinning — are probably unimportant. Grain boundaries and twinning occur infrequently in $NbSe_3$ crystals,[35] at levels of less than once in 100 μm^3; such levels are too low to explain the nonuniform pinning that is observed in temperature gradient experiments. On the other hand, smaller defects — such as dislocation lines — could strongly pin a CDW at densities low enough to give large variations in pinning. For example, a dislocation line density of 4 μm^{-3} with an average line length of 0.25 μm (corresponding to a dislocation density of 1 μm^{-2}) would lead to $\pm 50\%$ pinning energy fluctuations between 1 μm^3 segments in $NbSe_3$. Roughly order-of-magnitude pinning fluctuations would be relatively common, and $\pm 50\%$ variations would persist over distances of 100 μm (assuming a 1 μm^2 crystal cross-section).

Little has been published about defect densities in $NbSe_3$. Satellite dark field micrographs of some $NbSe_3$ crystals show lattice dislocation densities of roughly 1 μm^{-2}, while other crystals are apparently defect free.[36] The conventional method of sample growth of $NbSe_3$ and $Fe_x NbSe_3$ should lead to vacancy densities of about 10 ppm, and vacancies are known to precipitate dislocations. The observed "aging" effect of switching crystals may be due to

physical or chemical changes around dislocation sites. Etches of H_2SO_4 preferentially attack dislocation sites in niobium,[37] and they may preferentially attack dislocations in $NbSe_3$. This might explain why H_2SO_4 would restore switching in aged batches, but not induce switching in originally nonswitching crystals, as observed. It would be highly desirable to examine the strong pinning centers in switching crystals by TEM.

IV. Summary

This chapter has reported the dc characteristics of switching crystals of $NbSe_3$. Most of the detailed experimental results have been summarized at the beginning of Sec. III. Besides the abrupt depinning and hysteresis observed in dc I-V curves, the characteristics of switching crystals include:

1)   Discontinuities in CDW current, which imply the existence of phase-slip centers.

2)   Sublevels within hysteresis loops, which suggest avalanche-type depinning among phase-slip centers; and

3)   Changes in subthreshold resistivity, which indicate large polarization of the CDW phase before the onset of abrupt depinning.

The origin of these three effects — phase slippage, avalanche depinning, and CDW polarization — is explained by strong, non-uniform pinning of a CDW within a switching crystal. The existence of strong, non-uniform pinning is demonstrated in independent experiments, such as cutting and cleaving $NbSe_3$ crystals.

In order to explain the origin of abrupt depinning and hysteresis, the analysis section of this chapter examined a variety of models. The experimental results are most consistent with a phase-slip interpretation of switching that is based on fluctuations of the CDW amplitude. In essence, the pinning of a CDW depends on the elasticity of the CDW phase, and amplitude fluctuations can cause the elasticity to become unstable. If the elasticity becomes unstable, then abrupt depinning occurs because the forces which impede CDW motion effectively collapse.

Finally, a distinction is drawn between abrupt depinning, which can occur in the presence of isolated strong impurities, and current discontinuities, which require the presence of much larger pinning centers. These so-called ultrastrong pinning centers are presumed to be phase inclusions (in the case of iron-doped $NbSe_3$) or lattice defects (in the case of undoped $NbSe_3$). The characteristic size of an ultrastrong pinning center in $NbSe_3$ is estimated to be about 0.1 μm.

CHAPTER 4: AC CHARACTERISTICS

CHAPTER 4: AC CHARACTERISTICS

The dynamics of switching CDWs are explored further in this chapter, by studying the response of both pinned and sliding CDWs to small ac electric fields. Results show that when switching CDWs are pinned, their dynamics are equivalent to the dynamics of nonswitching CDWs; but when switching CDW are depinned, their dynamics are quite different. Analysis of the results suggests that the dichotomy between pinned and sliding CDW dynamics is consistent with a phase-slip interpretation of switching. Thus the results and analysis emphasize that switching represents a unique regime of CDW motion, in which amplitude dynamics are as important as phase dynamics to a description of CDW sliding.

I. Methods and Results

Measurements of ac conductivity were performed on single crystals of $NbSe_3$ or iron-doped $NbSe_3$.[6] Chapter 3 describes the preparation and characteristics of the crystals used in these experiments. Only results on $NbSe_3$ are reported here, because results on iron-doped $NbSe_3$ are essentially identical. The ac conductivity of a sample was measured in either the presence or absence of a dc bias field. A voltage of the form

$$V = V_{dc} + V_{ac} \cos \omega t \qquad (4.1)$$

was applied to the sample and the current response I_{ac} of the sample was detected synchronously using a phase-sensitive amplifier. At low frequencies $10\,\mathrm{Hz} \leq \omega/2\pi \leq 5\,\mathrm{MHz}$, an HP 4192 impedance analyzer was used to make two- and four-probe measurements of the sample response. At higher

frequencies, $4\,\mathrm{MHz} \le \omega/2\pi \le 500\,\mathrm{MHz}$, an HP 8754A network analyzer was used to make two-probe measurements. The ac test signal was 1.0 or 2.5 mV rms, for high and low frequencies, respectively; whereas threshold voltages for the onset of CDW sliding were 3 to 30 mV in a typical sample, at high and low temperatures, respectively. The dc bias voltage varied between zero and several times the sample threshold voltage.

Measurements were made at temperatures below 59 K, in the lower CDW state of $NbSe_3$. In principle, the response of a crystal consists of contributions from the upper ($T_c = 144$ K) and lower CDW states of $NbSe_3$, as well as from uncondensed electrons. However, at the frequencies and voltages applied in these experiments, the upper CDW state of $NbSe_3$ does not contribute to the total electronic current. Furthermore, the conductivity due to uncondensed electrons (measured at temperatures above 144 K) has no frequency dispersion. Therefore the ac conductivity of the lower CDW state is defined as

$$\sigma_{\mathrm{CDW}} = I_{\mathrm{ac}}/V_{\mathrm{ac}} - \sigma_o , \qquad (4.2)$$

where σ_o is the low-field dc conductivity of the crystal (due to uncondensed electrons).

The experimental set-up permitted measurements of dc I-V curves and narrowband noise spectra, in addition to measurements of ac conductivity. In order to make a connection with the results of Chapter 3, Figure 1 shows the (current-controlled) I-V characteristics of a switching crystal at high and low
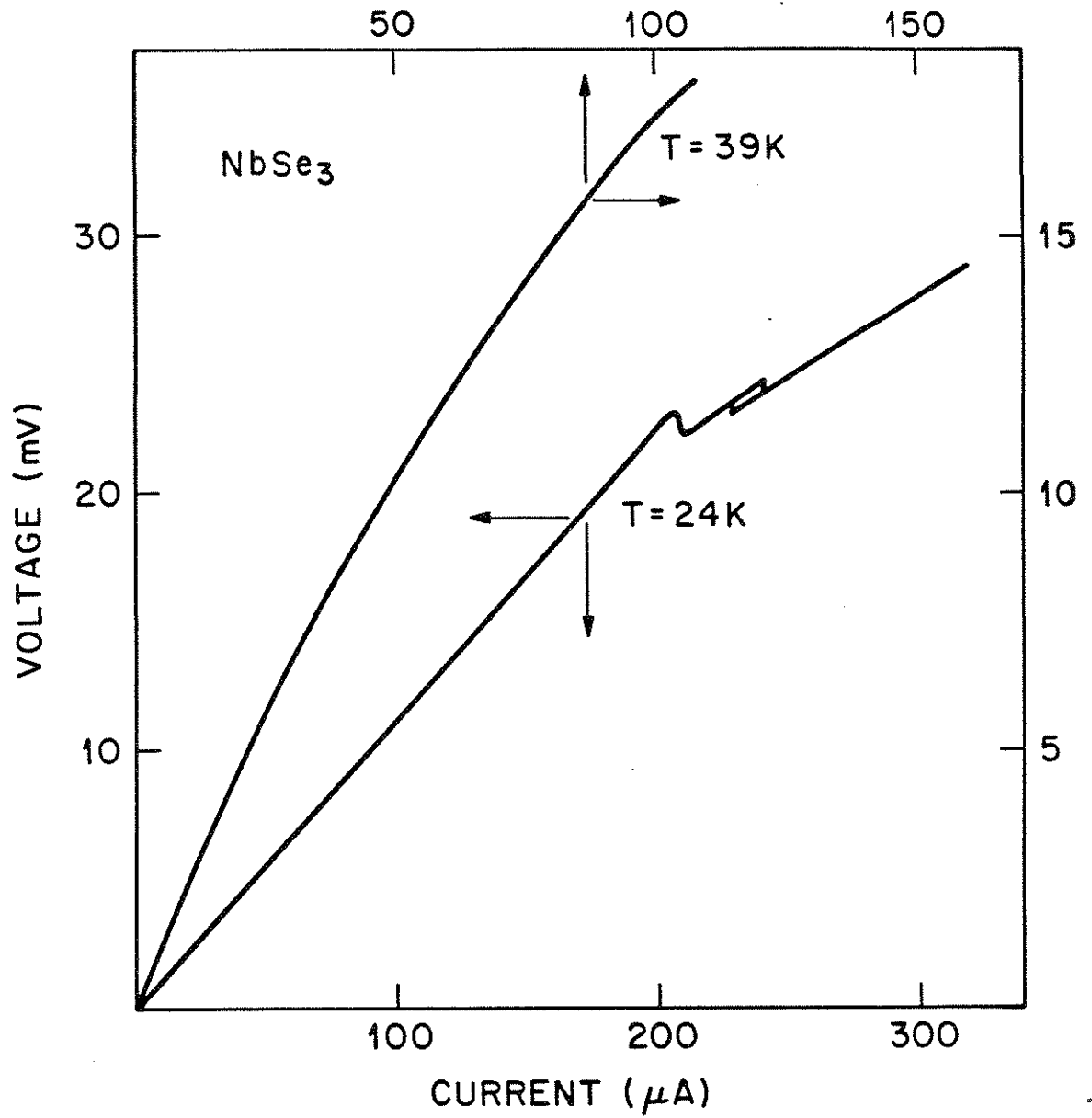
Fig.4-1)   Current-controlled I-V curves for a switching crystal of NbSe₃, at temperatures above (39 K) and below (24 K) the onset of switching.

temperatures. At the higher temperature, 39 K, the response of the crystal is indistinguishable from the response of a nonswitching crystal. The I-V curve becomes smoothly nonlinear for bias currents exceeding 24 μA (corresponding to a threshold field of $E_T = 41$ mV/cm), and narrowband noise spectra show that the departure from ohmicity is due to uniform depinning of the CDW throughout the crystal. But at the lower temperature, 24 K, the I-V curve is broken at two critical biases, $I_{C1} = 206$ μA and $I_{C2} = 242$ μA (corresponding to critical fields of $E_{C1} = 328$ mV/cm and $E_{C2} = 348$ mV/cm, respectively). The first break is produced by a region of steep negative differential resistance,[2,8] whereas the second break is marked by a sharp, hysteretic switch. The existence of two critical fields indicates that the CDW does not depin uniformly. Instead, the CDW forms two current domains and each domain depins separately. Narrowband noise spectra confirmed the presence of two incommensurable noise fundamentals, and hence the existence of two independent current domains. The drastic change in the dc characteristics of this crystal between high and low temperatures is typical for switching crystals, but does not occur in nonswitching crystals.

In contrast to dc conductivity, the ac conductivity of a switching crystal does not change qualitatively between high and low temperature, as long as the CDW remains pinned. Figure 2 shows the pinned, $V_{dc} = 0$ conductivity of the same crystal at 47 and 24 K. At 47 K, the in-phase component of conductivity (Re σ_{CDW}, open circles) is zero at low frequencies and increases monotonically with increasing frequency. The out-of-phase component (Im σ_{CDW}, open
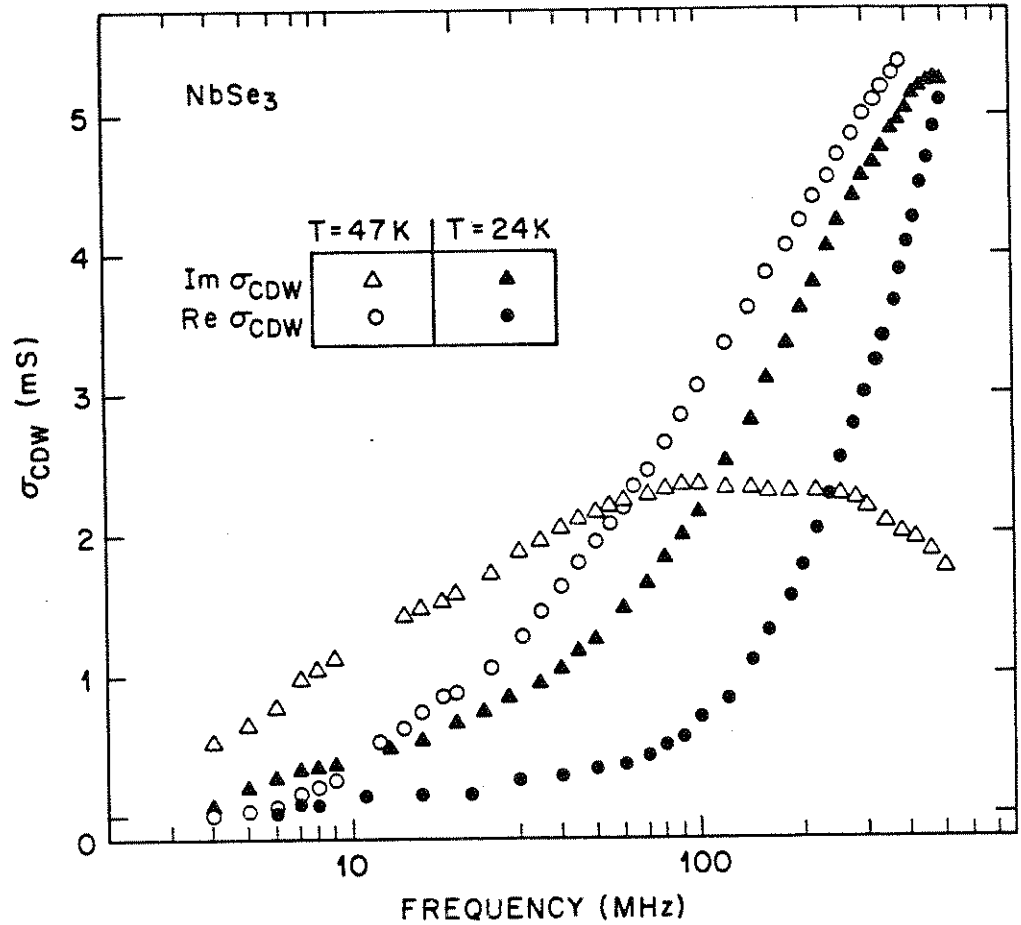
Fig.4-2)   The zero-bias, complex conductivity of the crystal in Figure 4-1. Circles and triangles indicate the in-phase and out-of-phase components of conductivity, respectively. Open and filled symbols indicate data taken at 47 and 24 K, respectively.

triangles) is small but nonzero at low frequencies; increases until moderately high frequencies; and then decreases for frequencies past 200 MHz. A crossover frequency,[9] $\omega_c/2\pi = 60$ MHz, defines the frequency above which Re σ_{CDW} exceeds Im σ_{CDW}. The general shape of σ_{CDW} is described by the response of an overdamped harmonic oscillator. In particular, Im σ_{CDW} remains positive even at frequencies exceeding the crossover frequency by an order of magnitude.

Some relatively minor changes are apparent in the conductivity at 24 K (filled symbols). The crossover frequency has increased from 60 to 500 MHz, and the conductivity at the crossover frequency has increased from 2.25 to 5.25 mS. Also, the shape of σ_{CDW} has changed slightly. The slopes of Re and Im σ_{CDW} are flatter at low frequency and steeper near the crossover frequency. However, similar changes in the shape of $\sigma_{CDW}(\omega)$, and in the magnitudes of ω_c and $\sigma_{CDW}(\omega_c)$, are observed in nonswitching CDWs.[5] The pinned conductivities of switching and nonswitching CDWs are generally indistinguishable, whether at high or low temperatures.

Many of the similarities in the ac response of switching and nonswitching CDWs disappear when the CDWs begin to slide. Figure 3 shows the low-temperature conductivity of the crystal in Figs. 1 and 2 at three dc biases: a subthreshold bias, 186 μA, just below I_{C1}; and two sliding biases, 210 μA and 243 μA, just above I_{C1} and I_{C2} respectively. The subthreshold conductivity is identical to the conductivity in Fig. 2, but the sliding responses deviate substantially.
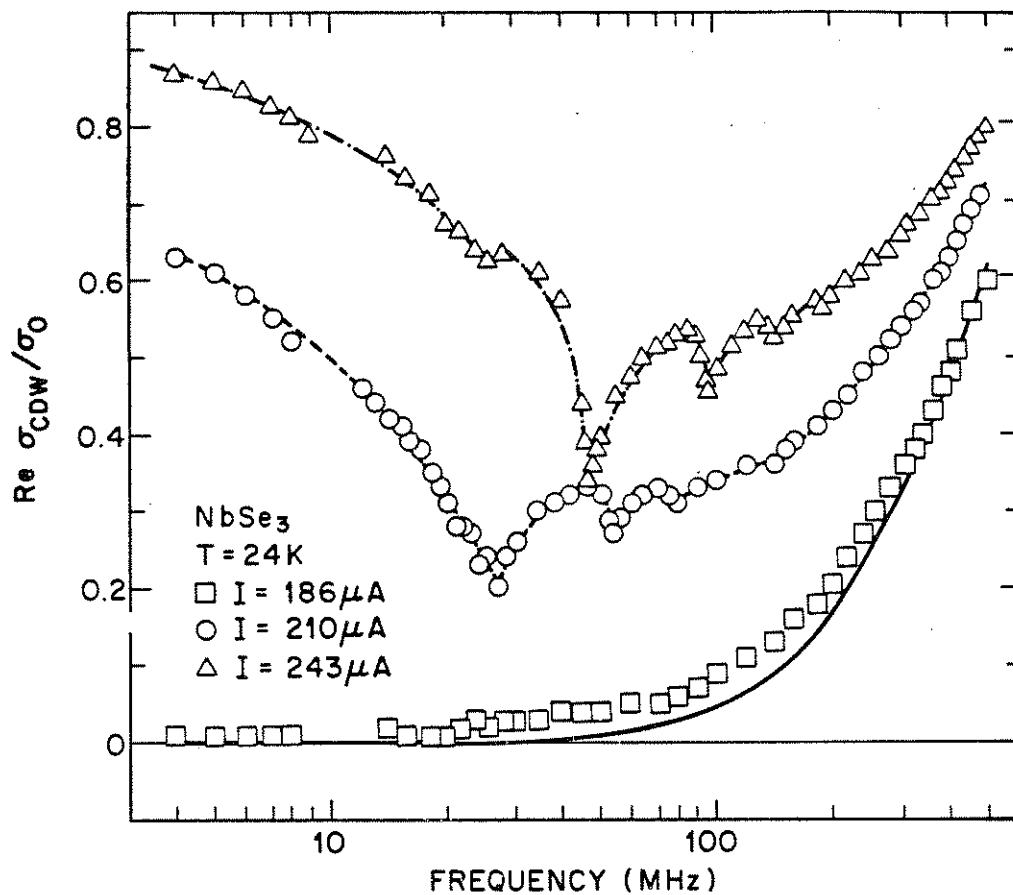
Fig. 4-3.a)   The in-phase component of ac conductivity, at 24 K, for the crystal from Figure 4-1. The data are taken at three dc biases: just below the first break in the I-V curve of Fig. 4-1, just above the first break, and just above the second break. The lines are guides for the eye.
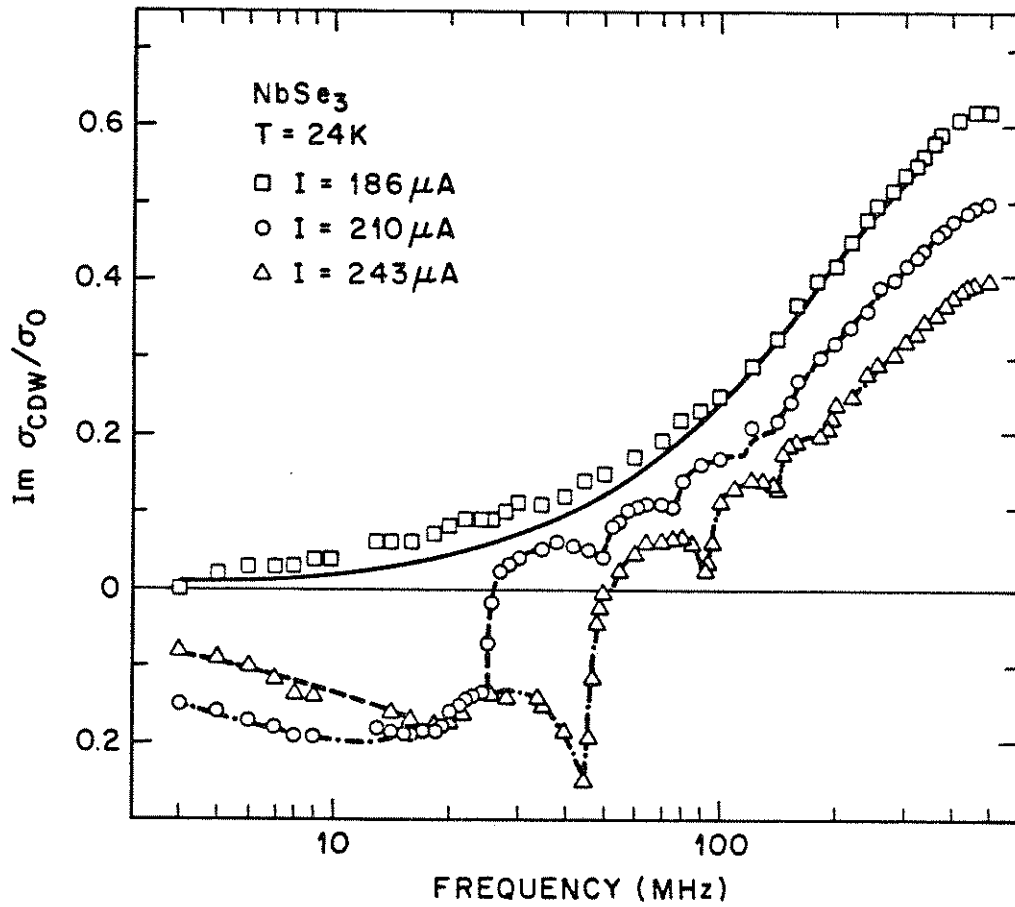
Fig. 4-3.b)   The out-of-phase component of ac conductivity, taken at the same three dc biases as in Fig. 4-3a.

At high frequencies, differences between the pinned and sliding CDW responses are the least pronounced. In Fig. 3, the sliding response of the CDW asymptotically approaches the pinned response at frequencies above 200 MHz. The real component of conductivity approaches the pinned data from above, while the imaginary component approaches from below. As the dc bias increases, from 210 to 243 μA, convergence recedes to higher frequencies. Similar behavior is observed in the high frequency behavior of nonswitching CDWs.[9] As discussed in Sec. II, the high-frequency convergence of pinned and sliding responses, both in switching and nonswitching CDWs, can be attributed to the effect of internal deformations of the CDW phase.[15]

At intermediate frequencies, the sliding conductivities in Fig. 3 are marked by a series of sharp interference features that occur when the ac frequency matches a narrowband noise fundamental or one of its leading harmonics. With a current bias of 210 μA, interference effects occur at 27, 54, and 81 MHz due to the narrowband noise associated with the first current domain that depins at 206 μA. With a current bias of 243 μA, the interference features that are prominent at 46, 92, and 138 MHz are again due to the first domain. In addition, a small feature occurs at 26 MHz due to the second current domain. (The narrowband noise signal of the second current domain was much smaller than the signal of the first, which presumably explains why the interference effect produced by the second domain is so weak.) Interference effects also occur in nonswitching crystals,[9] although only one series of peaks is usually observed.

Differences between the pinned and sliding CDW responses are largest, both quantitatively and qualitatively, at frequencies below the narrowband noise frequency. For example, Re σ_{CDW} in the pinned data is less than $0.03\,\sigma_0$ between 4 and 27 MHz, while Re σ_{CDW} in the 210 μA data begins at $0.60\,\sigma_0$ and then decreases by over 60 percent. Similarly, Im σ_{CDW} in the pined data begins at zero and increases to $0.10\,\sigma_0$, while Im σ_{CDW} in the sliding data begins at $-0.15\,\sigma_0$ and decreases to $-0.20\,\sigma_0$ before slightly increasing again. At least for Re σ_{CDW}, the difference between pinned and sliding conductivities at the lowest frequencies can be explained by the I-V curve in Fig. 1. The dc differential conductance of a CDW is the $\omega = 0$ limit of ac conductivity. In Fig. 1, the conductance of the CDW at 210 μA is $0.67\,\sigma_0$, a value which is close to the observed value of Re σ_{CDW} at 4 MHz. But the other aspects of Fig. 3 — the large dispersion in Re σ_{CDW} and the inductive behavior of Im σ_{CDW} over a decade in frequency — are quite striking and are without parallel in the conductivity of nonswitching CDWs.

In nonswitching CDWs, the sliding conductivity remains equal to $\omega = 0$ limit, Re $\sigma_{CDW} = dI/dV - \sigma_0$ and Im $\sigma_{CDW} \cong 0$, until just below the narrowband noise frequency.[9] Inductive features are sometimes seen in nonswitching CDWs over narrow frequency ranges where the ac frequency matches the narrowband noise frequency, but the features in Fig. 3 are much larger. To underscore the size of inductive features in switching crystals, Figure 4 shows the conductivity of a second NbSe$_3$ crystal, measured at frequencies from 10 Hz to the narrowband noise frequency of 1 MHz. Both Re
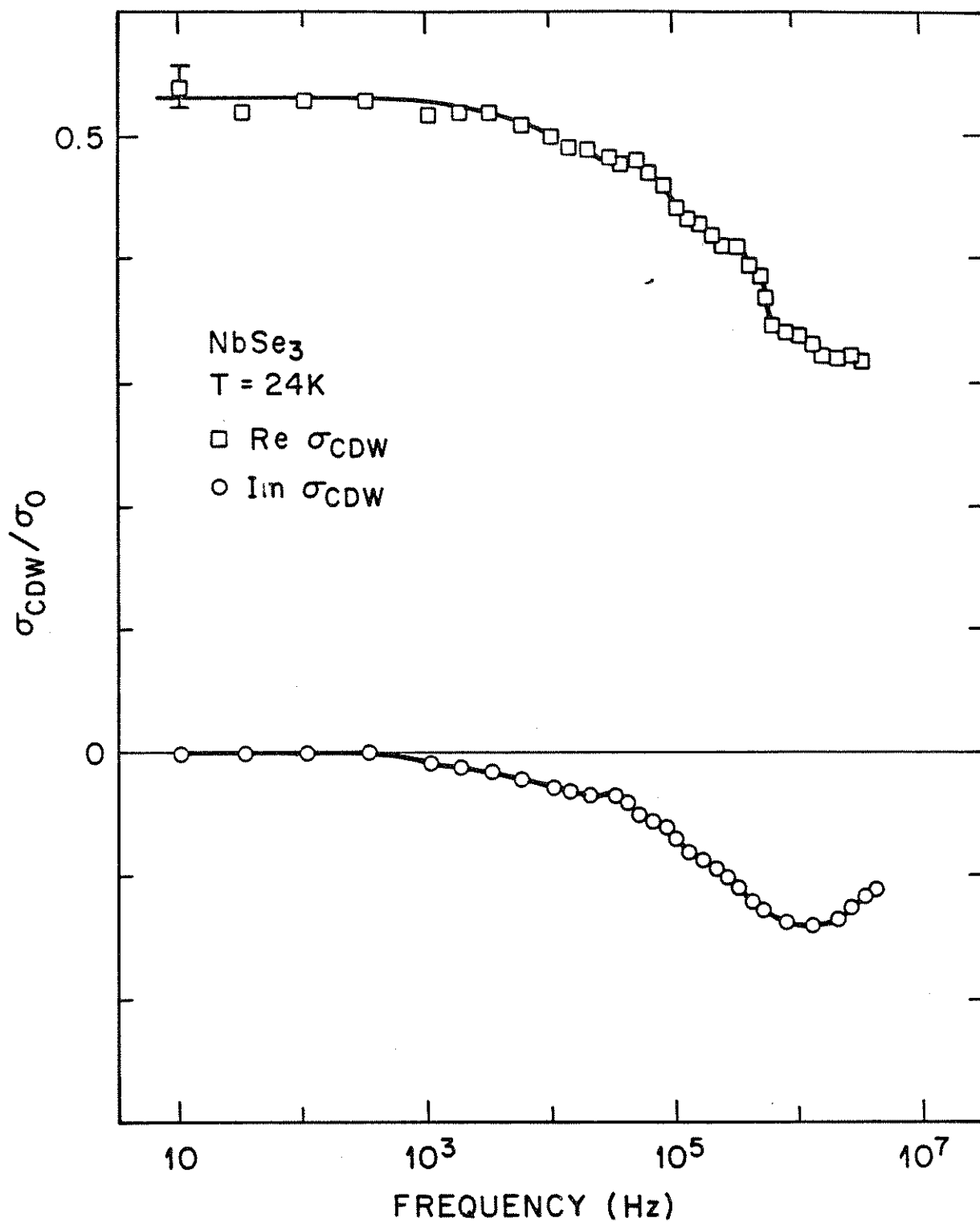
Fig. 4-4) The low-frequency, complex conductivity of a second switching crystal of NbSe$_3$, taken at a dc bias where the narrowband noise frequency is about 1 MHz. The lines are guides for the eye.

and Im σ_{CDW} are reduced below their $\omega = 0$ limits over very broad frequency ranges, 3 decades in frequency from 1 kHz to 1 MHz. These large, broad reductions in Re and Im σ_{CDW} are characteristic features in the conductivities of all the switching crystals that were examined. These features shall be refered to as *inductive anomalies.*

The effect of inductive anomalies can be displayed in an alternative fashion by fixing the ac frequency and sweeping the dc bias. Figure 5 shows the conductivity at 4 and 50 MHz for the crystal of Figs. 1-3. Two separate depinnings of the CDW, one by each current domain, are evident in the data for Re and Im σ_{CDW}. Each depinning causes an abrupt increase in Re σ_{CDW} and an abrupt decrease in Im σ_{CDW}. In addition, both Re and Im σ_{CDW} decrease as the narrowband noise frequency (of the first current domain) approaches the frequency of the ac signal. This effect is observable only in the 50 MHz data, since narrowband noise frequencies in this crystal are always well above 4 MHz because of switching. A striking feature of Fig. 5a is that the 4 MHz data is *larger* than the 50 MHz data when the CDW is depinned. The 50 MHz data exceed the 4 MHz data only when the CDW is pinned or when the current bias is much greater than 300 μA. In a nonswitching crystal, a conductivity measured at 50 MHz always exceeds a conductivity measured at 4 MHz, because the conductivity of a nonswitching CDW is a monotonically increasing function of ac frequency and dc bias. The inversion of conductivities in a switching CDW is produced by the unusual dispersion of inductive anomalies, in which CDW conductivity decreases with increasing frequency.
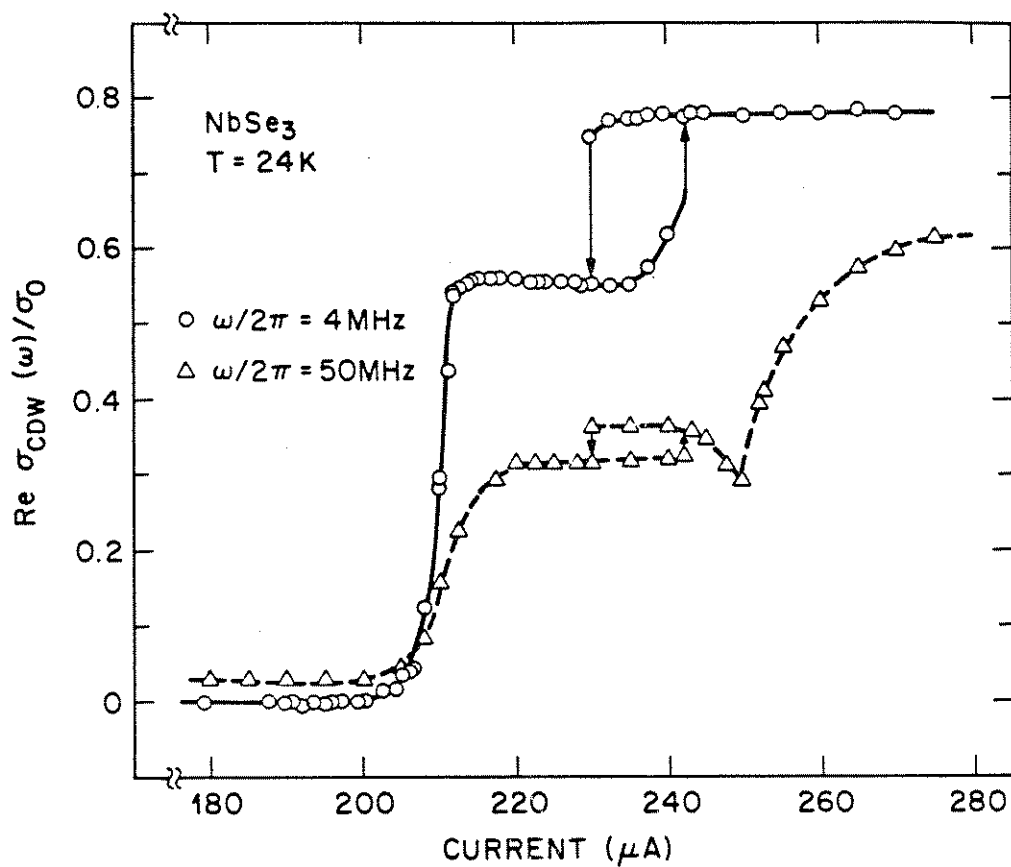
Fig. 4-5.a)   The in-phase conductivity, measured at 4 and 50 MHz, for the crystal from Fig. 4-1 as a function of dc bias. Except when the CDW is pinned, the 50 MHz conductivity is smaller than the 4 MHz conductivity. The lines are guides for the eye.
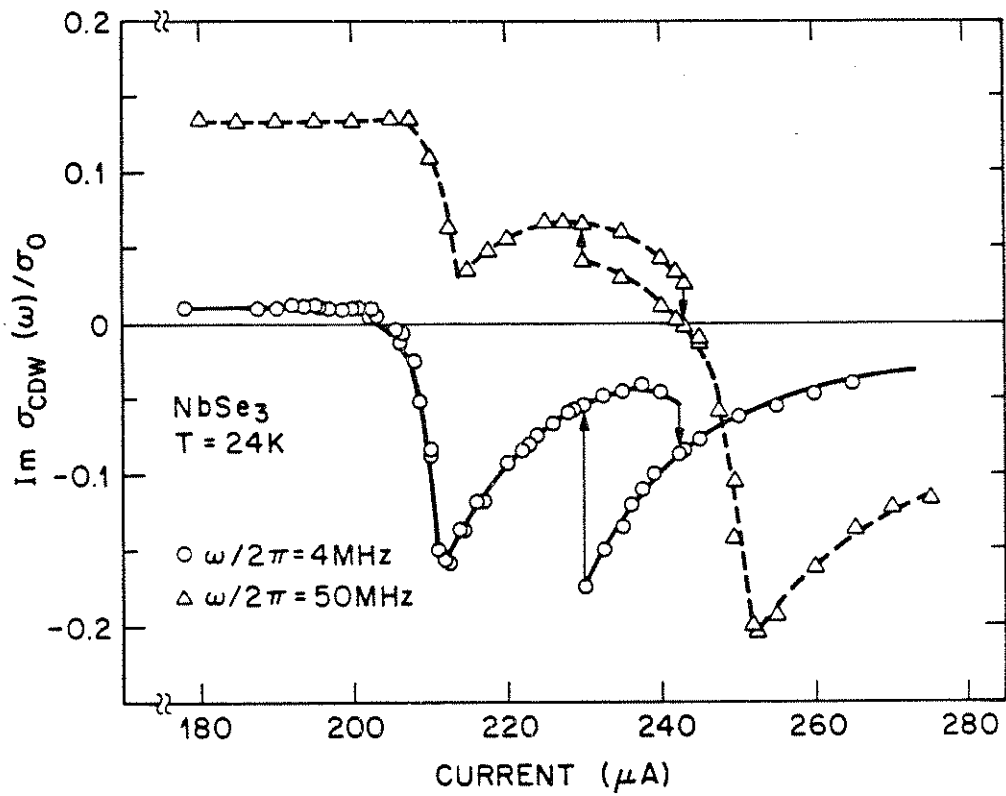
Fig. 4-5.b) The out-of-phase conductivity as a function of dc bias, measured
as in Fig. 4-5a.

A final observation concerns the temperature dependence of inductive anomalies. Although inductive anomalies have been observed only in crystals that display switching, inductive anomalies have been observed at temperatures well above the onset of switching. For example, switching and hysteresis in one crystal were observed starting at temperatures below 30 K, but inductive anomalies were observed at temperatures as high as 42 K. Inductive anomalies are not unusual in this respect. Other phenomena connected with switching, such as a bistable low-field resistance[1] or a period-doubled response to ac signals,[2,10] also are observed above the onset of switching. In fact, all three phenomena are closely related by their dependence on a polarized CDW phase, as shall be explained in the next section.

II. Analysis

CDW dynamics may be analyzed in terms of the classical, rigid-phase model of Grüner, Zawadowski, and Chaikin.[11] The model is relatively simple, possesses an intuitive physical interpretation, and qualitatively reproduces many aspects of the ac conductivity of nonswitching CDWs. These advantages make the rigid-phase model a useful starting point for a discussion of the ac conductivity of switching CDWs.

The rigid-phase model treats the CDW amplitude as fixed and the CDW phase as uniform throughout a CDW conductor. The equation of motion is

$$\frac{d^2\phi}{dt^2} + \frac{1}{\tau}\frac{d\phi}{dt} + \omega_0^2 F(\phi) = \frac{e}{m^*}EQ \ , \qquad (4.3)$$

where ϕ is the CDW phase; m^* is the effective CDW mass; Q is the CDW wavevector; and τ is a phenomenological time-constant describing dissipation.

The frequency ω_0 parametrizes the strength of CDW pinning, and the function $F(\phi)$ is a dimensionless pinning force. The pinning force is a periodic function of the CDW phase, and is usually approximated by its first Fourier component, $F(\phi) = \sin\phi$. Equation 3 may be rewritten in a dimensionless form,

$$\beta\ddot{\phi} + \dot{\phi} + F(\phi) = e_{dc} + e_{ac}\cos\Omega t , \qquad (4.4)$$

where superscript dots represent differentiation with respect to time, which is measured in units of $(\omega_0^2\tau)^{-1}$. The frequency of the ac field is normalized to the corresponding unit of frequency, $\Omega = \omega/(\omega_0^2\tau)$, and the dc and ac field strengths are normalized to the threshold field: $e_{dc} = E_{dc}/E_T$ and $e_{ac} = E_{ac}/E_T$, where $E_T = m^*\omega_0^2/eQ$.

The remaining coefficient in Eq. 4 is the inertial parameter, $\beta = (\omega_0\tau)^2$. The inertial parameter is basically the time-constant with which the CDW velocity approaches equilibrium. When β is zero or small, the CDW velocity is a deterministic function of the electric field and CDW phase, $\dot{\phi} = e - F(\phi)$. In this case, CDW dynamics are referred to as *overdamped*. When β is large, the CDW velocity lags behind the difference of the field and pinning forces, and CDW dynamics are called *underdamped*. In nonswitching crystals of NbSe$_3$, the inertial parameter is negligibly small and CDW dynamics are overdamped.[12] Typical numbers are $\tau = 2.3\times10^{-12}$ sec and $\omega_0 = 16$ GHz, which yield an inertial parameter of $\beta = 1.4\times10^{-3}$. But in switching crystals, the magnitude (or even the relevance) of the inertial term is ambiguous. On one hand, Eq. 4 predicts switching and hysteresis[10,13] when $\beta \gtrsim 1$, and analysis of the chaotic response in switching crystals leads to values of β that are as large as 2.3 (Ref. 10). On the other hand, large values of β are grossly inconsistent with

estimates of ω_0 and τ obtained from dc I-V characteristics.[1] In the analysis that follows, the ac conductivity of switching CDWs shall be compared to the ac conductivity of the under- and over-damped rigid-phase equations. Comparison shall show that switching CDWs appear overdamped when pinned, but underdamped when sliding. It is physically implausible, however, to interpret the results in terms of phase inertia. Instead, the analysis shall argue that phase slippage can mimic the effect of a motion-dependent inertia.

A. *Pinned response*

For ac signals of small amplitude, the pinned conductivity of Eq. 4 is equivalent to the response of a harmonic oscillator with a linear restoring force. When the applied bias is zero, the in-phase and out-of-phase components of conductivity are given respectively by

$$\text{Re } \sigma(\Omega) = \frac{ne^2\tau}{m^*} \frac{\Omega^2}{(1-\beta\Omega^2)^2 + \Omega^2}$$

$$\text{Im } \sigma(\Omega) = \frac{ne^2\tau}{m^*} \frac{\Omega(1-\beta\Omega^2)}{(1-\beta\Omega^2)^2 + \Omega^2} . \tag{4.5}$$

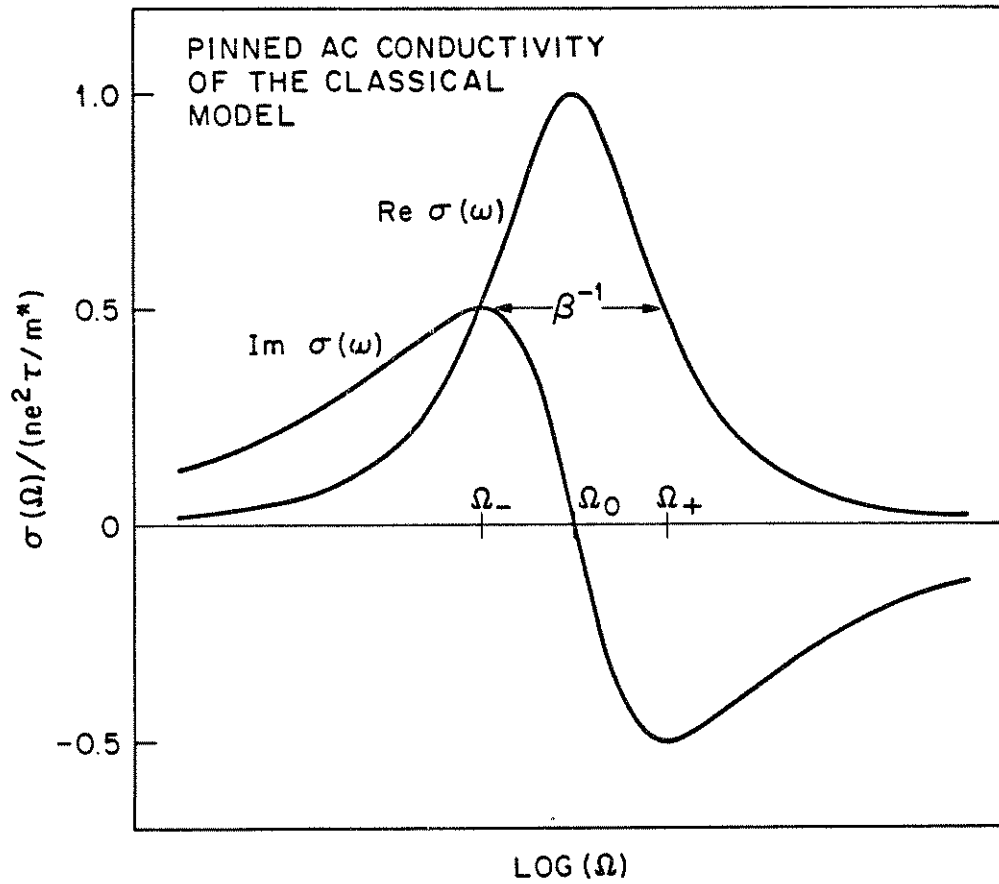Figure 6 shows these components as functions of the ac frequency. The curves

Fig. 4-6)   The zero-bias ac conductivity of the classical, rigid-phase model of CDW dynamics, Eq. 4.5.

in Fig. 6 define three characteristic frequencies:

$$\Omega_0 = \beta^{-\frac{1}{2}}$$
$$\Omega_\pm = (\sqrt{1+4\beta} \pm 1)/2\beta \ .$$

<div align="right">(4.6)</div>

The quantity Ω_0 is the normalized pinning frequency $\omega_0/(\omega_0^2\tau)$. The quantities $\Omega_\pm$ are the frequencies at which Im $\sigma = \pm$ Re σ. For overdamped CDWs, Ω_- reduces to $(\omega_0^2\tau)$, which is called the crossover frequency, and Ω_+ reduces to the damping frequency τ^{-1}. The frequencies Ω_- and Ω_+ demarcate regimes of CDW response. For frequencies between 0 and Ω_-, CDW conductivity is mainly capacitive; between Ω_- and Ω_+, mainly dissipative; and between Ω_+ and ∞, mainly inductive.

As shown in Fig. 6, the inertial parameter may be determined directly from a measurement of ac conductivity, as long as measurement frequencies extend into the inductive regime of CDW conductivity. Measurements in the present experiments, such as in Fig. 2, were restricted to the capacitive regime of CDW response. However, the inertial parameter still may be determined, or at least bounded, by its effect on the shape of CDW conductivity. As the inertial parameter increases, the CDW conductivity flattens out at low frequencies and rises more steeply at frequencies approaching the crossover frequency Ω_-. This effect is shown in Fig. 7, where Eqs. 5 have been plotted for two values of the inertial parameter. The other parameters in Eqs. 5 have been adjusted so that Ω_- and $\sigma(\Omega_-)$ respectively match the crossover frequency and conductivity of the 24 K data in Fig. 2, which are superimposed on the theoretical curves.
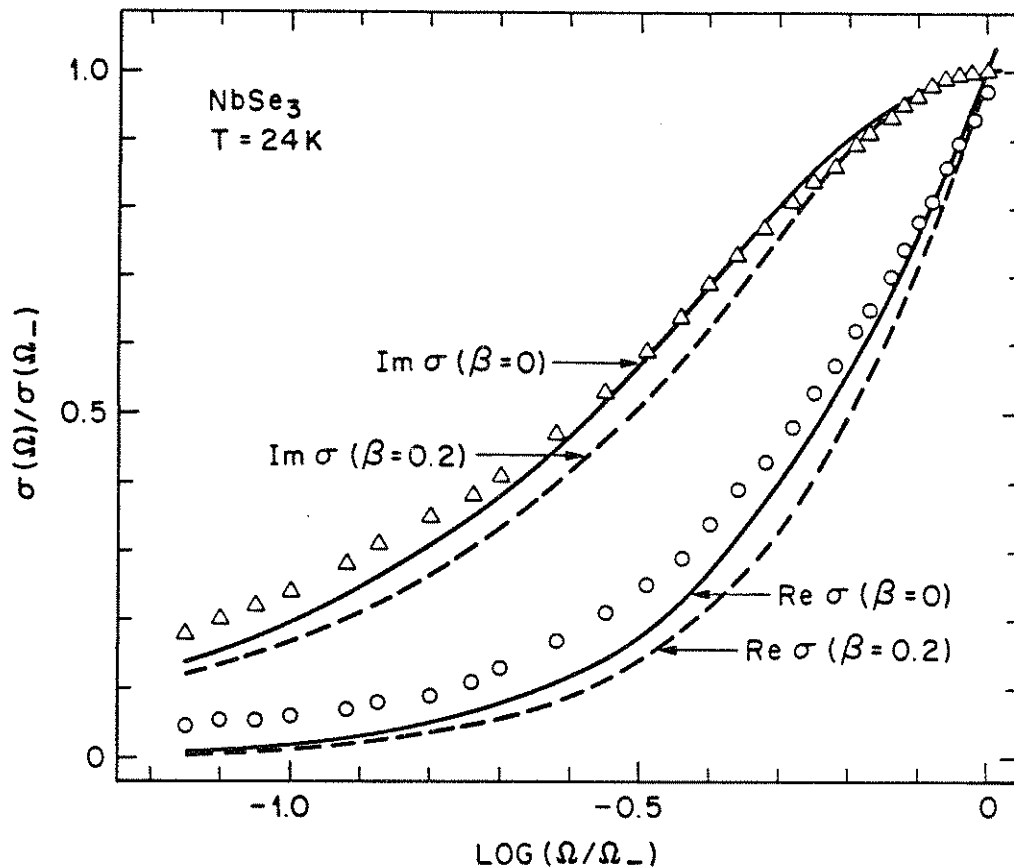
Fig. 4-7) The effect of the inertial parameter on the low-frequency, pinned conductivity of the rigid-phase model, for two values of the inertial parameter: $\beta = 0$ and $\beta = 0.2$. The other parameters in the rigid-phase model are chosen so that the cross-over frequency Ω_- is 500 MHz and the conductivity at the cross-over frequency is $\sigma(\Omega_-) = 5.25$ mS. The theoretical curves are superimposed on the 24 K data from Figure 4-2.

Although neither the $\beta = 0$ nor the $\beta = 0.2$ curves fit the data in detail, the data are consistent with an over damped inertial parameter somewhere in the range $0 \leq \beta \leq 0.2$. Furthermore, as remarked earlier, the data are essentially identical to data measured on nonswitching crystals in this temperature range. Therefore switching CDWs, when pinned, are dynamically overdamped.

B. Sliding response

When the CDW slides in Eq. 4, the dc-induced narrowband noise frequency Ω_N replaces the frequencies $\Omega_{\mp}$ as a characteristic frequency of CDW dynamics. In the context of Eq. 4, the narrowband noise frequency is usually referred to as the *washboard frequency*. It is equal to the reciprocal of the time-averaged phase velocity in Eq. 4, $\Omega_N = <\dot{\phi}>^{-1}$. For ac frequencies below or far above the washboard frequency, the ac conductivity of a sliding CDW may be calculated perturbatively. At frequencies below the washboard frequency, the main effect of an ac test signal is to produce a slow modulation of the dc bias. Therefore the ac conductivity is closely related to the dc differential conductivity of the CDW:

$$\text{Re } \sigma(\Omega) = \frac{ne^2\tau}{m^*} \frac{d<\dot{\phi}>}{de} \{1 - (\beta\Omega)^2\}$$
$$\text{Im } \sigma(\Omega) = -\frac{ne^2\tau}{m^*} \frac{d<\dot{\phi}>}{de}(\beta\Omega) . \tag{4.7}$$

The prefactor $(ne^2\tau/m^*) \, d<\dot{\phi}>/de$ is the slope of the (voltage-controlled) I-V curve. As a function of frequency, the real component of conductivity starts at dI/dV and decreases quadratically with increasing frequency. The imaginary component starts at zero and decreases linearly. The rate of decrease for both Re and Im σ is set by the inertial parameter. For overdamped CDWs, in which

β is small, reductions in Re and Im σ are negligible.[14] For underdamped CDWs, in which $\beta\Omega$ can approach 1, reductions in Re and Im σ are appreciable and in fact resemble the inductive anomalies that characterize the sliding conductivity of switching CDWs.

At ac frequencies above the washboard frequency and its leading harmonics, the role of the ac and dc signals in Eq. 4 is reversed. The dc signal now produces a slow variation of the potential tested by the ac signal, and therefore the CDW conductivity is given by

$$\sigma(\Omega) = \frac{ne^2\tau}{m^*} \frac{i\Omega}{\sqrt{(i\Omega-\beta\Omega^2)^2 - 1}} .$$

For overdamped CDWs the limit $1 \ll \Omega \ll \beta^{-1}$ is relevant. To order Ω^{-2}, the CDW conductivity reduces to

$$\text{Re } \sigma(\Omega) = \frac{ne^2\tau}{m^*}\left\{1 - \frac{1}{2}\Omega^{-2}\right\}$$
$$\text{Im } \sigma(\Omega) = 0 . \tag{4.8}$$

The sliding conductivity of an overdamped CDW is essentially constant and in-phase with the test signal at high frequencies. For underdamped CDWs the limit $\beta\Omega \gg 1$ is relevant, and the CDW conductivity reduces to

$$\text{Re } \sigma(\Omega) = \frac{ne^2\tau}{m^*}(\beta\Omega)^{-2}$$
$$\text{Im } \sigma(\Omega) = -\frac{ne^2\tau}{m^*}(\beta\Omega)^{-1} . \tag{4.9}$$

The sliding conductivity of an underdamped CDW quickly approaches zero at high frequencies.

At ac frequencies that are comparable to the washboard frequency or its

harmonics, an ac signal interacts nonlinearly with the sliding motion of a CDW. In addition, ac-induced oscillations of the CDW are difficult to separate from the dc-induced narrowband noise. Rather than calculate ac conductivities in this frequency range, an analog computer (Philipp-Gillette JA-100) was used instead to simulate Eq. 4 and to measure conductivities directly. The simulated measurements are identical to the experimental measurements in Sec. I. A small ac signal is applied to the analog and the analog response is measured synchronously with a phase-sensitive detector. As with the experimental measurements, the simulated measurements do not distinguish between ac and dc-induced oscillations of the CDW. The measurement procedure is equivalent to defining conductivity in Eq. 4 as

$$\sigma(\Omega) = \frac{ne^2\tau}{m^*} \frac{\overset{\rightharpoondown}{\phi}(\Omega)}{e_{ac}}$$

where $\overset{\rightharpoondown}{\phi}(\Omega)$ is the Fourier component of the CDW phase velocity at the applied frequency.

Figures 8a and 8b show the results of analog simulations appropriate to overdamped and underdamped dynamics, respectively. In Fig. 8a, the fitting parameters of Eq. 4 were chosen to be $(\omega_0^2\tau)/2\pi = 500\,\text{MHz}$ and $\beta = 0.005$, values which are consistent with the pinned ac conductivity in Fig. 7. In Fig. 8b, the fitting parameters were chosen to be $(\omega_0^2\tau)/2\pi = 22\,\text{MHz}$ and $\beta = 2.1$, values which are suggested by Shapiro step and hysteresis experiments on NbSe$_3$ (Ref. 10). In both figures, the dc bias was adjusted so that the narrowband noise frequency was comparable to the noise frequencies in Fig. 3.

The results in Fig. 8 agree with the results of Eqs. 7 - 9. At low frequencies, Re $\sigma(\Omega)$ decreases quadratically from dI/dV and Im $\sigma(\Omega)$ decreases linearly from zero. The rate of decrease is set by β, so reductions in Re and Im σ are negligible in Fig. 8a, where β is small, and appreciable in Fig. 8b, where β is large. (In Fig. 8a, the increase in Re σ just before the washboard frequency is due to mode-locking between the ac and washboard frequencies.[14]) At high frequencies, the behavior of $\sigma(\Omega)$ depends on whether the CDW is under- or over-damped. For the overdamped calculation, Re σ attains the high-field, high-frequency limit of $(ne^2\tau/m^*)$, while Im σ is identically zero. For the underdamped calculation, Re σ rolls off as Ω^{-2}, while Im σ decreases as $-\Omega^{-1}$. At intermediate frequencies, both the under- and over-damped conductivities display a series of large interference peaks where the test frequency matches the washboard frequency or its harmonics.

The sliding ac conductivity of the rigid-phase model — whether underdamped or overdamped — obviously does not agree with the experimental data on switching CDWs. The model also does not agree with experimental data on nonswitching CDWs.[9] Three discrepancies are notable:

1. In the rigid-phase model, Re σ is larger at low frequencies than at high frequencies. In experiment, just the opposite behavior is observed: Re σ is smaller at low frequencies than at high frequencies.

2. At high frequencies in the rigid-phase model, Im σ is zero, but in experiment, Im σ approaches its pinned value.

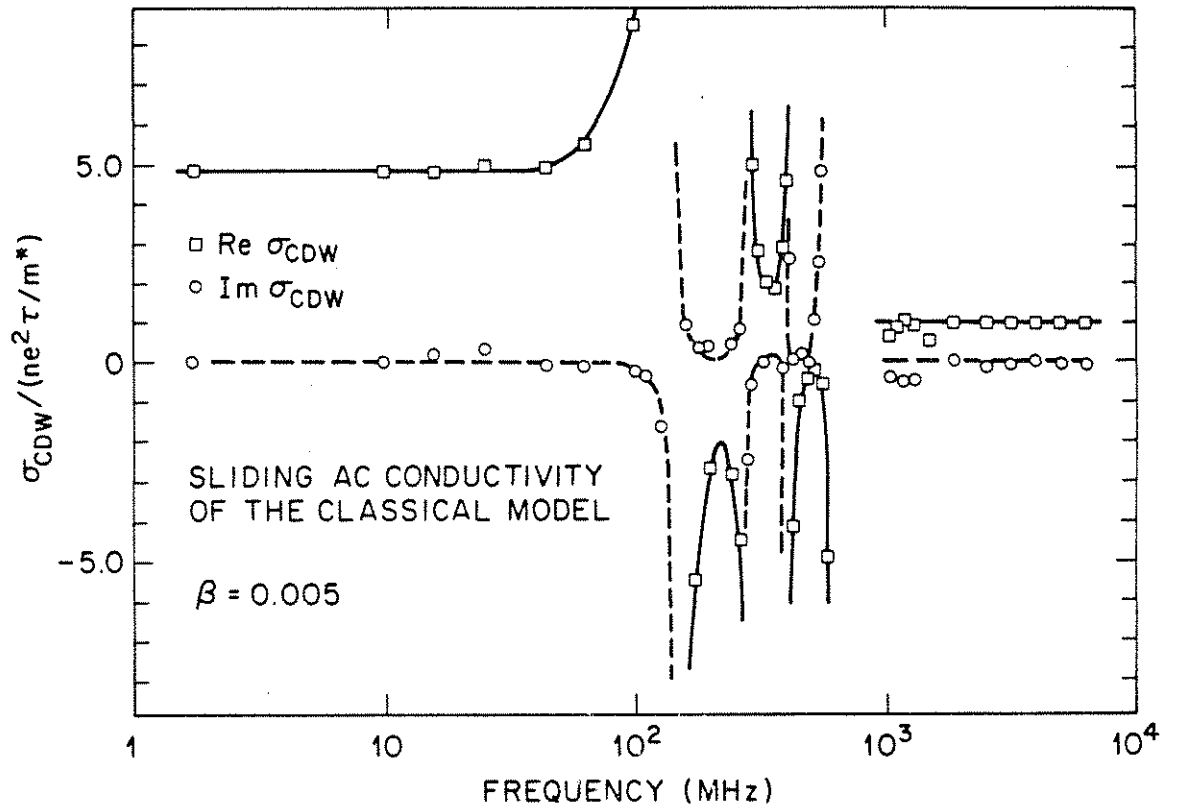3. Interference effects are much larger in the rigid-phase model than they are

Fig. 4-8.a)   The sliding conductivity of the over damped rigid-phase model, $\beta = 0.0005$. The lines are guides for the eye.
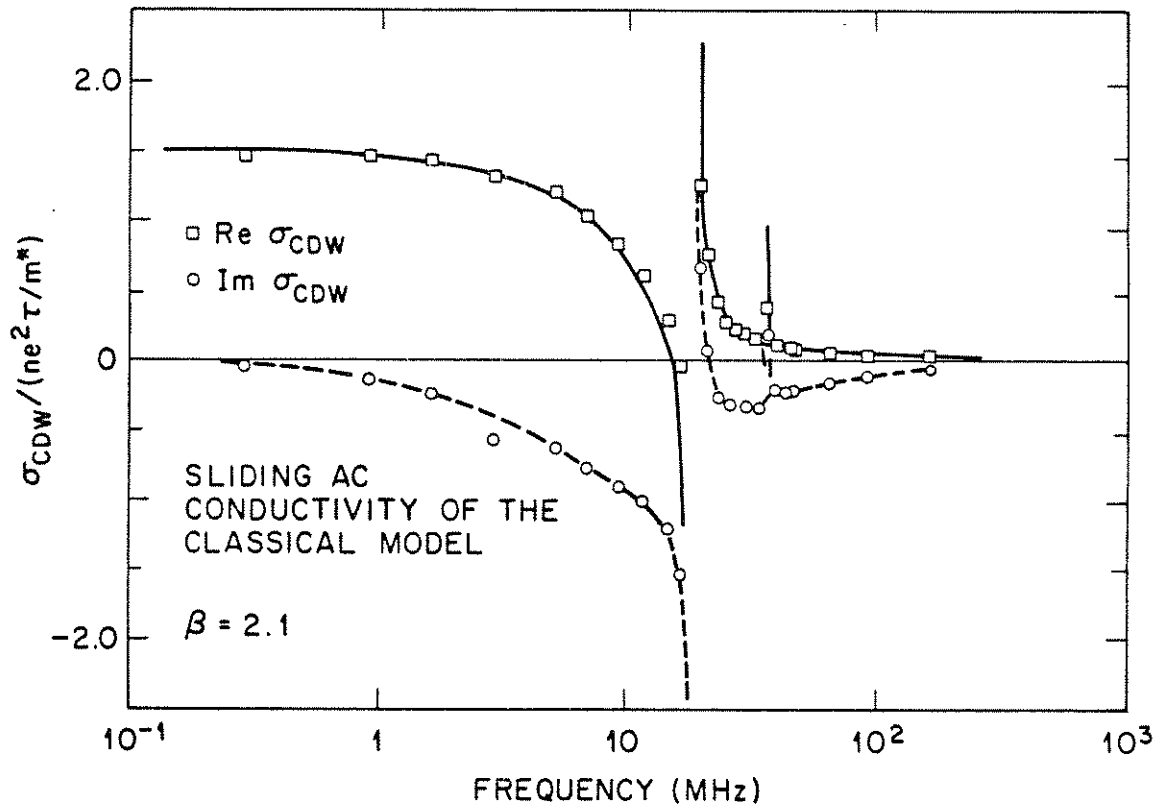
Fig. 4-8.b)   The sliding ac conductivity of the under damped rigid-phase model, $\beta = 2.1$. The lines are guides for the eye.

in experiment.

These discrepancies, however, can be traced to the model's assumption of a rigid CDW phase. Better results are obtained if the CDW phase is treated as deformable.[15] Fukuyama and Lee showed that a deformable CDW breaks up into a series of phase-coherent domains.[16] Within a domain, the CDW phase is fairly rigid. The dynamics of an individual domain may be modeled by Eq. 4 if an elastic coupling of the CDW phase to neighboring domains is included.[17]

Application of an electric field to a deformable CDW not only produces sliding motion of the CDW, but also internal motion of the CDW domains with respect to one another. The internal modes of a deformable CDW have three effects on its dynamics. First, the slope dI/dV of the dc I-V curve is reduced below the high-field limit $ne^2\tau/m^*$ (Ref. 18). Consequently, Re σ becomes smaller at low frequencies than at high frequencies. Second, internal modes dominate the CDW response at high frequencies.[15] Therefore Im σ approaches its high-frequency, pinned value even when a CDW is sliding. Third, internal modes reduce the size of the narrowband noise signal.[18] This in turn reduces the interference features in $\sigma(\Omega)$ to a size which is consistent with experiment.

While improving agreement with the low-frequency limit of Re σ, the high-frequency limit of Im σ, and the size of interference features, a deformable CDW phase does not account for the inductive anomalies that are characteristic of switching CDWs. Discounting the discrepancies caused by the rigid-phase assumption, Eqs. 5 and Fig. 8 show that inductive anomalies are indicative of a CDW phase velocity that lags behind the applied ac signal. (The literature contains no underdamped, deformable-phase calculations of ac conductivity,

therefore the experimental results cannot be compared with theoretical curves.) However, it is unlikely that the lag in CDW response is literally caused by phase inertia, only that the lag can be modeled by inertia. Phase inertia is an unappealing explanation of the CDW response for several reasons. As Chapter 3 points out, the origin of inertia would be difficult to explain in switching crystals. Furthermore, phase inertia would have to depend on CDW motion in a peculiar manner. Because the CDW response is overdamped when pinned but underdamped when sliding, a hypothetical inertia would have to appear whenever a CDW started to slide. On the other hand, a velocity-dependent inertia would be evident in the high-frequency response of a pinned CDW, since the rms velocity of a CDW increases as the ac frequency increases. Because there is no evidence for an underdamped pinned mode, a hypothetical inertia would have to depend on the sliding motion of a CDW without depending on the CDW velocity. With such a complicated dependence on CDW motion, phase inertia does not provide a natural explanation for the underdamped response of switching CDWs.

C. Phase slippage

This section will argue that phase slippage can explain the ac characteristics of switching CDWs. To summarize the model presented in Chapter 3, switching crystals are distinguished from nonswitching crystals by the presence of a small member of strong (or "ultrastrong") pinning sites. Strong-pinning sites, which are present in addition to the weak impurities found in nonswitching crystals, nucleate the phase-slip centers that enable a switching CDW to slide. Strong-pinning sites produce large gradients in the CDW phase when an electric field is

applied to a crystal. Polarization of the CDW phase leads to collapse of the CDW amplitude as the electric field increases.[3] When the amplitude collapses, the phase slips by a factor of 2π to relieve polarization. Then the amplitude reforms; phase polarization reaccumulates; and the phase-slip cycle repeats as the CDW amplitude collapses again. Each cycle of the phase-slip process advances the CDW phase by a factor of 2π.

Phase slippage causes switching when the polarization that accumulates at strong-pinning centers is very large.[3,19] Large polarization of the CDW phase is not relieved appreciably by a single phase-slip event, therefore the CDW amplitude reforms only partially during the phase-slip cycle. The elasticity of the phase depends on the CDW amplitude, and in turn the pinning of a CDW depends on phase elasticity. As a result, CDW pinning is restored only partially during each phase-slip cycle, and the effective collapse in pinning produces switching. When a CDW is pinned, its amplitude does not fluctuate and phase elasticity restrains motion of the CDW. When the CDW begins to slide, phase elasticity is reduced and the CDW velocity jumps from zero to a large value.

The phase-slip model explains the $\omega = 0$ limit of ac conductivity, since it accounts for the shape of the dc dI/dV curve in switching crystals.[1] The phase-slip model may be extrapolated to finite frequencies by considering separately the cases of pinned and sliding CDWs. For the case of a pinned CDW, the interactions that determine the ac response of a switching CDW are the same as those for a nonswitching CDW. In a nonswitching CDW, phase domains respond to an ac signal like a collection of overdamped oscillators coupled together by the elasticity of the CDW phase. In a switching CDW, the only

difference is the additional presence of strong-pinning sites. But the phase is essentially fixed at strong-pinning sites, because pinning frequencies there are comparable to the Peierls gap frequency. Therefore strong-pinning interactions do not contribute to the ac response of a CDW for frequencies below the far-infrared. Furthermore, because of their small number, strong-pinning sites do not appreciably reduce the oscillator strength of weak impurities. Therefore the pinned conductivity of switching CDWs should be nearly identical to the response of nonswitching CDWs.

For the case of a switching CDW, phase slippage produces a delayed motion of the CDW phase that has no counterpart in nonswitching CDWs. In order for the phase to advance in a switching CDW, the abrupt phase changes that occur at phase-slip centers must diffuse from the centers into the bulk of neighboring phase domains. The time required for a 2π change of phase to diffuse across a domain is on the order of the phase relaxation time. In the overdamped rigid-phase model, the relaxation time is given by $(\omega_0^2 \tau)^{-1}$, or by $\beta = 1$ in normalized units. When an ac signal is applied to a switching crystal, the phase diffusion time produces a delay between advances of the CDW phase and the maximum field of the ac cycle. Therefore the CDW velocity lags the ac signal with a time-constant of $\beta \sim 1$. The lag has exactly the same effect that a phase inertia would have, and produces inductive anomalies in the ac response of the crystal. Because phase slippage occurs only when a CDW slides, inertia-like effects are present only in the sliding, and not in the pinned, CDW state.

Significantly, switching and hysteresis are not required in the dc characteristics of a crystal in order for inertial effects to be present in its ac

response. Switching and hysteresis require special conditions of phase polarization and impurity concentrations, but inertial effects require only phase slippage. This explains why inductive anomalies are observed in the ac response of a crystal at temperatures above the complete onset of switching.

III. Summary

This chapter has presented the results of ac conductivity measurements on switching crystals of $NbSe_3$. At temperatures well above the onset of switching, the ac response of switching and nonswitching crystals are equivalent. At temperatures below the onset of switching, the ac response of switching and nonswitching crystals are distinguishable only when the CDWs within the crystals are sliding. The sliding ac conductivity in switching crystals is marked by inductive anomalies, which are broad dips in Re and Im $\sigma_{CDW}(\omega)$ at frequencies below the narrowband noise frequency. The ac response of switching crystals has been analyzed in terms of the rigid-phase model, which is the simplest differential equation of CDW transport. Although the data are not described in detail by this model, the model does show that switching CDWs are overdamped when pinned and underdamped when sliding. It has been argued that inertial effects in the sliding state do not arise from an actual phase inertia, but rather from the same phase-slip mechanism that produces bistability and hysteresis in dc I-V curves. Thus phase slippage provides a unified explanation for both the ac and dc characteristics of switching CDW transport.

CHAPTER 5:   DYNAMICAL INSTABILITIES

CHAPTER 5: DYNAMICAL INSTABILITIES

This chapter describes dynamical instabilities associated with the motion of switching CDWs. The term *dynamical instability* refers to complex, apparently random motion by a CDW in response to simple, noise-free combinations of ac and dc electric fields. Two types of instability are observed.[1] The first type occurs under the application of a dc current when a CDW is biased into a region of negative differential resistance.[2] This type of instability is characterized by an intermittent broadband noise that is much larger than the usual broadband noise generated by CDW sliding. The second type of instability occurs under the joint application of large dc and ac voltages, and is characterized by period-doubling routes to chaos.[3]

Dynamical instabilities are important for three reasons. First, they experimentally distinguish switching from nonswitching crystals. None of the instabilities described in this chapter are observed in nonswitching crystals. Second, the instabilities provide insight into different aspects of switching dynamics. Negative-differential-resistance instabilities depend on the interactions *between* the current domains of a crystal, whereas period-doubling instabilities develop from order-parameter dynamics *within* the domains. Finally, the instabilities provide benchmarks for any proposed model of switching. For example, very specific criteria must be met in order for period-doubling to occur, and even if a model does display period-doubling, it must do so for realistic values of its parameters.

The approach of this chapter is different from that of preceeding chapters. Preceeding chapters minimized the complexity of CDW dynamics by either time-averaging (through dc measurements) or linearizing (through small-signal measurements) the CDW response. As a result, the chapters extracted quantitative measures of switching dynamics, such as the dependence of threshold fields or cross-over frequencies on temperature. In contrast, the present chapter intentionally maximizes the complexity of CDW dynamics. CDWs are driven into regimes of extremely nonlinear response where their temporal behavior is characterized by frequency spectra. Consequently, results are often qualitative, such as broad descriptions of regimes where period-doubling is observed. Results on negative-differential resistance are reported first, in Sec. I, and results on period-doubling are described next, in Sec. II. Section III concludes the chapter with a summary.

I. Negative Differential Resistance

A. Experimental Results

Negative differential resistance occurs in current-driven crystals at temperatures just above the appearance of complete switching. For example, negative differential resistance occurs in the temperature range 30-32 K for the $NbSe_3$ crystal of Fig. 3.1a, whereas it occurs in the range 46-48 K for the $Fe_x NbSe_3$ crystal of Fig. 3.1b. Because negative differential resistance in switching crystals is a single-valued function of current and a double-valued function of voltage, it is classified as *s-type*. The terminology refers to the s-like shape of the I-V curve when plotted with voltage along the horizontal axis.

Figure 1 shows the threshold region of an NbSe$_3$ crystal at 42 K. The threshold current I_T for CDW depinning is identified with an arrow. In a well-defined region somewhat above I_T, an increase in the current bias I results in a smooth decrease in the sample voltage V. The differential resistance dV/dI is negative in this region, except for a small "step", over which the differential resistance is close to zero. Power spectra of the CDW response were monitored simultaneously with the dc I-V characteristics. For currents exceeding I_T, narrowband noise and broadband noise are observed in the spectra. Just before the NDR region, however, a sudden onset of high-level broadband noise occurs, illustrated in Fig. 2. The power distribution of the noise follows a power law in frequency, f^{-a}, with an exponent $a = 1.2$ between 0.5 and 20 MHz.

The noise in Fig. 2 is notable for two reasons. First, the amplitude of the noise completely dominates the usual conduction noise associated with CDW sliding. The power level of the noise at 1 MHz is about four orders of magnitude larger than the conventional broadband noise and about two orders of magnitude larger than the narrowband noise that are observed before the start of the NDR region. Second, the temporal behavior of the noise is extremely intermittent, as shown in Fig. 3. Plots a) through f) in Fig. 3 represent power spectra between 0 and 25 kHz taken sequentially one second apart in real time. All experimental conditions for the plots are identical. The large, intermittant structure in the plots appears spontaneously with a frequency between 0.1 and several hertz, and with a duration of about 0.1 seconds. The structure occurs predominately on the $dV/dI = 0$ step of the NDR region. Intermittent structure is also observed at frequencies between 0.5
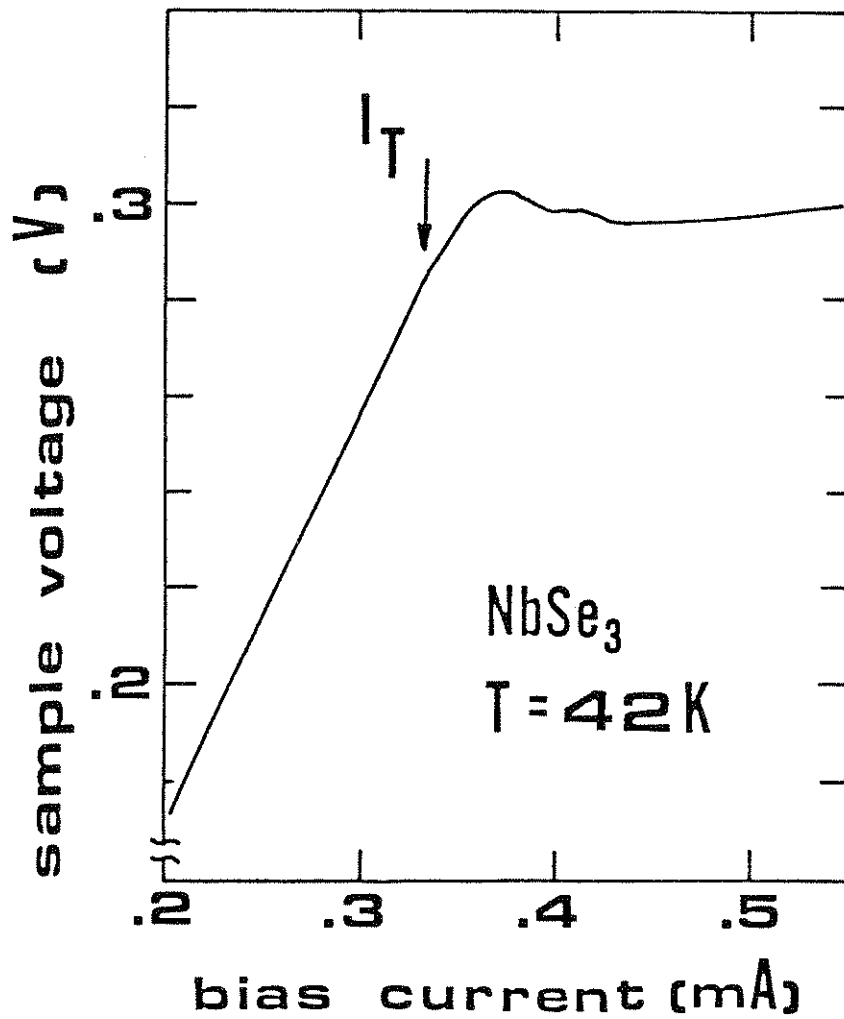
Fig. 5-1)   Negative differential resistance in NbSe₃. The arrow identifies the
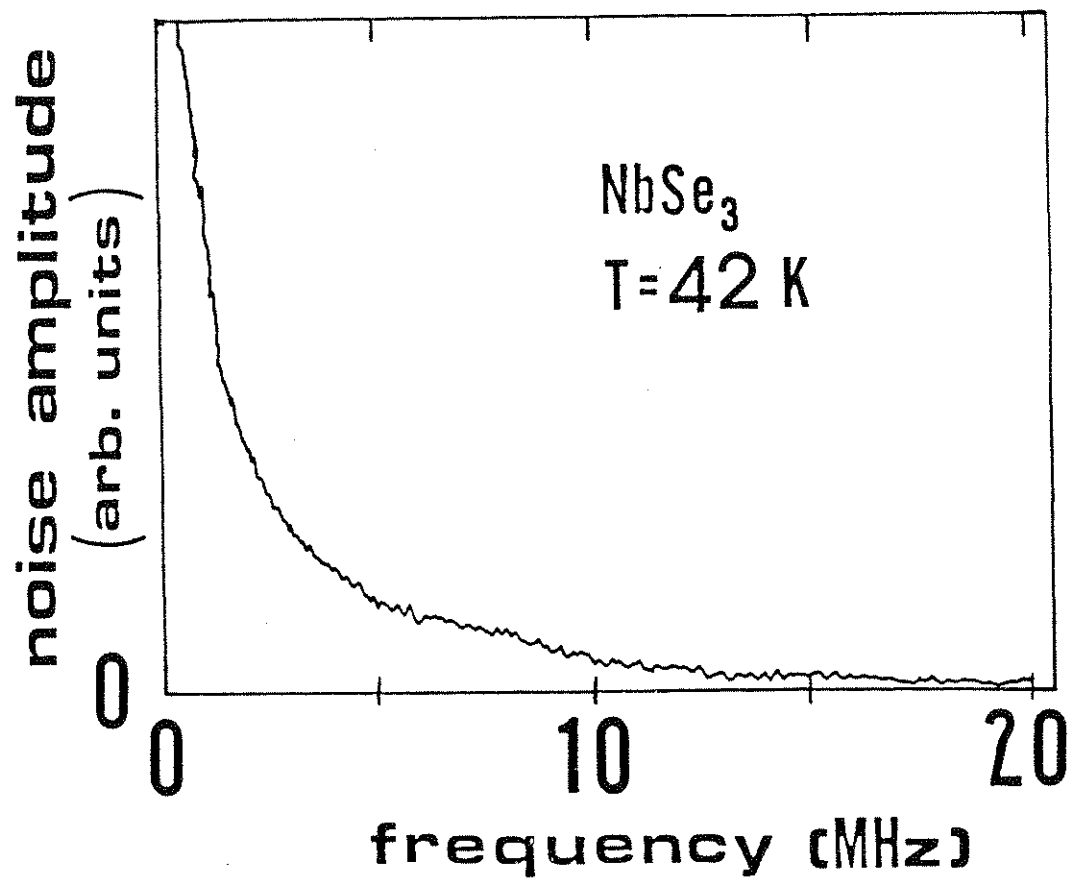threshold current for CDW depinning.

Fig. 5-2) Broadband noise associated with negative differential resistance, 0.1 - 20 MHz. The noise has been digitally averaged over several seconds.
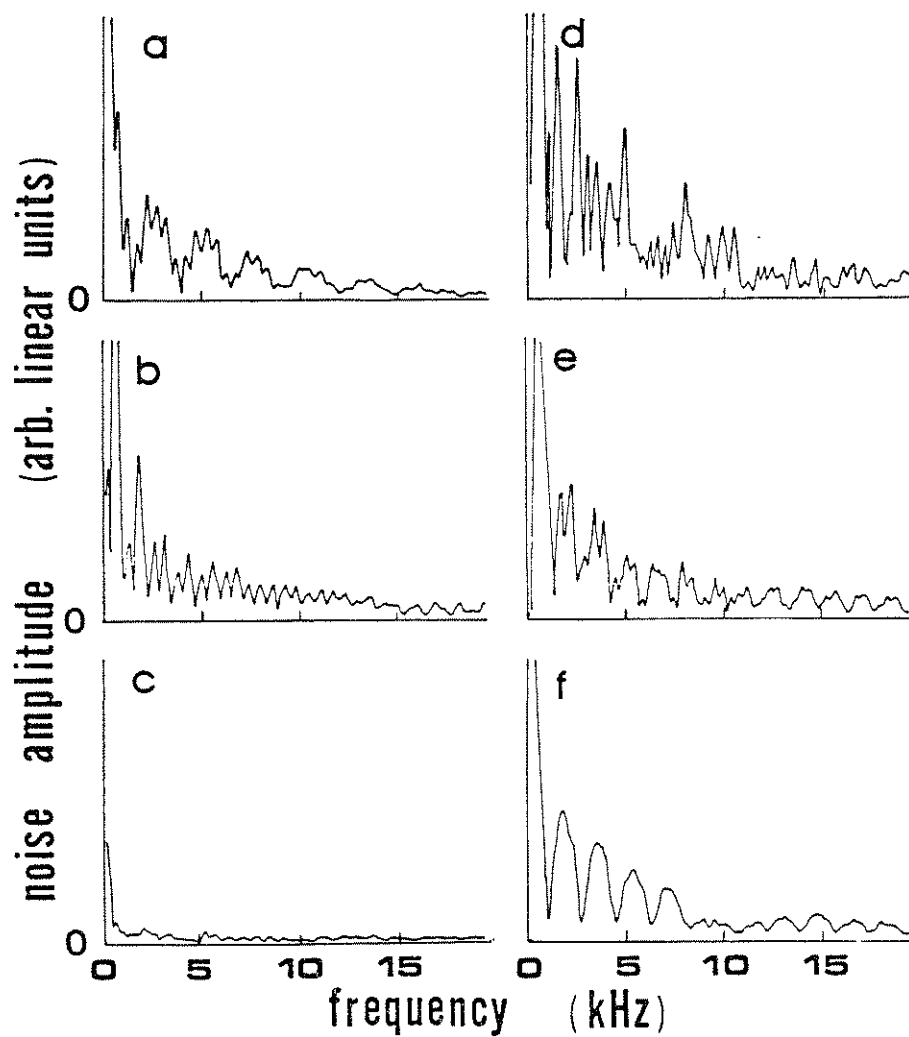
Fig. 5-3)   Broadband noise associated with negative differential resistance, 10 Hz - 25 kHz. Spectra a) - f) were taken sequentially at about 1 second intervals. The spectra were not averaged.

and 20 MHz, but is not apparent in Fig. 2 because the spectrum was averaged over a duration of several seconds.

The f^{-a} noise is closely related to the presence of negative differential resistance. As mentioned above, the onset of the noise corresponds to the beginning of the NDR region. Although the noise persists even after the NDR region, the frequency spectrum of the noise becomes distorted and no longer follows a power law distribution. The temperature dependence of the f^{-a} noise also closely parallels the temperature dependence of the NDR region. At temperatures above 42 K, the NDR region in Fig. 1 becomes progressively broader, and above 45 K only a slight decrease in the positive differential resistance is observed for current biases above I_T. At temperatures below 42 K, the NDR region narrows and moves closer to I_T, and below 35 K, the NDR region sharpens into an abrupt switch. Correspondingly, the f^{-a} noise is not observed for temperatures either above 45 K or below 35 K.

B. Analysis

Negative differential resistance is expected in any model of CDW dynamics in which the CDW conductivity σ_{CDW} increases rapidly as the local electric field exceeds the threshold field for CDW depinning. In this context, "rapidly" means in comparison to the normal conductivity σ_N of the non-CDW electrons that also contribute to electrical conductivity. Negative differential resistance can arise in both switching and nonswitching models of CDW dynamics. For example, in the overdamped model of Gruner, Zawadowski, and Chaikin, the voltage-driven I-V curve is nonswitching. However, under current-driven boundary conditions, Monceau *et al.* show that this model produces an s-

shaped I-V curve.[4] As a second example, the voltage-driven phase-slip model of Chap. 6 displays switching for appropriate values of certain parameters. In terms of switching, a noncritical parameter in the model is κ, which may assume the value 0. When $\kappa = 0$, the procedure of Monceau *et al.* may be applied to show that the current-driven I-V curve displays a region of negative differential resistance. Thus the presence of negative differential resistance, by itself, can not differentiate between phase-depinning and phase-slip mechanisms of CDW motion.

The presence of intermittency and f^{-a} noise is less ambiguous. No phase-depinning mechanisms exist for intermittency or f^{-a} noise, but a phase-slippage mechanism, based on the formation of current domains, provides a possible explanation for both phenomena.[1,2] The model treats a crystal as an array of current domains. Each domain can be in one of two states: either active, with CDW phase sliding within the domain, or dormant, with CDW phase pinned. In the negative differential resistance regime, the crystal contains a mixture of active and dormant domains. As the current bias through the crystal increases, more domains become active, until eventually all the domains achieve the active state at the end of the negative differential resistance region.

An important assumption of the model is that for a given current bias, there are a number of nearly equivalent domain configurations that have almost the same energy. The degeneracy of the configurations makes the system unstable against external perturbations, such as temperature or resistance fluctuations, which force the system to hop among several accessible states. Indeed, a system with several competing domain configurations may be intrinsically unstable, so

that it spontaneously fluctuates between accessible states. Whether intrinsic or extrinsic, configurational hopping can produce both $1/f$ noise and intermittency. Ben-Jacob *et al.*[5] show that even a system hopping between just two states can possess power spectra very similar to Figs. 2 and 3. The assumption of nearly degenerate domains appears well-justified, based on the discussion of avalanche depinning in Chap. 3. That discussion showed that strong pinning centers effectively create latent current domains within a crystal. The estimated size of the domains is small compared to typical crystal sizes, so it is plausible that for any given current bias there are several equivalent domain configurations. Thus the domain model appears to offer a viable explanation of intermittency and $1/f$ noise.

Period-Doubling Routes to Chaos

A. Experimental Results

1. Mode-locking and period-doubling

Period-doubling is a phenomenon that is observed in certain nonlinear dynamical systems when they are driven by large, periodic forces. In a typical period-doubling sequence, a driven system is observed to respond periodically to an external force as long as the force is small. When the amplitude of the force is small, the period of the system response exactly matches the period of the force. As the amplitude of the force increases, however, the period of the system response increases in step-like increments. The response period first increases to twice the drive period; then to four times the drive period; then to eight times; and so on. Eventually the response period becomes infinite and the

system appears to react stoichastically to the external force. However, the apparent stoichasticity of the system is not true randomness, since the system remains governed by a deterministic equation of motion. The response of the system is known as *deterministic chaos*, or just simply *chaos*, to distinguish it from truly probabilistic dynamics.

Period-doubling routes to chaos are observed in CDW transport, but only in switching crystals and only under conditions of *mode-locking*.[3] Mode-locking occurs when large ac and dc fields are applied to a CDW, and refers to a synchronization of the CDW narrowband noise frequency to the frequency of the ac field. In the absence of an ac signal, the frequency of the narrowband noise is determined by the dc bias. When the dc bias increases, for example, the noise frequency also increases. But when an ac signal is applied, the narrowband noise frequency can lock onto the ac frequency or one of its harmonics over a limited range of dc bias. When this happens, the noise frequency becomes independent of the dc bias.

One signature of mode-locking is the appearance of Shapiro steps in the I-V characteristic of an $NbSe_3$ crystal (see Chap. 2). Shapiro steps are illustrated in Fig. 4, which shows a series of I-V curves measured across a switching crystal. The curves are parametrized by the amplitude of a 15 MHz radio-frequency (rf) signal applied to the crystal. When the rf amplitude is zero, a large switch marks the onset of (hysteretic) CDW sliding. When the rf amplitude is increased, sharp steps appear in the I-V curves. The slope of the steps is equal to the low-field differential resistance of the crystal, which indicates that the time-averaged phase velocity of the CDW is *constant* on each step.[6] A
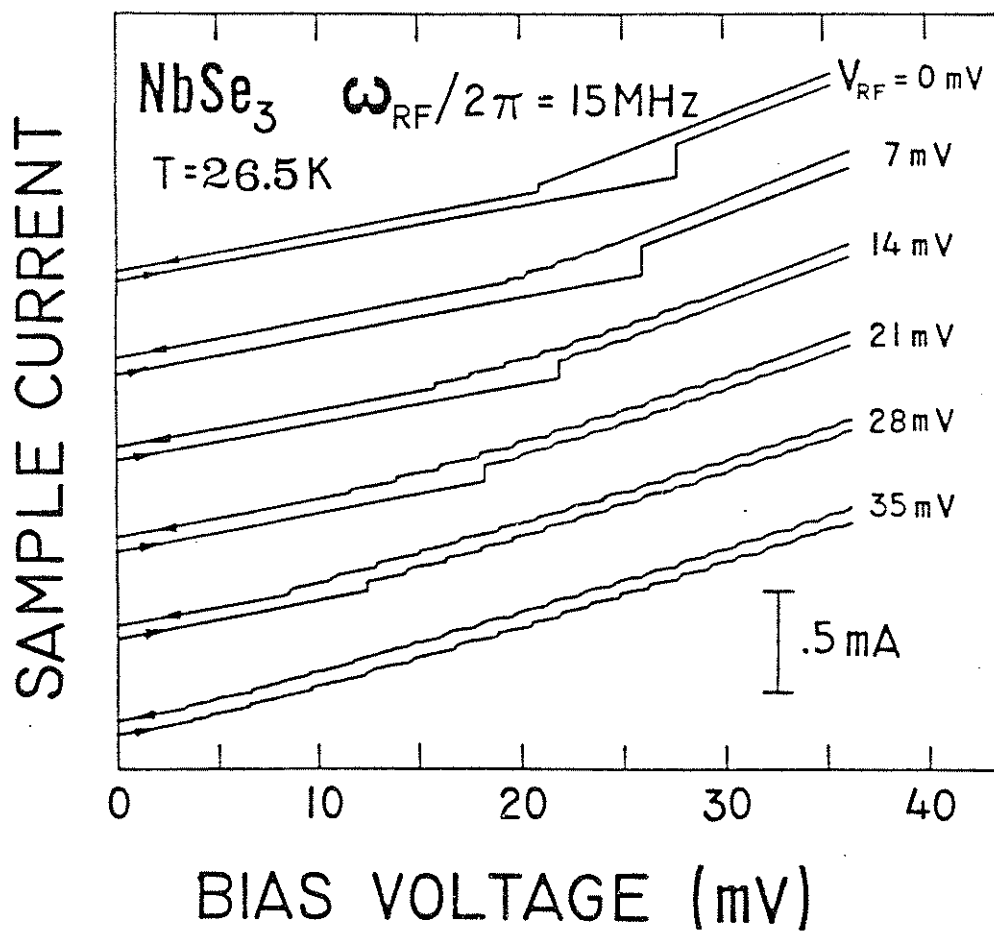
Fig. 5-4)   Shapiro steps in the I-V characteristics of a switching crystal.

measurement of the narrowband noise spectrum shows that this is caused by the noise frequency locking onto the oscillations of the 15 MHz signal. The nth Shapiro step in the I-V curve represents synchronization of the noise frequency with the nth harmonic of the rf signal.

Shapiro steps are also observed in the I-V characteristics of nonswitching crystals, as mentioned in Chap. 2. However, Shapiro steps in a switching crystal, such as those of Fig. 4, are remarkable in three respects:

1. The steps are very broad. Near threshold, the steps are so wide that they completely fill up the I-V curve. This indicates that the CDW is always locked to one or another harmonic of the rf signal.

2. The steps are very sharp. Each step resembles a small switch, because the CDW makes abrupt transitions from one locked step to the next. This indicates that unlocked CDW motion is energetically unfavorable.

3. The steps are hysteretic. Once locked to a harmonic of the rf signal, the CDW tends to remain locked, and this produces hysteresis.

These observations suggest that mode-locking is particularly stable in switching CDWs. Paradoxically, stability in mode-locking leads to a dynamical instability in the temporal response of a CDW.

Figure 5 shows one measure of the temporal response. The figure displays oscilloscope traces of the current through an $NbSe_3$ crystal plotted against the rf voltage applied across the crystal. The current has two components, the CDW current and the normal current (from uncondensed electrons). The normal current is always in-phase with the rf signal, but the response of the

(For page sequence only.)

Fig. 5-5)   Oscilloscope traces of current (measured across a series resistor) versus rf voltage for a switching NbSe$_3$ crystal. (a) Measured near the beginning of a Shapiro step: $V_{dc} = -23.35$ mV and $V_{rf} = 3.5$ mV. (b) Measured near the middle of a Shapiro step: $V_{dc} = -23.30$ mV and $V_{rf} = 3.2$ mV. The rf frequency is 1.2 MHz for both traces.
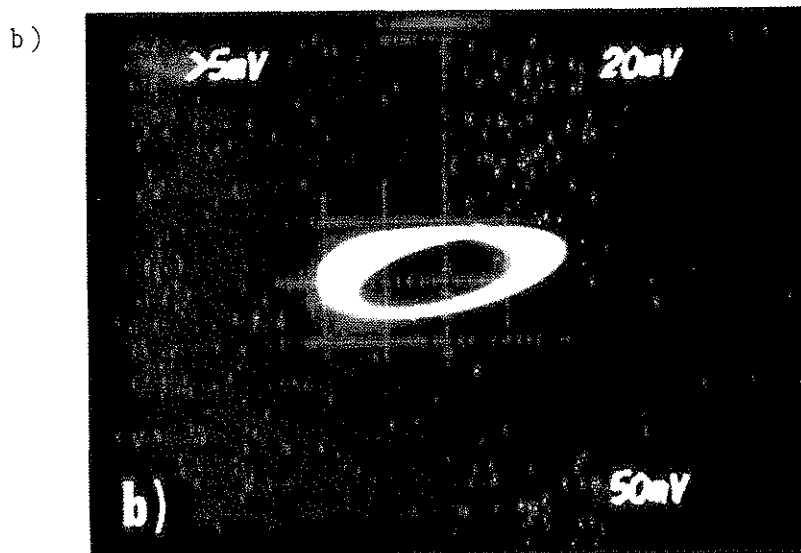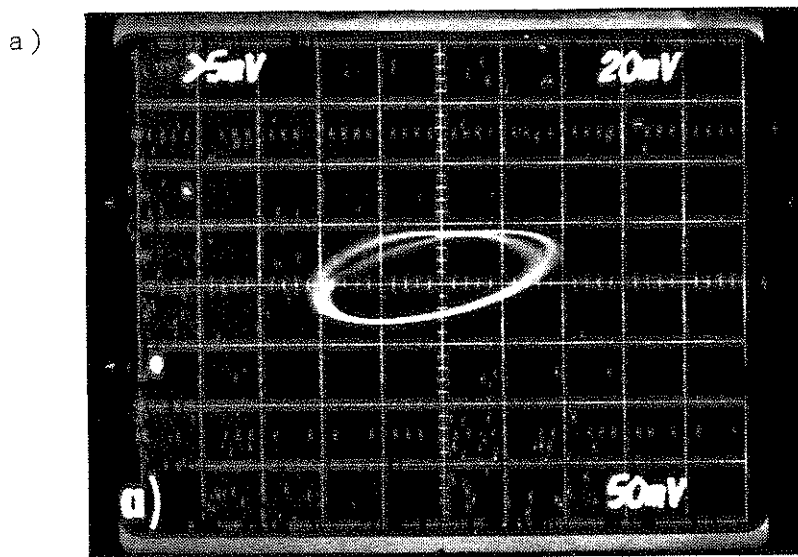
a)

b)

Fig. 5-5

CDW current depends on the dc bias. At the beginning of a Shapiro step, CDW motion is simply periodic, and a trace of total current versus voltage forms a single, closed loop. Away from the beginning of a Shapiro step, however, CDW motion is more complex and current-voltage traces form multiple, intersecting loops. Figure 5a shows a trace at a dc bias slightly beyond the beginning of a Shapiro step. The CDW current has a periodicity of twice the rf periodicity, and therefore two intersecting loops appear in the trace. The *average* CDW phase velocity remains locked to the rf frequency, but the instantaneous velocity alternates between two distinct states in order to maintain that average. Closer to the middle of a Shapiro step, CDW behavior is more complex, as shown in Fig. 5b. A broad smear of intersecting loops is present, indicating that the instantaneous velocity jumps between a large or infinite number of states in order for the average velocity to remain mode-locked.

Figure 6a shows a second, more quantitative measure of the temporal response.[3] The figure displays the harmonic content of the current in a switching crystal for fixed values of the rf amplitude and frequency. Power spectra (i)-(iv) correspond to four dc biases ranging from the beginning to the middle of a Shapiro step. As the dc bias increases, the harmonic content of the CDW response increases. At the beginning of a Shapiro step, spectrum (i), the CDW response is simply periodic and the spectrum contains only harmonics of the rf drive frequency f. (Harmonics that are an integer multiple of the drive frequency are produced by the nonlinearity of the I-V curves.) With a slight increase in bias, spectrum (ii), the CDW response bifurcates, and the spectrum
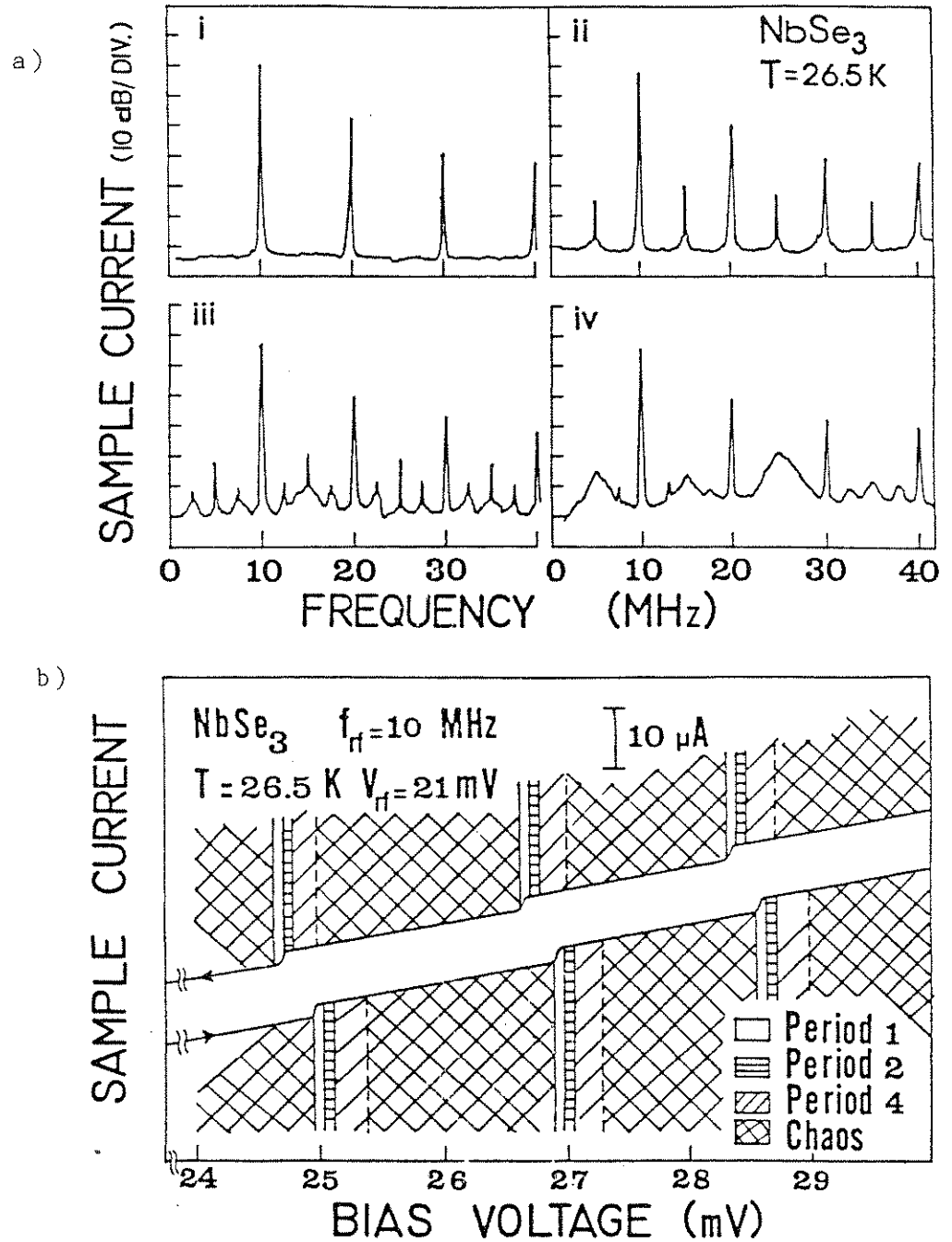
Fig. 5-6) Period-doubling in a switching NbSe3 crystal. The rf bias and
frequency are fixed at 21 mV and 10 MHz, respectively. (a) Power
spectra of the crystal response: (i) period-one, (ii) period-two,
(iii) period-four, and (iv) chaos. (b) Correspondence between the
period-doubling response and dc bias, plotted schematically against
the rf-induced Shapiro steps of the dc I-V characteristic.

contains subharmonic components at multiples of $f/2$. The bifurcated spectrum corresponds to a current-voltage trace similar to Fig. 5a. With a further increase in bias, spectrum (iii), the CDW response bifurcates again, and additional subharmonic components appear at multiples of $f/4$. Finally, at the middle of the Shapiro step, the CDW response contains a continuous distribution of components, spectrum (iv), which corresponds to the apparently stoichastic trace of Fig. 5b.

Figure 6b shows the detailed correspondence between dc bias and CDW response, plotted schematically against the rf-induced Shapiro steps in the dc I-V characteristic. In the figure, responses corresponding to spectra (i)-(iv) are labelled *period-one, period-two, period-four*, and *chaos*, respectively. Starting at the beginning of a Shapiro-step, the CDW response bifurcates through period-one, period-two, and period-four until finally reaching the chaotic state near the middle of the step. The chaotic state persists until the end of the step, where a further increase in dc bias produces a jump to the next Shapiro step and a return to simple periodicity. The period-doubling sequence is periodic in dc bias, repeating over many Shapiro step cycles until disappearing at very large electric fields.

The chaotic response in spectrum (iv) is distinguished from other types of CDW conduction noise by both its frequency distribution and its magnitude. Its frequency distribution is neither discrete, as with narrowband noise, nor monotonically decaying, as with conventional broadband noise or negative differential resistance noise. At frequencies above 10 MHz, the integrated power in spectrum (iv) is hundreds of times larger than the power observed at

comparable frequencies in narrowband, broadband, or negative differential resistance noise. The chaotic and bifurcated spectra of Fig. 6 represent a qualitatively new phenomenon in CDW transport.

The observation of chaos and period-doubling has important implications for the dynamics of switching CDWs. The implications are discussed in the analysis section, but for now the complex dynamics of Fig. 6 can be thought of as *frustration* in the CDW response.[7] The rf signal tends to lock the CDW phase velocity to the rf frequency, while the dc bias tends to pull the velocity away. The CDW response is a compromise between conflicting constraints: the average phase velocity remains locked to the rf frequency, while the instantaneous velocity becomes unlocked. The frustrated response of switching CDWs requires unusually stable mode-locking, because in nonswitching CDWs mode-locking is broken before frustration occurs. The analysis section will show that both period-doubling and strong mode-locking can occur if switching CDWs are effectively underdamped. Thus, the broad Shapiro steps of Fig. 4 and the period-doubling response of Figs. 5 and 6 have a common dynamical origin in transport behavior of switching CDWs.

2. *Conditions for mode-locking instabilities*

Period-doubling bifurcations, chaos, and other mode-locking instabilities (described in the next section) are observed over large regions of the parameter space defined by temperature, dc bias, rf frequency, and rf amplitude.[1] Period-doubling bifurcations are the most ubiquitous instabilities. They are observed at temperatures from 15 to 40 K; at dc biases from 50% to 120% of the threshold field; and at rf frequencies from 0.5 to 50 MHz. Other instabilities,

including chaos, are restricted to lower temperatures and narrower bias and frequency ranges.

This section will describe the parameter regime in which mode-locking instabilities are observed. Because the regime is part of a four-dimensional space, it is difficult to visualize in its entirety. A useful approach is to sketch two- or three-dimensional slices through the regime. For example, at fixed temperature, the regime is a convoluted function of dc bias, rf frequency, and rf amplitude. Figure 7 depicts the regime at 36 K by showing its intersection with planes of constant rf frequency and rf amplitude. In the figure, both dc bias and rf amplitude are normalized to the threshold field of the sample: $i_{dc} = I_{dc}/I_T$ and $i_{rf} = I_{rf}/I_T$. The parameter planes themselves are shown in more detail in Fig. 8 and 9. (The parameter regimes sketched out in these figures are somewhat sample dependent. The crystal used for Figs. 7-9 is different from the crystals used for Fig. 5, Figs. 4 and 6, and Figs. 10-14, respectively.)

Figure 8 shows the fixed-frequency (35 MHz) plane. For small values of the rf amplitude, a single period-doubling bifurcation is observed over a small range in dc bias just above threshold. As the rf amplitude increases, the period-doubling threshold decreases while the period-doubling range increases. When the rf amplitude is about 70% of I_T, period doubling is observed at dc biases between 80% and 100% of I_T. At this point, Fig. 9 shows the corresponding behavior in the fixed-amplitude plane. Period-doubling occurs for frequencies between 5 and 100 MHz. As the rf frequency increases from 5 to 45 MHz, the dc threshold increases and the dc range expands. At 45 MHz, the
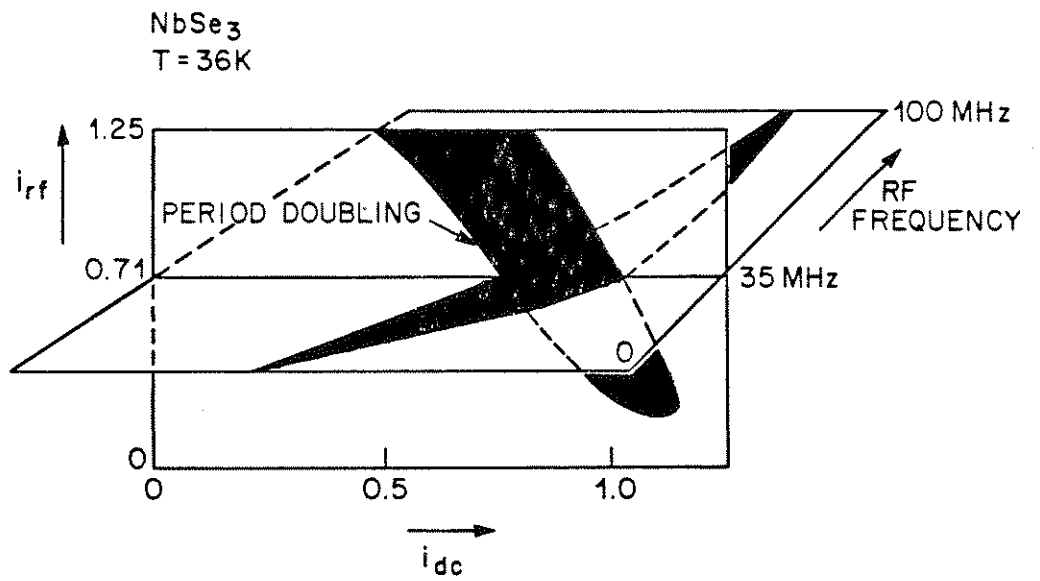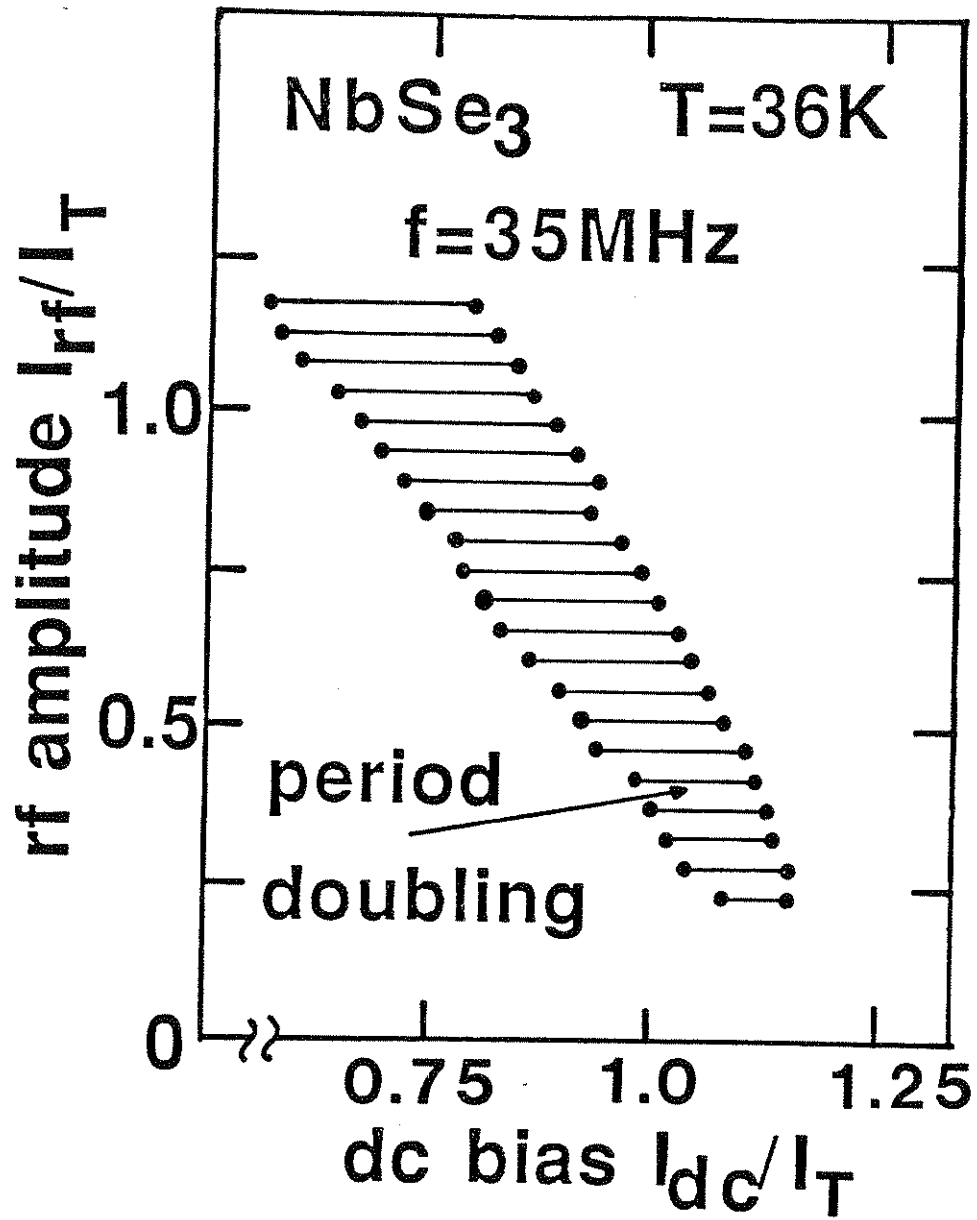
Fig. 5-7)   The period-doubling regime at 36 K.

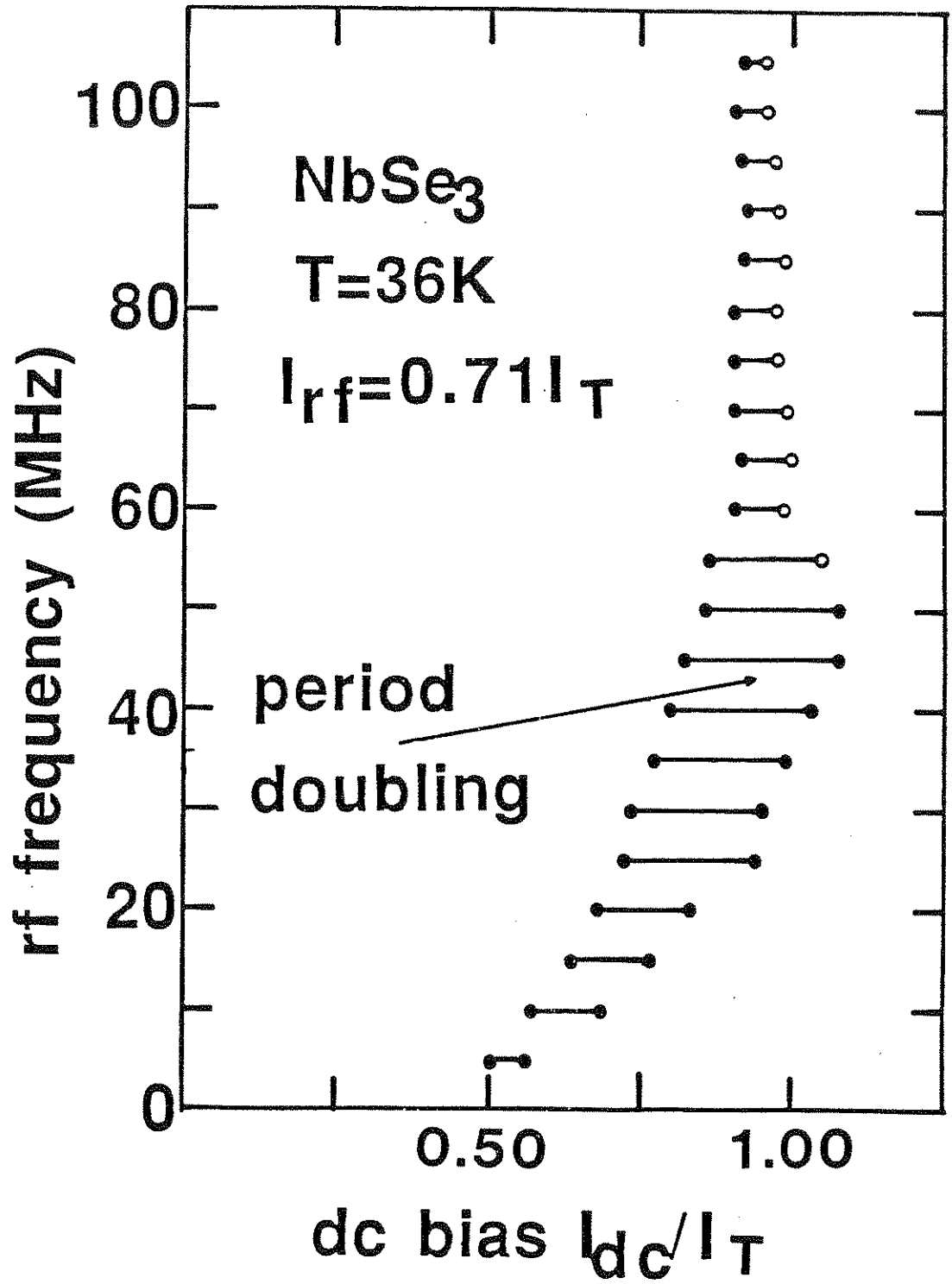Fig. 5-8)   Period-doubling at 36 K for a fixed rf frequency of 35 MHz.

Fig. 5-9)   Period-doubling at 36 K for a fixed rf amplitude of 0.71 I_T.

dc range is at a maximum, extending from 80% to 105% of I_T. >From 45 to 100 MHz, the dc range shrinks while the dc threshold remains roughly constant. For this sample at this temperature, the CDW response is only period-two in the period-doubling regime; no period-four or chaotic response is observed.

Period-doubling may also be mapped out as a function of rf amplitude and frequency. Figure 10 shows a *projection* of the period-doubling region, for a different sample, onto the rf amplitude-frequency plane. The projection was achieved by fixing the rf amplitude and frequency, and sweeping the dc bias from below threshold to above threshold. The most nonlinear behavior observed during the sweep was defined as the projection of the sweep onto the plane. The degree of nonlinearity is ordered in an ascending scale of period-one, period-two, period-four, and chaos. For example, in the region denoted period-four, both period-one and period-two behavior are observed, in addition to the period-four behavior that is indicated. Note that period-four behavior only occurs at relatively low frequencies, between 5 and 20 MHz, and at moderate rf amplitudes, between 50% and 130% of V_T. Period-two behavior occurs over a much wider range, from 5 to 70 MHz and from 4% to 150% of V_T.

In contrast to the high-temperature response displayed in Figs. 7-10, the low-temperature CDW response is much more complex. Figure 11 shows the CDW response at 19 K for the crystal of Fig. 10. Chaos and two new types of CDW response are now observed. The response labelled "virtual Hopf" is a precursor to period-doubling behavior, and the response labelled "period-two plus noise" is a variant of period-two behavior (see below). Figure 11 shows that as the temperature is lowered from 37 to 19 K, the period-doubling regime
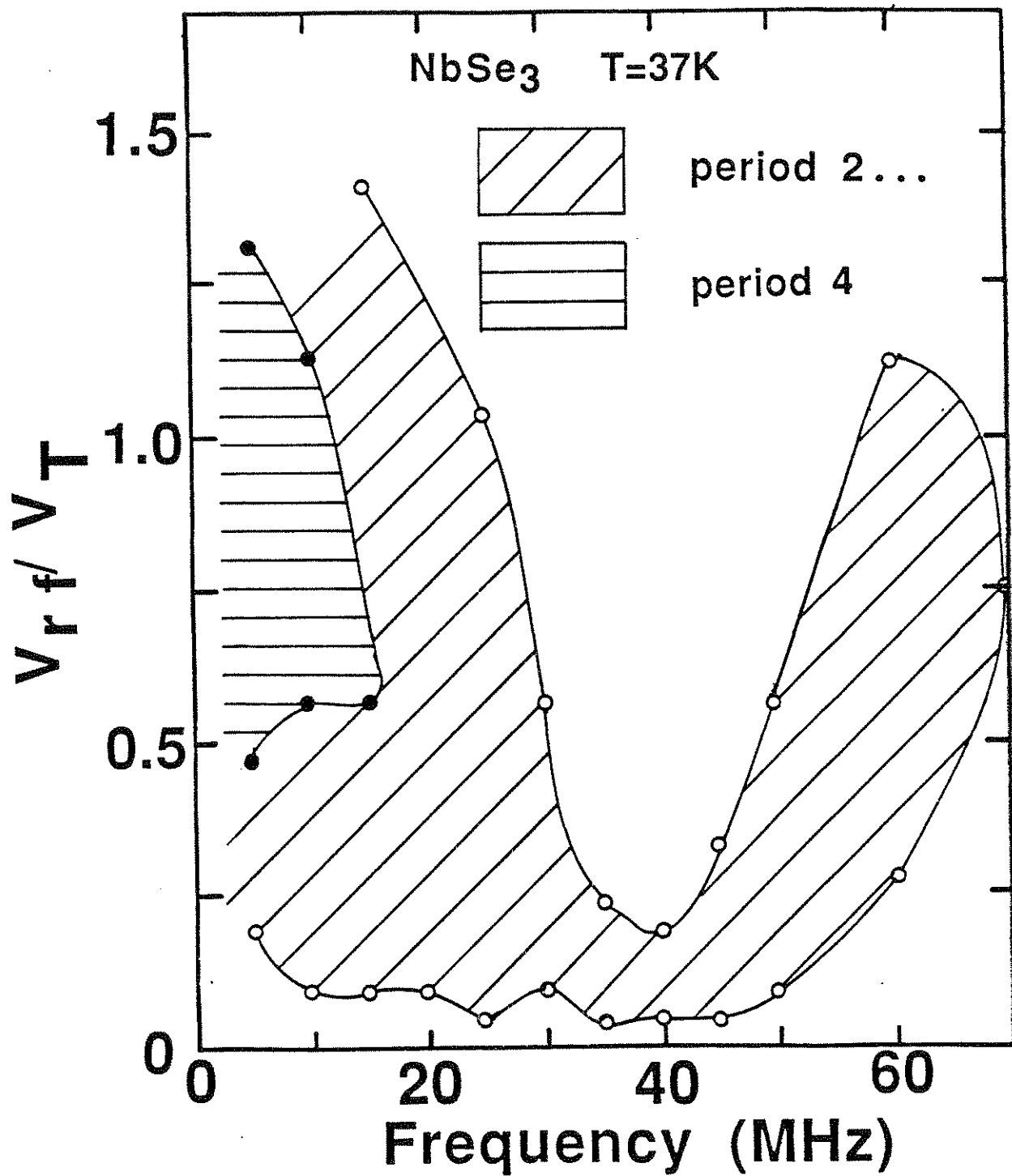
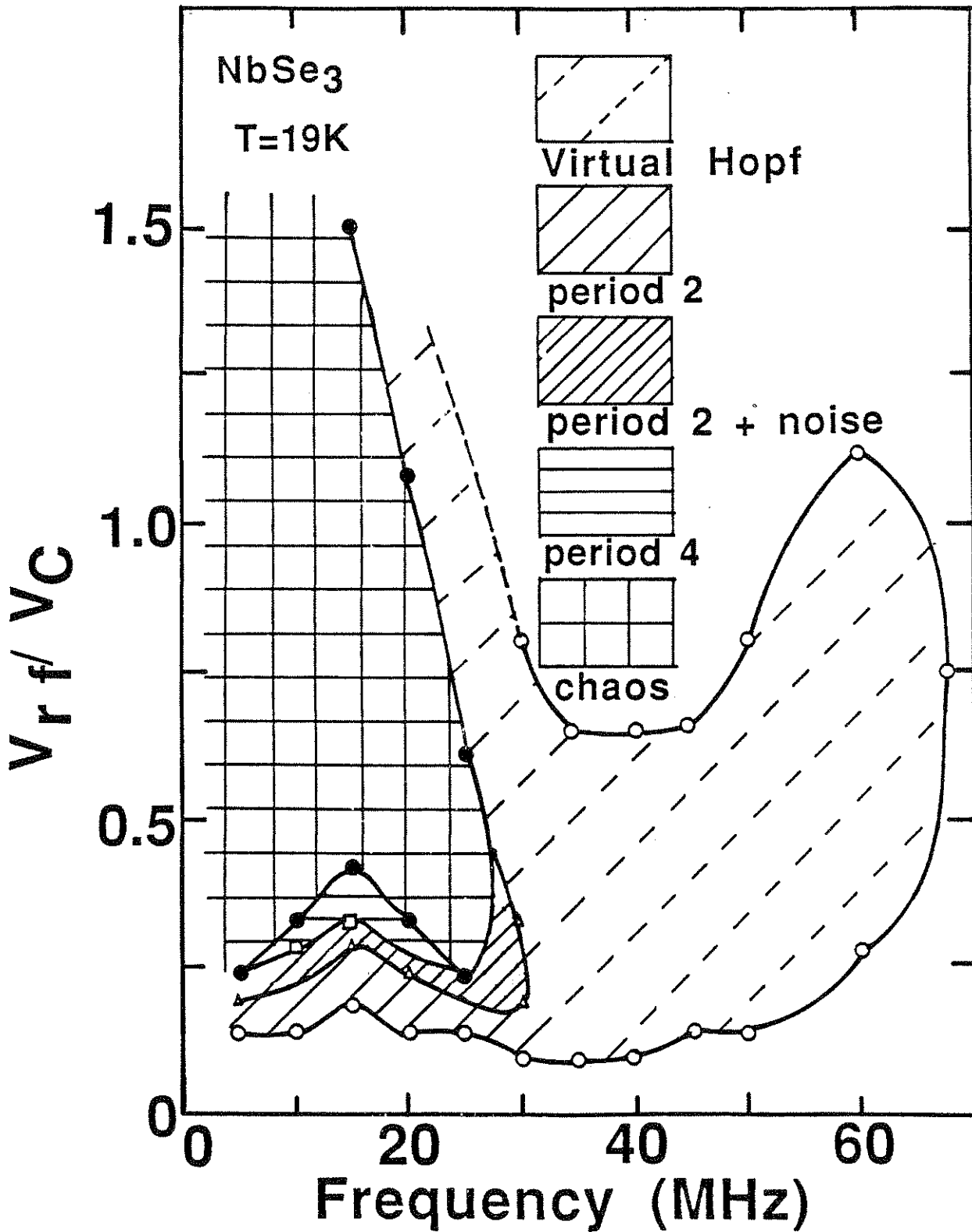Fig. 5-10) A projection of the period-doubling regime at 37 K onto the rf amplitude-frequency plane.

Fig. 5-11)   A projection of the period-doubling regime at 19 K onto the rf
amplitude-frequency plane.

of CDW response both shrinks and becomes more fully developed. Excluding the virtual Hopf regime, period-doubling at 19 K occurs only for frequencies between 5 and 30 MHz, and for amplitudes between 9% and 150% of V_T. Within in this region, however, a fully chaotic response is usually observed. Incomplete period-doubling cascades are observed only at low rf amplitudes.

3. Noisy Precursors

Besides period-doubling and chaos, a number of other mode-locking instabilities are observed in the rf response of switching CDWs. Unlike period-doubling and chaos, these instabilities are difficult to categorize. The phenomena that they most closely resemble are *noisy precursor instabilities.*[8] A noisy precursor is a nearly divergent response to external noise by a dynamical system that is close to becoming unstable. For example, when a system driven at a frequency f near a period-doubling bifurcation, a noisy precursor appears in the response spectrum of the system as a broad bump centered at $f/2$. When the system actually undergoes the period-doubling bifurcation, the period-two precursor sharpens into a narrow peak. Period-two precursors are representative of a more general class of instabilities known as *virtual Hopf transitions.*

Figure 12 shows the CDW response that is identified as a virtual Hopf transition. The power spectra in the figure are parametrized by dc bias, which increases from top to bottom. At the lowest bias, $V_{dc} = 57.8$ mV, the CDW is mode-locked on a harmonic Shapiro step. The spectrum is featureless, except for peaks at the rf drive frequency, $f = 20$ MHz, and its harmonics. As the dc bias increases, broad bumps appear discontinuously in the spectrum,
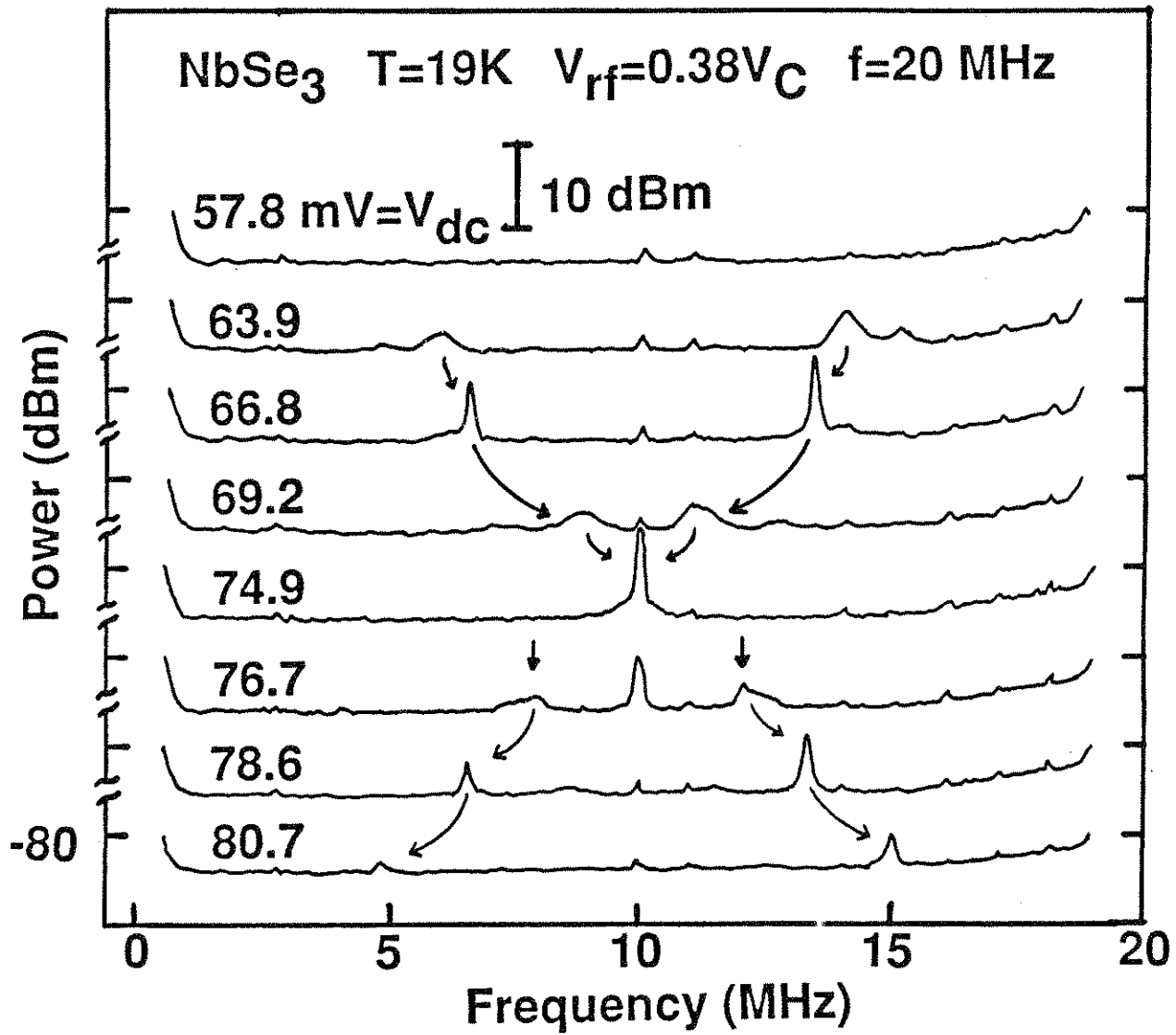
Fig. 5-12)   An example of a noisy period-two precursor.

$V_{dc} = 63.9$ mV. The lower-frequency bump is caused by the narrowband noise signal, and the higher-frequency bump is its mixing signal with the rf frequency. The appearance of the bumps signals the end of mode-locking. This kind of a response is often called *quasi-periodic* in the literature, which is a misnomer, because the narrowband noise signal is incommensurable with the rf frequency.

As the dc bias increases further, the bumps move symmetrically towards half the drive frequency, $f/2 = 10$ MHz. The bumps sharpen into narrow peaks at $f/3$ and $2f/3$, which signals subharmonic locking at $V_{dc} = 66.8$ mV. Subharmonic locking occurs again at $V_{dc} = 74.9$ mV, when the bumps abruptly coalesce into a single sharp peak at $f/2$. For a finite range of bias, the power spectrum does not change, but it eventually breaks discontinuously into *three* peaks, $V_{dc} = 76.7$ mV. The lowest-frequency bump corresponds to the mixing signal, the highest-frequency bump corresponds to the narrowband noise signal, and the sharp intermediate peak at $f/2$ is identified as a period-two precursor. With a continuing increase in dc bias, the period-two precursor gradually fades as the narrowband noise and mixing signals move symmetrically away from 10 MHz.

The period-two precursor in Fig. 12 is superficially similar to a simple mixing response between the two bumps that surround it, but several features mark it as special. First, the precursor is comparable in magnitude to the narrowband noise and mixing signals. If the precursor were a simple mixing response, it would be much smaller in amplitude. Second, the precursor signal is much narrower than either the narrowband noise or the mixing signal. If the precursor were a mixing response, its shape would be a convolution of the two

bumps and therefore its width would be much larger. Finally, the precursor signal appears discontinuously as a function of dc bias. If the precursor signal at 76.7 mV were a mixing signal, then an equally large and well-defined peak should be present in the spectrum at 69.2 mV. No such peak is evident.

The size, sharpness, and discontinuous appearance of the precursor signal strongly suggest that it represents a latent instability in the CDW response. This conclusion is supported by the precursor's evolution with decreasing rf amplitude. As the rf amplitude is lowered, the precursor signal is observed over a larger and larger range of dc bias. In contrast, the narrowband noise and mixing signals are observed over a diminishing range. Eventually the spectra in Fig. 12 cross over into an unmistakable period-doubling sequence. As the dc bias is increased, the CDW response changes discontinuously from the featureless spectrum of the top trace, to the bifurcated spectrum of the fifth trace, and then back to a featureless spectrum like the first trace. The intervening spectra of Fig. 12 are completely absent. If the rf amplitude is lowered further, a period-doubling route to chaos develops (see Fig. 11).

Figure 13 shows what may be another type of noisy precursor instability, the CDW response identified as period-two plus noise. The power spectra in this figure are again parametrized by dc bias, but for this sequence the dc bias increases from bottom to top. The sequence begins in the middle of a harmonic Shapiro step, $V_{dc} = 138$ mV, where the CDW response is period-two. The period-two response gradually disappears into period-one mode-locking on the next Shapiro step, $V_{dc} = 142.7$ mV. With a slight increase in bias, to $V_{dc} = 142.9$ mV, a sharp peak appears discontinuously at $f/2$. The $f/2$ peak
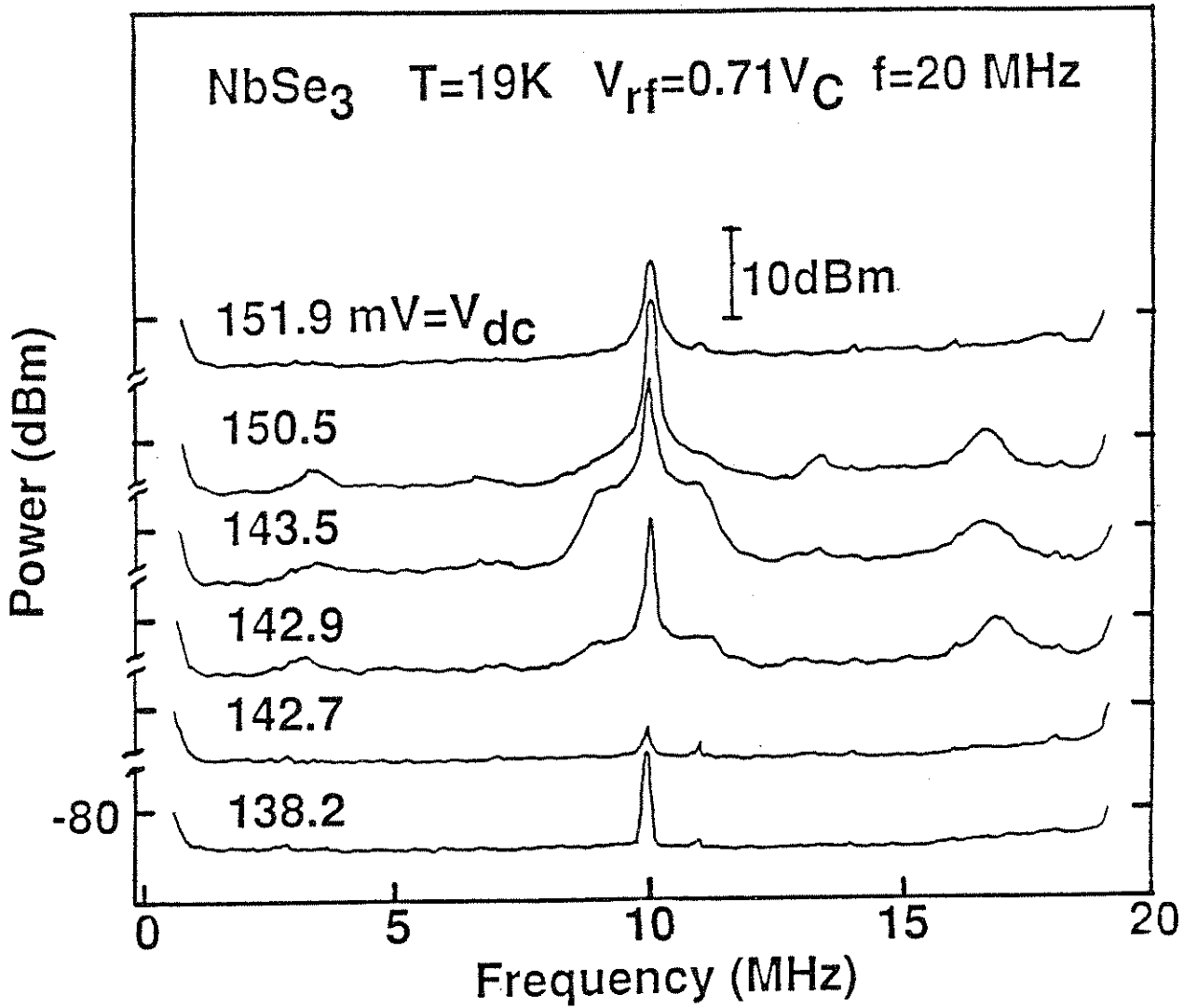
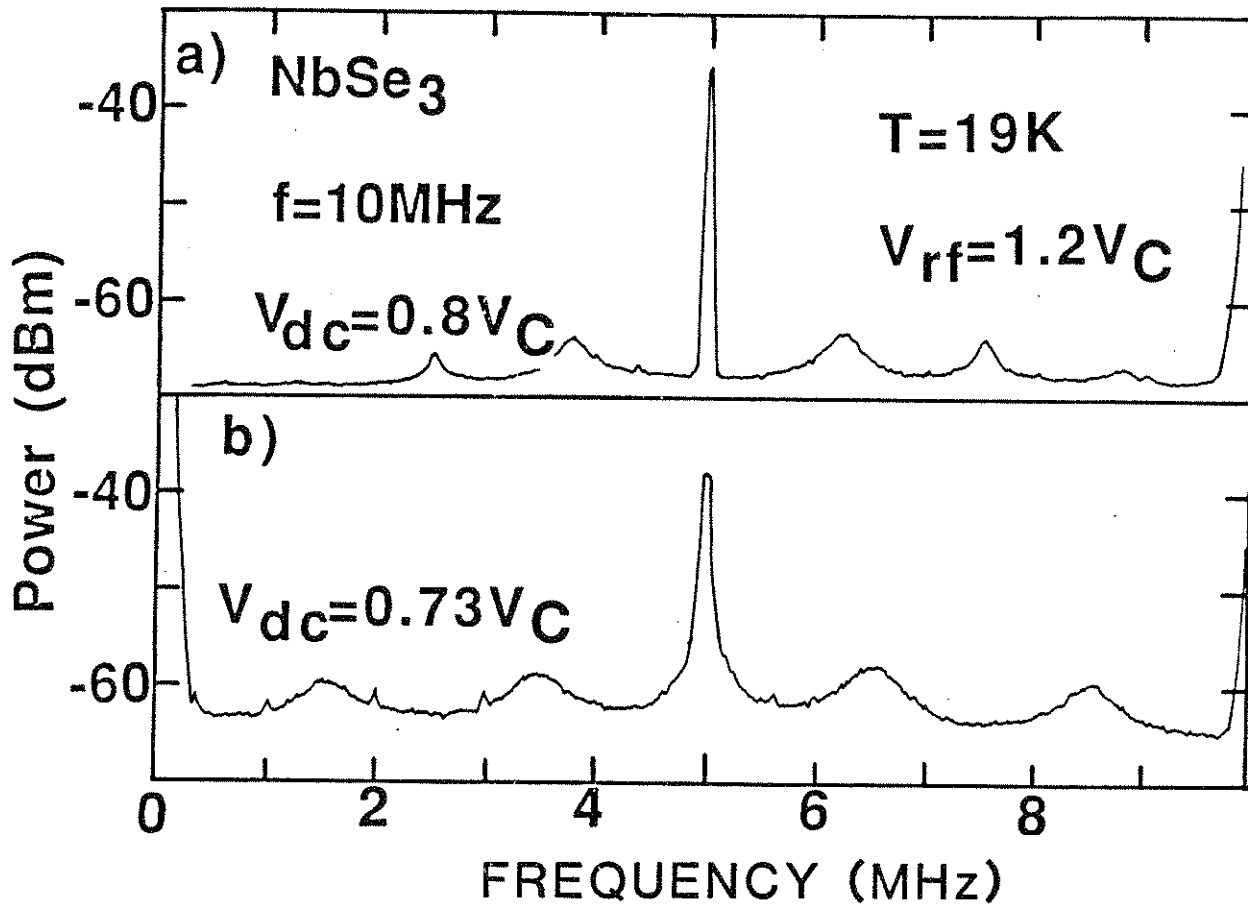Fig. 5-13)   An example of a period-two-plus-noise spectrum.

Fig. 5-14)   Examples of noisy period-eight (a) and period-six (b) precursors.

is 23 dB off the noise floor and flanked by large, symmetric structure near $f/2$, $f/6$, and $5f/6$. As the bias increases further, the $f/2$ peak grows smoothly; the flanking structure becomes more prominent; and new peaks appear new $2f/6$ and $4f/6$. Then the flanking structure abruptly disappears, leaving a conventional period-two response. The spectra from $V_{dc} = 142.9$ mV to 150.5 mV represent the period-two-plus-noise phenomenon.

Figure 14 shows what may be a third and final type of noisy precursor instability. Figure 14a shows a power spectrum with a sharp peak at $f/2 = 5$ MHz and broad peaks spaced symmetrically at intervals of $f/8$. Figure 14b shows a power spectrum with broad peaks at intervals of $f/6$. The spectra are suggestive of period-eight and period-six precursors, respectively.

B. Analysis

The most significant feature of period-doubling routes to chaos is their universality.[9] Period-doubling routes are observed in a wide variety of phenomena,[10] but they always display characteristic features that are independent of the system in which they are observed. The universality of these features is a reflection of the common dynamics underlaying period-doubling systems.

The dynamics of period-doubling systems is usually discussed in terms of *return maps*. Return maps are constructed from periodic samplings of a system's dynamical history and are an alternate way of describing the dynamics of a system driven by a periodic force. Dynamics is usually specified by a differential equation that describes how a system will evolve with time. But for

a system with a single (effective) degree of freedom, just a sampling of the system's history is sufficient to determine the system's periodicity. If x represents the dynamical variable of a system, construction of a return map begins by recording values of x at intervals of the reciprocal drive frequency. The value of x at the mth interval is denoted x_m. The return map for the system is a function G which assigns a value to x_{m+1} based on the value of x_m:

$$x_{m+1} = G(x_m) . \qquad (5.1)$$

As an example, a damped pendulum or a resistivity shunted Josephson junction obeys an equation of motion that is identical in form to the classical, rigid-phase model of Grüner, Zawadowski, and Chaikin:

$$\beta\ddot{\phi} + \dot{\phi} + F(\phi) = e_{dc} + e_{ac}\cos\Omega t \qquad (5.2)$$

(see Eq. 4.4). For small values of β, the return map of these systems is the so-called *circle map*,[11]

$$\phi_{m+1} = \phi_m + 2\pi\nu + \beta\sin\phi_m , \qquad (5.3)$$

where ν is a function of e_{dc} and e_{ac}.

Period-doubling is observed in systems with return maps of the form

$$G(x) = \lambda g(x) , \qquad (5.4)$$

where λ is a (positive) parameter and $g(x)$ is a mildly restricted function.[9] The most important restrictions on $g(x)$ are sketched in Fig. 15: $g(x)$ must go to zero at $x = 0$ and at large x, and $g(x)$ must possess a single central maximum. With only these constraints, the period-doubling behavior of $G(x)$ is completely determined.[9] For small values of λ, $G(x)$ displays period-one behavior. As λ
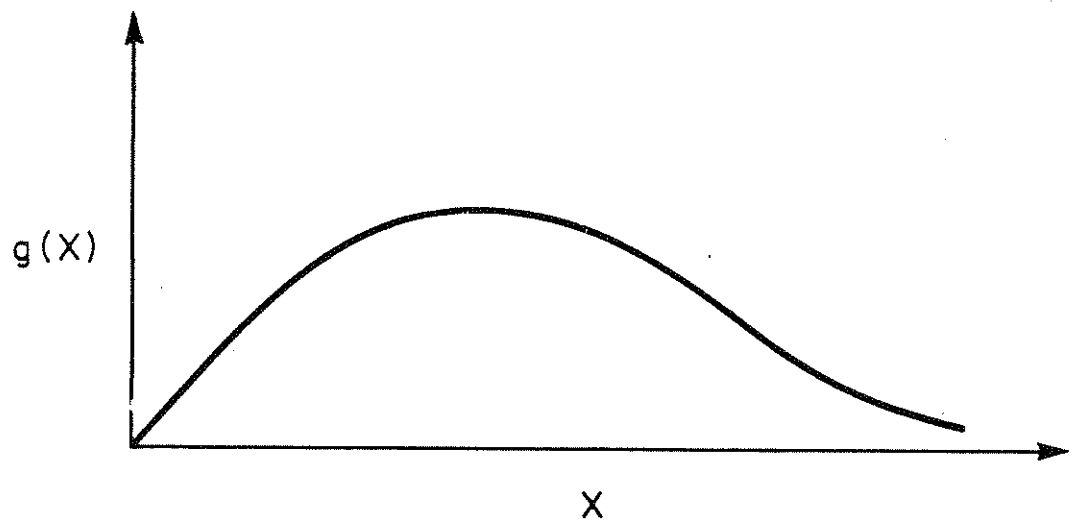
Fig. 5-15)   The generic form of a return map that exhibits period-doubling.
              After ref. 9.

increases, $G(x)$ undergoes successive period-doubling bifurcations at $\lambda = \Lambda_o$, $\Lambda_1,...$ and eventually achieves the chaotic state at $\lambda = \Lambda_\infty$. Beyond Λ_∞, $G(x)$ may display windows of period-three or other odd-period behavior. The asymptotic spacing of the bifurcation thresholds Λ_m is determined by a constant:

$$\lim_{m \to \infty} \frac{\Lambda_{m+1} - \Lambda_m}{\Lambda_{m+2} - \Lambda_{m+1}} = \delta . \qquad (5.5)$$

The asymptotic size of the system's subharmonic Fourier components A_m is determined by a second constant:

$$\lim_{m + \infty} A_m / A_{m+1} = \alpha . \qquad (5.6)$$

The constants α and δ are universal; they depend on only the functional form of $g(x)$ near its maximum. When $g(x)$ has a quadratic maximum — as would be expected for a physical system — the universal values of α and δ are 2.5029078750957... and 4.6692016091029..., respectively.

The constants α and δ *completely* specify the behavior of a period-doubling system. Because the constants are universal, an analysis of a system's period-doubling behavior can determine *only* the functional form of its return map near the return map's maximum. Because the return functions of physical systems are expected to have quadratic maxima, this means that *all physical systems undergoing period-doubling are dynamically equivalent.* The dynamical equivalence of period-doubling systems is a double-edged sword in the analysis of CDW dynamics. On one hand, an analysis of period-doubling in switching crystals can not determine a specific equation of motion for CDW dynamics. On

the other hand, an analysis can provide insights into the form of the equation.

The most basic insight provided by period-doubling is that, in the period-doubling regime, switching CDWs are governed by an equation of motion that has a single (effective) degree of freedom. This statement does not rule out equations with many degrees of freedom as models for CDW dynamics. But it does imply that any many-degree-of-freedom model must undergo a form of self-organization during mode-locking. Self-organization has been proposed for CDW dynamics in other contexts: *e.g.* "fluctuation freeze-out" (Ref. 12) or "phase-homogenization" (Ref. 6) during the mode-locking of nonswitching CDWs. However, the evidence for self-organization has been ambiguous. Some researchers claim that fluctuations are not frozen out during mode-locking, but rather masked by changes in differential resistance.[13] Period-doubling rebuts this argument, at least for switching CDWs. Period-doubling offers unambiguous evidence for the collapse of CDW dynamics onto a single degree of freedom.

Period-doubling also implies that mode-locked CDWs are dynamically underdamped. This conclusion follows from a comparison with the circle map, Eq. 5.3. The circle map is a valid return map for many systems besides pendulums and Josephson junctions; it is a generic return map for any (one-dimensional) system with competing intrinsic and extrinsic frequencies. The intrinsic frequency in the circle map is the rate at which ϕ_m changes; its analogy in CDWs is the narrowband noise frequency. The extrinsic frequency in the circle map is the rate at which the map is iterated; its analogy in CDWs is the ac drive frequency. The extrinsic frequency does not appear in Eq. 5.3, except

implicitly as the inverse unit of time. The circle map contains two parameters, ν and β. The parameter ν is roughly equivalent to a dc electric field. In the absence of mode-locking, ν determines the ratio of the intrinsic and extrinsic frequencies. The parameter β is equivalent to the inertial coefficient in the Grüner-Zawadowski-Chaikin model, as noted above.

The circle map displays both mode-locking and period-doubling.[14-16] When $\beta > 0$, the map possesses two harmonic "Shapiro steps", centered at $\nu = 0$ and $\nu = 1$, with mode-locking indices $n = 0$ and $n = 1$, respectively. As long as $\beta < 1$, the map also possesses subharmonic Shapiro steps at every rational value of ν between 0 and 1. The harmonic and subharmonic steps form a descending hierarchy, just as in CDWs. The harmonic steps $n = 0$ and $n = 1$ are the widest; the subharmonic step $n = 1/2$ is the next widest; the steps $n = 1/3$ and $n = 2/3$ are the third widest; and so on. The step widths depend on β and increase as β increases; see Fig. 16. The value $\beta = 1$ represents a critical value for mode-locking, beyond which subharmonic steps begin to overlap.

The value $\beta = 1$ also represents a critical point for the stability of periodic solutions. Below $\beta = 1$, no chaotic solutions exist. Above $\beta = 1$, two routes to chaos are observed. The first route is a quasiperiodic transition to chaos, a route which has not been observed in switching CDWs. The second route is the period-doubling cascade, which occurs inside mode-locked Shapiro steps. As a function of β, period-doubling bifurcations are observed first in smaller and then in larger Shapiro steps. The harmonic Shapiro steps, for example, period-doubling cascades are present only for $\beta > 2$. As a function of ν, period-doubling bifurcations occur as solutions move from a Shapiro step edge toward
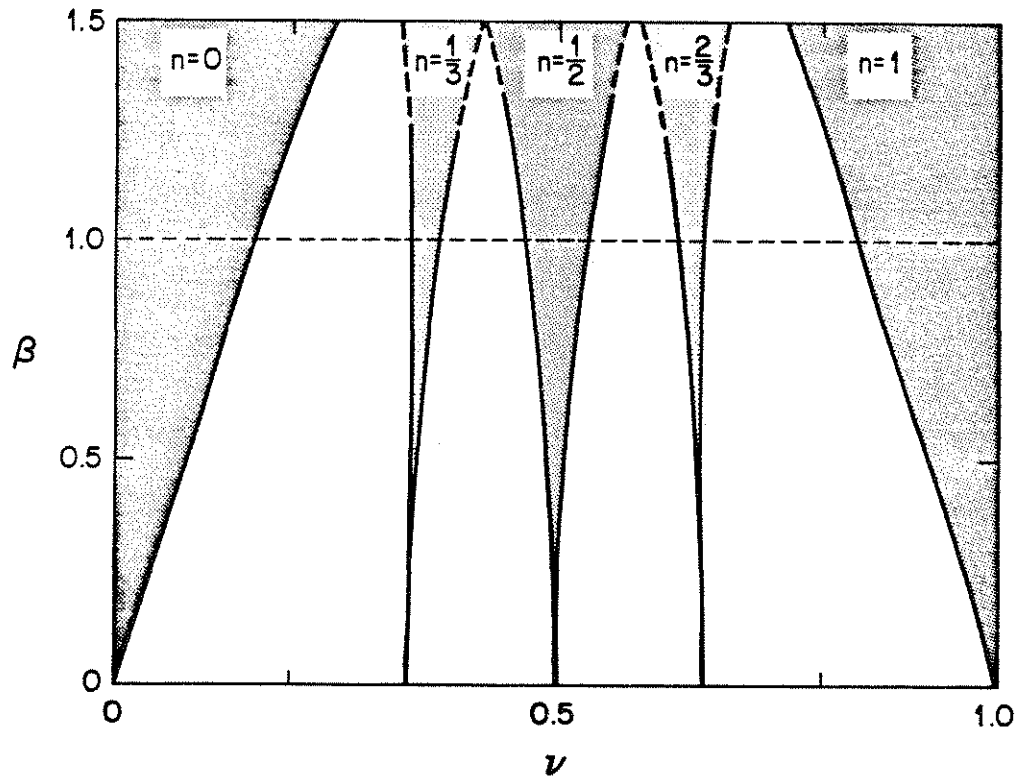
Fig. 5-16)   The   width   of   harmonic $(n = 0, 1)$ and   subharmonic
$(n = 1/3, 1/2, 2/3, \cdots)$ steps in the circle map. After ref. 14.

the Shapiro step center.

A comparison between CDW and circle-map dynamics is strictly valid only inside mode-locked Shapiro steps, where the presence of period-doubling indicates that the dynamics of both systems reduce to one-parameter return maps. For the circle map, the explicit form of the map may be derived at the center of a harmonic step:

$$\Phi_{m+1} = \beta \ g(\Phi_m) \ . \tag{5.7}$$

Here Φ is an invertable function of ϕ, the function g satisfies the constraints of Eq. 5.4, and the coefficient β acts as a bifurcation parameter. As β increases, solutions move upward in Fig. 16 along the lines $\nu = 0$ or $\nu = 1$. When β crosses 2, the solutions undergo period-doubling bifurcations.

A similar sequence may be obtained experimentally for switching CDWs. By adjusting dc bias, a CDW may be held at the center of a harmonic Shapiro step as temperature is changed. (An adjustment of dc bias is required to compensate the temperature dependence of the threshold field and the crossover frequency.) At temperatures above the switching regime ($\gtrsim 42$ K), the CDW response is period-one. At temperatures within the switching regime, the CDW response displays period-doubling bifurcations provided that the rf frequency and amplitude were fixed at appropriate values. Thus, a switching CDW possesses a return map of the form (5.7), where the bifurcation parameter β is a function of temperature. The physical significance of β is suggested by a comparison with the rigid-phase equation, where it acts as an inertial coefficient. To the extent that the CDW response can be modelled by a second-order differential equation,

the above analysis implies that acceleration terms (second-order time derivatives) are significant compared to damping terms (first-order time derivatives). In this sense, CDW dynamics are underdamped.

A direct comparison of CDW dynamics and the rigid-phase model also points to underdamped dynamics.[3] In the rigid-phase model, hysteresis and switching in the dc I-V curve are determined solely by the inertial coefficient. A hysteresis parameter may be defined for the rigid-phase model by $H = (e_{c1} - e_{c2})/e_{c1}$, where e_{c1} and e_{c2} are the respective dc thresholds for CDW depinning and repinning. Figure 17 shows the calculated dependence of H on $Q = \beta^{\frac{1}{2}}$. From the figure, the inertial coefficient may be determined for a real crystal, such as in Fig. 4, by measuring H in the dc I-V curve under zero rf bias. In the top trace of Fig. 4, H is 0.24, which implies an underdamped inertial coefficient of $\beta = 2.3$. The close agreement of $\beta > 2$ in the circle map and $\beta = 2.3$ in the rigid-phase equation is probably fortuitous, because the threshold value of β necessary for period-doubling depends on details of the return function $g(x)$. For example, a model is derived in the next chapter whose small-signal response is given by the rigid-phase and circle map equations. In this model, however, period-doubling bifurcations begin for values of the inertial coefficient as small as 0.3. (See Fig. 6.8; the inertial coefficient in the figure is the parameter κ.)

Divergent values of the inertial parameter are a reminder that period-doubling can not be used to deduce a specific equation of motion for CDW dynamics, only the general form of such an equation. The validity of a specific equation must be decided by other criteria, such as whether the model produces
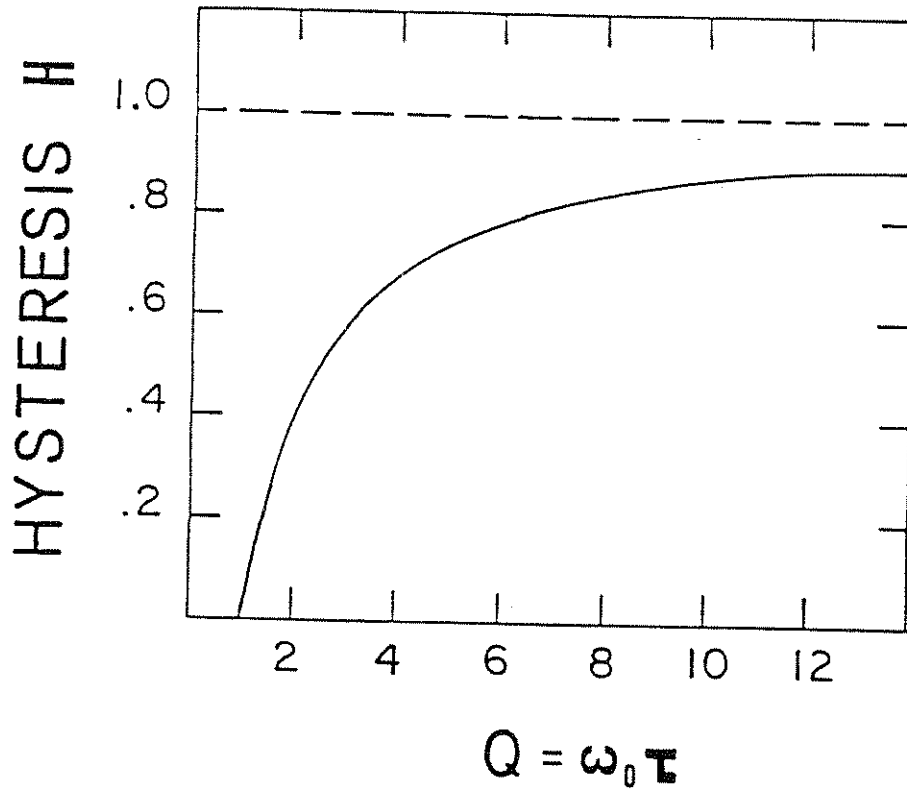
Fig. 5-17)   Hysteresis in the rigid-phase model, Eq. 5.2, as a function of $Q = \beta^{\frac{1}{2}}$.

period-doubling for reasonable values of its parameters. The rigid-phase model does not. The inertial parameter in the model depends on a pinning frequency ω_o and a damping constant τ:

$$\beta = (\omega_o \tau)^2 \ . \tag{5.7}$$

(See Eq. 4.3 or 2.55.) The parameters ω_o and τ may be separately calculated once the crossover frequency $\omega_o^2 \tau$ is known. The crossover frequency may be determined from the variation of the first Shapiro step height δV_1 with rf bias:

$$\delta V_1 = V_{c1} \, | \, J_1(V_{rf} \omega_o^2 \tau / V_{c1} \omega_{rf}) | \ . \tag{5.8}$$

(See Eq. 2.58.) Here $J_1(z)$ is the first-order Bessel function which attains its maximum at $z = 1.84$. The maximum value of δV_1 in Fig. 5.4 is found to occur at $V_{rf} = 35$ mV when $\omega_{rf}/2\pi = 15$ MHz. From these values, the crossover frequency is determined to be $\omega_o^2 \tau / 2\pi = 22$ MHz. The corresponding values of pinning frequency and damping constant are calculated to be $\omega_o/2\pi = 15$ MHz and $\tau^{-1} = 61$ MHz. These values are orders of magnitude smaller than values obtained from ac conductivity. Hence, the rigid-phase model is an inconsistent model of switching, even though it predicts the correct period-doubling behavior.

III. Summary

This chapter has discussed nonlinear instabilities which distinguish switching from nonswitching CDW transport. Negative-differential-resistance instabilities are characterized by intermittent, large amplitude noise that is close to 1/f in its spectral distribution. The instabilities are observed over a narrow temperature range, typically a few degrees, and can be explained by metastable

hopping of CDW current between two or more current configurations. Period-doubling instabilities occur over a broader temperature range, 15-40 K, and can be explained by an effective inertial parameter in the CDW equation of motion. Period-doubling instabilities indicate that CDW dynamics collapses onto a single degree of freedom when mode-locking occurs.

Negative-differential-resistance and period-doubling instabilities are observed in different frequency ranges. Negative-differential-resistance instabilities are largest at frequencies below 1 MHz, while period-doubling instabilities occur at frequencies between 1 and 100 MHz. The different frequency ranges reflect different physical origins for the phenomena. The time scale of negative-differential resistance instabilities is set by the delay required to establish a new CDW current path within a crystal. Pulsed experiments by Zettl and Grüner[17] show that delays can range from 1 to 100 μsecs. The time scale of period-doubling instabilities is set by CDW dynamics at a single phase-slip center. Sliding CDW dynamics occur at a rate equal to the narrowband noise frequency. Narrowband noise frequencies typically start above 1 MHz in switching crystals, and can in principle achieve frequencies above 1 GHz at very high electric fields. But at frequencies above 100 MHz, the results of Chap. 4 show that internal phase deformations become important in CDW dynamics. When internal deformations are important, CDW dynamics can not collapse onto a single dynamical variable, which precludes period-doubling routes to chaos. Thus the frequency ranges of both period-doubling and negative-differential-resistance instabilities are consistent with time scales established independently in other experiments. At frequencies below 1 MHz, a crossover from single to multiple

domain dynamics can be observed in so-called ac switching noise, a phenomenon which is described in ref. 1.

CHAPTER 6:   PHASE-SLIP MODEL OF SWITCHING

CHAPTER 6: PHASE-SLIP MODEL OF SWITCHING

This chapter develops and then analyzes a phenomenological model of CDW dynamics that describes the motion of both the CDW phase and amplitude. Specifically, a Hamiltonian is introduced in which the CDW amplitude is reduced by large amounts of phase polarization and in which the CDW phase elasticity is in turn diminished by the reduction in CDW amplitude. At strong pinning centers, these two processes reinforce one another and lead to transient collapse of the CDW order-parameter. From the Hamiltonian, a set of coupled equations is derived for the CDW amplitude and phase, and a subset of these equations is studied numerically under combined dc and ac electric fields. (The numerical calculations were performed by M. Inui.) The subset of equations predicts not only switching and hysteresis, but also period-doubling, chaos, and an inductive sliding ac conductivity. Thus this chapter has two main results. First, a set of equations is derived that model the dynamics of strongly pinned CDWs; and second, a self-consistent explanation is provided for the unusual dynamics associated with switching CDWs.

The chapter is organized into three sections. In Section I, the so-called phase-slip equations are derived from a generalization of the Fukuyama-Lee Hamiltonian.[3-5] In Section II, the response of the phase-slip equations to external electric fields is analyzed from Inui's numerical integration of the equations.[1] In Section III, the chapter concludes by comparing results of the equations to experiments on switching CDWs.

I. Phase-Slip Model

A. Hamiltonian and equations of motion

The order-parameter of a CDW may be written as $u e^{i\phi}$ where u specifies the amplitude and ϕ the phase of the lattice distortion associated with a CDW. For small distortions of a CDW from equilibrium, Lee, Rice and Anderson have shown[2] that the CDW amplitude and phase define approximate normal modes whose respective frequencies Ω_+ and Ω_- are given by

$$\Omega_+^2 = \lambda \omega_Q^2 + \frac{1}{3} c^2 k^2$$

$$\Omega_-^2 = c^2 k^2 .$$

Here k is the distortion wavevector, measured from the Fermi wavevector k_F; λ is the dimensionless electron-phonon coupling constant; and Q is the $2k_F$ wavevector with ω_Q the $2k_F$ phonon frequency. The phason velocity c is given by $(\hbar^2 k_F^2 / m^*)^{1/2}$ where m^*, the effective CDW mass, depends on the CDW amplitude as well as the normal electronic mass. In the amplitude dispersion relation, the first term dominates the second, except at large wavevectors. Therefore the wavevector dependence of Ω_+ can be neglected for the rest of this discussion.

Fukuyama has shown[3] that, in order to treat phason dynamics, the phase mode may be regarded as an elastic continuum. For strongly pinned CDWs, the Fukuyama Hamiltonian must be generalized to account for the dynamics of the amplitude mode. An appropriate Hamiltonian is

$$\int dx \{ \mu u_o^2 (d\phi/dt)^2 + \mu (du/dt)^2 + Y_o^2 u_o^2 (d\phi/dx)^2 + \mu \lambda \omega_Q^2 (u - u_o)^2 \}$$

where μ is the ionic mass density and u_o is the equilibrium value of the CDW amplitude. Young's modulus for the phase mode is given by $Y = \mu c^2$ and Y_o denotes its equilibrium value. (Henceforth the subscript on Y_0 will be dropped.) In the Hamiltonian, the (small) electronic contribution to m^* has been neglected.

The CDW phase and amplitude coordinates are mixed by large distortions of the CDW order-parameter, because they are not exact normal modes of CDW motion. A coupling term must be introduced in order to produce mixing of the amplitude and phase modes; a particularly simple coupling is obtained by requiring that the phase-mode elasticity depend upon the CDW amplitude:

$$Yu_o^2(d\phi/dx)^2 \longrightarrow Yu^2(d\phi/dx)^2 \ .$$

Besides being simple, this coupling possesses a feature which is critical to later results: as the CDW amplitude goes to zero, the elasticity of the phase mode vanishes. The discussion below will show that this feature, which must be found in any amplitude-phase coupling term, leads to the phenomena characteristic of switching CDW conduction. A generalized Fukuyama Hamiltonian is thus given by[5]

$$H_o = \int dx \Big\{ u^2 [\mu(\frac{d\phi}{dt})^2 + Y(\frac{d\phi}{dx})^2] + \mu(\frac{du}{dt})^2 + \mu\lambda\omega_Q^2(u - u_o)^2 \Big\} \ . \qquad (6.1)$$

The standard Fukuyama-Lee-Rice terms will be used to describe the interaction of CDWs with applied electric fields and with lattice defects:[3-5]

$$H_{field} = - \int dx \{ \rho_{eff} n \, e \, E \, \phi / Q \}$$

$$H_{pin} = - \int dx \{ \sum_j V_j \, \rho \, \delta(x - R_j) \cos(Qx + \phi) \}$$

$$(6.2)$$

where n is the electronic density; E is the applied electric field; ρ is the electronic amplitude of the CDW; ρ_{eff} is an effective, normalized CDW density; and summation is over all pinning sites R_j, whose respective pinning strengths are denoted by V_j. Both ρ and ρ_{eff} depend on the CDW amplitude u, so both act as dynamical variables in Eq. 2.

CDW phase dynamics are well-known to be overdamped.[18] CDW amplitude dynamics will be assumed to be overdamped also so that both the CDW phase and amplitude obey relaxational equations of motion:[5]

$$\frac{d\phi}{dt} = - \Gamma_\phi \frac{\delta H}{\delta \phi}$$

$$\frac{d}{dt}\left(\frac{u}{u_o}\right) = - \Gamma_u \frac{\delta H}{\delta\left(\frac{u}{u_o}\right)} .$$

$$(6.3)$$

Here Γ_ϕ and Γ_u are damping parameters for the phase and amplitude modes, and H is the combined Hamiltonian density of Eqs. 1 and 2.

Several approximations simplify Eqs. 3 to a more tractable form. First, the equations may be converted into a discretized form by neglecting variations of the CDW order-parameter on length scales shorter than the average defect spacing. The discretized Hamiltonians will be taken to be

$$H_o = \sum_j \{\ell_j Y u_{j+1} u_j (\frac{\phi_{j+1} - \phi_j}{\ell_j})^2 + \xi\mu\lambda\omega_Q^2 (u - u_o)^2\} \ ,$$

$$H_{field} = -\sum_j \ell_j' \rho_j^{eff} n \, e \, E \, \phi_j / Q \ ,$$

(6.4)

$$H_{pin} = -\sum_j \rho_j \, V_j \cos(QR_j + \phi_j) \ ,$$

where time derivatives have been dropped from H_o because of the assumption of relaxational dynamics. Here the length ℓ_j is the distance $R_{j+1} - R_j$ between sites, the length ℓ_j' is the average distance $\frac{1}{2}(\ell_j + \ell_{j-1})$, and the length ξ is the CDW amplitude coherence length. The dynamical variables ϕ_j, u_j, ρ_j and ρ_j^{eff} denote respective values of ϕ, u, ρ and ρ_{eff} at the jth pinning site. The concentration n_D of defect sites is related to the average defect spacing by $n_D^{-1} = \overline{\ell}_j$. Typically, the amplitude coherence length is much shorter than the average defect spacing: $\xi << \overline{\ell}_j$.

Eqs. 3 are further simplified if the CDW coupling to defects and applied electric fields is independent of the CDW amplitude. Amplitude independence is valid when pinning centers are either very weak ($\rho_j V_j$ much weaker than the phase energy $n_D u_0^2 Y$) or very strong ($\rho_j V_j$ much larger than the condensation energy $\xi\mu\lambda\omega_Q^2 u_0^2$). At weak centers, the CDW amplitude remains very close to its equilibrium value because the CDW phase depins before sufficient polarization accumulates to suppress the CDW amplitude. At very strong centers, the opposite limit applies: the CDW phase never depins, at least not until the CDW amplitude has collapsed or has nearly collapsed. Except for these transient, singular moments when $u_j \cong 0$, the large value of V_j at a strong pinning center completely dominates any variations in ρ_j or ρ_j^{eff}. (The transient

moments when $u_j \cong 0$ will be dealt with in the next section.) Thus at both very weak and very strong impurity sites, the amplitude dependences of H_{field} and H_{pin} are unimportant. Eqs. 3 may be rewritten as

$$\frac{d\phi}{dt} = -\Gamma_\phi \frac{\delta H}{\delta \phi}$$

$$\frac{d\Delta}{dt} = -\Gamma_u \frac{\delta H_o}{\delta \Delta}$$

(6.3′)

where Δ is the normalized amplitude (u/u_o). The resulting equations of motion are

$$\dot{\phi}_j = \ell_j' \Gamma_\phi \rho_{eff} n Q E - \Gamma_\phi \rho V_j \sin(Q R_j + \phi_j)$$
$$- 2\Gamma_\phi Y u_o^2 \Delta_j \left\{ \Delta_{j+1} \left(\frac{\phi_j - \phi_{j+1}}{\ell_j} \right) + \Delta_{j-1} \left(\frac{\phi_j - \phi_{j-1}}{\ell_{j-1}} \right) \right\}$$
$$\dot{\Delta}_j = -2\Gamma_u \xi \mu \lambda \omega_Q^2 u_o^2 (\Delta_j - 1)$$
$$- \Gamma_u Y u_o^2 \left\{ \ell_j \Delta_{j+1} \left(\frac{\phi_{j+1} - \phi_j}{\ell_j} \right)^2 + \ell_{j-1} \Delta_{j-1} \left(\frac{\phi_j - \phi_{j-1}}{\ell_{j-1}} \right)^2 \right\}$$

(6.5)

where ρ_{eff} and ρ are now regarded as constants.

B. Phase slippage

Eqs. 5 are valid only for $\Delta_j > 0$. The equilibrium value of Δ_j is given by

$$\Delta_j^{(eq)} = 1 - \frac{1}{2} \frac{Y}{\xi \mu \lambda \omega_Q^2} \left[\Delta_{j+1} \frac{(\phi_{j+1} - \phi_j)^2}{\ell_j} + \Delta_{j-1} \frac{(\phi_j - \phi_{j-1})^2}{\ell_{j-1}} \right].$$

At a strong pinning center, the phase distortions $|\phi_{j\pm1} - \phi_j|$ can become so large that $\Delta^{(eq)} \leq 0$. Vanishing or negative values of $\Delta^{(eq)}$ drive the CDW order-parameter $\psi = u e^{i\phi}$ toward collapse. Depending on various relaxation rates, ψ may or may not collapse completely, but the effect on the strongly

pinned phase is identical. In the case of near collapse, H_{pin} becomes so reduced that the accumulated phase polarization forces the phase to move in the direction of E. Because V_j is large at a strong pinning site, the accumulated phase polarization is also quite large and the phase velocity tends to be high when $\Delta_j \approx 0$. The phase therefore abruptly advances by about 2π, whereupon the phase polarization is relieved, the amplitude Δ_j regenerates; and the phase again becomes stuck at the strong impurity site.

In the case of complete collapse, the CDW phase becomes indeterminate at the strong pinning site. It may therefore "slip" so that phase polarization is again relieved and the CDW amplitude regenerates. This process is known as phase slippage in superconductors and superfluids.[19,20] Because of phase pinning, the details of phase slippage are slightly different in charge-density waves. If the CDW order-parameter is viewed as a variable in the complex plane, then the first-order differential equations of 6.3 and 6.5 require that ϕ change by exactly $\pm\pi$ (modulo 2π) when ψ crosses zero; the sign and modulus of the phase change are chosen so that $\Delta^{(eq)}$ becomes equal to its smallest possible positive value. Following a $\pm\pi$ phase change at a strong pinning center, the potential energy of the CDW is at its maximum value. Because V_j is very large at strong pinning centers, a $\pm\pi$ phase-flip is followed by a quick advance of the CDW phase through an additional factor of π.

Thus for either complete or near complete collapse of the CDW order-parameter, the CDW phase abruptly advances by 2π (modulo 2π) at a strong pinning site. Since the discusison will deal with CDW dynamics on relatively long time-scales, both processes will be called "phase-slips" and will be

approximated both by instantaneous 2π (modulo 2π) hops of the CDW phase. The complete equations of motion are therefore Eqs. 5 augmented by the condition that ϕ changes by $\pm 2\pi$ (modulo 2π) whenever Δ collapses.

C. Reduced phase-slip equations

It will now be shown how Eqs. 5 can produce switching and hysteresis. It is convenient to consider a (one-dimensional) crystal of N weak pinning centers and impose periodic boundary conditions, so that the crystal may be thought of as closed loop. Each weak impurity is assumed to be of strength $V_\omega \ll n_D Y u_o^2/\rho$. Fukuyama and Lee[4] have shown that when N is large enough, the crystal breaks into a series of phase domains whose average length is given by

$$L_o = (\eta\pi\epsilon)^{-2/3} n_D^{-1}$$

where η is a constant of order unity, n_D is the (weak) pinning center concentration, and ϵ is the Fukuyama-Lee pinning parameter:

$$\epsilon = \frac{V_w \rho}{u_o^2 Y n_D} \ .$$

Since the CDW phase within a domain is nearly rigid, the number of dynamical variables is reduced from N (one for the phase at each pinning site) to $N/n_D L_o$ (one for the phase within each domain).

If the average phase within a weakly pinned domain is $\overline{\phi}$, then the effective pinning within the domain is approximately $\overline{V}\cos(\phi-\overline{\phi})$, where $\overline{V} \sim V_\omega \rho (n_D L_o)^{1/2}$. If a single, very strong pinning center is added to the domain, then presumably the pinning center has three main effects. First, the

entire domain will become strongly pinned, because the average phase within the domain can not depin until the CDW amplitude at the strong pinning center has collapsed. Second, the average phase within the strongly-pinned domain will shift to the phase ϕ_o that is preferred at the strong pinning center. Finally, since the amplitude relaxation rate Γ_u is generally much faster than the phase relaxation rate Γ_ϕ, the strongly-pinned domain may respond faster than a weakly pinned domain to applied forces.

Now suppose that a single strong pinning center is added to the model crystal, say at site $j = M$, and that the total number N of weak pinning centers is small enough so that just two domains are present in the crystal: a strongly-pinned domain centered at $j = M$ and a weakly-pinned domain in the rest of the crystal. The phase of the strongly-pinned domain will be denoted by ϕ_o and the phase of the weakly-pinned domain by ϕ. The only other dynamical variable in the problem is the CDW amplitude Δ at the strong pinning center. The phase-slip equations of Eqs. 5 are greatly simplified:

$$\frac{1}{\Omega_o}\dot{\phi} = e - \sin\phi - \alpha\Delta(\phi - \phi_o) \tag{6.6a}$$

$$\frac{1}{\Omega_o}\dot{\Delta} = -\frac{1}{\kappa}\{\Delta - [1 - (\frac{\phi - \phi_o}{\theta})^2]\} \tag{6.6b}$$

$$\phi_o \longrightarrow \begin{cases} \phi_o & \text{if } \Delta > 0 \\ \phi_o \pm 2\pi & \text{if } \Delta \leq 0 . \end{cases} \tag{6.6c}$$

The phase change in ϕ_o is chosen to minimize $|\phi - \phi_o|$. Here e represents the external electric field applied to the crystal. The electric field is normalized to the characteristic field of the weakly pinned domain:

$$e = E/E_p ,$$

where

$$E_p = Q\overline{V}/neL_o .$$

CDW current in these equations is proportional to $\dot{\phi}$, so dc current is proportional to $<\dot{\phi}>$ where $<...>$ indicates time averaging.

The reduced phase-slip equations are a generalization of the Grüner-Zawadowski-Chaikin model.[6] The equations were previously written down by Hall et al.[17] without derivation. From the present derivation, the phase-slip parameters Ω_o, α, κ, and θ can be related to microscopic quantities:

$$\Omega_o = \Gamma_\phi \overline{V}$$

$$\alpha = 2\ Y\ u_o^2/\overline{V}L_o$$

$$\kappa = \Gamma_\phi \overline{V}/2\Gamma_u \xi \mu \lambda \omega_Q^2 u_o$$

$$\theta = (4\xi\mu\lambda\omega_Q^2 u_o L_o/Y u_o^2)^{1/2} .$$

The first two parameters, Ω_o and α, are common to classical models of CDW phase dynamics. The frequency Ω_o is the so-called "crossover frequency" observed in ac conductivity experiments on CDWs.[21] This frequency is the characteristic relaxation rate of a weakly-pinned domain. For the lower CDW state of NbSe$_3$, Ω_o is about 100 MHz. The parameter α represents the phase elasticity of a CDW, normalized to the weak impurity pinning potential. The value of α depends on the lengthscale over which one considers CDW dynamics. On the Fukuyama-Lee-Rice lengthscale, weak impurity pinning just dominates CDW phase elasticity, so a conventional value of α is 0.2. The remaining two parameters, κ and θ, are new to this model of strongly-pinned CDW dynamics.

The parameter κ represents the relaxation time of the strongly-pinned domain. The parameter θ represents the amount of phase polarization necessary to cause amplitude collapse. No conventional choices exist for κ and θ, which will be treated as adjustable parameters in order to fit experimental data. Appropriate values of θ and κ are discussed in Section III.

To show that Eqs. 6 can exhibit hysteresis and switching, consider the limit that $\alpha\theta \gg 1$ and $\Omega_o/\kappa \gg 1$. This limit corresponds to an extremely polarizable phase and an extremely fast amplitude relaxation rate. In Eqs. 6, the weak-pinning term becomes negligible and the CDW amplitude follows the CDW phase polarization without any lag. The CDW equation of motion simplifies to

$$\dot{\phi} \cong e - \alpha(\phi-\phi_o)\{1 - [(\phi-\phi_o)/\theta]^2\}$$

$$\phi_o \longrightarrow \begin{cases} \phi_o & \text{if} \quad |\phi-\phi_o| < \theta \\ \\ \phi_o \pm 2\pi & \text{otherwise .} \end{cases}$$

(6.8)

The elasticity term $\alpha(\phi-\phi_o)\{1 - [(\phi-\phi_o)/\theta]^2\}$ is shown in Fig. 1. As e increases from zero, the CDW does not begin to slide until e exceeds the maximum value of the potential. This maximum sets an *upper threshold field* given by

$$e_{t2} = \frac{2}{3\sqrt{3}} \alpha\theta .$$

(6.9)

After the CDW begins to slide, phase slippage keeps $(\phi-\phi_o)$ in the range $[\theta-2\pi, \theta]$. In this range, the maximum value of the elasticity potential sets a *lower threshold field* given by
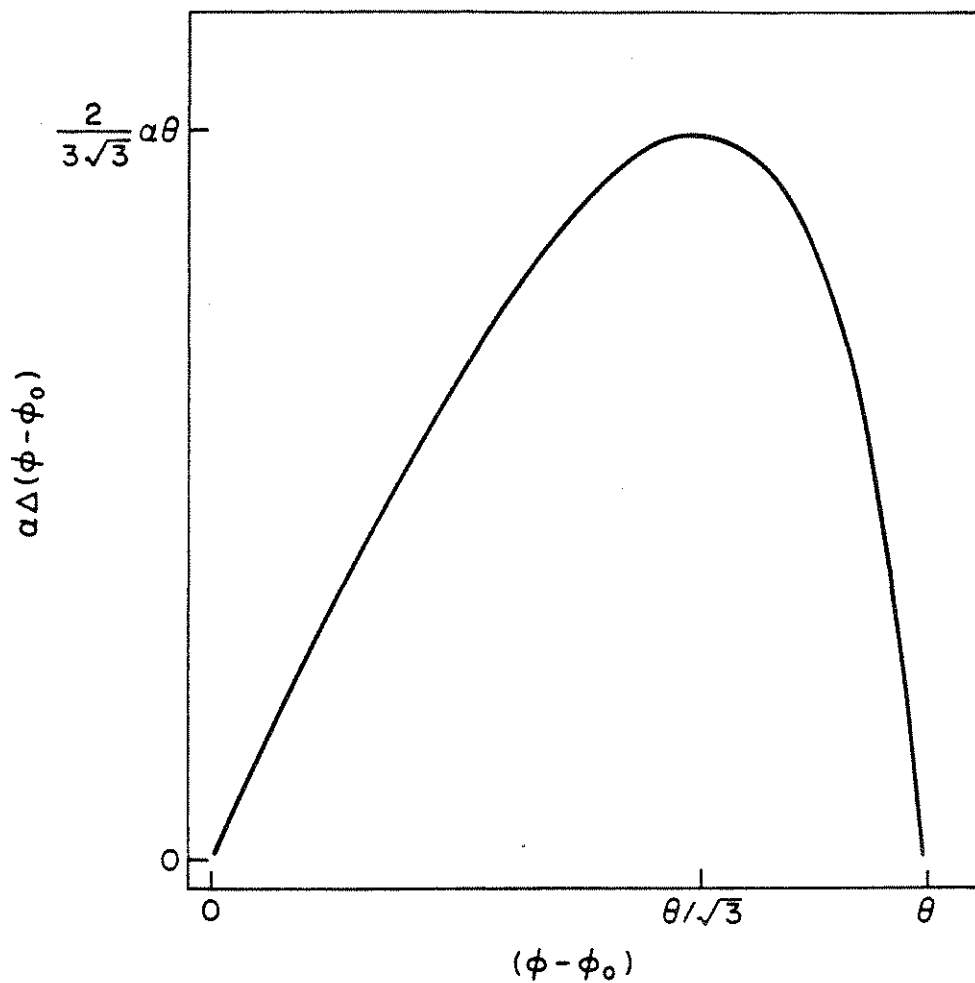
Fig. 6-1) The phase elasticity $\alpha\Delta(\phi - \phi_0)$ as a function of phase polarization $(\phi - \phi_0)$. The figure applies to the limit that $\Omega_0/\kappa \gg 1$, in which the CDW amplitude becomes a simple function of phase polarization.

$$e_{t1} = \begin{cases} e_{t2} & \text{if } \theta \leq (3+\sqrt{3})\pi \\[2ex] \alpha\theta(1-\dfrac{2\pi}{\theta})[1-(1-\dfrac{2\pi}{\theta})^2] & \text{otherwise .} \end{cases} \qquad (6.10)$$

Once e exceeds e_{t2}, the CDW continues to slide as long as e continues to exceed e_{t1}. Therefore when $e_{t1} < e_{t2}$, the CDW stops sliding at a electric field which is lower than the field at which it began sliding; i.e. the motion of the CDW becomes hysteretic. Equation 10 defines a critical polarizability $\theta_H \equiv (3+\sqrt{3})\pi$ which determines the onset of hysteresis: if $\theta > \theta_H$, then $e_{t1} < e_{t2}$ and CDW current is a bistable function of the applied electric field.

In Eqs. 8, hysteresis is caused by an abrupt collapse in the elasticity potential once the CDW begins sliding. This collapse also causes switching. Just above the upper threshold field, the minimum instantaneous CDW velocity is $e_{t2} - e_{t1}$, so the time-averaged dc CDW current is larger than this:

$$<\dot{\phi}>\Big|_{e=e_{t2+}} > e_{t2} - e_{t1} .$$

When $\theta > \theta_H$, dc CDW current jumps from zero to a finite value as e exceeds e_{t2}.

Even away from the limit $\alpha\theta \gg 1$ and $\Omega_o/\kappa \gg 1$, switching and hysteresis occur in Eqs. 6 when θ becomes sufficiently large. As $\alpha\theta$ becomes comparable to 1, the upper and lower threshold fields are given by

$$e_{t2} = \max_{\phi \in [0, \theta]} \left[\sin\phi + \alpha(\phi - \phi_o)\{1 - [(\phi - \phi_o)/\theta]^2\} \right]$$

$$e_{t1} = \max_{\phi \in [\theta - 2\pi, \theta]} \left[\sin\phi + \alpha(\phi - \phi_o)\{1 - [(\phi - \phi_o)/\theta]^2\} \right] . \tag{6.11}$$

As Ω_o/κ becomes comparable to 1, e_{t1} shifts to lower values and the critical polarizability decreases from $(3 + \sqrt{3})\pi$. In the limit that $\kappa \rightarrow \infty$, both e_{t1} and θ_H go to zero.

D. Inertial effects

In order to gain insight into the dynamics of the phase-slip equations, it is useful to compare the equations to a phase-only model of switching. Switching behavior has been analyzed in terms of the rigid-phase model of Grüner, Zawadowski, and Chaikin.[14-16] The rigid-phase model ignores the existence of phase domains and treats the CDW phase as uniform throughout a crystal.[6] The dimensionless equation of motion is

$$\beta \ddot{\phi} + \dot{\phi} = e - F(\phi) , \tag{6.12}$$

where the periodic function $F(\phi)$ represents a pinning force; β is a so-called inertial parameter; and time is measured in units of $(\Omega_0)^{-1}$. When β is small, the phase velocity is a deterministic function of the electric field e and the pinning force F. In this case, the dynamics of Eq. 12 are overdamped and the equation does not lead to switching. When $\beta \gtrsim 1$, however, the dynamics of 6.12 are underdamped and the equation leads to both switching and hysteresis.[16]

Except for the inertial term $\beta\ddot{\phi}$, the rigid-phase equation is very similar to Eq. 6a of the reduced phase-slip equations. In fact, the equations become

identical when $\kappa = 0$ and $\theta = 2\pi$, because then the elasticity term $\alpha\Delta(\phi-\phi_0)$ in Eq. 6a is a deterministic, periodic function of the phase ϕ. But even when $\kappa > 0$ and $\theta \neq 2\pi$, the phase-slip and rigid-phase equations are still dynamically equivalent, at least in the following sense: for small ac signals, the ac response of the phase-slip equations maps onto the response of the rigid-phase equation, as long as the inertial parameter β is assumed to be motion-dependent.

The response of either the phase-slip or rigid-phase equations is conveniently measured in terms of ac conductivity. For an electric field of the form $e = e_{dc} + e_{ac} \exp(i\Omega t)$, ac conductivity may be defined as

$$\sigma(\Omega) = \tilde{\dot{\phi}}(\Omega)/e_{ac} ,$$

where $\tilde{\dot{\phi}}(\Omega)$ is the Fourier component of phase-velocity at the applied ac frequency. When the CDW in the reduced phase-slip equations is pinned, the CDW phase has an equilibrium value ϕ_{eq} that is determined by the dc bias:

$$0 = e_{dc} - \sin \phi_{eq} - \alpha\Delta_{eq}(\phi_{eq}-\phi_0) .$$

Here the equilibrium value of the CDW amplitude is given by $\Delta_{eq} = 1 - (\phi_{eq}-\phi_0/\theta)^2$. To first order in κ, linearization of the phase-slip equations gives

$$\sigma(\Omega') = \frac{1}{[1 + 2\alpha\kappa(1-\Delta_{eq})]} \frac{i(\Omega'/\Omega_e)}{1 + i(\Omega'/\Omega_c)} \tag{6.13}$$

where $\Omega' = \Omega[1 + 2\alpha\kappa(1-\Delta_{eq})]$ and $\Omega_c = [\cos \phi_{eq} + \alpha(3\Delta_{eq}-2)]$. Except for a change in the unit of time (of order $\alpha\kappa \ll 1$), the rigid-phase model yields an identical expression for $\sigma(\Omega)$ if $\beta = 0$ and $F(\phi) = \sin \phi + \alpha(\phi-\phi_0)[1-(\phi-\phi_0/\theta)^2]$ in Eq. 12. Therefore the phase-slip equations have a

pinned response that is overdamped.

When the CDW in the phase-slip equations is sliding, the elasticity term $\alpha\Delta(\phi-\phi_0)$ is essentially periodic in phase as long as the ac field is not large. In the limit that $\theta \gg 4\pi$ and $\alpha \gg (4\pi)^{-1}$, the pinning term $\sin\phi$ may be dropped from the phase-slip equations, which then reduce to

$$\dot{\phi} \cong e_{dc} + e_{ac}e^{i\Omega t} - \alpha\Delta(\phi - \phi_0) \qquad (6.6')$$

$$\Delta = [1 - (\phi - \phi_0/\theta)^2] - \kappa\Delta \qquad (6.6b')$$

$$\phi_0 \rightarrow \begin{cases} \phi_0 & \text{if } (\phi - \phi_0) < \theta \\ \phi_0 + 2\pi & \text{otherwise .} \end{cases} \qquad (6.6c')$$

Phase polarization in 6a' is bounded by $(\theta - 2\pi) \leq \phi - \phi_0 \leq \theta$, and therefore the elasticity term may be approximated by $\alpha\theta\Delta$ if terms of order $2\pi/\theta$ are neglected. Phase acceleration is then given by $\ddot{\phi} = i\Omega e_{ac}e^{i\Omega t} - \alpha\theta\dot{\Delta}$, and substitution of this expression into Eq. 6a' yields

$$\kappa\ddot{\phi} + \dot{\phi} = e_{dc} + e_{ac}'e^{i\Omega t} - F_o(\phi) , \qquad (6.14)$$

where $F_o(\phi) = \alpha(\phi - \phi_0)[1 - (\phi - \phi_0/\theta)^2]$ and $e_{ac}' = e_{ac}(1 + i\Omega)$. Thus the sliding response of the phase-slip equations is determined by an effective inertial parameter equal to κ.

The constraints on α and θ that lead to Eq. 14 are not unreasonable, since values of $\alpha = 0.2$ and $\theta = 10\pi$ are consistent with experiments (see below). Because appropriate values of κ fall in the range 0.5 to 1.0, the phase-slip equations are dynamically overdamped when pinned, but underdamped when sliding. Therefore the equations should exhibit a strong nonlinear response above threshold. For example, if the constraint on e_{ac} is ignored, then Eq. 14 predicts that the sliding phase-slip equations should exhibit period-doubling

bifurcations, chaos, and broad inductive features in ac conductivity.[15, 16] The next section will discuss numerical calculations which show explicitly that these phenomena do indeed occur.

II. Numerical Analysis

A. Method

Analytical solutions to Eqs. 6 are difficult to obtain except in a few limiting cases. Therefore, the equations must be integrated numerically. Numerical integration of the equations is relatively easy if only dc electric fields are used to probe the CDW response, and is particularly easy if the relaxation time κ is set to zero. Figure 2 shows I-V curves that result from integration of Eqs. 8. (The curves were calculated by Hall.[17]) As expected from the discussion of the previous section, the I-V curve for $\theta = 2\pi$ displays nonswitching behavior and is equivalent to an I-V curve obtained from the overdamped limit of the Grüner-Zawadowski-Chaikin model. The I-V curve for $\theta = 5.5\pi$ displays both switching and hysteresis, because in this case the polarization parameter is larger than the critical value θ_H.

The most interesting regime of Eqs. 2.6 is for nonzero values of the relaxation time κ and the ac field e_{ac}. Numerical integration in this regime is highly nontrivial, because there are four competing time scales which determine the dynamics of the CDW response: the phase relaxation time Ω_0^{-1}, the amplitude relaxation time κ, the period of the ac signal $2\pi/\Omega$, and finally the so-called washboard period $2\pi/<\dot{\phi}>$ that is set by the time-averaged velocity of the CDW. When both ac and dc fields are present, it becomes convenient to
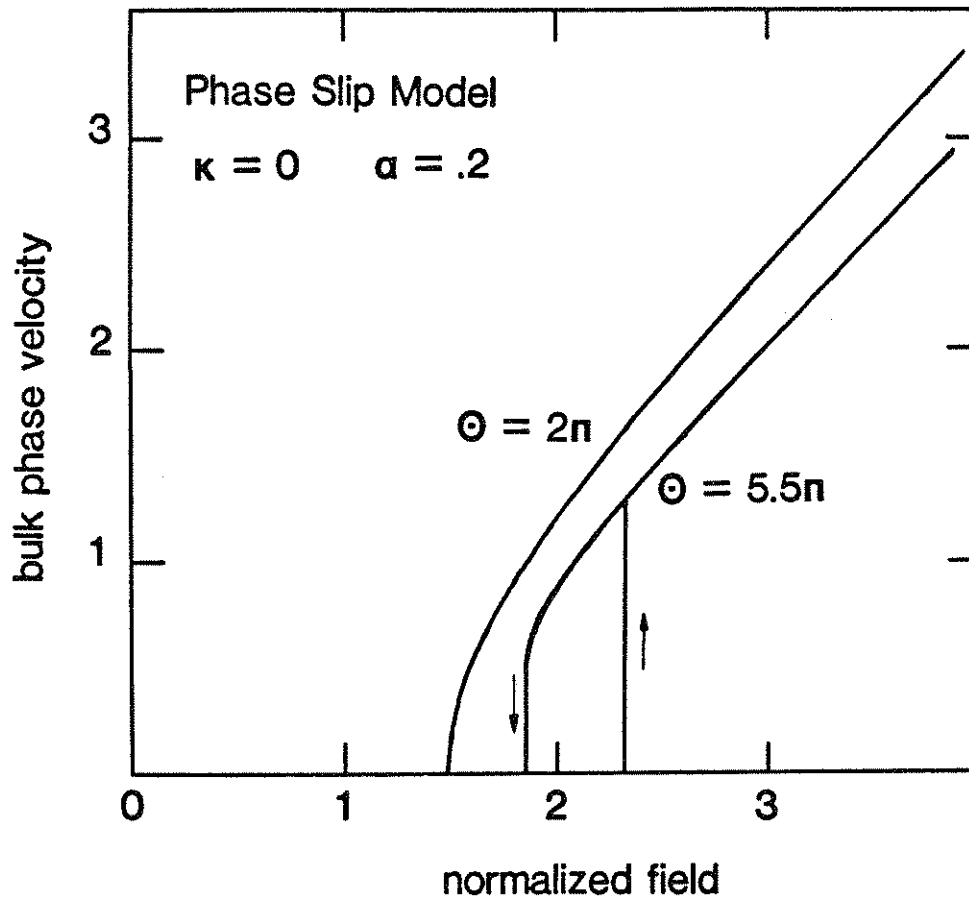
Fig. 6-2)   Nonswitching ($\theta=2\pi$) and switching ($\theta=5.5\pi$) I-V characteristics of the reduced phase-slip equations when $\kappa = \theta$.   Calculation by Hall, ref. 17.

rescale the unit of time in Eqs. 6. Writing the external field as $e = e_{dc} + e_{ac} \cos \Omega t$, a new time variable can be defined by $\tau = \Omega t$. The reduced phase-slip equations become

$$\omega_{ext} \phi' = e_{dc} + e_{ac} \cos \tau - \sin \phi - \alpha \Delta (\phi - \phi_o)$$

$$\omega_{ext} \Delta' = -\frac{1}{\kappa} \{ \Delta - [1 - (\frac{\phi - \phi_o}{\theta})^2] \} \tag{6.15}$$

$$\phi_o \longrightarrow \begin{cases} \phi_o & \text{if } \Delta > 0 \\ \\ \phi_o \pm 2\pi & \text{otherwise} \end{cases}$$

where $\omega_{ext} = \Omega / \Omega_o$. Primes indicate differentiation with respect to τ. If no ac field is present, ω_{ext} may be set to 1.

Eqs. 15 were solved by M. Inui using a very accurate integration scheme.[1] As long as a phase-slip did not occur, the equations were numerically integrated to find $\phi(\tau)$ and $\Delta(\tau)$. To account for phase-slips, Inui halted integration whenever $\dot{\Delta}$ became nonpositive. Inui then calculated the time that Δ crossed zero, allowed ϕ_o to slip by $\pm 2\pi$, and then restarted integration from the zero-crossing time. As Fourier transforms and Poincare sections of Eqs. 15 were very sensitive to systematic errors generated by the computer code, Inui was careful to eliminate this effect from his solutions. In intervals where $\Delta > 0$, Eqs. 15 were integrated using a double precision (about 14 significant digits), fifth-order Runge-Kutta method. Variable step sizes were used in the integration, but absolute local errors were kept smaller than 4×10^{-8}. The zero-crossing time of Δ was estimated by fitting a seventh-order polynomial to $\Delta(\tau)$ and using Newton's method to find the polynomial's zero. The corresponding phase ϕ was evaluated at the zero-crossing time by a similar fitting procedure. To avoid

systematic errors and singularity problems, it was necessary to use 30 significant digits in evaluating the polynomial coefficients. After the pinned phase was slipped, integration was restarted with a small initial step size of $2\pi \times 10^{-5}$ in order to minimize the effect of the code interruption.

To check the stability of his integration scheme, Inui added a small amount of Gaussian noise (standard deviation $\approx 2\pi \times 10^{-5}$) to displacements in Δ and ϕ. The only observable effect was an increase in the background noise level of the Fourier transforms; the general nature of the solutions (e.g. period 1, period 2, etc.) did not change. To check the accuracy of his solutions, Inui employed an alternate integration scheme: a variable order (one through twelve) Adams method, with absolute local errors less than 8×10^{-10}, and twelfth-degree polynomial fits. Inui found no significant difference in results between the integration methods. These checks showed that the integration method was stable and that any systematic errors were negligible.

Apart from the issue of numerical accuracy, solutions to Eqs. 15 depend on the choice of initial conditions. In his study, Inui always used "sliding" conditions: the CDW was started from the state $\Delta = 0$ and $\phi - \phi_0 = \theta$ at $\tau = 0$. He then allowed the system to relax over many periods of the CDW motion. Before computing any quantities of interest, Inui checked the stability of solutions to a further increase in the number of relaxation periods. Experimentally, the initialization procedure corresponds to biasing a CDW far above threshold, and then reducing the bias to the desired electric field.

B. *Parameter values*

The phase-slip equations of 6.15 contain seven free parameters: four CDW parameters (α, κ, θ, and ϕ_o) and three external field parameters (e_{dc}, e_{ac}, and ω_{ext}). A complete study of CDW dynamics in this seven-dimensional parameter space would be tedious and prohibitively time-consuming. In his calculations, Inui fixed α, θ, ϕ_o and ω, and varied only κ, e_{dc} and e_{ac}. As discussed previously, an appropriate choice for α is 0.2. The value of the strongly-pinned phase ϕ_o is expected to have a trivial effect on CDW dynamics, so it was set to $\phi_o = 0$ (modulo 2π). The polarizability θ was chosen so that hysteresis in the theoretical I-V curves is close to the amount of hysteresis observed experimentally. The relative magnitude of hysteresis is about equal to

$$(e_{t2} - e_{t1})/e_{t2} \cong 1 - \frac{3\sqrt{3}}{2}(1 - \frac{2\pi}{\theta})[1 - (1 - \frac{2\pi}{\theta})^2]$$

Inui used $\theta = 5 \times 2\pi$ since this value of θ gives $(e_{t2} - e_{t1})/e_{t2} \sim 0.25$, which is typical of experiment[16] (see Fig. 5-4). Finally, Inui chose $\omega_{ext} = 1$, which corresponds to an experimental frequency of about 100 MHz.

To estimate appropriate ranges for κ, e_{dc} and e_{ac}, Inui considered typical I-V curves obtained from Eqs. 15. Figure 3 shows traces of $<\phi'>$ vs e_{dc} when $e_{ac} = 0$ and κ varies from 0.5 to 1.0. As expected, the I-V curves exhibit both switching and hysteresis. Where the I-V curves are bistable, dashed and solid lines respectively indicate CDW current under monotonically increasing and decreasing bias. Lower and upper threshold fields are indicated in the top figure, as well as the magnitudes δ_1 and δ_2 of the lower and upper current switches.
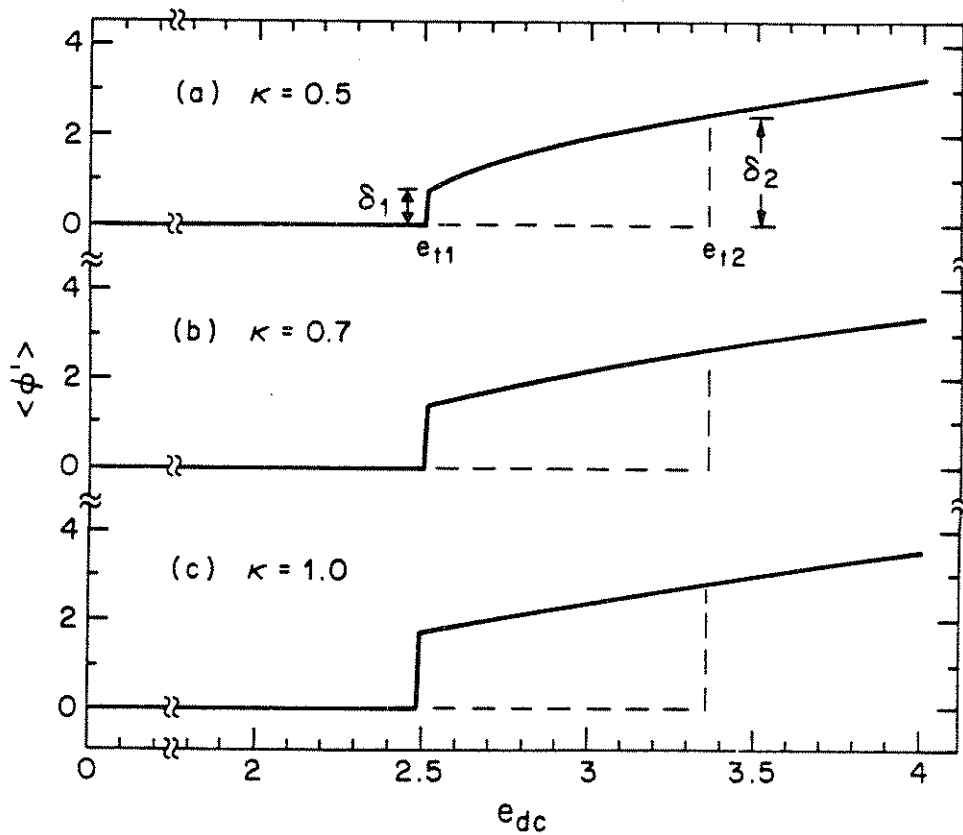
Fig. 6-3) I-V curves, $<\phi'>$ vs e_{dc}, obtained from the reduced phase-slip equations 6.15. The applied ac field is zero and the amplitude relaxation rate assumes three representative values: (a) $\kappa = 0.5$, (b) $\kappa = 0.7$, and (c) $\kappa = 1.0$. (In this figure and the figures which follow, the other phase-slip parameters are fixed at $\alpha = 0.2$, $\theta = 10\pi$, $\phi_0 = 0$, and $\omega_{ext} = 1.0$.) Calculation by Inui, ref. 1.

As mentioned above, the parameter κ represents the relaxation time of a strongly-pinned domain. Since a strongly-pinned domain should respond at least as quickly as a weakly-pinned domain, one expects $\kappa \lesssim 1$. Fig. 3 shows that switching and hysteresis do not depend strongly on κ for $\kappa \gtrsim 0.5$. The main difference between the traces in Fig. 3 is the size δ_1 of the lower current switch and the position e_{t1} of the lower current threshold. As κ decreases, δ_1 decreases and e_{t1} slightly increases. In the limit that $\kappa \rightarrow 0$, δ_1 vanishes completely and there is only an $\sqrt{e - e_{t1}}$ cusp at the lower threshold. In experimental I-V curves, there is always a finite current jump at the lower threshold, so Inui considered only nonvanishing values of κ in the range 0.2 to 1.0.

Under the application of an ac electric field, the I-V curves of Fig. 3 display a series of plateaus or "Shapiro steps".[22] On the nth Shapiro step, CDW velocity is mode-locked to the nth harmonic of the external frequency: $\langle \dot{\phi} \rangle = n\omega_{ext}$. Inui limited e_{dc} to the range that corresponds to the fourth Shapiro step. Since the width of a Shapiro step depends on the amplitude of the applied ac field, Inui chose e_{ac} to be in the range $e_{t2} \lesssim e_{ac} \lesssim 2e_{t2}$. It turns out that this is the most interesting range of ac amplitude. With this choice, e_{dc} lies in the range 4.0 to 5.5. Figure 4 summarizes the parameter ranges used by Inui.

C. Chaos and period-doubling

The response of the phase-slip equations to combined ac and dc fields is qualitatively different depending on whether the ac field is large $(e_{ac} \gtrsim 1)$ or small $(e_{ac} \ll 1)$. With small ac fields, the CDW phase-velocity is not entrained

Fig. 6-4)   Parameter planes of the phase-slip model studied by Inui, ref. 1.

by the external frequency. Two independent frequencies characterize the phase-velocity, which may be written as a double Fourier series:

$$\dot{\phi}(t) = \omega_N \sum_{\ell=0}^{\infty} A_\ell \cos(\ell \omega_N t + \chi_\ell) \tag{6.16}$$

$$+ \sum_{m=0}^{\infty} B_m \cos(m \omega_{ext} t + \chi_m) \, .$$

Here ω_N is the so-called washboard frequency and is equal to the time-averaged phase-velocity $<\dot{\phi}>$. When e_{ac} is small, ω_N is essentially determined only by the dc electric field. Except at special values of e_{dc}, the external ac frequency is incommensurable with the washboard frequency, so the CDW phase-velocity is a quasi-periodic function of time.

With large ac fields, the CDW phase-velocity mode-locks to the external frequency over wide ranges of dc bias.[23] When the CDW is mode-locked, the CDW washboard frequency is a rational fraction of the external frequency,

$$\omega_N \equiv \; <\dot{\phi}> \; = (p/q)\omega_{ext} \, ,$$

and the CDW phase-velocity may be written as

$$\dot{\phi}(t) = \omega_N \sum_{n=0}^{\infty} C_n \cos(n\omega_N t / P + \chi_n) \, .$$

Here P is an integer index characterizing the fundamental periodicity of CDW motion with respect to the external frequency. When $P = 1$, CDW motion is described as period-one; when $P = 2$, as period-two; and so on.

This section examines the effect of large ac fields on the phase-slip equations of 6.15. To begin with, the amplitude relaxation time is fixed to a moderate value: $\kappa = 0.5$. (The effect of κ is investigated later in this section.) The
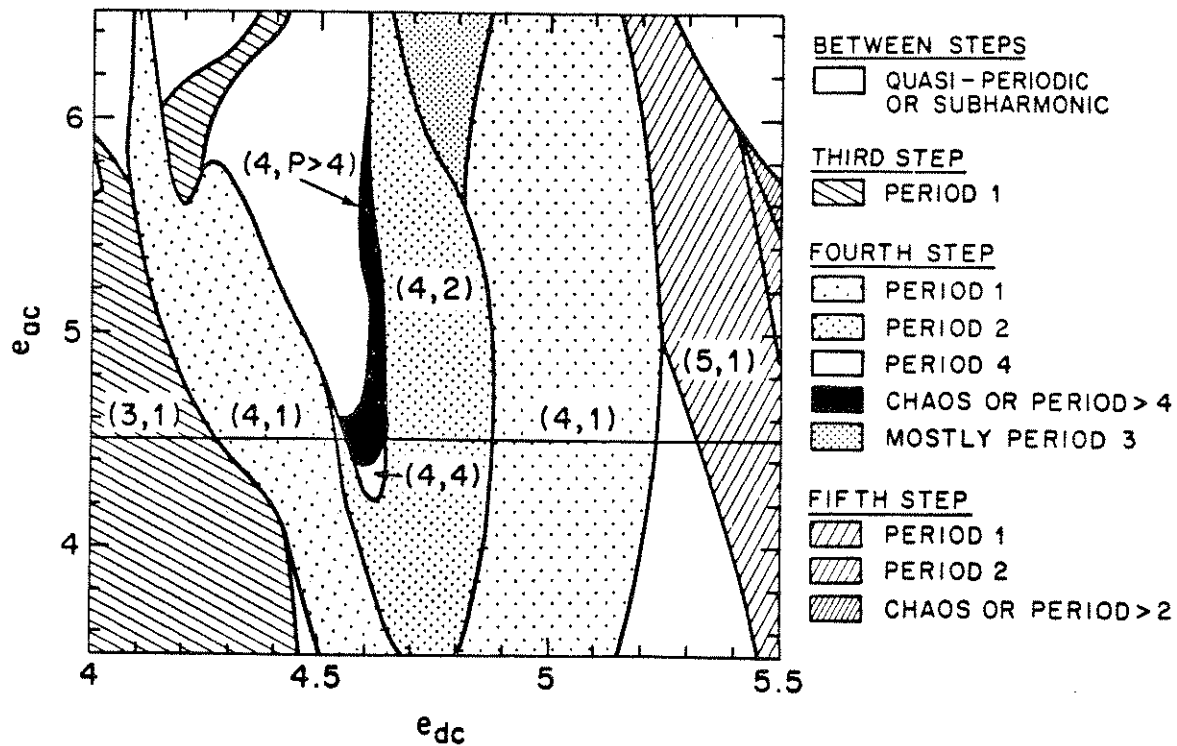
Fig. 6-5) A schematic picture of the solutions that are found in the $e_{dc} - e_{ac}$ plane of Fig. 3. Harmonically mode-locked solutions are characterized by an index pair (n, P) which represents their entrainment n and periodicity P. (Boundaries between different regions are only approximate.) The horizontal line represents the intersection of parameter planes in Fig. 6-3. Calculation by Inui, ref. 1.

applied ac and dc bias is then varied over the vertical parameter plane shown in Fig. 4. Solutions to 6.15 are characterized by their mode-locking index $(p/q) = <\phi'>/\omega_{ext}$ and their periodicity index P. Fig. 5 summarizes the type of solutions found in the $e_{dc} - e_{ac}$ plane. Typically, solutions are periodic and mode-locked to harmonic $(p/q = \text{integer})$ Shapiro steps. The symbol (n,P) is used to represent these solutions, where the integer n is $<\phi'>/\omega_{ext}$. Other solutions in the region are chaotic but still harmonically mode-locked, and these solutions are represented by (n, C). The remaining solutions in parameter plane correspond to quasi-periodic motion or subharmonic $(p/q \neq \text{integer})$ Shapiro steps. For simplicity, these solutions are denoted by (Q/S) and represented by blank areas in Fig. 4.

In a typical experiment on CDWs, the amplitude of the ac field is fixed and the dc bias is swept through a range of values. To facilitate comparison with experiment, Fig. 5 is discussed in terms of dc sweeps. For instance, the horizontal line in Fig. 5 corresponds to a dc sweep in which the ac amplitude is fixed at 4.5. (This line also corresponds to the intersection of the horizontal and vertical parameter planes in Fig. 4.) As e_{dc} increases along this line, solutions move from the third Shapiro step, through the fourth Shapiro step and an unlocked region, and finally onto the fifth Shapiro step:

$$(3, 1) \rightarrow (4, P \geq 1) \rightarrow (Q/S) \rightarrow (5, 1) .$$

Fig. 6 shows the details of this dc sweep. The dashed line in the figure represents the entrainment ratio $<\phi'>/\omega_{ext}$. Over most of the figure, solutions are mode-locked to a harmonic step. For example, the third Shapiro step
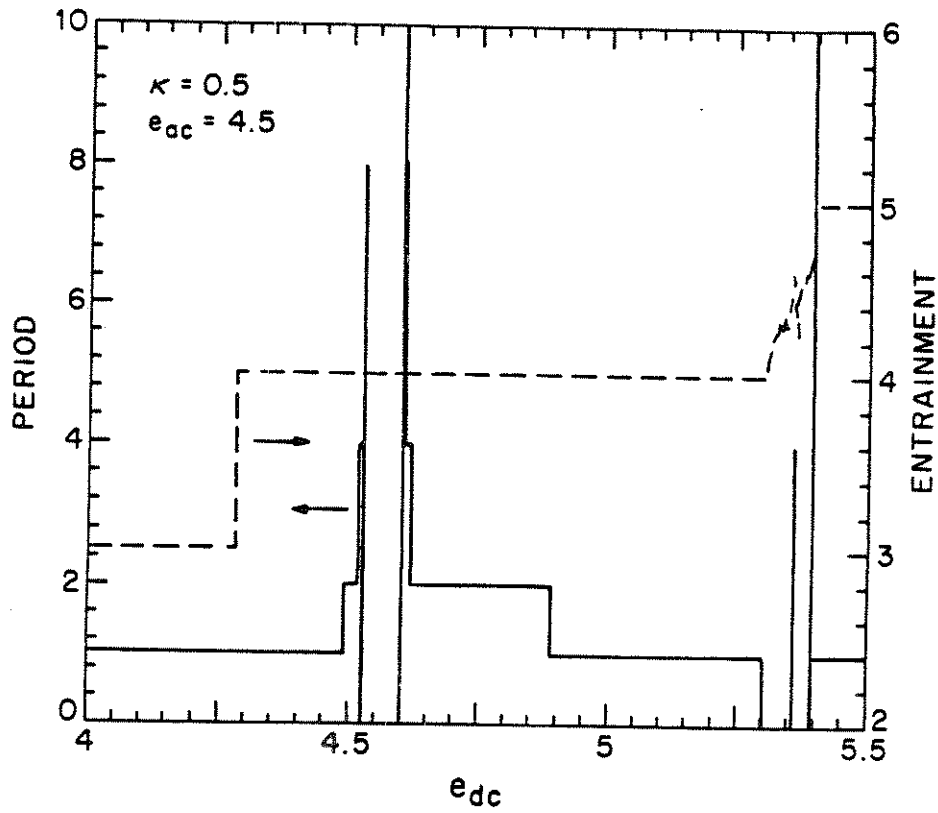
Fig. 6-6)   A dc sweep along the intersection of parameter planes in Fig. 6-4. The dashed and solid lines respectively indicate the entrainment and periodicity of solutions found in this range of dc bias. Calculation by Inui, ref. 1.

extends from $e_{dc} \cong 4.0$ to 4.3; the fourth Shapiro step from 4.3 to 5.3, and the fifth step from 5.4 to 5.5. Harmonic mode-locking breaks down only between $e_{dc} \cong 5.3$ and 5.4.

The solid line in Fig. 6 represents the periodicity index P. (Inui adopted a convention of assigning $P = 0$ to solutions where periodic behavior is not observed, including both chaotic and quasi-periodic solutions.) Even though solutions are usually mode-locked in Fig. 6, the periodicities of the solutions are often not 1. In fact, the most important feature of Fig. 6 is the region of locked but aperiodic solutions that occurs on the fourth Shapiro step. Between $e_{dc} \cong 4.3$ and 4.53, solutions follow a period-doubling cascade to chaos:

$$(4, 1) \rightarrow (4, 2) \rightarrow (4, 4) \rightarrow \cdots \rightarrow (4, C) .$$

Between $e_{dc} \cong 4.\complement$ and 5.3, solutions return to simple periodicity via a period-halving cascade:

$$(4, C) \rightarrow \cdots \rightarrow (4, 4) \rightarrow (4, 2) \rightarrow (4, 1) .$$

Although the figure only resolves periodicities of up to $P = 8$, solutions with periodicities of up to $P = 32$ were confirmed by Fourier transforms. Figs. 7a-c show a few of these transforms, for $P = 1$, 2, and 32 at $e_{dc} = 4.45$, 4.5, and 4.5258 respectively. Note that the noise level in these transforms is smaller than $\sim 10^{-8}$. In contrast, solutions are chaotic for e_{dc} between 4.53 and 4.6. Fig. 7d shows the Fourier transform of a typical chaotic solution, at $e_{dc} = 4.53$. The noise level is roughly 10^{-2}, six orders of magnitude larger than the noise level of periodic solutions. Because of this large increase in noise, chaotic solutions are clearly distinguished from periodic or quasi-periodic solutions.
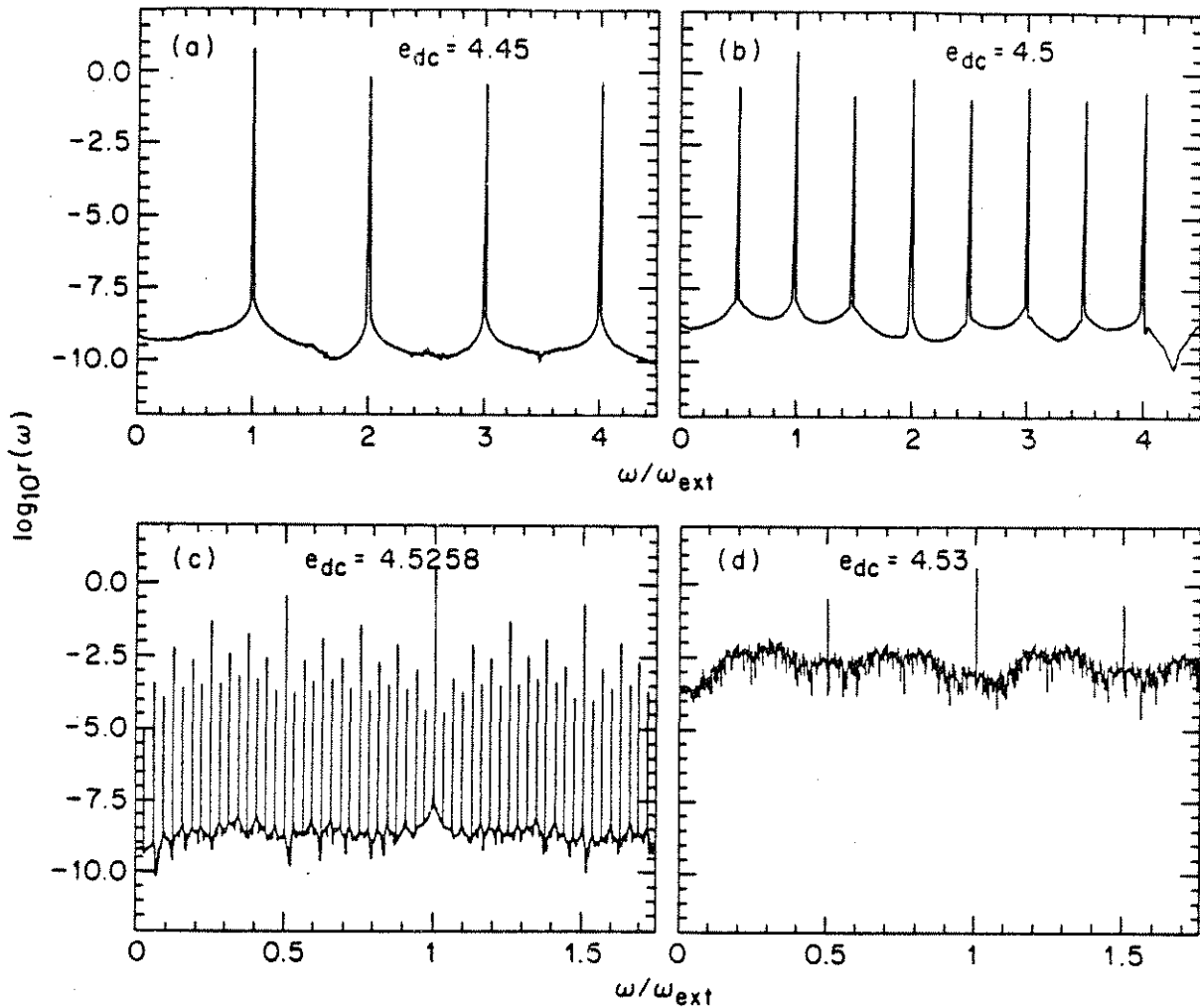
Fig. 6-7) Fourier transforms for selected solutions from Fig. 6-6. The vertical scale represents the amplitude of the transformed phase velocity, $r(\omega) = |\dot{\phi}|$. Although all of the selected solutions are mode-locked to the fourth Shapiro step, the solutions are part of a period-doubling cascade to chaos: (a) period 1 ($e_{dc} = 4.45$); (b) period 2 ($e_{dc} = 4.5$); (c) period 32 ($e_{dc} = 4.5258$); and (d) chaos ($e_{dc} = 4.53$). The horizontal scale has been expanded in the lower figures in order to show the details of these transforms. Calculation by Inui, ref. 1.

Having considered a particular dc sweep in detail, the discussion returns to Fig. 5 to discuss the general behavior of solutions at other values of e_{ac}. As the ac amplitude decreases below 4.5, Fig. 5 shows that the chaotic region shrinks on the fourth Shapiro step. Below $e_{ac} \cong 4.2$, only period-one and period-two solutions exist on the fourth step. Also as e_{ac} decreases, the unlocked regions between steps become larger. Below $e_{ac} \cong 4.0$, for example, an unlocked region develops between the third and fourth Shapiro steps. As would be expected, Fig. 5 suggests that only period-one and quasi-periodic solutions exist for small ($\lesssim 3$) values of e_{ac}.

As e_{ac} increases above 4.5, chaotic solutions remain present until e_{ac} exceeds about 6. However, period-doubling and chaotic solutions begin to be unstable against mode-dephasing above $e_{ac} \cong 4.6$. Thus in the range $4.6 \lesssim e_{ac} \lesssim 6.0$, the fourth Shapiro step is split by a region of quasi-periodic and subharmonic solutions. For instance, a typical dc sweep at $e_{ac} = 5.0$ produces a sequence like

$$(3, 1) \rightarrow (4, 1) \rightarrow (Q/S) \rightarrow (4, C) \rightarrow \cdots \rightarrow (4, 1) \rightarrow (5, 1) \, .$$

Due to the system's strong tendency to mode-lock, subharmonic Shapiro steps occupy much of the region marked (Q/S) in the sequence. In fact, for $e_{ac} \gtrsim 5.6$, the system begins to relock to the $n = 3$ Shapiro step when it isn't locked to the $n = 4$ step.

Two new types of solutions appear at large values of e_{ac}. The first type of solution corresponds to $P > 1$ solutions on the $n = 5$ Shapiro step. For example, when $e_{ac} \cong 5.6$, a sweep of dc bias encounters two regimes of chaotic solutions:

$$(3, 1) \rightarrow (4, 1) \rightarrow (Q/S) \rightarrow (4, C) \rightarrow \cdots \rightarrow (4, 1)$$
$$\rightarrow (5, 1) \rightarrow (5, 2) \rightarrow \cdots \rightarrow (5, C) \, .$$

The second type of solution corresponds to periodicities of the form $P = p \times 2^n$ where p is a prime number. Although p can be as large as 19, the dominant periodicity of this form is $P = 3$. The disappearance of chaotic solutions at $e_{ac} \cong 6$ coincides to the proliferation of $P = 3$ solutions beyond this point.

On a heuristic level, the disappearance of chaotic solutions at either large or small values of e_{ac} is reasonable. In Eqs. 15, three ingredients are apparently required for chaos. The most basic ingredient is a non-zero value of κ, as will be discussed shortly. The next ingredient is that the system is close to the center of a Shapiro step. The last ingredient is that e_{ac} and e_{dc} are of comparable magnitude. This last ingredient is required because chaotic motion in some sense represents a frustrated response of the system, when neither e_{ac} nor e_{dc} dominates the CDW equation of motion. When the system is near the center of a Shapiro step, this frustration is not easily relieved by changing the system's degree of mode-locking. Thus chaotic solutions appear in Fig. 5 when e_{ac} and e_{dc} are roughly comparable and near the center of a Shapiro step, at $e_{ac} \cong e_{dc} \cong 4.5$ and 5.5.

The sensitivity of chaotic and $P > 1$ solutions to changes in κ is discussed next. In the limit that $\kappa \rightarrow 0$ the CDW amplitude becomes a deterministic function of the CDW phase polarization:

$$\Delta \rightarrow 1 - \left(\frac{\phi - \phi_0}{\theta} \right)^2 \, .$$

In this limit, the phase space of Eqs. 15 becomes two-dimensional. Therefore, the equations are unable to support chaotic solutions. This conclusion agrees with the observed absence of chaotic solutions in the overdamped rigid-phase model.

The presence or absence of $P > 1$ solutions is not obvious when κ is small but nonzero. Inui therefore investigated the nature of solutions found in the $e_{dc} - \kappa$ plane shown in Fig. 4, where $0.2 \leq \kappa \leq 1.0$, $4.0 \leq e_{dc} \leq 5.5$, and $e_{ac} = 4.5$. Fig. 8 summarizes the solutions found in this plane.

The structure of solutions in Fig. 8 is much simpler than the structure in Fig. 5. A series of entrainment tongues is clearly evident. The $n = 3$, $n = 4$, and $n = 5$ Shapiro steps form three tapered, vertical strips. As κ decreases, these tongues become narrow and the quasi-periodic regions between them become wider. Conversely, as κ increases, the tongues become wider and sub-tongues develop within them. The first sub-tongue to form is the period-two strip within the fourth Shapiro step; the next sub-tongue is a period-four strip within the period-two tongue; and so on. When $\kappa = 0.5$, the dc sweep of Fig. 6 shows that a chaotic sub-tongue is fully developed within the fourth Shapiro step. Because the tongue structure is stable above $\kappa \cong 0.4$, Fig. 8 suggests that the phase-slip equations of 6.15 are relatively insensitive to κ for $\kappa \gtrsim 0.4$.
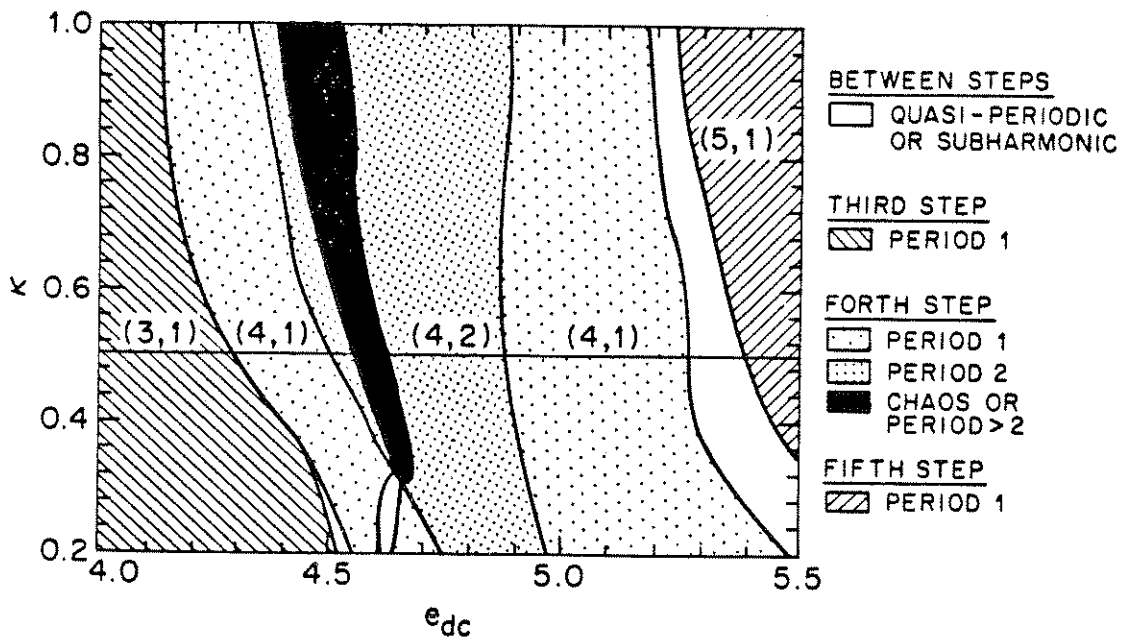
Fig. 6-8)   Solutions in the $e_{dc} - \kappa$ plane of Fig. 6-4. The horizontal line marks the intersection with the $e_{dc} - e_{ac}$ plane of Fig. 6-5. Calculation by Inui, ref. 1.

D. AC conductivity

This section examines the response of the phase-slip equations to small ac fields. The effect of small ac fields is best measured by ac conductivity, which is defined as

$$\sigma(\omega_{ext}) = \overset{\sim}{\dot{\phi}}(\omega_{ext})/e_{ac} \, . \qquad (6.17)$$

When the CDW is sliding, a complication to computing $\sigma(\omega_{ext})$ is that a dc field causes the CDW phase-velocity to oscillate at the washboard frequency, even in the absence of an ac field. This phenomenon is known as "narrow-band noise".[6,24] In Eq. 16, for example, the CDW phase-velocity has a Fourier component $\omega_N A_1$ at the washboard frequency ω_N. The amplitude of this component is about 1. Hence if a small ac field is applied with a frequency that matches the CDW washboard frequency, the definition of $\sigma(\omega_{ext})$ diverges in the limit that $e_{ac} \longrightarrow 0$:

$$|\sigma(\omega_{ext} = \omega_N)| \sim \frac{1}{e_{ac}} \, .$$

The definition of $\sigma(\omega_{ext})$ similarly diverges at the second, third, and higher harmonics of ω_N. Although $\sigma(\omega_{ext})$ could be redefined to eliminate these divergences, the definition in 6.17 corresponds to how ac conductivity is actually measured in experiment. Therefore Eq. 17 will be used to define $\sigma(\omega_{ext})$, even in the sliding regime of the phase-slip equations.

The sliding ac conductivity of the phase-slip equations is displayed in Fig. 9 for two values of the ac test signal. For the calculations in this figure, Inui fixed amplitude relaxation rate at $\kappa = 0.5$ and kept the other phase-slip parameters

at $\alpha = 0.2$ and $\theta = 10\,\pi$. The dc bias was fixed at $e_{dc} = 2.6$, about 104% of the lower threshold field e_{t1}.

Fig. 9a shows $\sigma(\omega_{ext})$ when the ac test signal is 1% of the lower threshold field. Sharp resonances are present in Re σ and Im σ at the washboard frequency and its harmonics. Near the washboard frequency, $\omega_N = 1.13$, the main effect of the test signal is to fix the phase of the narrow-band noise relative to the test-frequency. Thus the magnitude of $\sigma(\omega_{ext})$ is constant near ω_N and roughly equal to $1/e_{d}$. At frequencies below ω_N, the in-phase component of $\sigma(\omega_{ext})$ is equal to the slope $d<\dot{\phi}>/de_{dc}$ of the I-V curve, while the out-of-phase component of $\sigma(\omega_{ext})$ is zero. At high frequencies, Im σ goes to zero when ω_{ext} is not close to a harmonic of the washboard frequency. Although not apparent in Fig. (8a), Re σ goes to 1 at high frequencies.

Fig. 9b shows $\sigma(\omega_{ext})$ when the ac test signal has increased to 5% of e_{t1}. New subharmonic resonances are present at $(2/3)\,\omega_N$ and $(3/2)\,\omega_N$, and the harmonic resonances at $2\omega_N$, $3\omega_N$ and $4\omega_N$ are now much larger. More importantly, the fundamental resonance at $\omega_{ext} = \omega_N$ is no longer sharp. The real and imaginary components of $\sigma(\omega_{ext})$ display broad regions in which conductivity decreases with increasing frequency. Furthermore, Im σ is negative over a wide frequency range, from $\omega_{ext} = 0.6$ to $\omega_{ext} = 1.2$. An inductive response (i.e. Im $\sigma < 0$) over such a wide frequency range is unusual in an overdamped model of CDW dynamics. Inductive behavior is observed in overdamped classical models,[6,7] as well as the quantum tunneling model,[8] but only over narrow frequency ranges. The widths of inductive dips in these
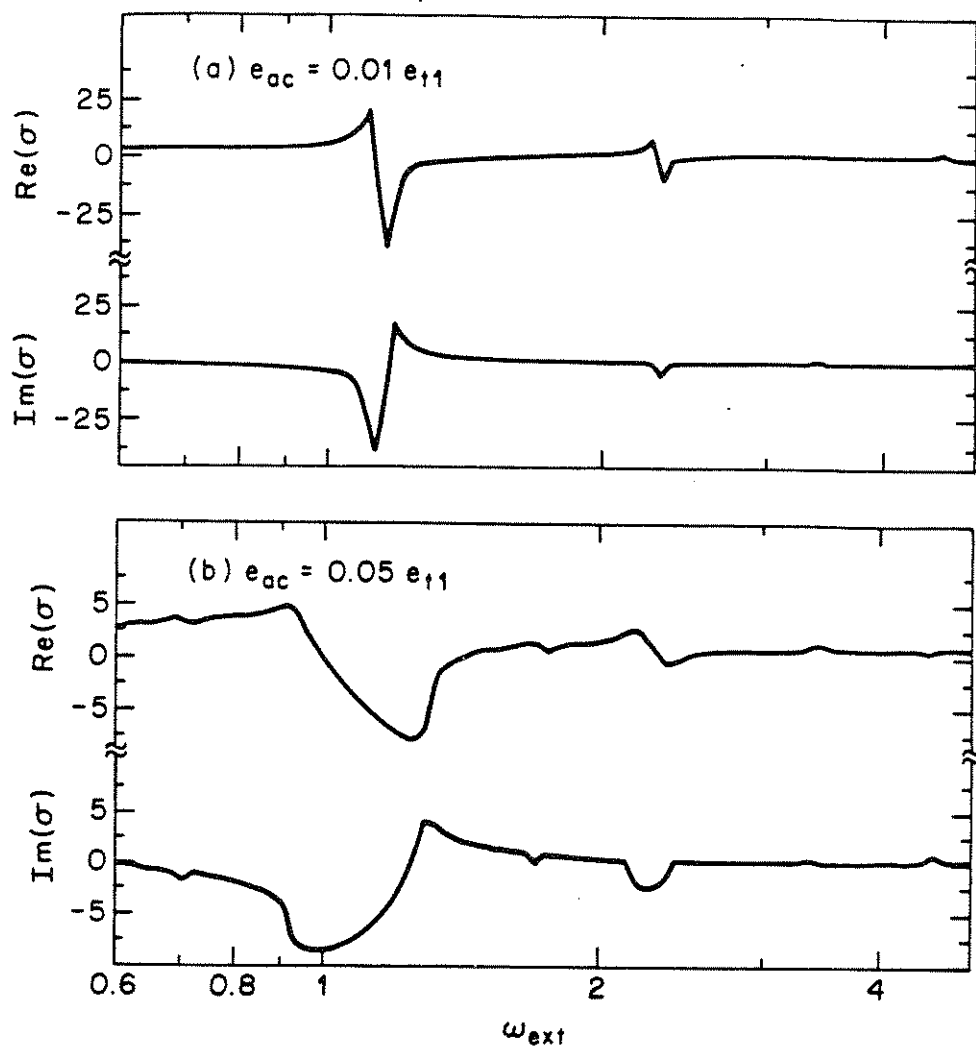
Fig. 6-9)   Sliding ac conductivity of the reduced phase-slip equations. The conductivity is sensitive to mode-locking, as shown by the effect of an increasing ac test signal: (a) $e_{dc} = 0.01\ e_{t1}$ and (b) $e_{dc} = 0.05\ e_{t1}$. Calculation by Inui, ref. 1.

models are typically 10% or less of ω_N, regardless of the test signal magnitude. In Fig. 9b, the width of the inductive region is over 50% of ω_N.

III. Comparison of Theory and Experiment

This section examines the agreement between predictions of the phase-slip equations and experimental results on switching crystals. The best quantitative agreement between theory and experiment is obtained for singly applied ac or dc fields. For example, the I-V characteristic of Fig. 3a matches the $NbSe_3$ I-V curve in Fig. 5-4 quite closely. In both I-V curves, the differential conductance dI/dV is constant past the upper threshold field; the hysteresis loop extends over a bias range which is about 25% as large as the threshold field; and the ratio of upper to lower current switches is about four to one. This agreement is trivial, of course, since it is built into the phase-slip equations. In both the phase-slip model and real crystals, switching is (arguably) caused by an effective collapse of the CDW pinning potential. This collapse produces a constant dI/dV past threshold. And the phase-slip parameters α, θ, and κ allow the I-V characteristic of the phase-slip equations to be adjusted arbitrarily. Since the phase-slip equations can therefore fit any single-switch I-V characteristic of $NbSe_3$, the shape of dc I-V curves is not a critical test of the phase-slip model. (Some I-V characteristics of $NbSe_3$ display more than one switch, a point which will be discussed shortly.)

A nontrivial point of agreement, however, is the relative size of switching versus nonswitching threshold fields. A comparison of threshold fields is difficult to make experimentally, because of large sample-to-sample variations

even among nonswitching crystals. In NbSe$_3$, comparison can be made indirectly by studying the temperature dependences of threshold fields.[14] In the lower CDW state of nominally pure crystals, switching is never observed at 48 K, but is usually observed (if it is observed at all) when the crystal temperature is lowered to 30 K. In nonswitching crystals, threshold fields typically increase by a factor of three as the temperature is lowered from 48 to 30 K. In contrast, threshold fields in switching crystals typically increase by a factor of ten over this temperature range. The onset of switching is therefore experimentally associated with an additional threefold increase in threshold field. (Some experiments on cleaved crystals also point to a ratio of 3:1 between switching and nonswitching thresholds.[14])

In the phase-slip model, switching is caused by the coupling of a weakly pinned domain to a strongly pinned domain. When this coupling is absent, the nonswitching threshold field is 1. But if this coupling is present, and if the phase-slip parameters are chosen to reproduce experimental I-V characteristics, then the switching threshold field is about 3. Thus threshold fields in the phase-slip model are three times larger for switching than for nonswitching CDWs. This agreement with experiment is significant, because other models require threshold fields that are up to a thousand times larger for switching than for nonswitching CDWs.

The pinned ac conductivity of the phase-slip model also agrees quite closely with experiment. In NbSe$_3$, the pinned ac conductivity of either switching or nonswitching crystals is described reasonably well by the frequency dependence of Eqs. 6.13. Furthermore, the crossover frequencies in switching and

nonswitching crystals are equal to within the uncertainty of sample-to-sample fluctuations. In the phase-slip model, Eqs. 6.13 apply to both switching and nonswitching CDWs, and crossover frequencies are shifted by only $\sim 20\%$ because of switching.

For jointly applied ac and dc fields, nonlinear instabilities are a distinguishing feature of switching in both theory and experiment. In $NbSe_3$ crystals, period-doubling and chaos are observed only in switching crystals.[16] In the phase-slip model, period-doubling and chaos occur only when $\theta > \theta_H$ and $\kappa > 0$; i.e. only when the phase-slip equations predict switching. Theory and experiment also agree on other qualitative aspects of chaotic dynamics. For instance, nonlinear instabilities are associated with period-doubling routes to chaos, rather than quasi-periodic routes; chaotic states remain mode-locked to Shapiro steps; and period-doubling routes to chaos occur on each Shapiro step when the dc bias is comparable to the ac field. In addition, the external field parameters required for chaotic motion are comparable in theory and experiment. In $NbSe_3$, period-doubling bifurcations or chaos have been observed at ac frequencies between 0.5 and 50 MHz, and for ac fields between 50% and 100% of the threshold field.[16] In this paper, chaos occurs at an ac frequency comparable to 100 MHz and for ac fields between 100% and 200% of the threshold field.

Both switching $NbSe_3$ crystals and the phase-slip equations exhibit a strong tendency to mode-lock to external ac signals. At temperatures where switching is prominently developed in $NbSe_3$, Shapiro steps are much broader (as a function of dc bias) than they are at higher temperatures.[16] In the switching

regime, the regions of dc bias between harmonic Shapiro steps are so narrow that quasi-periodic or subharmonically locked CDW motion can not be resolved. Furthermore, strong mode-locking in NbSe$_3$ is closely correlated with chaotic dynamics. As the temperature of an NbSe$_3$ crystal is raised above the switching regime, Shapiro steps become narrower and nonlinear instabilities gradually disappear. Similar mode-locking characteristics are displayed by the phase-slip equations. In the parameter regime where switching occurs ($\theta > \theta_H$), Shapiro steps are much broader than in the overdamped Grüner-Zawadowski-Chaikin model, which is the nonswitching limit of the phase-slip equations. In the switching regime of the phase-slip equations, no unlocked regions are observed between some Shapiro steps; for example, between the third and the fourth steps in Fig. 6. And finally, strong mode-locking appears to be a prerequisite for nonlinear instabilities in the phase-slip equations, as was discussed in Sec. II.

The last point of agreement between theory and experiment is the inductive behavior observed in sliding ac conductivity measurements. Two characteristics distinguish the sliding ac conductivity of switching crystals from that of nonswitching crystals.[15] For frequencies below the washboard frequency, Im $\sigma(\omega)$ is negative, and both Im $\sigma(\omega)$ and Re $\sigma(\omega)$ decrease with increasing frequency. The same behavior is displayed by the phase-slip equations in Fig. 9b. In addition, the qualitative difference in $\sigma(\omega)$ between Figs. 9a and 9b suggests that inductive behavior is due to a nonlinear interaction of the phase-slip equations with the applied ac test signal. Indeed, additional calculations have shown that broad inductive clips in $\sigma(\omega)$ are caused by mode-locking between the external frequency and the CDW washboard frequency.[25]

Preliminary experiments on NbSe$_3$ suggest that inductive behavior in switching crystals is also dependent on the ac test signal.[26]

In some important aspects, however, the behavior of the reduced phase-slip equations differs significantly from that of NbSe$_3$ switching crystals. There are several discrepancies in sliding ac conductivity, for example. In experiment,[15] unlike the reduced equations, the in-phase component of $\sigma(\omega)$ is never negative; the low frequency limit of Re $\sigma(\omega)$ is less than the high frequency limit; the out-of-phase component of $\sigma(\omega)$ does not go to zero at high frequencies; and the inductive dip in Im $\sigma(\omega)$ occurs over a frequency range much wider than 0.5 ω_N. There is also qualitative disagreement over the features of nonlinear instabilities. Deterministic noise in the phase-slip model is much larger than the chaos observed experimentally.[16] *Complete* period-doubling cascades have not been observed in NbSe$_3$, and period halving cascades, whether complete or incomplete, are totally absent.[16] Small regions of period-three or period-five response may be present in some crystals, but these regions occupy a much smaller amount of parameter space than shown in Fig. 5.[16] Even in dc response, the reduced phase-slip equations differ from experiment, because some NbSe$_3$ crystals display multiple, rather than just single, switches in their I-V characteristics.[14]

Many of these discrepancies, however, can be traced to the neglect of internal CDW degrees-of-freedom. The reduced phase-slip equations treat the weakly pinned regions of a CDW as rigid. Experiments on nonswitching CDWs show that this is a crude approximation. A better approximation is to treat weakly pinned regions as internally deformable. Inclusion of internal CDW

modes has several important effects on CDW dynamics.[27] First, narrow-band noise is suppressed. The relative amplitude of narrow-band noise decreases as $1/\sqrt{N}$ where N is the number of internal CDW modes. Second, the dc conductivity near threshold changes from a $(E-E_T)^{1/2}$ to a $(E-E_T)^{\nu}$ behavior, where $\nu > 1$. As a result, the differential conductivity dI/dV remains finite and less than the high-field, high-frequency limit. Third, the high-frequency ac conductivity becomes dominated by internal CDW modes. Consequently, the sliding ac conductivity approaches the pinned ac conductivity at frequencies larger than the washboard frequency.

The complete phase-slip equations, Eqs. 6.5, should give much closer agreement with experiment than the reduced equations. In the complete equations, the weakly pinned regions of a CDW are deformable. The sliding ac conductivity of the complete equations will be improved, therefore, over that of the reduced equations. The out-of-phase component of $\sigma(\omega)$ will be nonzero at high frequencies, since it will approach its pinned value. The in-phase component of $\sigma(\omega)$ will be smaller at low frequencies than high frequencies, since dI/dV is reduced by internal CDW modes. Finally, Re $\sigma(\omega)$ will remain positive at all frequencies, at least for reasonable values of the ac test signal. Negative values of Re $\sigma(\omega)$ occur because the narrow-band noise signal is larger than the in-phase CDW response. In real experiments, narrow-band noise is typically a hundred or thousand times smaller than $V_{ac}(dI/dV)$, where V_{ac} is the amplitude of the applied ac field. (The current $V_{ac}(dI/dV)$ represents a lower bound on the in-phase CDW response.) If narrow-band noise is comparably small in the complete phase-slip equations, Re $\sigma(\omega)$ will not be negative.

The complete phase-slip equations should also yield more realistic levels of deterministic noise. Bifurcations and chaos in the phase-slip model are due to the dynamical instability of phase elasticity. In the complete phase-slip equations, however, the majority of phase-phase coupling terms will not be driven into the regime of unstable elasticity. By a simple counting argument, the relative amplitude of deterministic noise should decrease as the fraction of unstable coupling terms decreases.

An interesting question is whether, in the complete phase-slip equations, period-doubling cascades will be truncated, period-halving cascades will be eliminated, and period-three responses will be suppressed. The introduction of random noise into deterministic dynamical systems is known to produce these effects. And real CDW systems are known to exhibit broad-band noise that is induced by CDW transport.[28] If the introduction of internal CDW modes were known to cause broad-band noise, then one might speculate that this broad-band noise could indeed truncate bifurcation cascades. Unfortunately, internal CDW modes alone do not lead to broad-band noise.[29] However, deformable CDW models are only marginally stable against the development of broad-band noise.[29] The presence of some highly nonlinear phase-phase coupling terms could induce broad-band noise, which would in turn truncate bifurcation cascades. If this scenario is correct, then the complete phase-slip equations would not only provide more realistic levels of chaos, but also they would provide an explanation of the origin of broad-band noise.

As a final observation, the complete phase-slip equations provide an obvious mechanism for multiple switching by a CDW.[14] Instability of the phase-mode

elasticity can occur independently at each strong pinning site within a crystal, and hence each strong pinning site can produce a switch. In real crystals, apparently single switches in an I-V characteristic are often the result of an avalanche of switches at multiple strong pinning sites. A distribution of strong pinning centers, along with an associated distribution of phase-slip parameters, could also explain the wide frequency range of the inductive dip in Im $\sigma(\omega)$.

CHAPTER 7: CONCLUSION

CHAPTER 7: CONCLUSION

The most important results of this thesis are experimental and theoretical demonstrations that switching is an intrinsic regime of CDW transport. Experimentally, narrowband noise spectra (Fig. 3.7) show that switching marks the abrupt onset of CDW conduction. Nonperturbative four-probe measurements (Fig. 3.6) prove that switching occurs in the bulk of a crystal and that switching is independent of the measurements used to observe CDW conduction. Scanning electron microscopy (Figs. 3.4 and 3.10) shows that switching is not associated with external crystal defects. On the contrary, cutting and cleaving experiments (Figs. 3.3 and 3.5), as well as threshold field studies (Figs. 3.2 and 3.17), indicate that switching arises from strong pinning at localized internal defects. Theoretically, general arguments show that switching should arise whenever weak pinning effects are negligible and strong pinning centers are sparsely distributed within a crystal. Thus, both theory and experiment point to strong pinning as the origin of switching. In this sense, switching is as fundamental as nonswitching transport to CDW dynamics. Switching transport occurs in the presence of strong, nonuniform pinning, whereas nonswitching transport occurs for uniform pinning, whether strong or weak.

Switching transport is characterized by four types of phenomena:

1. *CDW current discontinuities*; e.g. multiple switches within an I-V characteristic (Fig. 3.6); formation of current domains within a crystal (Fig. 3.8); and several fundamental frequencies within a narrowband noise spectrum (Fig. 3.7). Current discontinuities imply the existence of phase-slip centers

(Fig. 3.9), at which the CDW amplitude periodically collapses and reforms.

2. *CDW polarization*; e.g. low-field resistance states (Fig. 3.15); convex or step-like dV/dI curves (Figs. 3.13 and 3.14); and abrupt depinning and hysteresis. Polarization effects result from the application of large electric fields to strongly pinned CDWs.

3. *Avalanche depinning*; e.g. sublevels within hysteresis loops (Fig. 3.12) and negative differential resistance instabilities (Figs. 5.2 and 5.3). Avalanche depinning is caused by the interaction of strong pinning centers within a crystal, in which phase slippage at one center triggers phase slippage at neighboring centers.

4. *Pseudo-inertia*; e.g. the small- and large-signal response of switching CDWs to ac electric fields. In response to small ac electric fields, switching CDWs appear to be overdamped when pinned (Figs. 4.2 and 4.7), but underdamped when sliding (Figs. 4.3 - 4.5). In response to large ac signals, switching CDWs display unusually stable mode-locking (Fig. 5.4), which leads to period-doubling instabilities (Figs. 5.5 and 5.6), noisy precursor phenomena (Figs. 5.12 - 5.14), and the collapse of CDW dynamics onto a single effective degree of freedom.

Nonswitching transport is characterized by none of these phenomena, and therefore switching represents a qualitatively different regime of CDW dynamics. The differences between switching and nonswitching transport have been addressed on an *ad hoc* basis by various phase-only models: the polarization model of Janossy and Kriza,[1] the avalanche model of Joos and Murray,[2] the inertial model of Hall *et al*,[3] and the current noise model of

Wonneberger.[4] The current noise model is fundamentally inconsistent with the experimental results, and none of the other models provide a general framework that describes all aspects of switching. The most serious shortcoming of the models is their neglect of current discontinuities.

The thesis has proposed a new model of switching which is based on phase slippage. The model starts with the observation that CDW pinning depends on the elasticity of the CDW phase. During phase slippage, the elasticity of the phase can become unstable in the presence of strong, nonuniform pinning. If the elasticity becomes unstable, then abrupt depinning occurs because the pinning forces which impede CDW motion effectively collapse. The thesis has argued in general terms why phase slippage is consistent with the experimental results. Table 1 summarizes the arguments very briefly. Current discontinuities arise naturally in the model from phase slippage at strong and ultrastrong pinning centers. Polarization effects are produced by the amplitude dependence of the phase elasticity. Avalanche effects result from size and spatial distributions of strong pinning centers within a crystal. And pseudo-inertial effects occur because of the finite response times of strongly pinned domains. Thus, phase slippage provides a framework that describes the four general types of switching phenomena.

The thesis has also proposed a set of partial differential equations to describe the dynamics of switching CDWs. The equations are derived from a Hamiltonian which is based on the dispersion relations of Lee, Rice, and Anderson.[5] Under certain conditions, the equations reduce to a simpler set of coupled first-order differential equations. The first-order equations were

EXPERIMENT	THEORY
Current discontinuities	Phase-slippage
Polarization effects	Amplitude-dependent phase elasticity
Avalanche effects	Multiple phase-slip centers
Pseudo-inertial effects	Response time of a strongly pinned domain

Table 7-1)   Origin of switching phenomena within the phase-slip model.

analyzed in collaboration with Masahiko Inui, and were shown to display dynamics that is qualitatively, and sometime quantitatively, similar to real CDWs. Chapter 6 contains a detailed analysis of the generally satisfactory agreement between theory and experiment.

In conclusion, switching is a fascinating and apparently rather general feature of CDW dynamics. It is the first transport phenomenon in which amplitude dynamics is as important as phase dynamics to a description of CDW motion. The thesis has demonstrated the important relationship between phase polarization, strong pinning, and phase slippage in the switching process. Many of the ideas expressed here for $NbSe_3$ and Fe_xNbSe_3 should be applicable to other sliding CDW systems, for example $K_{0.30}MoO_3$, TaS_3, and $(NbSe_4)_{3.33}I$. Experiments on these compounds, analogous to the experiments reported here, will be important for a complete understanding of CDW switching.

APPENDICES

APPENDIX A1: PERTURBATION CALCULATION OF CDW FORMATION

This appendix provides the details of a perturbation calculation of CDW formation using single-electron wavefunctions and classical lattice dynamics.

I. General Distortions of a Lattice

Consider an undistorted, one-dimensional crystal in which single-electron energies $E_o(k)$ are determined by Bloch function solutions $\chi_k^{(o)}(x)$ of the Hamiltonian $H_o = p^2/2m + V_o(x)$. The crystal potential $V_o(x)$ may be written as a sum of individual lattice site potentials:

$$V_o(x) = \sum_j v(x - x_j), \qquad (A1.1)$$

where $x_j = ja$, with a the crystal lattice constant. The summation is over lattice sites of the crystal.

A distortion of the crystal lattice perturbs the crystal potential experienced by the Bloch electrons. A general (aperiodic) distortion may be specified by enumerating the set $\{u_j\}$ of displacements at each of the N lattice sites within the crystal. The new potential due to the displacements is $V_o(x) + V_1(x)$, where to first-order in the u_j,

$$V_1(x) = -\sum_j u_j \frac{d}{dx} v(x - x_j). \qquad (A1.2)$$

A general set $\{u_j\}$ of displacements may be decomposed into Fourier components (normal modes):

$$u_j = \sum_q u_q e^{iqz} , \tag{A1.3}$$

so that the perturbation may be written as

$$V_1(x) = - \sum_q \sum_j u_q e^{iqz_j} \frac{d}{dx} v(x - x_j) . \tag{A1.4}$$

For a general wavevector k, the lowest order change in energy is

$$E_1(k) - E_o(k) = \sum_{k'} \frac{|V_1(k, k'; \{u_j\})|^2}{E_o(k) - E_o(k')} , \tag{A1.5}$$

provided that $E_o(k') = E_o(k)$ for any nonvanishing value of the matrix element $V_1(k, k'; \{u_j\})$. The matrix element is given by

$$V_1(k, k'; \{u_j\}) = \int dx \chi_{k'}^*(x) \chi_k(x) V_1(x) . \tag{A1.6}$$

The Bloch functions are assumed to be normalized over the entire crystal. By decomposing $V_1(x)$ according to Eq. 4, the matrix element may be written as a sum of integrals over the individual lattice potentials dv/dx. Using the Bloch condition and the periodicity of dv/dx, each integral may be translated back to the origin. The translated integrals are independent of the index j, but multiplied by factors of $e^{i(k-k'+q)ja}$, so that summation over j gives zero unless the wavevector k' is equal to $k + q$ modulo a reciprocal lattice vector g. The matrix element reduces to

$$V_1(k, k'; \{u_j\}) = \sum_q \delta_{g, k-k'+q} G_1(k, q) u_q \tag{A1.7}$$

where $\delta_{g,k-k'+q}$ is a Kronecker delta and

$$G_1(k,q) = - \int dx \tilde{X}^*_{k+q}(x) \tilde{X}_k(x) \frac{d}{dx} v(x) . \tag{A1.8}$$

In Eq. 8, the tildes over the Bloch functions indicate that the functions are normalized to unity over one unit cell; the integrand in Eq. 8 is nonnegligible only over a unit cell or so.

Using Eqs. 4 - 8, the perturbation potential may be converted to an operator in k-space:

$$V_1(x) \longleftrightarrow \sum_{k,k',q} \delta_{g,k-k'+q} u_q G_1(k,q) | k' > < k | . \tag{A1.9}$$

the normal-mode amplitudes u_q may be expressed in terms of phonon creation and annihilation operators, and the matrix element $| k' > < k |$ may be written as the many-body operator $a^+_{k'}, a_k$. The perturbation $V_1(x)$ reduces to the electron-phonon interaction term of the Frohlich Hamiltonian, Eq. 2.2, where the coefficients $g(k,q)$ and $G_1(k,q)$ are related by:

$$g(k,q) = G_1(k,q)(\hbar/2M\omega_q)^{\frac{1}{2}} . \tag{A1.10}$$

II. Mean-Field Approximation

Eqs. 5, 7 and 8 are as far as one can go for a general set $\{u_j\}$ of distortions. A mean-field calculation of the Peierls distortion specifies a special set of $\{u_j\}$ that correspond to a sinusoidal modulation of the lattice:

$$u_j = u_Q e^{iQz_j} + u_{-Q} e^{-iQz_j} . \tag{A1.11}$$

Because the displacement u_j must be real, u_{+Q} and u_{-Q} are complex conjugates and may be written as $u_Q = u\exp(+i\phi)$. The choice of the phase ϕ is generally arbitrary, although not if the distortion is commensurate with the lattice. In considering static distortions, ϕ may be set to zero. The mean-field matrix elements (A1.7) become

$$V_1(k,k';Q) = u \sum_{q=\pm Q} \delta_{g,k-k'+q} G_1(k,q) . \tag{A1.12}$$

For bands less than half-filled, umklapp processes do not occur in one-dimension, so the lattice vector g may be set to zero. Henceforth, the discussion shall consider only bands that are less than half-filled.

The matrix element $V_1(k,k';Q)$ is generally nonzero when $k' = k + Q$. The second-order response in Eq. 5 becomes first-order whenever $E_o(k\pm Q)$ is about equal to $E_o(k)$; in this case, the energy shifts $E_1(k) - E_o(k)$ must be calculated using degenerate perturbation theory. The simplest degenerate calculations correspond to incommensurate distortions, in which either $E_o(k+Q)$ or $E_o(k-Q)$ is close to $E_o(k)$. For definiteness, the case $E_o(k+Q) = E_o(k)$ shall be considered; results for the case $E_o(k-Q) = E_o(k)$ are obtained by substituting $-Q$ for $+Q$. A linear combination,

$$\chi_k^{(1)} = A_1 \chi_k^{(o)} + A_2 \chi_{k+Q}^{(o)} , \tag{A1.13}$$

must be found such that $(H_o + V_1)\chi_k^{(1)} = E_1(k)\chi_k^{(1)}$. This differential equation leads to two coupled equations for the mixing coefficients A_1 and A_2:

$$[E_o(k) - E_1(k)]A_1 + \Delta^*(k, +Q)A_2 = 0 \qquad (A1.14a)$$

$$\Delta(k + Q)A_1 + [E_o(k + Q) - E_1(k)]A_2 = 0 , \qquad (A1.14b)$$

where $\Delta(k, +Q) = V_1(k, k+Q; Q)$. The new energies $E_1(k)$ are given by

$$E_1(k) = \frac{1}{2}[E_o(k+Q) + E_o(k)] \pm$$

$$\frac{1}{2}\{[E_o(k+Q) - E_o(k)]^2 + 4|\Delta(k, +Q)|^2\}^{1/2} . \qquad (A1.15)$$

The plus sign applies for $|k| > Q/2$; the minus sign for $|k| < Q/2$. When the energy splitting between $E_o(k)$ and $E_o(k+Q)$ is large, Eq. 15 reduces to Eq. 5 if the large denominator terms in that equation are neglected.

Commensurate distortions are handled in a similar fashion to incommensurate distortions, except that a larger linear combination of Bloch functions must be used to determine the perturbed wavefunction $\chi_k^{(1)}(x)$. For a commensurate distortion of order M', the energy $E_o(k+M'Q)$ is equal to $E_o(k)$, so

$$\chi_k^{(1)} = \sum_{m=0}^{M'} A_m \chi_{k+mQ}^{(o)}(x) . \qquad (A1.16)$$

This leads to a matrix equation which may be approximated by Eq. 15, provided that $\phi = 0$. For nonzero values of ϕ, the energy per state is increased by $[|\Delta|^2/E_o(k_F)] [|\Delta|/W]^{M'-2} [\cos(M'\phi) - 1]$ where W is the bandwidth.

For both commensurate and incommensurate distortions, Eq. 15 shows that the unperturbed band $E_o(k)$ splits into two bands, $E_1^-(k)$ and $E_1^+(k)$. States in the lower band, $E_1^-(k)$, have lower energies after the distortion than before.

States with wavevectors close to $k = -Q/2$ undergo the largest energy shifts:

$$E_1^\pm(-Q/2) = E_o(-Q/2) \pm |\Delta(-Q/2, +Q)| . \qquad (A1.17)$$

The gap parameter is $\Delta_{+Q} = \Delta(-Q/2, +Q)$ and its modulus is denoted $\Delta = |\Delta_{+Q}|$. In a nearly free electron approximation, $\Delta(k, +Q)$ is the Fourier component of $V_1(x)$ and is equal to Δ_{+Q}. Outside of the nearly free electron approximation, $\Delta(k, +Q)$ is assumed to be largely independent of k and well approximated by Δ_{+Q}. (For the case $E_o(k-Q) = E_o(k)$, note that $\Delta(+Q/2, -Q) = \Delta^*(-Q/2, +Q)$ so that $\Delta(k, -Q)$ is approximated by $\Delta_{-Q} = \Delta_{+Q}^*$.)

For $Q = 2k_F$, the electronic gap opens at the Fermi surface and at zero temperature the total energy of the occupied states is lowered. The energy of the occupied states may be calculated by integrating $E_1^-(k)$ from $-k_F$ to $+k_F$. The electronic energy actually consists of two components: $E_{el}^{(o)}$, the unperturbed electronic energy; and $E_{el-lattice}$, the perturbation due to the lattice distortion:

$$E_{el}^{(o)} = \int_{-k_F}^{+k_F} dk\, D(k)\, E_o(k) \qquad (A1.18)$$

$$E_{el-lattice} = \int_{-k_F}^{+k_F} dk\, D(k)\{E_1^-(k) - E_o(k)\} . \qquad (A1.19)$$

Here $D(k)$ is the density of states in phase space; in one dimension $D(k)$ is a constant, Na/π, and may be taken outside the integrals. Since the electronic energies are changed appreciably only near the Fermi surface, unperturbed

energies in the integrand of Eq. 19 may be linearized about the Fermi energy:

$$E_o(k) = E_F + \hbar v_F(|k| - k_F), \tag{A1.20}$$

where $\hbar v_F = dE_F/dk$. With this linearization, the integrand of Eq. 17 reduces to

$$E_1 - E_0(k) = - \left\{ [\hbar^2 v_F^2(|k| - k_F)^2 + \Delta_o^2]^{\frac{1}{2}} - \hbar v_F(k_F - |k|) \right\}. \tag{A1.21}$$

The electron-lattice interaction term becomes

$$E_{el-lattice} = - n(0) \int_o^{E_B} d\epsilon \left\{ (\epsilon^2 + \Delta^2)^{\frac{1}{2}} - \epsilon \right\}, \tag{A1.22}$$

where $n(0)$ is the Fermi level density of states. The upper bound E_B of the integral is the energy range over which the linearization (A1.20) is valid. The electron-lattice interaction energy may be integrated to give

$$\underset{\sim}{E}_{el-lattice} \cong \underset{\sim}{\Delta}^2 \ln \underset{\sim}{\Delta}, \tag{A1.23}$$

where single subscript tildes indicate normalized variables: $\underset{\sim}{E}_{el-lattice} = E_{el-lattice}/[2n(0)E_B]$, and $\underset{\sim}{\Delta} = \Delta/[2E_B]$. Figure 2.2 shows a graph of $E_{el-lattice}$.

The lattice may be treated as a classical, linear array of ionic masses M that are tied together by springs of spring constant C. The classical, unperturbed energy of the lattice is

$$E_{lattice}^{(o)} = \sum_j p_j^2 / 2m + \frac{1}{2} C \sum_j (u_j - u_{j-1})^2 . \tag{A1.24}$$

For a static distortion, the momenta $p_j = 0$. Because of the mean-field approximation, the elastic energy of the lattice may be summed directly:

$$E_{lattice} = N M \omega_{2k_F}^2 u_Q u_{-Q} = N M \omega_{2k_F}^2 u^2 , \tag{A1.25}$$

where ω_{2k_F} is the unperturbed frequency of the $2k_F$ normal mode:

$$M \omega_{2k_F}^2 = 4 C \sin^2 k_F \tag{A1.26}$$

The total crystal energy is given by crystal energy is given by Eq. 2.14 and the equilibrium value of Δ_o by 2.18.

III. Charge-Density Wave Induced By A Peierls Distortion

The electronic charge density in the distorted state is

$$\rho^{(1)}(x) = \sum_k |\chi_k^{(1)}(x)|^2 . \tag{A1.27}$$

Neglecting niceties of normalization, the distorted wavefunctions are given by Eqs. 13 and 14:

$$k < 0: \quad \chi_k^{(1)}(x) = \chi_k^{(o)}(x) + \frac{E_1(k) - E_o(k)}{\Delta_{-Q}} \chi_{k+Q}^{(o)}(x) \tag{A1.28a}$$

$$k > 0: \quad \chi_k^{(1)}(x) = \chi_k^{(o)}(x) + \frac{E_1(k) - E_o(k)}{\Delta_{+Q}} \chi_{k-Q}^{(o)}(x) \tag{A1.28b}$$

The $+Q$ Fourier component of $\rho^{(1)}(x)$ is found in the usual way:

$$\rho_{+Q} = \frac{1}{Na} \int_{xtal} dx \, \rho^{(1)} e^{-iQx} \tag{A1.29}$$

The integral over the entire crystal may be written as the sum of N unit-cell integrals. Exploiting the Bloch condition, only cross-terms in $\rho^{(1)}(x)$ survive summation. These remaining terms are multiplied by factors of the form

$$\int_{\substack{unit \\ cell}} dx \, \tilde{X}_{k+Q}^{*}(x) \tilde{X}_{k}(x) e^{+iQx} \,, \tag{A1.30}$$

which may be set to 1. (In the nearly free electron approximation, these factors are exactly 1.) The $+Q$ Fourier component reduces to

$$\rho_{+Q} \cong \frac{1}{Na\Delta_{-Q}} E_{el-lattice} \tag{A1.31}$$

$$\cong - \frac{M\omega_{2k_F}^2}{a\,G^2} \Delta_{+Q}$$

The $-Q$ Fourier component is similar except that $-Q$ replaces $+Q$, and vice versa.

The distorted electronic charge density is a superposition of a background density $\bar{\rho}(x)$ and a density wave $\rho_{CDW}(x)$:

$$\rho_{CDW}(x) = \rho_{+Q} e^{iQx} + \rho_{-Q} e^{-iQx} \tag{A1.32}$$

$$= - \rho\cos(Qx + \xi_o)$$

The CDW amplitude may be rewritten in a form that clarifies the significance of the electron-phonon coupling constant, Eq. 2.20. Since the density of states at the Fermi level is about $n(0) \cong nNa/E_F$, the ratio of the normalized CDW gap

to the normalized amplitude is about equal to the electron-phonon coupling constant: $(\Delta_o/E_F) = \lambda(\rho_o/n)$.

The orientation ξ_o of the density wave is determined by $G_{+Q} = G_1(-Q/2, Q)$; see Eq. 2.23. In the nearly free electron approximation,

$$G_{+Q} = -\frac{1}{a} \int_{xtal} dx \; e^{-iQx} \frac{dv}{dx} . \qquad (A1.33)$$

Integrating by parts and assuming that $v(x)$ is symmetric about $x = 0$ gives

$$G_{+Q} = -i(Q/a) \int dx \; v(x)\cos(Qx) . \qquad (A1.34)$$

As long as $v(x)$ falls off monotonically as $|x|$ increases, the integral in Eq. 34 has the opposite sign as $v(x)$. Thus the phase ξ_o is $-\pi/2$ for $v > 0$ and $+\pi/2$ for $v < 0$. (This statement about ξ_o is actually more general than the nearly free electron approximation, but a less restrictive proof is too far afield from the purposes of this paper.)

IV. Lindhard Response Function

Derivation of the Lindhard function is closely related to the derivation of the induced charge-density wave. Consider the electronic response of a crystal acted upon by a static, external perturbation V_{ext}:

$$V_{ext}(x) = V_{ext}(e^{iqx} + e^{-iqx}) . \qquad (A1.35)$$

An electronic state of wavevector k is mixed by V_{ext} with states of wavevectors $k \pm q$. A state's *response* to V_{ext} is the difference between its probability density in the presence and absence of V_{ext}. Summing the response of all occupied

electronic states and thermally averaging the result gives the total electronic response $\delta\rho$. The response $\delta\rho$ may be calculated by nondegenerate perturbation theory:

$$\delta\rho = - \; X(q,T;u_o)V_{ext} \; , \tag{A1.36}$$

where X is given by Eq. 2.25.

The response function X is related to the electron-lattice interaction energy. From Eq. 19, the electron-lattice interaction energy may be generalized to nonzero temperatures:

$$E_{el-lattice} = \int dk \; D(k) \; f^o(k)\{E_1(k) - E_o(k)\} \; . \tag{A1.37}$$

The integration in equation extends over all of k-space, but is effectively cut off by f^o for states far beyond the Fermi surface. At temperatures above the Peierls temperature, f^o smears the Fermi surface sufficiently that the first-order effect of a Peierls distortion on electronic energies may be neglected and the energy difference $[E_1(k) - E_o(k)]$ may be approximated by second-order perturbation theory:

$$E_{el-lattice} = \int dk \; D(k) \; f^o(k) \sum_{k'} \frac{|\; V_1(k,k';q_o)|^2}{E_o(k) - E_o(k')} \; . \tag{A1.38}$$

The matrix element $V_1(k,k';q)$ is nonzero only for $k' = k \pm q$. The coupling constant $G_1(k,q)$ may be approximated by $G = |\; G_1(-k_F,2k_F)|$. The electron-lattice energy reduces to

$$E_{el-lattice} = \int dk \, D(k) \left\{ \frac{f^o(k)G^2 u^2}{E_o(k) - E_o(r-q)} + \frac{f^o(k)G^2 u^2}{E_o(k) - E_o(k+q)} \right\} \quad (A1.39)$$

$$= - G^2 u^2 \chi(q, T; u_o = 0) .$$

Eq. 39 is also valid for $Q = 2k_F$ at temperatures below the Peierls temperature if u is allowed to assume nonzero values. This has already been implicitly demonstrated for the case of $T = 0$. Rewriting Eq. 31 gives

$$E_{el-lattice} = Na\Delta_{-Q}\rho_{+Q} . \quad (A1.40)$$

The response $\delta\rho$ is equal to $Na\rho_{+Q}$ and the perturbation energy Δ_{+Q} may be identified with V_{ext}, so that

$$E_{el-lattice} = (G_{+Q}u_{-Q})(-x_Q G_{-Q} u_{+Q}) \quad (A1.41)$$

$$= - G^2 u^2 x(Q, T = 0; u_o) .$$

The response function χ is also closely related to the normal mode vibrational frequencies of a crystal. Given a $2k_F$ normal mode excitation, the total crystal energy may be written as

$$E_{Xtal} = E_{el}^{(\rho)} - xG^2 u_{-Q} u_{+Q} + N\frac{p_{+Q}p_{-Q}}{M} + NM\omega_Q^2 u_{+Q} u_{-Q} , \quad (A1.42)$$

where p_Q is the momentum associated with the $+2k_F$ normal mode. Hamilton's equations of motion give

$$NM\ddot{u}_Q = \{NM\omega_Q^2 - G^2\chi\}u_Q . \quad (A1.43)$$

Above the Peierls temperature, the frequency of the $2k_F$ normal mode is

reduced by the electron-lattice interaction:

$$\Omega_Q^2 = \omega_Q^2 - \frac{G^2 \chi}{NM} .$$ (A1.44)

In fact, above the Peierls temperature, the frequency of any normal mode q is given by $\Omega_q^2 = \omega_q^2 - [G^2 \chi(q, T;0)/NM]$, where ω_q is the frequency of the mode in the absence of electrons. Below the Peierls transition, the qth normal mode frequency must be zero as q approaches $2k_F$ from below. Eq. 4 gives a condition on $\chi(q = 2k_F, T < T_p; u = 0)$:

$$\chi = \frac{NM\omega_Q^2}{G^2} .$$ (A1.45)

The linearization of Eq. A1.17, applied to the definition of χ, leads to the self-consistency condition on Δ_o, Eq. 2.30.

APPENDIX A2: PEIERLS DISTORTIONS
IN A KRONIG-PENNEY CRYSTAL

This appendix calculates the magnitude of a Peierls distortion for a simple example, the Kronig-Penney model. The calculation demonstrates how a reduction in symmetry reduces the groundstate energy of a metal. For a Kronig-Penney crystal, the reduction in groundstate energy may be calculated without resort to perturbation theory. This "exact" calculation is presented first in Sec. I. The calculation is repeated in Sec. II, this time using the perturbation results from App. A1. In Sec. III, the Kronig-Penney model is reviewed briefly for reference. In the last section, Sec. IV, the Kronig-Penney equation is derived for a dimerized lattice.

I. "Exact" Calculation

The Kronig-Penney model is a standard model of how electrons interact with the ions of a crystal, and is discussed in most textbooks. Basically, the model consists of a linear chain of ions, rigidly spaced with lattice constant a, interacting with some electrons confined to the lattice. The interaction of an electron with an ion is highly idealized: the electron-ion potential is simplified to a Dirac delta function. The total potential $V_0(x)$ experienced by an electron is the sum of the ionic delta functions at all the lattice sites in the crystal, Eq. A2.21. In the limiting case of a strong electron-ion interaction, solutions may be obtained for electronic Bloch functions $\chi_k^{(0)}(x)$ and energies $E_0(k)$ which are parameterized by the wavevector k of an electron, Eqs. A2.28 - 31. The strength of the electron-ion interaction is parameterized by an energy V, so the

strength of a single ionic delta function is equal to aV. In the following calculation, only the repulsive case $V > 0$ will be considered, but the attractive case $V < 0$ is handled in a similar manner, mainly by substituting hyperbolic for trigonometric functions.

Left undiscussed by textbooks is the instability of a Kronig-Penney crystal whose lattice is not absolutely rigid. An absolutely rigid lattice is unphysical because real crystals are deformable. In a simple model of real lattice, neighboring ions are spaced apart by springs. *Regardless of the stiffness of the springs*, the lattice of a Kronig-Penney crystal with a half-filled band always dimerizes so that the ionic spacing is modulated with a periodicity of twice the lattice constant a. The distortion occurs because a dimerized crystal has a lower total energy than an undistorted crystal.

To compute the energy difference between the uniform and dimerized states of a crystal, first consider the energy difference for a single electronic state of wavevector k. The energy $E_0(k)$ of an electron in an undistorted crystal is given by Eq. 28; the energy $E_1(k)$ in a dimerized crystal by Eq. 41. In these equations, lengths are expressed in units of a, wavevectors in units of $(1/a)$, and energies in units of $(\hbar^2/2ma^2)$, where m is the electron mass. For example, the normalized strength of the ionic delta functions is $v = (2ma^2V/\hbar^2)$. If the distorted lattice is dimerized by an amount u around each lattice site, then the change in energy for a single electronic state is

$$E_1^{\mp}(k) - E_0(k) = \pm v_F\{[\cos^2(k) + (vu)^2]^{\frac{1}{2}} - \cos(k)\} . \qquad (A2.1)$$

Here $v_F = 4\pi^2/v$ is the Fermi velocity $dE(k_F)/dk$. The plus sign in Eq. 1

applies for $|k| > k_F$ and the minus sign for $|k| < k_F$. The new energy spectrum is split by a gap that occurs at the Fermi wavevector. The magnitude of the energy gap is $2\Delta = 2vv_Fu$. States below the gap are lowered in energy, whereas states above the gap are raised in energy.

At zero temperatures, only states below the Fermi surface are occupied, so the *electronic* energy of a Kronig-Penny crystal with a half-filled band is reduced by a distortion of its lattice. Integrating the energy difference A2.1 over all occupied states gives the change in total electronic energy due to electrons interacting with a dimerized lattice:

$$E_{el-lattice} = \int_{-k_F}^{+k_F} dk \, D(k)\{E_1^-(k) - E_0(k)\} \, . \qquad (A2.2)$$

Here $D(k)$ is the density of electronic states in k-space; in one dimension, $D(k)$ is independent of k and may be taken outside the integral. The remaining summation reduces to an elliptic integral:

$$E_{el-lattice} = -2v_F D(k)\left\{\sqrt{1 + (vu)^2} \, E\left(\frac{1}{\sqrt{1 + (vu)^2}}\right) - 1\right\}. \qquad (A2.3)$$

The function $E(x)$ is the complete elliptic integral of the second kind. $E(x)$ is ≥ 1 with equality only for $x = 0$, so the electron-lattice interaction energy is always reduced when the dilation u is nonzero. Just as importantly, $E_{el-lattice}$ is slightly subquadratic in u for small values of u. The slope of $|E_{el-lattice}|$ on a logarithmic plot is asymptotic to (but always slightly less than) 2 as u approaches zero. This subquadratic behavior means that $E_{el-lattice}$ will eventually be larger than any quadratic function at sufficiently small values of

$u.$

In contrast to $E_{el-lattice}$, the lattice strain energy $E_{lattice}$ is a quadratic function of the distortion amplitude u. If C is the effective spring constant for elastic deformations of the lattice, then the increase in lattice energy due to dimerization is

$$E_{lattice} = \frac{1}{2}NC(2u)^2 .$$

(A2.4)

For small distortions, the magnitude of $E_{el-lattice}$ will exceed $E_{lattice}$. Since $E_{el-lattice}$ is negative, the net energy of a Kronig-Penney crystal is reduced by small dimerizations of its lattice.

The optimal amount of dimerization may be found by minimizing the combined lattice and interaction energy:

$$0 = \frac{d}{du}\{E_{lattice} + E_{el-lattice}\}$$

(A2.5)

$$= 2u\left\{2NC - \frac{v_F v^2 D(k)}{\sqrt{1+(vu)^2}} K\left(\frac{1}{\sqrt{1+(vu)^2}}\right)\right\}.$$

Here $K(x)$ is the complete elliptic integral of the first kind. For small distortions u, the elliptic integral may be expanded as

$$K\left(\frac{1}{\sqrt{1+(vu)^2}}\right) \cong \ln\frac{4}{vu} .$$

(A2.6)

The minimization condition A2.5 becomes

$$0 = 2u \left\{ 2NC - v_F v^2 D(k) \ln \frac{4}{vu} \right\}. \tag{A2.7}$$

There are two solutions to Eq. 7. The first, $u = 0$, corresponds to an unstable, uniform lattice. The solution for a stable, dimerized lattice is given by

$$u = \frac{4}{v} \exp \left\{ - \frac{2NC}{v_F v^2 D(k)} \right\}. \tag{A2.8}$$

The corresponding gap in the electronic spectrum is

$$2\Delta_0 = 2W \exp \left\{ - \frac{2NC}{v_F v^2 D(k)} \right\}, \tag{A2.9}$$

where $W = 4v_F$ is the electronic bandwidth of an undistorted crystal. The gap $2\Delta_0$ and the distortion amplitude u are proportional to one another, so either parameter equally well describes the degree of lattice dimerization.

The amount of dimerization depends exponentially on the ratio of lattice stiffness to electron-ion interaction strength. As would be expected, the distortion u is suppressed by a very stiff effective spring constant between the lattice ions, i.e. large values of C. The dependence on the ionic potential strength v is more complicated. A very small electron-ion interaction, i.e. a small value of v, leads to a small distortion since the electrons are nearly free and therefore largely unaffected by the lattice. The opposite extreme, a large value of v, also leads to a small distortion because of the pre-exponential factor, the Kronig-Penney bandwidth. A large repulsive ionic potential forces all electronic wavefunctions to have nodes close to the crystal's lattice sites, which

leads to a narrow bandwidth. The gap in the electronic spectrum can be no larger than the electronic bandwidth, so the gap, and hence the degree of dimerization, is reduced by a very large electron-ion potential.

Many of the Kronig-Penney results just derived apply to real crystals. In particular, the electron-lattice interaction energy is a subquadratic function of the lattice distortion amplitude u. In the absence of electron-electron interactions, the electron-lattice interaction will cause a Peierls distortion of the crystal. Also, the subquadratic behavior of the electron-lattice interaction is generally given by function that is very close to the elliptic integral of Eq. 3. As a result, the Kronig-Penney gap equation is a specific case of the general Peierls gap equation. And finally, the gap parameter Δ and the distortion parameter u are always proportional; in the language of Landau phase transitions, they are equivalent order parameters for a Peierls instability.

II. Perturbation Calculation

Using the perturbation theory outlined in the previous appendix, this section will recalculate the dimerization of a Kronig-Penney crystal with a half-filled band. Not surprisingly, the results agree with those obtained in Sec. I. The point of this section is twofold. First, to evaluate some of the most important equations of the perturbation theory using a concrete model, and second, to illustrate the validity of the approximation made by the perturbation theory.

Unfortunately, a Kronig-Penney crystal with a half-filled band is a somewhat pathological example. Because the crystal's band is half-filled, the $+2k_F$ normal mode of the lattice is *identically* equal to the $-2k_F$ normal mode. This identity

leads to double-counting if all of the perturbation equations are applied literally. Also, because of the ionic delta functions, spatial derivatives of the electronic Bloch functions are discontinuous. These discontinuities can give additional factor-of-two errors. If these two sources of "two" error are avoided, however, application of the perturbation theory to a Kronig-Penney crystal is straightforward.

Eq. A1.11, an expansion of a Peierls distortion in normal modes, is the first and most basic equation to be modified by the identity of the $+2k_F$ and $-2k_F$ normal modes. This equation becomes

$$u_j = u_Q e^{iQx_j} , \qquad (A2.10)$$

where u_j is *real* because $e^{iQx_j} = \pm 1$. This change in u_j ripples down through several other equations. The matrix element $V_1(k, k'; Q)$ becomes

$$V_1(k, k'; Q) = u \delta_{g, k-k'+Q} G_1(k, Q) . \qquad (A2.11)$$

The lattice vector g must be included because $k + Q$ and $k - Q$ are the same wavevector, differing only by g. The next major change is in $E_{lattice}$, which becomes

$$E_{lattice} = \frac{1}{2} N M \omega_Q^2 u^2 . \qquad (A2.12)$$

Expressed in terms of ω_Q, the lattice strain energy appears to be halved. Because of this change in $E_{lattice}$, the equation for the gap parameter becomes

$$\Delta = 2E_B \exp\left\{-\frac{NM\omega_{2k_F}^2}{n(0)G^2}\right\} . \tag{A2.13}$$

The dimensionless electron-phonon coupling constant λ appears to be doubled:

$$\lambda = 2\frac{n(0)G^2}{2NM\omega_{2k_F}^2} . \tag{A2.14}$$

The coupling constant G needs to be evaluated in order to compare Eqs. 13 and 9 for the gap parameter Δ_0. Equation A1.8 for $G_1(-k_F, 2k_F)$ may be used without modification:

$$G_1 = -\int dx\ \tilde{X}_{+k_F}^*\tilde{X}_{-k_F}\frac{d}{dx}\{v\delta(x)\} . \tag{A2.15}$$

The evaluation of the integral requires the standard definition of the derivative of a delta function (which is integration by parts):

$$G_1 = +v\frac{d}{dx}[\tilde{X}_{+k_F}(x)\tilde{X}_{-k_F}(x)]_{x=0} . \tag{A2.16}$$

Here the discontinuity in the Bloch function derivatives becomes important. Schrodinger's equation requires that the spatial derivative of a Bloch function be discontinuous at $x = 0$:

$$X_k'(0+\epsilon) - X_k'(0-\epsilon) = \frac{v}{a}X_k(0) . \tag{A2.17}$$

For large values of v, the spatial derivative of a Bloch function changes sign at $x = 0$. The average *magnitude* of the spatial derivative is therefore $(v/2a)X_k(0)$. Using the average magnitude of spatial derivatives in the equation for G_1 gives:

$$G_1 = - v_F v e^{i\pi/2} . \tag{A2.18}$$

The modulus G of G_1 is $v_F v$; the phase ξ_0 of G_1 is $-\pi/2$, as predicted for a repulsive potential.

Combining Eqs. 13 and 18 gives

$$2\Delta_0 = 4E_B \exp\left\{ - \frac{NM\omega_{2k_F}^2}{v_F v^2 D(k)} \right\} . \tag{A2.19}$$

The density of states is $n(0) = 2D(k)/v_F$. Using $M\omega_Q^2 = 4C$, the gap parameter finally reduces to

$$2\Delta_0 = 4E_B \exp\left\{ - \frac{2NC}{v_F v^2 D(k)} \right\} . \tag{A2.20}$$

This agrees with Eq. 9 if E_B is taken to be half the bandwidth W. The important feature of Eqs. 9 and 20, however, is the exponential factor, which is correctly given by perturbation theory without any adjustment.

The subquadratic behavior of $E_{el-lattice}$ in both the "exact" and perturbation calculations leads to the gap equation A2.20. In turn, the subquadratic behavior of $E_{el-lattice}$ is caused by a "resonance" condition which the perturbation calculation exploits explicitly: for some range E_B of energies about the Fermi surface, states of wavevector k are roughly degenerate in energy with states of wavevector $k \pm 2k_F$. Chapter 2 generalizes this resonance condition so that it may be applied to three-dimensional crystals at nonzero temperatures.

III. Review of the Rigid Kronig-Penney Model

The Kronig-Penney model consists of a periodic array of Dirac delta functions. The crystal potential $V_0(x)$ experienced by an electron is the sum of the ionic potentials at each lattice site:

$$V_0(x) = \sum_j aV\delta(x-ja) , \qquad (A2.21)$$

where a is the lattice constant, and V is the strength of a single ionic potential. The potential strength V may be either positive or negative. Positive values of V lead to solutions which resemble nearly free electron states, whereas negative values lead to tightly bound solutions. For definiteness, V will be assumed to be positive in the following discussion.

Solutions to Schrodinger's equation are written in the form

$$\chi^{(0)}(x) = A_1 e^{ik_0 x} + A_2 e^{-ik_0 x} , \qquad (A2.22)$$

where the energy of the wavefunction $\chi^{(0)}$ is $E_0 = -\hbar^2 k_0^2/2m$. Solutions of Schrodinger's equation satisfy Bloch's condition:

$$\chi_k^{(0)}(x+a) = e^{ika}\chi_k^{(0)}(x) , \qquad (A2.23)$$

where k is the wavevector of the state $\chi_k^{(0)}$. Schrodinger's equation leads to two equations for mixing coefficients A_1 and A_2:

$$A_1\{e^{ika} - e^{ik_0 a}\} + A_2\{e^{ika} - e^{-ik_0 a}\} = 0, \tag{A2.24a}$$

$$A_1\left\{\left(1 + i\,\frac{v}{k_0}\right) - e^{i(k_0-k)a}\right\} - A_2\left\{\left(1 - i\frac{v}{k_0}\right) - e^{-i(k+k_0)}\right\} = 0,$$

$$\tag{A2.24b}$$

where $v = 2ma^2 V/\hbar^2$. These equations lead to a relationship between k_0 and k, which is an implicit equation for electron energy E_0 as a function of wavevector k:

$$\cos(ka) = \cos(k_0 a) + \frac{1}{2} V \frac{\sin k_0 a}{k_0 a}. \tag{A2.25}$$

Equation 25 is a transcendental equation which may be solved graphically, Fig. 1. The right-hand side is plotted as a function of k_0. Given a particular value of k, a horizontal line is drawn starting at a vertical offset given by $\cos ka$. Intersections of the horizontal line with the plotted curve are allowed values of k_0 for that value of k. Since $\cos ka$ is bounded by ± 1, only certain regions of the curve lead to allowed values of k_0. Gaps exist in a plot of $E_0(k)$ vs. k which separate the electronic energy spectrum into bands of allowed energy.

For the rest of this discussion, it will be convenient to measure lengths in units of a, wavevectors in $(1/a)$, and energy in $(\hbar^2/2ma^2)$. Eq. 25 may be rewritten as

$$\cos(k) = \cos(k_0) + \frac{1}{2} V \frac{\sin k_0}{k_0}. \tag{A2.26}$$

Energy is now k_0^2.
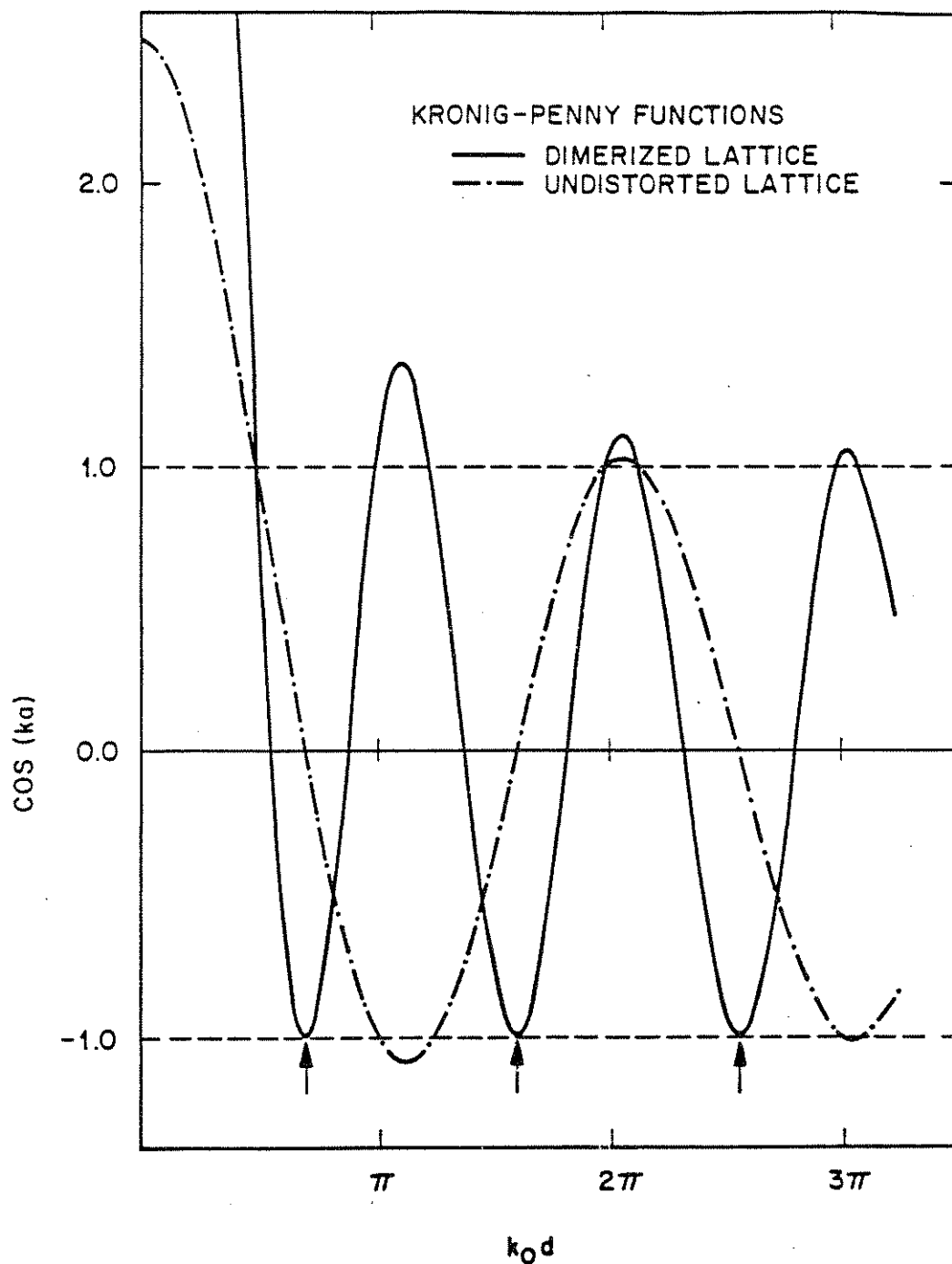
Fig. A2-1) Graphical solutions to the Kronig-Penney equations for an undistorted lattice, Eq. A2.25, and a dimerized lattice, Eq. A2.39. The solution for the dimerized lattice is shown in the limit of zero distortion. For finite distortions, new energy gaps open up at the locations indicated by the arrows.

When the ionic delta functions are very repulsive, $v \gg 1$, nodes of the electronic Bloch functions are close to the lattice sites. Approximate solutions of k_0 are given by

$$k_0 \cong n\,\pi - \frac{2\pi}{v}\{1 + \cos(k)\} \qquad (A2.27)$$

$$= n\,\pi - \frac{4\pi}{v}\cos^2\left(\frac{1}{2}k\right).$$

Here $n = 1, 2, 3, \cdots$ labels the energy band of k_0. Only solutions in the first energy band will be considered, where $n = 1$. To first order in $(1/v)$, energy is given by

$$E_0(k) \cong \pi^2 - v_F\{1 + \cos(k)\} \qquad (A2.28)$$

$$= \pi^2 - 2v_F\cos^2\left(\frac{1}{2}k\right),$$

where $v_F = (4\pi^2/v)$. The maximum energy of the first energy band is π^2 and occurs at the Brillouin zone edge, $k = \pm\pi$. The bandwidth is $W = 4v_F$, with a midband energy of $E_0(\pi/2) = \pi^2 - v_F$. For values of k close to the midband value of $k = \pi/2$, Eq. 28 may be approximated by $E_0(k) = E_0(\pi/2) + v_F(|k| - \pi/2)$.

Exact Bloch functions corresponding of Eq. 26 may be written as

$$\chi_k^{(0)}(x) = A_k e^{ik_0 x} + B_k e^{ik_0 - ik_0 x}, \qquad (A2.29)$$

where for normalization to one unit cell the coefficients A_k and B_k are given by

$$A_k = \left\{ 1 + B_k^2 - 2B_k \, \frac{\sin(k_0)}{k_0} \right\}^{-\frac{1}{2}} \tag{A2.30}$$

$$B_k = \frac{\sin \frac{1}{2}(k - k_0)}{\sin \frac{1}{2}(k + k_0)} \; .$$

IV. The Dimerized Kronig-Penney Model

Derivation of the dimerized Kronig-Penney equation follows the same path as for the regular Kronig-Penney equation. The Kronig-Penney lattice is allowed to dimerize an amount $\pm u$ at each lattice site. Two types of regions are created by the dimerization: regions I, contracted segments of length $a - 2u$; and regions II, dilated segments of length $a + 2u$. The wave function in these regions is written as:

$$\text{Region I:} \quad \chi_k(x) = A_1 e^{ik_0 x} + B_1 e^{-ik_0 x} \; ; \tag{A2.32}$$

$$\text{Region II:} \quad \chi_k(x) = A_2 e^{ik_0 x} + B_2 e^{-ik_0 x} \; . \tag{A2.33}$$

The Bloch condition and the Schrodinger equation lead to four coupled equations for the coefficients A_1 through B_2. To simplify the appearance of the equations, the dimensionless notation of the preceding section will be used. Also, the following constants are defined: $\delta = 2u/a$, $\eta = v/k_0$, $\phi_1 = \frac{1}{2}k_0(1-\delta)$, and $\phi_2 = \frac{1}{2}k_0(3+\delta)$. In terms of these constants, the equations are:

$$(A2.34)$$

Continuity at $\frac{1}{2}(1-\delta)$:

$$0 = A_1 e^{i\phi_1} + B_1 e^{-i\phi_1} - A_2 e^{i\phi_1} - B_2 e^{-i\phi_1} \;;$$

$$(A2.35)$$

Continuity at $- \frac{1}{2}(1-\delta)$:

$$0 = A_1 e^{-i\phi_1} + B_1 e^{i\phi_1} - A_2 e^{-2ik} e^{i\phi_2} - B_2 e^{-2ik} e^{-i\phi_2} \;;$$

$$(A2.36)$$

Derivatives at $\frac{1}{2}(1-\delta)$:

$$0 = A_1(1-i\eta) e^{i\phi_1} - B_1(1+i\eta) e^{-i\phi_1} - A_2 e^{i\phi_1} + B_2 e^{-i\phi_1} \;;$$

$$(A2.37)$$

Derivatives at $- \frac{1}{2}(1-\delta)$:

$$0 = A_1(1+i\eta) e^{-i\phi_1} - B_1(1-i\eta) e^{i\phi_1} - A_2 e^{-2ik} e^{i\phi_2} + B_2 e^{-2ik} e^{-i\phi_2} \;.$$

Solution of Eqs. 34 - 37 gives a transcendental equation which may be written in one of two equivalent forms:

$$\cos^2(k) = \left\{\cos(k_0) + \frac{1}{2} v \, \frac{\sin(k_0)}{k_0}\right\}^2 + \left\{\frac{1}{2} v \, \frac{\sin k_0 \delta}{k_0}\right\}^2 \;; \qquad (A2.38)$$

$$\cos(2k) = \cos(2k_0) + 2v \, \frac{\sin(2k_0)}{2k_0} + \left(\frac{v}{2k_0}\right)^2 \{\cos(2k_0\delta) - \cos(2k_0)\} \quad (A2.39)$$

These equations reduce to the usual Kronig-Penney equations in either of the limits $\delta \rightarrow 0$ (undistorted lattice) or $\delta \rightarrow 1$ (doubled lattice).

Eq. 38 is the most generally useful form of the dimerized equation, because it is in a convenient form for calculating small perturbations from the undimerized

lattice. Eq. 39 is sometimes useful, however, because it is in a form similar to the rigid Kronig-Penney equation. Fig. 1 shows a graph of the right-hand side of Eq. 39 superimposed on the rigid Kronig-Penney equation, for the case $\delta = 0$. The arrows mark the locations where Eq. 39 is tangent to the horizontal line $\cos k = -1$. Any nonzero value of δ causes the curve to become less than -1 at these points and Peierls gaps to form in the electronic spectrum.

Given a value of $v \gg 1$, Eq. 38 may be solved for small amounts of dimerization u such that $(v\delta) \ll 1$. The first energy band is determined by

$$k_\delta^+ = \pi - \frac{2\pi}{v}\{1 \pm [\cos^2(k) + (vu)^2]^{\frac{1}{2}}\} . \qquad (A2.40)$$

The plus sign applied for $|k|$ larger than midband; the minus sign for $|k|$ smaller than midband. Corresponding energies are given by

$$E_I^+(k) = \pi^2 - v_F\{1 \pm [\cos^2(k) + (vu)^2]^{\frac{1}{2}}\} . \qquad (A2.41)$$

APPENDIX A3: NONPERTURBATIVE MEASUREMENTS
OF LOCAL CONDUCTIVITIES

This appendix describes a four-probe sample holder that was designed and built as a part of the thesis research. The sample holder facilitated conductivity measurements across small, localized regions of an $NbSe_3$ crystal. The need for such a device is apparent in Chapter 3. There, localized conductivity measurements revealed discontinuities in CDW current and thus provided direct evidence of phase slippage. The design of the sample holder described in this appendix was originally inspired by the work of Mihaly et al.[1] with much simpler devices.

The lead geometry of the sample holder is shown in Figure 1. An $NbSe_3$ crystal rests on top of a rectangular sapphire block that has a slightly convex surface. Two gold wires, extending from the top and bottom of the photograph, are attached to the crystal ends and the sapphire surface by small amounts of silver paint. Two additional nichrome wires are suspended perpendicularly across the $NbSe_3$ crystal. Attached to each nichrome wire is a fine Wollaston wire that is barely visible in the photograph. The Wollaston and nichrome wires form a bow-and-drawstring arrangement, with the Wollaston held taut by the nichrome wire and resting lightly on the $NbSe_3$ crystal. The gold wires serve as current-injection leads, labelled "1" and "4" in Fig. 3-8a. The Wollaston wires serve as movable voltage probes, labelled "2" and "3". Probe 1 is at the top of the figure, and the remaining probes are labelled sequentially. For scale, the sapphire block is 5 mm long; the gold and nichrome wires are

(For page sequence only.)

Fig. A3-1) Detail of the sample and lead geometry used in nonperturbative four-probe measurements. Magnification of 25 times. See text for explanation.
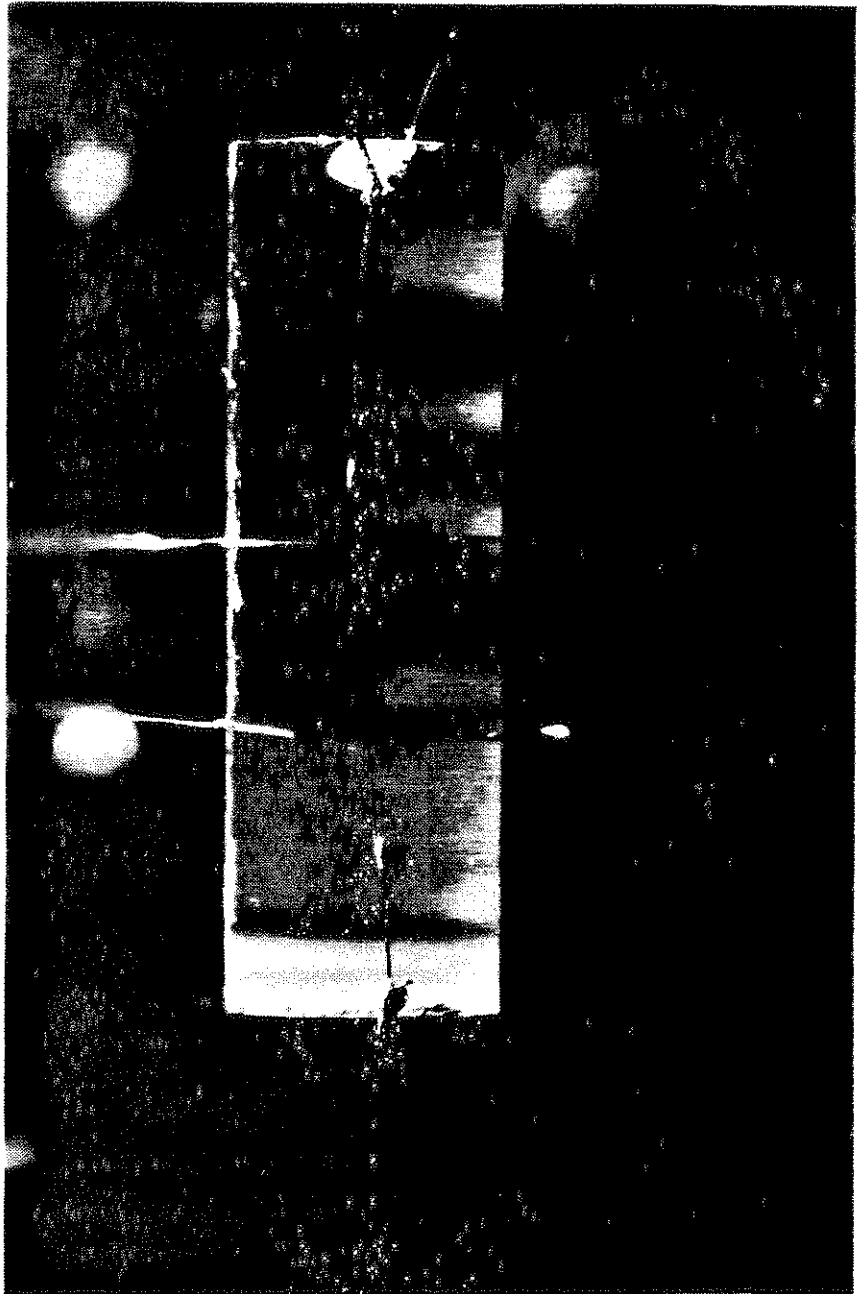
Fig. A3-1

Fig. A3-2) Detail of the mechanism used to raise and lower voltage probes 2
and 3. Magnification of 9 times.

Fig. A3-2

(For page sequence only.)

25 μm in diameter; and the NbSe$_3$ crystal and the Wollaston wires are 2-3 μm in width.

Figure 2 shows the mechanism for raising and lowering the Wollaston probes. At the center of the photograph is the sapphire block, and beneath the block is a copper support platform, which is slightly out of focus. At the top of the figure are two coaxial conductors whose inner conductors are attached to lead 1 by gold wires. At the bottom of the photograph is a third coax, whose inner conductor is attached to lead 4. On either side of the sapphire block is a coax and a steel rod. Each steel rod has a protruding tip which is paired with the inner conductor of a coax on the opposite side of the block.

Each coax-rod pair in Fig. 2 raises and lowers one nichrome wire, and hence one Wollaston voltage probe. For example, probe 3 is controlled by the coax-rod pair that is closest to the focal plane of the photograph. A nichrome wire is lowered by winching it toward the sapphire block. One end of the nichrome wire is soldered to the inner conductor of a coax, and the other end is tied to the tip of a steel rod by a fine Kevlar filament. When the steel rod is turned, the Kevlar filament is wound around the rod's tip and the nichrome wire is pulled down. When the Wollaston wire touches the NbSe$_3$ crystal, a current path is established through the wire and crystal, which signals that the voltage probe is in electrical contact with the crystal. The voltage probe is raised by releasing tension on the nichrome wire.

Figure 3 shows the mechanism for moving the coax-rod pairs along the NbSe$_3$ crystal. At the top of the photograph is the copper platform that supports the sapphire block, which is just visible at the platform center.

Fig. A3-3) Top view of the complete sample holder, showing the mechanism
use to position voltage probes along a sample. The area detailed in
Figs. 1 and 2 is at the top.
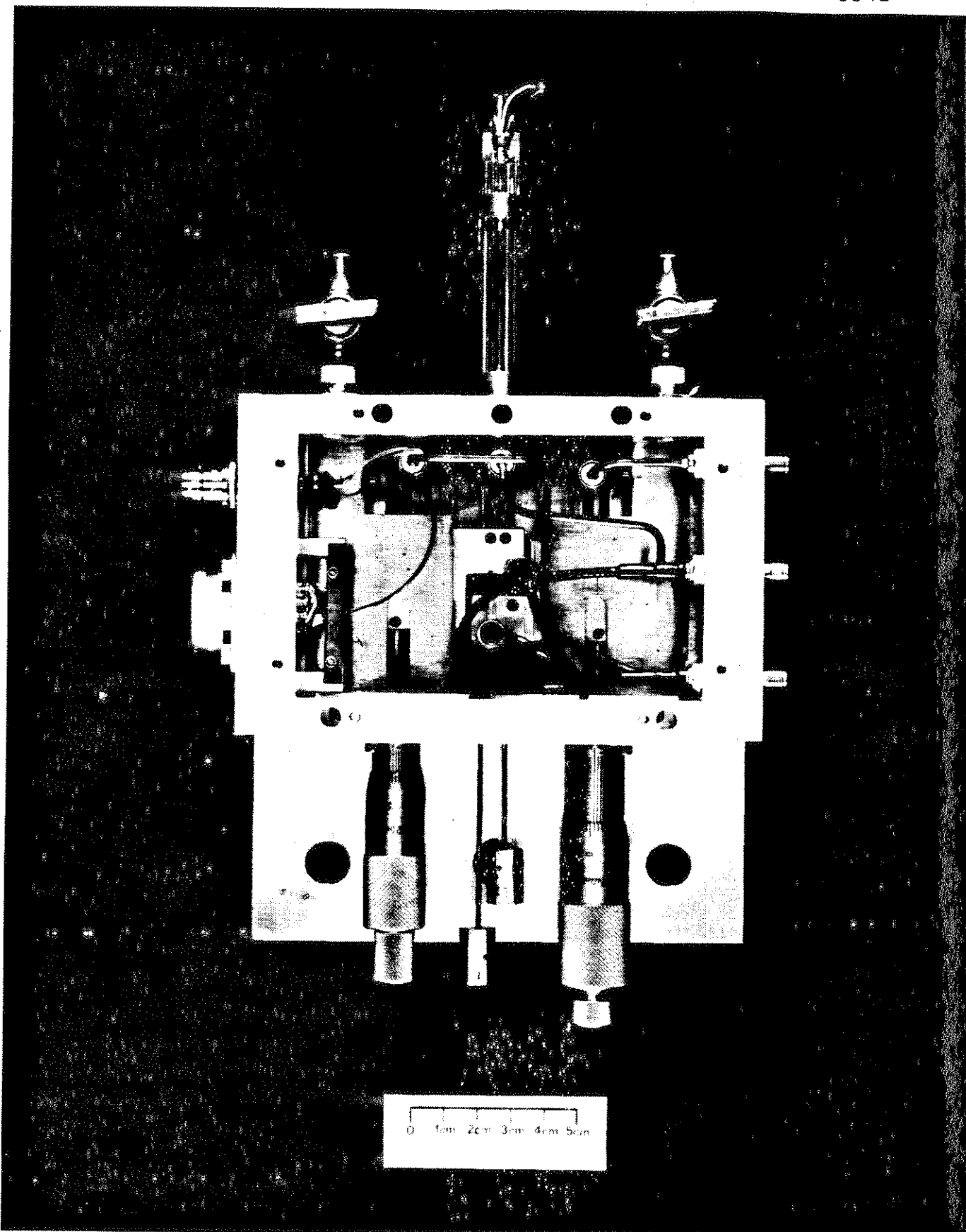
Fig. A3-3

Fig. A3-4) Side view of the sample holder. The area detailed in Figs. 1 and 2
is covered by a white heater cap.
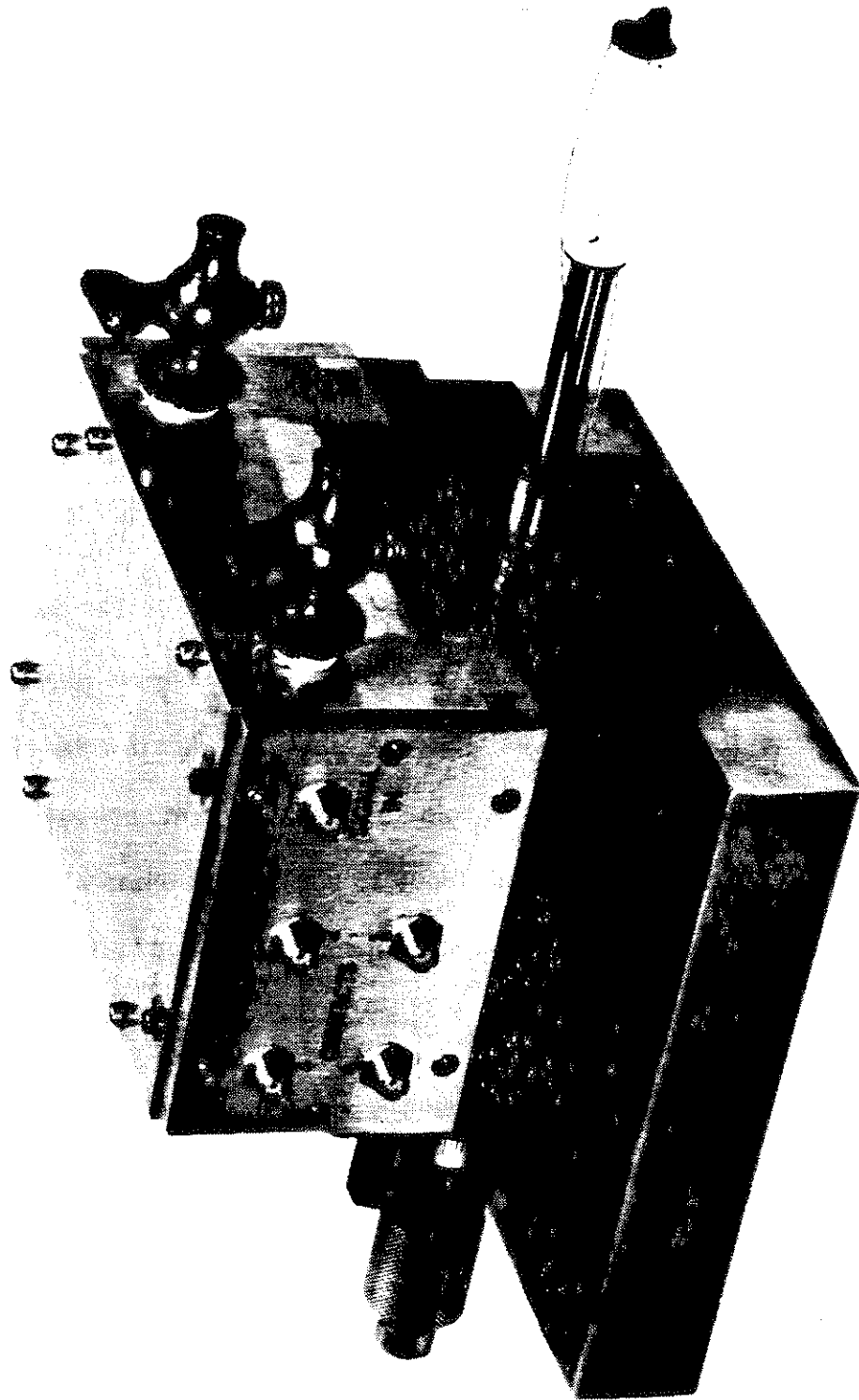
Fig. A3-4

Coaxial conductors and steel rods run back from the platform to an aluminum and brass housing, inside of which are two stainless steel slides. Each slide is attached to a coax-rod pair and controls its position by moving back and forth within the housing. The slides are moved by the micrometers which are visible at the bottom of the photograph. Inside the housing, the coaxial conductors are attached by flexible cables to feedthroughs on the right side of the housing. The steel winch rods exit the housing near the micrometers. Other feedthroughs on the left side of the housing provide electrical leads for thermometry at the copper support platform.

Figure 4 shows a three-dimensional view of the sample holder, which is mounted on an aluminum base. The copper support platform is covered with a white heater cap. The platform and cap are inserted into a custom-made cryostat. In the cryostat, cold ^{4}He gas flows past the cap and cools the platform to a base temperature of about 15 K. The aluminum housing remains outside the cryostat and at a temperature at close to 273 K. Nozzles on the housing allow nitrogen gas to flow through its interior, which prevents icing of the slides.

The sample holder in Figs. 1-4 is a third generation design. Previous designs were considerably simpler, but did not permit accurate and repeatable positioning of voltage leads *in situ*. The sample holder shown required about 300 hours of design, 300 hours of machining, and 100 hours of assembly.

APPENDIX A4: PUBLICATION LIST

1. Charge density wave depinning and switching in NbSe$_3$, R. P. Hall and A. Zettl, Solid State Commun. *50*, 813 (1984).

2. Chaotic response of NbSe$_3$: evidence for a new charge-density-wave phase, R. P. Hall, M. Sherwin, and A. Zettl, Phys. Rev. *B29*, 7076 (1984).

3. Negative differential resistance and instability in NbSe$_3$, R. P. Hall, M. Sherwin, and A. Zettl, Phys. Rev. Lett. *52*, 2293 (1984).

4. Role of current oscillations in ac-dc interference effects in NbSe$_3$, R. P. Hall and A. Zettl, Phys. Rev. *B30*, 2279 (1984).

5. Chaotic ac conductivity in the charge-density-wave state of $(TaSe_4)_2I$, M. Sherwin, R. Hall and A. Zettl, Phys. Rev. Lett. *53*, 1387 (1984).

6. Collective-mode ac conduction in the blue bronze $K_{0.3}MoO_3$, R. P. Hall, M. S. Sherwin, and A. Zettl, Solid State Comm. *54*, 683 (1985).

7. AC dynamics of NbSe$_3$ in the switching regime, R. P. Hall and A. Zettl, Solid State Comm. *55*, 307 (1985).

8. Distinct current-carrying charge-density-wave states in NbSe$_3$, R. P. Hall and A. Zettl, Solid State Comm. *57*, 21 (1986).

9. Switching and phase slip centers in charge-density-wave conductors, R. P. Hall, M. F. Hundley, and A. Zettl, Phys. Rev. Lett. *56*, 2399 (1986).

10. A phase-slip model of switching, R. P. Hall, M. F. Hundley, and A. Zettl, Physica *143B*, 152 (1986).

11. A rf-induced dynamic coherence length in NbSe$_3$, R. P. Hall, M. F. Hundley, and A. Zettl, Synthetic Metals *19*, 813 (1987).

12. Switching and charge-density-wave transport in NbSe$_3$. I: dc characteristics, R. P. Hall, M. F. Hundley, and A. Zettl, Phys. Rev. B, to be published.

13. Switching and charge-density-wave transport in NbSe$_3$. II: ac characteristics, R. P. Hall and A. Zettl, Phys. Rev. B, to be published.

14. Switching and charge-density-wave transport in NbSe$_3$. III: dynamical instabilities, M. S. Sherwin, A. Zettl, and R. P. Hall, Phys. Rev. B, to be published.

15. Phase-slips and switching in charge-density-wave transport, M. Inui, R. P. Hall, S. Doniach, and A. Zettl, Phys. Rev. B, to be published.

LIST OF FIGURES

340

Chapter 5

Chapter 6

Appendix A2

Appendix A3

REFERENCES

Chapter 1

1. For a review, see G. Grüner and A. Zettl, *Phys. Rep.* **119**, 117 (1985).

2. A. Zettl and G. Gruner, *Phys. Rev. B* **26**, 2298 (1982).

3. P. Monceau, N. P. Ong, A. M. Portis, A. Meerschaut, and J. Rouxel, *Phys. Rev. Lett.* **37**, 602 (1976).

4. N. P. Ong and P. Monceau, *Phys. Rev. B* **16**, 3443 (1977).

5. R. M. Fleming and C. C. Grimes, *Phys. Rev. Lett.* **42**, 1423 (1979); R. M. Fleming, *Phys. Rev. B* **22**, 5606 (1980).

6. M. P. Everson and R. V. Coleman, *Phys. Rev. B* **28**, 6659 (1984).

7. R. P. Hall and A. Zettl, *Solid State Commun.* **50**, 813 (1984).

8. R. P. Hall, M. S. Sherwin, and A. Zettl, *Phys. Rev. Lett.* **52**, 2293 (1984).

9. R. P. Hall and A. Zettl, *Solid State Commun.* **55**, 307 (1985).

10. R. P. Hall, M. Sherwin, and A. Zettl, *Phys. Rev. B* **29**, 7076 (1984).

11. R. P. Hall and A. Zettl, *Solid State Commun.* **57**, 27 (1986).

12. R. P. Hall, M. F. Hundley, and A. Zettl, *Phys. Rev. Lett.* **56**, 2399 (1986).

13. R. P. Hall, M. F. Hundley, and A. Zettl, *Phys. Rev. B*, to be published.

14. R. P. Hall and A. Zettl, *Phys. Rev. B*, to be published.

15. M. S. Sherwin, A. Zettl, and R. P. Hall, *Phys. Rev. B*, to be published.

16. R. P. Hall, M. F. Hundley, and A. Zettl, *Physica* **143B**, 152 (1986).

17. M. Inui, R. P. Hall, S. Doniach, and A. Zettl, *Phys. Rev. B*, to be published.

18. R. E. Peierls, *Quantum Theory of Solids* (Oxford University Press, London, 1955), p. 108.

19. H. Frohlich, *Proc. Roy. Soc. London* **A223**, 296 (1954).

20. P. A. Lee, T. M. Rice, and P. W. Anderson, *Solid State Commun.* **14**, 703 (1974).

21. H. Fukuyama, *J. Phys. Soc. Japan* **41**, 513 (1976).

22. H. Fukuyama and P. A. Lee, *Phys. Rev. B* **17**, 535 (1978).

23. P. A. Lee and T. M. Rice, *Phys. Rev. B* **19**, 3970 (1979).

24. G. Kriza, A. Janossy, and G. Mihaly, in *Charge Density Waves in Solids*, edited by Gy. Hutiray and J. Solyom (Springer, New York, 1985), p. 426.

25. L. Mihaly and G. Gruner, *Solid State Commun.* **50**, 807 (1984).

26. Z. Z. Wang, P. Monceau, M. Renard, P. Gressier, L. Guemas, and A. Meerschaut, *Solid State Commun.* **47**, 439 (1983).

27. W. Wonneberger and H. J. Breymayer, *Z. Phys. B* **56**, 241 (1984).

28. H. Mutka, S. Bouffard, J. Dumas, and C. Schlenker, *J. Phys. (Paris) Lett.* **45**, L729 (1985).

29. J. Bardeen, *Phys. Rev. Lett.* **42**, 1498 (1979); J. Bardeen, *Phys. Rev. Lett.* **55**, 1010 (1985).

30. G. Grüner, A. Zawadowski, and P. M. Chaikin, *Phys. Rev. Lett.* **46**, 511

(1981).

31. Leigh Sneddon, M. C. Cross, and Daniel S. Fisher, *Phys. Rev. Lett.* **49**, 292 (1982).

32. B. Joos and D. Murray, *Phys. Rev. B* **29**, 1094 (1984).

33. A. Janossy, G. Mihaly, and L. Mihaly, in *Charge Density Waves in Solids*, p. 412.

34. W. Wonneberger and H. J. Breymayer, *Z. Phys. B* **56**, 241 (1984).

35. Phase slippage at current-injection contacts has been discussed previously. See N. P. Ong, G. Verma, and K. Maki, *Phys, Rev. Lett.* **52**, 663 (1984), and N. P. Ong and Kazumi Maki, *Phys. Rev. B* **32**, 6582 (1985); also L. P. Gorkov, *JETP Lett.* **38**, 87 (1983), and I. Batistic, A. Bjelis, and L. P. Gorkov, *J. Phys. (Paris)* **45**, 1049 (1984).

36. S. Sridhar, D. Reagor, and G. Grüner, *Phys. Rev. Lett.* **55**, 307 (1985).

37. A. Fournel, B. Oujia, and J. P. Sorbier, *Mol. Liquid Cryst.* **121**, 83 (1985); A. Fournel, J. B. sorbier, M. Konczykowski, P. Monceau, and F. Levy, *Physica* **143B**, 177 (1986).

38. M. Inui, private communication.

Chapter 2

1. R. E. Peierls, *Quantum Theory of Solids* (Oxford University Press, London, 1955), p. 108.

2. H. Frohlich, *Proc. Roy. Soc. London* **A223**, 296 (1954).

3. P. A. Lee, T. M. Rice, and P. W. Anderson, *Solid State Commun.* **14**, 703 (1974).

4. G. A. Toombs, *Phys. Reports* **40**, 181 (1978).

5. R. H. Friend and D. Jerome, *J. Phys. C* **12**, 1441 (1979).

6. G. Bilbro and W. L. McMillan, *Phys. Rev. B* **14**, 1887 (1976); C. A. Balseiero and L. M. Falicov, *Phys. Rev. B* **20**, 4457 (1979); J. Solyom, *Adv. Phys.* **28**, 201 (1979); D. Jerome and H. J. Schultz, *Adv. Phys.* **31**, 299 (1982); J. Solyom, *Adv. Phys.* **28**, 201 (1979).

7. J. M. Ziman, *Principles of the Theory of Solids* (Cambridge University Press, Cambridge, 1979), p. 149.

8. P. Pincus in *Low Dimensional Cooperative Phenomena*, ed. H. J. Keller (Plenum Press, New York, 1975), p. 1.

9. P. A. Lee, T. M. Rice, and P. W. Anderson, *Phys. Rev. Lett.* **31**, 462 (1973).

10. A. Briggs, P. Monceau, M. Nunez-Regueiro, J. Peyrard, M. Ribault, and J. Richard, *J. Phys. C* **13**, 2117 (1980).

11. J. L. Hodeau, M. Marezio, C. Roucau, R. Ayroles, A. Meerschaut, J. Rouxel, and P. Monceau, *J. Phys. C* **11**, 4117 (1978); A. Meerschaut and J.

Rouxel, *J. Less Common Metals* **39**, 197 (1975).

12. Nobuyuki Shima and Hiroshi Shima, in *Theoretical Aspects of Band Structures and Electronic Properties of Pseudo-One-Dimensional Solids*, edited by Hiroshi Kamimura (D. Reidel Publishing, Dordrecht, Holland).

13. N. P. Ong and P. Monceau, *Phys. Rev. B* **16**, 3443 (1977).

14. R. M. Fleming, D. E. Moncton, and D. B. McWhan, *Phys. Rev. B* **18**, 5560 (1978).

15. J. A. Wilson, *Phys. Rev. B* **19**, 6456 (1979); F. Devreux, *J. Phys.* (Paris) **43**, 1489 (1982).

16. A. Fournel, B. Oujia, and J. P. Sorbier, *Mol. Cryst. Liq. Cryst.* **121**, 83 (1985); A. Fournel, J. P. Sorbrier, M. Konczykowski, P. Monceau, and F. Levy, *Physica* **143B**, 177 (1986).

17. P. Monceau, *Solid State Commun.* **24**, 331 (1977); P. Monceau and A. Briggs, *J. Phys. C* **11**, L465 (1978); R. M. Fleming, J. A. Polo, and R. V. Coleman, *Phys. Rev. B* **17**, 1634 (1978).

18. S. Sridhar, D. Reagor, G. Grüner, *Phys. Rev. Lett* **55**, 307 (1985).

19. P. Monceau, L. Bernard, R. Currat, F. Levy, and J. Rouxel, *Synthethetic Metals* **19**, 819 (1987).

20. J. C. Lasjaunias and P. Monceau, *Solid State Commun.* **41**, 911 (1982).

21. G. Grüner and A. Zettl, *Phys. Rep.* **119**, 117 (1985).

22. P. W. Anderson, *Basic Notions of Condensed Matter Physics* (Benjamin/Cummings Publishing Co., Menlo Park, California, 1984).

23. M. J. Rice, in *Low Dimensional Cooperative Phenomena*, edited by H. J. Keller (Plenum Press, New York, 1975), p. 23.

24. E. Eisenreiger, in *Organic Conductors and Semiconductors*, edited by L. Pal, G. Grüner, A. Jánossy, and J. Solyom (Springer Verlag, Lecture Notes in Physics, Vol. 65, 1976), p. 73.

25. M. B. Walker, *Can. J. Physics* **56**, 127 (1978).

26. H. Fukuyama and P. A. Lee, *Phys. Rev. B* **17**, 535 (1978).

27. H. Fukuyama, *J. Phys. Soc. Japan* **41**, 513 (1976).

28. P. A. Lee and T. M. Rice, *Phys. Rev. B* **19**, 3970 (1979).

29. P. Monceau, N. P. Ong, A. M. Portis, A. Meerschaut, and J. Rouxel, *Phys. Rev. Lett.* **37**, 602 (1976).

30. For reviews of indirect evidence of CDW transport in $NbSe_3$, see ref. 21 and P. Monceau in *Electronic Properties of Inorganic Quasi-One-Dimensional Materials II* (D. Reidel Publishing, 1985), p. 139.

31. Direct evidence of CDW transport comes from NMR motional narrowing. See Joseph H. Ross, Zhiyue Wang, and Charles P. Slichter, *Phys. Rev. Lett.* **56**, 663 (1986).

32. R. M. Fleming and C. C. Grimes, *Phys. Rev. Lett.* **42**, 1423 (1979).

33. R. M. Fleming, *Phys. Rev. B* **22**, 5606 (1980).

34. M. Underweiser, M. Maki, B. Alavi, L. Mihaly, and G. Grüner, *Bull. Am. Phys. Soc.* **31**, 433 (1986).

35. A. Zettl and G. Grüner, *Phys. Rev. B* **29**, 755 (1984).

36. P. Monceau, J. Richard, and M. Renard, *Phys. Rev. Lett.* **45**, 43 (1980).

37. J. Richard, P. Monceau, M. Papoular, and M. Renard, *J. Physics C* **15**, 7157 (1982).

38. A. Zettl and G. Grüner, *Phys. Rev. B* **26**, 2298 (1982).

39. G. Grüner, A. Zawadowski, and P. M. Chaikin, *Phys. Rev. Lett.* **46**, 511 (1981).

40. Leigh Sneddon, M. C. Cross, and Daniel S. Fisher, *Phys. Rev. Lett.* **49**, 292 (1982).

41. The complexity introduced by treating the CDW as deformable has lead to a variety of theoretical analyses. See P. B. Littlewood, *Phys. Rev. B* **33**, 6694 (1986) for references.

42. L. Sneddon, Phys. Rev. Lett. **52**, 65 (1984).

43. N. P. Ong, G. Verma, and K. Maki, *Phys. Rev. Lett.* **52**, 663 (1984); N. P. ONg and K. Maki, *Phys. Rev. B* **32**, 6582 (1985).

44. L. P. Gorkov, *JETP Lett.* **38**, 87 (1983); I. Batistic, A. Bjelis, and L. P. Gorkov, *J. Phys. (Paris)* **45**, 1049 (1984).

45. *M. C. Escher: His Life and Complete Graphic Work*, by F. H. Bool, J. R. Kist, J. L. Locher, and F. Wierda (Harry N. Abrams Publishers, New York, 1981), p. 321.

Chapter 3

1. P. Monceau, N. P. Ong, A. M. Portis, A. Meerschaut, and J. Rouxel, *Phys. Rev. Lett.* **37**, 602 (1976).

2. R. P. Hall and A. Zettl, *Solid State Commun.* **50**, 813 (1984).

3. R. P. Hall, M. F. Hundley and A. Zettl, *Phys. Rev. Lett.* **56**, 2399 (1986).

4. R. P. Hall, M. F. Hundley, and A. Zettl, to be published.

5. R. M. Fleming and C. C. Grimes, *Phys. Rev. Lett.* **42**, 1423 (1979); R. M. Fleming, *Phys. Rev. B***22**, 5606 (1980).

6. R. V. Coleman, *Synthetic Metals* **19**, 795 (1987).

7. H. Mutka, S. Bouffard, J. Dumas, and C. Schlenker, *J. Phys. (Paris) Lett.* **45**, L729 (1985).

8. P. B. Littlewood, *Phys. Rev. B***33**, 6694 (1986).

9. W. J. Skocpol, M. R. Beasley, and M. Tinkham, *J. Low Temp. Phys.* **16**, 145 (1974).

10. P. W. Anderson, *Rev. Mod. Phys.* **38**, 298 (1966).

11. Phase slippage at current-injection contacts has been discussed previously. See N. P. Ong, G. Verma, and K. Maki, *Phys. Rev. Lett.* **52**, 663 (1984), and N. P. Ong and Kazumi Maki, *Phys. Rev. B***32**, 6582 (1985); also L. P. Gorkov, *JETP Lett.* **38**, 87 (1983), and I. Batistic, A. Bjelis, and L. P. Gorkov, *J. Phys. (Paris)* **45**, 1049 (1984).

12. R. P. Hall and A. Zettl, *Solid State Commun.* **57**, 27 (1986).

13. A. Zettl and G. Grüner, *Phys. Rev.* **B26**, 2298 (1982).

14. The term "depinning wave", used in a slightly different context, was originally coined by B. Joos and D. Murray, *Phys. Rev. B29*, 1094 (1984).

15. R. P. Hall, M. S. Sherwin, and A. Zettl, *Phys. Rev. Lett.* **52**, 2293 (1984).

16. M. S. Sherwin, A. Zettl, and R. P. Hall, to be published.

17. A. Janossy, G. Mihaly, and L. Mihaly, in *Charge Density Waves in Solids*, p. 412.

18. G. Kriza, A. Janossy, and G. Mihaly, in *Charge Density Waves in Solids*, edited by Gy. Hutiray and J. Solyom (Springer, New York, 1985), p. 426.

19. N. P. Ong, D. D. Dugan, C. B. Kalem and T. W. Jing, in *Charge Density Waves in Solids*, p. 387.

20. L. Mihaly and G. X. Tessema, *Phys. Rev. B33*, 5858 (1986).

21. R. P. Hall, M. Sherwin, and A. Zettl, *Phys. Rev. B29*, 7076 (1984).

22. W. Wonneberger and H. J. Breymayer, *Z. Phys. B56*, 241 (1984).

23. G. Grüner, A. Zawadowski, and P. M. Chaikin, *Phys. Rev. Lett.* **46**, 511 (1981).

24. D. E. McCumber, *J. Appl. Phys.* **39**, 3113 (1968); W. C. Steward, *Appl. Phys. Lett.* **12**, 277 (1968); P. Lindelof, *Rep. Prog. Phys.* **44**, 949 (1981).

25. R. P. Hall and A. Zettl, *Solid State Commun.* **55**, 307 (1985).

26. R. P. Hall and A. Zettl, to be published.

27. P. A. Lee, T. M. Rice, and P. W. Anderson, *Solid State Commun.* **14**, 703 (1974).

28. H. Fukuyama, *J. Phys. Soc. Japan* **41**, 513 (1976).

29. H. Fukuyama and P. A. Lee, *Phys. Rev. B* **17**, 535 (1978).

30. P. A. Lee and T. M. Rice, *Phys. Rev. B* **19**, 3970 (1979).

31. A. Fournel, J. P. Sorbier, M. Konczykowski, and P. Monceau, *Phys. Rev. Lett.* **57**, 2199 (1986).

32. J. S. Langer and M. E. Fisher, *Phys. Rev. Lett.* **19**, 560 (1967).

33. M. Tinkham, *Introduction to Superconductivity* (McGraw-Hill), New York, (1975).

34. J. C. Gill, in the Proceedings of the Yamada Conference (Japan, 1986).

35. J. L. Hodeau, M. Marezio, C. Roucau, R. Ayroles, A. Meerschaut, J. Rouxel and P. Monceau, *J. Phys. C* **11**, 4117 (1978).

36. C. H. Chen, R. M. Fleming and P. M. Petroff, *Phys. Rev. B***27**, 4459 (1983).

37. S. Amelinckx, *Direct Observation of Dislocations* (Academic Press, New York, 1964).

Chapter 4

1. R. P. Hall, M. F. Hundley, and A. Zettl, to be published.

2. M. S. Sherwin, R. P. Hall, and A. Zettl, to be published.

3. M. Inui, R. P. Hall, S. Doniach, and A. Zettl, to be published.

4. A. Zettl and G. Grüner, *Phys. Rev. B* **26**, 2298 (1982).

5. For a review of CDW transport, see G. Grüner and A. Zettl, *Phys. Rep.* **119**, 117 (1985).

6. M. P. Everson and R. V. Coleman, *Phys. Rev. B* **28**, 6659 (1984).

7. R. P. Hall, M. F. Hundley, and A. Zettl, *Phys. Rev. Lett.* **56**, 2399 (1986).

8. R. P. Hall, M. S. Sherwin, and A. Zettl, *Phys. Rev. Lett.* **52**, 2293 (1984).

9. A. Zettl and G. Grüner, *Phys. Rev. B* **25**, 2081 (1982).

10. R. P. Hall, M. S. Sherwin, and A. Zettl, *Phys. Rev. B* **29**, 7076 (1984).

11. G. Grüner, A. Zawadowski, and P. M. Chaikin, *Phys. Rev. Lett.* **46**, 511 (1981).

12. S. Sridhar, D. Reagor, and G. Grüner, *Phys. Rev. Lett.* **55**, 307 (1985).

13. D. E. McCumber, *J. Appl. Phys.* **39**, 3113 (1968); W. C. Stewart, *Appl. Phys. Lett.* **12**, 277 (1968).

14. P. S. Hagan and D. S. Cohen, *J. Appl. Phys.* **50**, 5408 (1979); H. Kanter and F. L. Vernon, *J. Appl. Phys.* **43**, 3174 (1972).

15. L. Sneddon, *Phys. Rev. Lett.* **52**, 65 (1984).

16. H. Fukuyama and P. A. Lee, *Phys. Rev. B* **17**, 535 (1978).

17. L. Pietronero and S. Strässler, *Phys. Rev. B* **28**, 5863 (1983); S. N. Coppersmith and D. S. Fisher, *Phys. Rev. B* **28**, 2566 (1983); P. B. Littlewood, *Phys. Rev. B* **33**, 6694 (1986).

18. D. S. Fisher, *Phys. Rev. B* **31**, 1396 (1985); L. Sneddon, *Phys. Rev. B* **29**, 725 (1984).

19. R. P. Hall, M. F. Hundley and A. Zettl, *Physica* **143B**, 152 (1986).

Chapter 5

1. M. S. Sherwin, A. Zettl, and R. P. Hall, *Phys. Rev. B*, to be published.

2. R. P. Hall, M. S. Sherwin, and A. Zettl, *Phys. Rev. Lett.* **52**, 2293 (1984).

3. R. P. Hall, M. S. Sherwin, and A. Zettl, *Phys. Rev. B* **29**, 7076 (1984).

4. P. Monceau, J. Richard, and M. Renard, *Phys. Rev. B* **25**, 931 (1982).

5. E. Ben-Jacob, I. Goldhirsch, Y. Imry, and S. Fishman, *Phys. Rev. Lett.* **49**, 1599 (1982).

6. R. P. Hall and A. Zettl, *Phys. Rev. B* **30**, 2279 (1984).

7. M. Inui, R. P. Hall, S. Doniach, and A. Zettl, *Phys. Rev. B*, to be published.

8. Kurt Wiesenfeld, *J. Stat. Phys.* **38**, 1071 (1985).

9. Mitchell J. Feigenbaum, *J. Stat. Phys.* **19**, 25 (1978); and *J. Stat. Phys.* **21**, 669 (1979).

10. Robert M. May, *Nature* **261**, 459 (1976).

11. M. Ya. Azbel and Per Bak, Brookhaven National Laboratories Report No. 34547 (1984).

12. M. S. Sherwin and A. Zettl, *Phys. Rev. B* **32**, 5536 (1985).

13. Shobo Bhattacharya, *Bull. Am. Phys. Soc.* **33**, 412 (1988).

14. Per Bak, Tomas Bohr, and Morgens Hogh Jensen, in the proceedings of the 59th Nobel Symposium "The physics of chaos and related phenomena", Gräftaavallen, Sweden, 1984, Physica Scripta.

15. M. H. Jensen, P. Bak, and T. Bohr, *Phys. Rev. Lett.* **50**, 1637 (1983); T. Bohr, P. Bak, and M. H. Jensen, *Phys. Rev. A* **30**, 1970 (1984); M. H. Jensen, P. Bak, and T. Bohr, *Phys. Rev. A* **30**, 1960 (1984); P. Bak, *Physics Today* **39**, 38 (1986).

16. L. Glass and R. Perez, *Phys. Rev. Lett.* **48**, 1772 (1983).

17. A. Zettl and G. Grüner, *Phys. Rev. B* **26**, 2298 (1982).

Chapter 6

1. M. Inui, R. P. Hall, S. Doniach, and A. Zettl, to be published.

2. P. A. Lee, T. M. Rice and P. W. Anderson, *Solid State Commun.* **14**, 703 (1974).

3. H. Fukuyama, *J. Phys. Society Japan* **41**, 513 (1976).

4. H. Fukuyama and P. A. Lee, *Phys. Rev. B* **17**, 535 (1978).

5. Hamiltonians similar to Eq. 6.1 were written down previously by W. L. McMillan, *Phys. Rev. B* **12**, 1187 (1975); and P. A. Lee and T. M. Rice, *Phys. Rev. B* **19**, 3970 (1979). An equation of motion similar to Eq. 6.3 was first written down by W. L. McMillan, *Phys. Rev. B* **12**, 1197 (1975).

6. G. Grüner, A. Zawadowski, and P. M. Chaikin, *Phys. Rev. Lett.* **46**, 511 (1981).

7. Leigh Sneddon, M. C. Cross, and Daniel S. Fisher, *Phys. Rev. Lett.* **49**, 292 (1982).

8. J. Bardeen, *Phys. Rev. Lett.* **42**, 1498 (1979); J. Bardeen, *Phys. Rev. Lett.* **55**, 1010 (1985).

9. N. P. Ong, G. Verma, and K. Maki, *Phys. Rev. Lett.* **52**, 663 (1984); N. P. Ong and Kazumi, *Phys. Rev. B* **32**, 6582 (1985).

10. L. P. Gorkov, *JETP Lett.* **38**, 87 (1983); I. Batistic, A. Bjelis, and L. P. Gorkov, *J. Phys. (Paris)* **45**, 1049 (1984).

11. R. P. Hall, M. F. Hundley, and A. Zettl, *Phys. Rev. Lett.* **56**, 2399 (1986).

12. M. F. Hundley and A. Zettl, *Phys. Rev. B* **33**, 2883 (1986).

13. A. Zettl and G. Grüner, *Phys. Rev. B* **26**, 2298 (1982).

14. R. P. Hall, M. F. Hundley, and A. Zettl, to be published.

15. R. P. Hall and A. Zettl, *Solid State Commun.* **50**, 813 (1984); R. P. Hall and A. Zettl, to be published.

16. R. P. Hall, M. S. Sherwin, and A. Zettl, *Phys. Rev. B* **29**, 7076 (1984); M. S. Sherwin, Z. Zettl, and R. P. Hall, to be published.

17. R. P. Hall, M. F. Hundley, and A. Zettl, *Physica* **143B**, 152-154 (1986).

18. S. Sridhar, D. Reagor, and G. Grüner, *Phys. Rev. Lett.* **55**, 307 (1985).

19. W. J. Skocpol, M. R. Beasley, and M. Tinkham, *J. Low Temp. Phys.* **16**, 145 (1974).

20. P. W. Anderson, *Rev Mod. Phys.* **38**, 298 (1966).

21. A. Zettl and G. Grüner, *Phys. Rev. B* **25**, 2081 (1982).

22. S. Shapiro, *Phys. Rev. Lett.* **11**, 80 (1963); A. Zettl and G. Grüner, *Solid State Commun.* **46**, 501 (1983).

23. For a general discussion of entrainment, period-doubling and chaos, see J. Guckenheimer and P. Holms, *Nonlinear Oscillations, Dynamical Systems, and Bifurcations of Vector Fields*, Springer-Verlag, New York, 1983.

24. R. M. Fleming and C. C. Grimes, *Phys. Rev. Lett.* **42**, 1423 (1979).

25. M. Inui and S. Doniach, unpublished.

26. R. P. Hall and A. Zettl, unpublished.

27. D. S. Fisher, *Phys. Rev. B* **31**, 1396 (1985); Leigh Sneddon, *Phys. Rev. B* **29**, 725 (1984).

28. P. Monceau, J. Richard, and M. Renard, *Phys. Rev. B* **25**, 931 (1982).

29. P. Littlewood, *Phys. Rev. B* **33**, 6694 (1986); and private communication.

Chapter 7

1. G. Kriza, A. Janossy, and G. Mihaly, in *Charge Density Waves in Solids*, edited by Gy. Hutiray and J. Solyom (Springer, New York, 1985), p. 426.

2. B. Joos and D. Murray, *Phys. Rev. B* **29**, 1094 (1984).

3. R. P. Hall, M. S. Sherwin, and A. Zettl, *Phys. Rev. Lett.* **52**, 2293 (1984).

4. W. Wonneberger and H. J. Breymayer, *Z. Phys. B* **56**, 241 (1984).

5. P. A. Lee, T. M. Rice, and P. W. Anderson, *Solid State Commun.* **14**, 703 (1974).

Appendix A3

1. L. Mihaly, G. Mihaly, and A. Janossy, in *Charge Density Waves in Solids*, edited by Gy. Hutiray and J. Solom (Springer, New York, 1985), p. 404.